UNIVERSITAT DE BARCELONA

Ni- and Sn-based Colloidal Nanoparticles for Electrochemical Energy Technologies

Junshan Li

Tesi doctoral

Ni- and Sn-based Colloidal Nanoparticles for Electrochemical Energy Technologies

Autor:

Junshan Li

Directors:

Prof. Andreu Cabot

UNIVERSITAT DE BARCELONA

Ni- and Sn-based Colloidal Nanoparticles for Electrochemical Energy Technologies

Memòria presentada per optar al grau de doctor per la Universitat de Barcelona

Programa de doctorat en Nanociències

Autor:

Junshan Li

Directors de la tesis:

Prof. Andreu Cabot

Tutora de la tesis:

Prof. Dr. Alejandro Pérez-Rodríguez

Lloc on s'ha dut a terme la tesi

Institut de Recerca en Energia de Catalunya (IREC)

UNIVERSITAT DE BARCELONA

Ni- and Sn-based Colloidal Nanoparticles for Electrochemical Energy Technologies

2019

UNIVERSITAT DE BARCELONA

Functional Nanomaterials
Catalonia Institute for energy research
Jardins de les Dones de Negre, 1, 2ª pl.
08930 Sant Adrià de Besòs
Barcelona, Spain

Faculty of Physics
University of Barcelona
Gran Via de les Corts Catalanes, 585
08007 Barcelona
Spain

Contents

诗

和

远

方

Life is not only about counting dollars, but also about counting atoms!

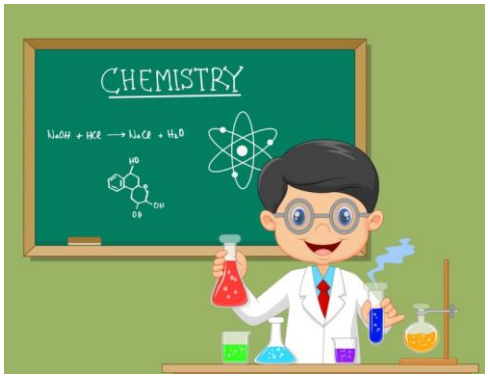

Acknowledgements

With ups and downs, finally I am so happy to say Goodbye here, and also this thesis is a summary of my PhD work at the University of Barcelona (*Universitat de Barcelona-UB*) and Catalonia Institute for Energy Research (*Institut de Recerca en Energia de Catalunya-IREC*) from Sep. 2016 to Mar. 2019 under the *China Scholarship Council (CSC)* scholarship *No. 201600010*. Thus, I would like to extend my deep appreciation to all those who have offered me practical, sincere and unselfish support during my stay here.

First and foremost, I would like to give my sincere gratitude to supervisor Prof. Andreu Cabot, who is leading the *Functional Nanomaterials* (FN) group at IREC. Thank you for bringing me to a fantastic world of nanoscience, providing first-rate facilities, guiding the project and correcting the thesis. I have learned quite a lot from your thinking, inspiring insight and logical rigor in a critical way. Of course, I should always express my thanks to Dr. Zhishan Luo, who opened a door of metallic NPs for me, especially when I was nearly lost and upset in the project.

Here at the same time, thanks go to the members in our FN group: Dr. Alex, Dr. Raquel, Dr. Michaela, Dr. Taisiia, Evgenii, Marcos Batista, Dr. Pablo, Arash, Junfeng Liu, Xiaoting Yu, prof. Kai Pan, Dr. Yu Liu, Yu Zhang, Yong Zuo, Chaoqi Zhang, Mengyao Li, Congcong Xing, Sergi, Albert, Ruifeng Du, Xiang Wang and Dawei Yang. And also I would like to thank these fantastic people from other groups at IREC, Dr. Haibing Xie, Dr. Qin Shi. I am appreciated with the staff of the IREC who helped in many ways. I am really happy and proud to have been working with you.

Furthermore, I am also grateful to these professionals that involved in my project. Thanks Prof. Jordi Arbiol's group at *Universitat Autònoma de Barcelona* (UAB) and *Catalan Institute of Nanoscience and Nanotechnology* (ICN2), including Zhang Ting,

Dr. Pengyi Tang and Maria F. Infante-Carrió for checking the wonderful HRTEM of my samples. And also I owe thanks to the XPS data and analysis from Prof. Jordi Llorca at *Universitat Politècnica de Catalunya* (UPC). Of course, I would like to express my gratitude to Prof. Jun Liu and Dr. Xijun Xu from *South China University of Technology* for the electrochemical measurements for the Li-ion and Na-ion batteries. In addition, thank Dr. He Feng at *Chinese Academy of Sciences* and *University of Chinese Academy of Sciences* for DFT calculations. Those close corporations really played an important role in my project and publications. Thank you very much for all your help.

To those who I knew and met in Barcelona as well as other places all over the world during my last years for PhD but not mention here-Thank you!

Last but not least, I thank every member in my family, especially my wife, parents and parents-in-law for their continuous support and understandings. And lastly, to my little boy *Lexu*, so sorry that I spent little time with you since you came to us with all the cares and love.

Gracias a todos.

With all my best wishes!

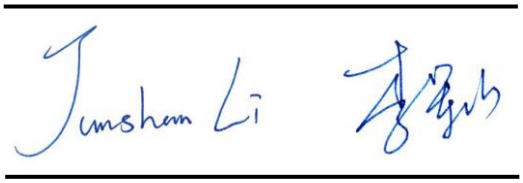

Junshan Li 李军山
Barcelona, Spain
25th April, 2019

没有什么能够阻挡
你对自由的向往
天马行空的生涯
你的心了无牵挂
穿过幽暗的岁月
也曾感到彷徨
当你低头的瞬间
才发觉脚下的路
心中那自由的世界
如此的清澈高远
盛开着永不凋零
蓝莲花

List of publications

My PhD research work have been included in five publications. Four that have already been published in peer-reviewed journals and one is currently in the peer review process. A full copy of each of the publications can be found in the Annex part. The following is the list of publications as the first author included in this thesis:

1. Junshan Li, Yong Zuo, Junfeng Liu, Xiaoting Yu, Ruifeng Du, Ting Zhang, Maria F. Infante-Carrió, Pengyi Tang, Jordi Arbiol, Jordi Llorca, Zhishan Luo, Andreu Cabot. Superior Methanol Electrooxidation Performance of (110)-Faceted Nickel Polyhedral Nanocrystals. Submitted.
2. Junshan Li, Zhishan Luo, Yong Zuo, Junfeng Liu, Ting Zhang, Pengyi Tang, Jordi Arbiol, Jordi Llorca, Andreu Cabot. NiSn Bimetallic Nanoparticles as Stable Electrocatalysts for Methanol Oxidation Reaction. Appl. Catal. B Environ., 2018, 234, 10–18.
3. Junshan Li, Yong Zuo, Ting Zhang, Chaoqi Zhang, Ruifeng Du, Junfeng Liu, Jordi Arbiol, Jordi Llorca, Zhishan Luo, Andreu Cabot. Colloidal Ni-Co-Sn Nanoparticles as Efficient Electrocatalysts for the Methanol Oxidation Reaction. J. Mater. Chem. A, 2018, 6, 22915-22924.
4. Junshan Li, Xijun Xu, Zhishan Luo, Chaoqi Zhang, Xiaoting Yu, Yong Zuo, Ting Zhang, Pengyi Tang, Jordi Arbiol, Jordi Llorca, Jun Liu, Andreu Cabot. Compositionally tuned Ni_xSn alloys as anode materials for lithium-ion and sodium-ion batteries with a high pseudocapacitive contribution. Electrochim. Acta, 2019, 304, 246–254.
5. Junshan Li, Xijun Xu, Zhishan Luo, Chaoqi Zhang, Ting Zhang, Maria Francisca Infante Carrió, Jordi Arbiol, Jordi Llorca, Jun Liu, Andreu Cabot. Co-Sn Solid Solution Nanoparticles as Anode Material for Lithium-Ion Batteries. ChemSusChem, 2019, 12, 1451–1458.

In addition to the publications listed above, I have contributed to some other projects during my PhD that resulted in other publications that are not included in the thesis. They are listed as follows:

1. Junfeng Liu, Zhenxing Wang, Jeremy David, Jordi Llorca, Junshan Li, Xiaoting Yu, Alexey Shavel, Jordi Arbiol, Michaela Meyns, Andreu Cabot. Colloidal $Ni_{2-x}Co_xP$ nanocrystals for the hydrogen evolution reaction. J. Mater. Chem. A, 2018, 6, 11453-11462.

2. Junfeng Liu, Zhishan Luo, Junshan Li, Xiaoting Yu, Jordi Llorca, Déspina Nasiou, Jordi Arbiol, Michaela Meyns, Andreu Cabot. Graphene-supported palladium phosphide PdP_2 nanocrystals for ethanol electrooxidation. Applied Catalysis B: Environmental 242, 258-

266.

3. Yong Zuo, Yongpeng Liu, Junshan Li, Ruifeng Du, Xiaoting Yu, Ting Zhang, Jordi Arbiol, Jordi Llorca, Kevin Sivula, Néstor Guijarro, Andreu Cabot. Solution-processed ultrathin SnS_2-Pt nanoplates for photoelectrochemical water splitting. ACS Appl. Mater. Interfaces, 2019, 11 (7), 6918–6926.

4. Mengyao Li, Yu Liu, Yu Zhang, Yong Zuo, Junshan Li, Khak Ho Lim, Doris Cadavid, Ka Ming Ng, Andreu Cabot. Crystallographically Textured SnSe Nanomaterials Produced from the Liquid Phase Sintering of Nanocrystals. Dalton Trans., Dalton Trans. 2019, 48, 3641-3647.

Apart from the above listed publications, I have some other manuscripts in preparation and will be sent to top journals soon.

Authors' contributions

The work within this thesis was conducted at the Catalonia Institute for Energy Research. Junshan Li, as a PhD candidate, contributed to the experimental work, data analysis and manuscript writing for all the publications presented in this thesis. The contributions of co-authors for each article are shown below this paragraph. The impact factor in 2017/2018 of the journals where the manuscripts were published is provided. All of the publications belong to the 1st quartile according to the Science Citation Index. None of these papers has been previously presented in any other PhD thesis. In all the publications, prof. Andreu Cabot conceived and guided the projects, participated in the results discussion and manuscript corrections.

Chapter 2:

Junshan Li, Yong Zuo, Junfeng Liu, Xiaoting Yu, Ruifeng Du, Ting Zhang, Maria F. Infante-Carrió, Pengyi Tang, Jordi Arbiol, Jordi Llorca, Zhishan Luo, Andreu Cabot. Superior Methanol Electrooxidation Performance of (110)-Faceted Nickel Polyhedral Nanocrystals.

Submitted

The manuscript was prepared through the contribution of all authors. A. Cabot and Z. Luo conceived and guided the project, and supervised the work. J. Li designed the experiments, produced the NCs, conducted XRD, TEM and FT-IR characterization, electrochemical measurements, and wrote the first draft of the manuscript. Y. Zuo, J. Liu, X. Yu and R. Du significantly contributed to the results discussion. T. Zhang, M. F. Infante-Carrió, P. Tang and J. Arbiol performed structural and compositional NCs characterization by means of HRTEM and EELS, and discussed the results. J. Llorca measured and discussed XPS data. The manuscript was corrected and improved by all authors.

Chapter 3:

Junshan Li, Zhishan Luo, Yong Zuo, Junfeng Liu, Ting Zhang, Pengyi Tang, Jordi Arbiol, Jordi Llorca, Andreu Cabot. NiSn Bimetallic Nanoparticles as Stable Electrocatalysts for Methanol Oxidation Reaction. Appl. Catal. B Environ. 2018, 234, 10–18.

Impact factor 2018: 11.698

The manuscript was prepared through the contribution of all authors. In this work, A. Cabot and Z. Luo conceived and guided the project, and supervised the work. J. Li designed the experiments, produced the nanoparticles, conducted XRD, TEM, SEM-EDS and FT-IR characterization, electrochemical measurements, and wrote the first draft of the manuscript. Y.

Zuo and J. Liu significantly contributed to the results discussion. T. Zhang, P. Tang and J. Arbiol performed structural and compositional NCs characterization by means of HRTEM and EELS, and discussed the results. J. Llorca measured and discussed XPS data. The manuscript was corrected and improved by all authors.

Chapter 4:

Junshan Li, Yong Zuo, Ting Zhang, Chaoqi Zhang, Ruifeng Du, Junfeng Liu, Jordi Arbiol, Jordi Llorca, Zhishan Luo, Andreu Cabot. Colloidal Ni-Co-Sn Nanoparticles as Efficient Electrocatalysts for the Methanol Oxidation Reaction. J. Mater. Chem. A 2018, 6 (45), 22915–22924.

Impact factor 2017: 9.931

In this work, the manuscript was prepared through the contribution of all the authors. A. Cabot and Z. Luo conceived and guided the project, and supervised the work. J. Li designed the experiments, produced the nanoparticles, conducted XRD, TEM, SEM-EDS and FT-IR characterization and electrochemical measurements, and wrote the first draft of the manuscript. F. He carried out the DFT calculations. Y. Zuo and C. Zhang performed experiments towards determining the ECSA. J. Liu, X. Yu and R. Du significantly contributed to the results and discussion. T. Zhang, M. F. Infante-Carri´o, P. Tang and J. Arbiol performed structural and compositional characterization of NPs by means of HRTEM and EELS, and discussed the results. J. Llorca measured and discussed XPS data. The manuscript was corrected and improved by all the authors.

Chapter 5:

Junshan Li, Xijun Xu, Zhishan Luo, Chaoqi Zhang, Xiaoting Yu, Yong Zuo, Ting Zhang, Pengyi Tang, Jordi Arbiol, Jordi Llorca, Jun Liu, Andreu Cabot. Compositionally tuned Ni_xSn alloys as anode materials for lithium-ion and sodium-ion batteries with a high pseudocapacitive contribution. Electrochim. Acta, 2019, 304, 246–254.

Impact factor 2017: 5.116

The manuscript was prepared through the contribution of all authors. A. Cabot and J. Liu conceived and guided the project, and supervised the work. J. Li designed the experiments, produced the NPs, conducted XRD, TEM, SEM-EDS and FT-IR characterization, and wrote the first draft of the manuscript. X. Xu performed the electrochemical measurements. Z. Luo, C. Zhang, X. Yu and Y. Zuo significantly contributed to the results discussion. T. Zhang, P. Tang, and J. Arbiol performed structural and compositional NCs characterization by means of HRTEM and EELS, and discussed the results. J. Llorca measured and discussed XPS data. The manuscript was corrected and improved by all authors.

Chapter 6:

Junshan Li, Xijun Xu, Zhishan Luo, Chaoqi Zhang, Ting Zhang, Maria Francisca Infante Carrió, Jordi Arbiol, Jordi Llorca, Jun Liu, Andreu Cabot. Co-Sn nanocrystalline solid solutions as anode materials in lithium-ion batteries with high pseudocapacitive contribution. ChemSusChem, 2019, 12, 1451–1458.

Impact factor 2017: 7.411

The manuscript was prepared through the contribution of all authors. A. Cabot and J. Liu conceived and guided the project, and supervised the work. J. Li designed the experiments, produced the nanoparticles, conducted XRD, TEM, SEM-EDS and FT-IR characterization, and wrote the first draft of the manuscript. Z. Luo, C. Zhang and Y. Zuo significantly contributed to the results discussion. X. Xu performed the electrochemical measurements. T. Zhang, P. Tang, M. F. Infante-Carrió and J. Arbiol performed structural and compositional NCs characterization by means of HRTEM and EELS, and discussed the results. J. Llorca measured and discussed XPS data. The manuscript was corrected and improved by all authors.

Prof. Andreu Cabot

certify the above-mentioned information is true.

Barcelona, 25th April 2019

Everybody is a genius. But if you judge a fish by its ability to climb a tree, it will live its whole life believing that it is stupid.

- Albert Einstein

Preface

The chapters included in this PhD thesis cover the work developed by the PhD candidate Junshan Li at IREC in the period Sep. 2016 - Mar. 2019, supported by *China Scholarship Council* (CSC) scholarship. The thesis is mainly focused on the development of high electrochemical performance alloy NPs in the field of energy conversion and storage, particularly methanol oxidation reaction (MOR) for the application of direct methanol fuel cells (DMFCs) and rechargeable batteries as lithium ion batteries (LIBs) and sodium ion batteries (SIBs) by means of the bottom-up assembly of nanocrystals (NCs) with finely tuned properties obtained by cost-effective and scalable colloidal synthesis routes.

The thesis is structured into 8 chapters. In the first chapter, a general introduction of background, current status, research interests and objectives is presented. Experimental work together with results and discussion are included in chapters 2 to 6. Within the general framework of the electrochemical performance of the fine NCs produced from solution-based process, these 5 chapters are divided into 2 blocks: energy conversion and energy storage.

The energy conversion block consists of 3 chapters. In chapter 2, we used colloidal synthesis methods to produce (110)-Faceted Ni polyhedral NCs with narrow size. After ligand exchange, they were combined with carbon black and Nafion and deposited over glassy carbon to study their electrocatalytic properties toward MOR in DMFCs. In the same work, as a reference for the catalytic activity, Ni spherical NCs were produced in solution and treated in the same way. Electrodes based on Ni polyhedral NCs displayed a notably higher stability in MOR conditions than Ni spherical NCs. They suffered an initial activity loss of ca. 30% during the first 10000 s of operation. Afterward activity stabilized and only a 0.5% decrease was obtained during operation from 20000 to 30000 s. However, the stability of Ni NCs during MOR was still not fully satisfactory.

In previous reports, Sn has been demonstrated to improve Pt performance toward MOR. Surprisingly, NiSn had yet to be tested as anode material for MOR in DMFCs. With this motivation, a new colloidal synthesis route of NiSn bimetallic NPs with 3-5 nm in size was developed. I further demonstrated these NPs to show high electrocatalytic activities towards methanol electroxidation in alkaline media and at the same time significantly improved stabilities when compared with nickel. These results are presented in Chapter 3.

A main advantage of bimetallic catalysts over elemental compositions is their additional degrees of freedom to control the surface electronic structure, to provide optimum active sites for one or various concatenated catalytic reactions, and to improve stability by combined catalytic

reactions. In the same direction, ternary compositions provide even larger opportunities to optimize electronic properties and provide suitable active sites for one or multiple reactions. Motivated by this reasoning, in chapter 4, I detail a procedure to produce ternary $Ni_{3-x}Co_xSn_2$ NPs with tuned composition in all the Ni/Co ratio range ($0 \leq x \leq 3$). The electrodes based on these ternary NPs provided improved catalytic performance toward MOR in alkaline medium when compared with binary Ni_3Sn_2 NPs. The excellent performance obtained with the substitution of small amounts of Ni by Co was concomitant to an increase of the surface coverage of active species and an enhancement of the diffusivity of the reaction limiting species. Additionally, the electrode stability was improved with respect to elemental Ni NP-based electrodes.

Chapters 5-6 display the results of the Sn-based alloy NCs as anode materials in LIBs and SIBs. With the same protocols developed, bimetallic Co_xSn and Ni_xSn NCs with tuned compositions was synthesized. After removing surface ligands, we demonstrated that anodes based on these NPs were characterized by relatively high energy storage capacities, with a high pseudocapacitive contribution and a notable stability.

The last 2 chapters present the conclusion and the future perspectives. Finally, the CV of the author is attached.

Summary of results

Materials produced by solution-based one-pot synthesis, particularly colloidal methods, exhibit excellent properties for different applications, including energy conversion and storage, catalysis, electronic and optoelectronic devices, medicine, etc. The colloidal synthesis of NCs is versatile with various advantages, such as: i) simple synthetic procedure with low reaction temperature and short reaction time; ii) fine control of size, shape and composition at nanoscale; and iii) the use of cheap and simple equipment.

In Chapter 2, colloidal (110)-Faceted Ni polyhedral NCs (16 ± 2 nm) were synthesized and tested as electrodes for methanol electrooxidation. Results obtained from electrodes based on Ni polyhedral NCs were compared with those obtained for electrodes based on Ni spherical NCs. The electrocatalytic properties of electrodes based on these NCs were first investigated in variable concentrations of KOH. We found the $Ni(OH)_2 \leftrightarrow NiOOH$ redox reaction rate was first order with the KOH concentration. The surface coverage of active species was much higher in electrodes based on polyhedral Ni NCs than in spherical ones. On the other hand, the diffusion coefficient of the rate limiting species was higher in electrodes based on spherical NCs. Electrodes based on Ni polyhedral NCs displayed impressive current densities (59.4 mA cm^{-2}) and mass activities (2016 mA mg^{-1}) at 0.6 V *vs.* Hg/HgO in the presence of 1.0 M methanol and 1.0 M KOH, which corresponds to a twofold increase over electrodes based on spherical Ni NCs and over most previous Ni-based electrocatalyts previously reported. Such superior catalytic performance should be ascribed to the proper facets of Ni polyhedral NCs, which provided abundant active sites to promote the oxidation of methanol in alkaline media. Electrodes based on faceted polyhedral NCs displayed a 30% loss of activity during the first few operation hours, but activity stabilized to around a 65% of the initial value after ca. 20000 s operation. These results suggested Ni polyhedral NCs as among the best candidates for MOR.

Chapter 3 reports a new synthetic route to produce NiSn intermetallic NPs with composition control. Detailed electrochemical measurements showed that these NPs exhibited excellent performance for MOR in alkaline solution. Ni-rich NiSn-based electrocatalysts displayed slightly improved performances over Ni-based electrocatalysts. Most notorious was the significantly improved stability of NiSn catalysts compared with that of Ni. This work represented a significant advance in developing cost-effective electrocatalysts with high activity and stability for MOR in DMFCs. This research work was published in *Appl. Catal. B Environ.*

In chapter 4, a series of $Ni_{3-x}Co_xSn_2$ ($0 \leq x \leq 3$) quasi-spherical NPs with narrow size distribution were synthesized by a solution-based one-pot method. Detailed catalytic investigation of methanol oxidation showed that the introduction of small amounts of Co into the structure of NiSn NPs improved the electrocatalytic performance. A preliminary optimized

catalyst composition, $Ni_{2.5}Co_{0.5}Sn_2$, showed a current density of 65.5 mA cm^{-2} and a mass current density of 1050 mA mg^{-1} at 0.6 V vs. Hg/HgO for the MOR in 1.0 M KOH containing 1.0 M methanol. While the introduction of Co slightly decreased the durability with respect to Ni_3Sn_2, $Ni_{2.5}Co_{0.5}Sn_2$ NP-based electrodes demonstrated significant stability during continuous cycling and increased activity at high methanol concentrations. The presence of Sn was found to be essential to improve stability with respect to elemental Ni, although Sn was observed to slowly dissolve in the presence of KOH. Overall, the excellent activity and stability towards the MOR of ternary $Ni_{3-x}Co_xSn_2$ NPs suggested them to be attractive anode materials for DMFCs.

In chapter 5, we reported the synthesis of Ni_xSn NPs with tuned composition ($0.6 \leq x \leq 1.9$) and their performance as anode material in LIBs and SIBs. Among the different compositions tested, best performances toward Li^+ ion and Na^+ ion insertion were obtained for $Ni_{0.9}Sn$ NP-based electrodes. This optimized cycling charge-discharge performance for LIBs provided 980 mAh g^{-1} at 0.2 A g^{-1} after 340 cycles. Additionally, $Ni_{0.9}Sn$ NP-based electrodes were tested in Na^+-ion half cells, exhibiting 160 mAh g^{-1} over 120 cycles at 0.1 A g^{-1}. From CV measurements at different current rates, it was found that the charging process was both capacitive and diffusion controlled, while the capacitive contribution was dominant in both LIBs and SIBs. The pseudocapacitive charge-storage accounted for a high portion of the whole energy storage capacity, which was associated to the small size and the composition of the Ni_xSn NPs used.

In the last chapter of the project, Co-Sn solid-solution NPs with average size in the 6-10 nm range were synthesized via a simple one pot colloidal-based approach. The Co_xSn NP composition was adjusted, $1.3 \leq x \leq 0.3$, by tuning the ratio of the initial precursors. The low synthesis temperature favoured the nucleation of Sn NPs and the subsequent inclusion of Co to the Sn lattice, forming a solid solution with the Sn crystal phase, instead of an intermetallic compound. The same strategy could be used to produce a much more extended range of Co-Sn compositions. Co-Sn NPs presented a Sn-rich surface after exposure to air. These Co-Sn solid solutions were tested as anode materials in LIBs on a half-cell battery system. Among the different compositions tested, $Co_{0.9}Sn$ and $Co_{0.7}Sn$ NPs provided the best performance, with a charge-discharge capacity above 1500 mAh g^{-1} at a current density of 0.2 A g^{-1} after 220 cycles and up to 800 mAh g^{-1} at 1.0 A g^{-1} after 400 cycles. These values were larger than that of graphite currently used in commercial devices and larger than the theoretical maximum for Co-Sn alloys and even for pure Sn. Through the kinetic analysis of $Co_{0.9}Sn$ NPs by the CV measurement, we found these charge-discharge capacities to include a very large pseudocapacitive contribution, up to 81% at a sweep rate of 1 mV s^{-1}, which we related to the small size of the particles.

Resum de Results

Els materials produïts en una síntesi basada en una solució, especialment per mètodes col·loïdals, presenten excel·lents propietats per a diferents aplicacions, incloent la conversió i l'emmagatzematge d'energia, la catàlisi, dispositius electrònics i optoelectrònics, medicaments, etc. La síntesi col·loïdal de nanocristalls (NCs) és versàtil amb diversos avantatges, com ara: i) procediment sintètic simple amb baixa temperatura de reacció i curt temps de reacció; ii) bon control de mida, forma i composició a escala nanomètrica; iii) l'ús d'equipament econòmic i senzill.

En el capítol 2, es van sintetitzar NCs de Ni polièdrics (16 ± 2 nm) que van ser testejats com a elèctrodes per a la electrooxidació de metanol (MOR). Els resultats obtinguts a partir d'elèctrodes basats en NCs de Ni polièdrics es van comparar amb els obtinguts per a elèctrodes basats en NCs de Ni esfèrics. Les propietats electrocatalítiques dels elèctrodes basades en aquests NC van ser investigats per primera vegada en concentracions variables de KOH. Es va trobar que la reacció redox de $Ni(OH)_2 \leftrightarrow NiOOH$ es de primer ordre amb la concentració de KOH. La cobertura superficial d'espècies actives va ser molt més alta en els elèctrodes basats en NCs de Ni polièdrics que en NCs de Ni esfèrics. D'altra banda, el coeficient de difusió d'espècies limitadores va ser major en els elèctrodes basats en NC esfèrics. Els elèctrodes basats en NCs de Ni polièdrics presentaven densitats de corrent sorprenents (59.4 mA cm^{-2}) i activitats màssiques (2016 mA mg^{-1}) a 0.6 V *vs.* Hg / HgO en presència d'1.0 M de metanol i 1.0 M KOH, que correspon al doble dels obtinguts amb elèctrodes basats en NCs esfèrics i en la majoria dels electrocatalizadors basats en Ni publicats prèviament. Aquest rendiment catalític superior s'hauria d'atribuir a les propietats pròpies de dels NCs de Ni polièdrics, que proporcionaven abundants llocs actius per promoure l'oxidació del metanol en mitjans alcalins. Els elèctrodes basats en NC polièdrics mostren una pèrdua d'activitat del 30% durant les primeres hores de funcionament, però l'activitat es va estabilitzar al voltant d'un 65% del valor inicial després de ca. de 20.000 s d'operació. Aquests resultats van suggerir els NC de Ni polièdric com un dels millors candidats per a la MOR.

En el capítol 3 es presenta una nova ruta sintètica per produir NCs de NiSn amb control de composició. Les mesures electroquímiques fetes amb aquests NCs van demostrar que aquests NCs presentaven un rendiment excel·lent per MOR en solució alcalina. Els electrocatalitzador rics en Ni mostren una petita millora respecte els electrocatalitzadors de Ni elemental. La més notòria millora va ser sobre l'estabilitat dels catalitzadors de NiSn en comparació amb la de Ni. Aquest treball va representar un avenç significatiu en el desenvolupament d'electrocatalitzadors

per MOR amb alta activitat i estabilitat. Aquest treball de recerca es va publicar a *Appl. Catal. B Environ*.

Al capítol 4, es va sintetitzar una sèrie de NCs quasi-esfèrics de $Ni_{3-x}Co_xSn_2$ ($0 \leq x \leq 3$) amb una distribució de mida estreta mitjançant un mètode basat en solució. Una investigació detallada del efecte catalític de l'oxidació de metanol va demostrar que la introducció de petites quantitats de Co en l'estructura del NiSn millorava l'activitat electrocatalítica. Una composició catalítica optimitzada preliminar, $Ni_{2.5}Co_{0.5}Sn_2$, va mostrar una densitat de corrent de 65.5 mA cm^{-2} i una densitat de corrent màssica de 1050 mA mg^{-1} a 0.6 V *vs*. Hg / HgO per MOR en 1.0 M KOH que contenia 1.0 M de metanol. Mentre que la introducció de Co disminuïa lleugerament la durabilitat respecte els elèctrodes basats en Ni_3Sn_2, els elèctrodes basats en $Ni_{2.5}Co_{0.5}Sn_2$ van demostrar una estabilitat significativa durant cicles continus i amb major activitat a altes concentracions de metanol. La presència de Sn es va considerar que era essencial per millorar l'estabilitat respecte a la Ni element, encara que es va observar que el Sn es dissolia lentament en presencia de KOH. En general, l'excel·lent activitat i estabilitat per MOR de $Ni_{3-x}Co_xSn_2$ suggerien que eren bons materials electrocatalitzadors per MOR.

En el capítol 5, es presenta la síntesi de NCs de Ni_xSn amb composició controlada ($0.6 \leq x \leq 1.9$) i el seu rendiment com a material d'ànode en LIBs i SIBs. Entre les diferents composicions provades, es van obtenir millors resultats cap a la inserció de ions de Li^+ i Na^+ per a elèctrodes basats en $Ni_{0.9}Sn$. L'optimització del cicle càrrega-descàrrega realitzat per LIBs va proporcionar 980 mAh g^{-1} a 0.2 A g^{-1} després de 340 cicles. Addicionalment, els elèctrodes basats en $Ni_{0.9}Sn$ es van provar en mitja cel·la d'ió Na^+ , que presentaven 160 mAh g^{-1} en 120 cicles a 0.1 A g^{-1}. A partir de les mesures de CV a diferents velocitats d'escaneig, es va trobar que el procés de càrrega va ser controlat tant en captació com en difusió, mentre que la contribució capacitiva era dominant tant en LIBs com en SIBs. La pseudocapacitat de càrrega-emmagatzematge representava una gran part de la capacitat total d'emmagatzematge d'energia, que es va associar a la petita mida i a la composició dels NCs de Ni_xSn utilitzats.

En l'últim capítol del projecte, NCs de Co-Sn amb una mida mitjana de 6 a 10 nm es van sintetitzar per un mètode de síntesis col·loïdal. La composició Co_xSn es va ajustar, $1.3 \leq x \leq 0.3$, ajustant la proporció dels precursors inicials. La baixa temperatura de síntesi va afavorir la nucleació de NCs de Sn i la posterior inclusió de Co al entramat de Sn, formant una solució sòlida amb una fase de cristalls de Sn, en comptes d'un compost intermetàl·lic. La mateixa estratègia es podria utilitzar per produir un rang molt més extens de composicions Co-Sn. Els NCs de Co-Sn presentaven una superfície rica en Sn després de l'exposició a l'aire. Aquestes solucions sòlides Co-Sn van ser provades com a materials d'ànode en LIBs en un sistema de bateria de mitja cel·la. Entre les diferents composicions provades, $Co_{0.9}Sn$ i $Co_{0.7}Sn$

proporcionen el millor rendiment, amb una capacitat de càrrega-descàrrega superior a 1500 mAh g^{-1} a una densitat de corrent de 0.2 A g^{-1} després de 220 cicles i fins a 800 mAh g^{-1} a 1.0 A g^{-1} després de 400 cicles. Aquests valors van ser més grans que els de grafit utilitzats actualment en els dispositius comercials i més grans que el màxim teòric per les aliatges de Co-Sn i fins i tot per a Sn pur. Mitjançant l'anàlisi cinètic de $Co_{0.9}Sn$ per voltametria cíclica, es va trobar que aquestes capacitats de càrrega-descàrrega incloïen una contribució pseudocapacitiva molt gran, fins al 81% a una velocitat d'escombrat de 1 mV s^{-1}, que em relacionat amb la petita mida de les partícules.

Simple is beautiful!

As desplayes in the right page.

Abbreviations

Γ*	surface coverage of redox species
ΔE_p	redox potential difference
A	geometrical electrode surface area (0.196 cm^{-2})
acac	acetylacetonate (pentane-2,4-dione, $C_5H_8O_2$)
ATR	attenuated total reflectance
C	initial concentration of redox species
CA	chronoamperometry
CAGR	compound annual growth rate
CB	carbon black
CE	counter electrode
CVC	cyclic voltammetry
D	diffusion coefficient
DEC	diethyl carbonate
DFT	density functional theory
DIBAH	diisobutylaluminium hydride solution
DMFC	direct methanol fuel cell
e.g.	exempli gratia (“for example”, common Latin abbreviation)
$E_{1/2}$	half wave redox potential
EC	ethylene carbonate
EDS	energy dispersive x-ray spectroscopy
EELS	electron energy loss spectroscopy
et al.	*et alii* (“and others”, common latin abbreviation)
etc.	*et cetera* (”and so on”, common latin abbreviation)
F	Faraday constant (96845 C mol^{-1})
FC	fuel cells
fcc	face-centered cubic
FEC	fluoroethylene carbonate
FTIR	Fourier transform infrared spectrometer
GC	glassy carbon
HAADF	high-angle annular dark-field imaging
HRTEM	high-resolution transmission electron microscopy
i	current
I_p	peak current
J_{pa}	peak anodic current densities

J_{pc}	peak cathodic current densities
LIB	lithium-ion battery
MOR	methanol oxidation reaction
n	number of transferred electron per reaction
NC	nanocrystal
NR	nanorod
NMP	*n*-methy1-2-pyrrolidone
NP	nanoparticle
OAc	oleic acid
OAm	oleylamine
OER	oxygen evolution reaction
ORR	oxygen reduction reaction
PVDF	polyvinylidene fluoride
Q	charge under the reduction/oxidation peak
R	gas constant (8.314 J K^{-1} mol^{-1})
RE	reference electrode
SEI	solid electrolyte interphase
SEM	scanning electron microscope
SIB	sodium-ion battery
STEM	scanning transmission electron microscopy
T	temperature
TBAB	borane tert-butylamine complex
TEM	transmission electron microscopy
THF	tetrahydrofuran
TOP	tri-*n*-octylphosphine
TOPO	trioctylphosphine oxide
VASP	Vienna ab-initio simulation package
WE	working electrode
XPS	x-ray photoelectron spectroscopy
XRD	x-ray diffraction
Γ	surface coverage of NiOOH species
v	sweep rate

Chapter 1

Background and Introduction

1.1 Our energy challenges

With the development of our society and explosion of population, we are facing critical challenges in the 21st century. Among the *humanity´s top 10 problems for the next 50 years*, energy is the biggest challenge and also the foundation of a sustainable future for the present and future generations.[1–3]

Recently, the U.S. *Energy Information Administration* (EIA) has released the *International Energy Outlook 2018* (IEO2018), which states that the world energy consumption will grow largely between 1990 and 2040, from 140 trillion kWh to 246 trillion kWh as shown in Figure 1.1a.[4] From the beginning of the century, most of this growth will come from non-OECD (Organization for Economic Cooperation and Development) countries, where demand is driven mainly by strong economic growth and large population. In addition, non-OECD nations are estimated to take up to 64% of the 217 trillion kWh global energy consumption in 2040.[4]

In the same report, as presented in Figure 1.1b, nonrenewable energy produced from petroleum, natural gas, coal and nuclear are displayed as the main energy sources in our daily life and massive industry. New technological developments, environmental considerations and the

limited source of fossil fuels are making renewable energy the world's fastest-growing energy sources, increasing 2.5% per year and accounting for 17.5% of the world energy consumption through the year 2040.

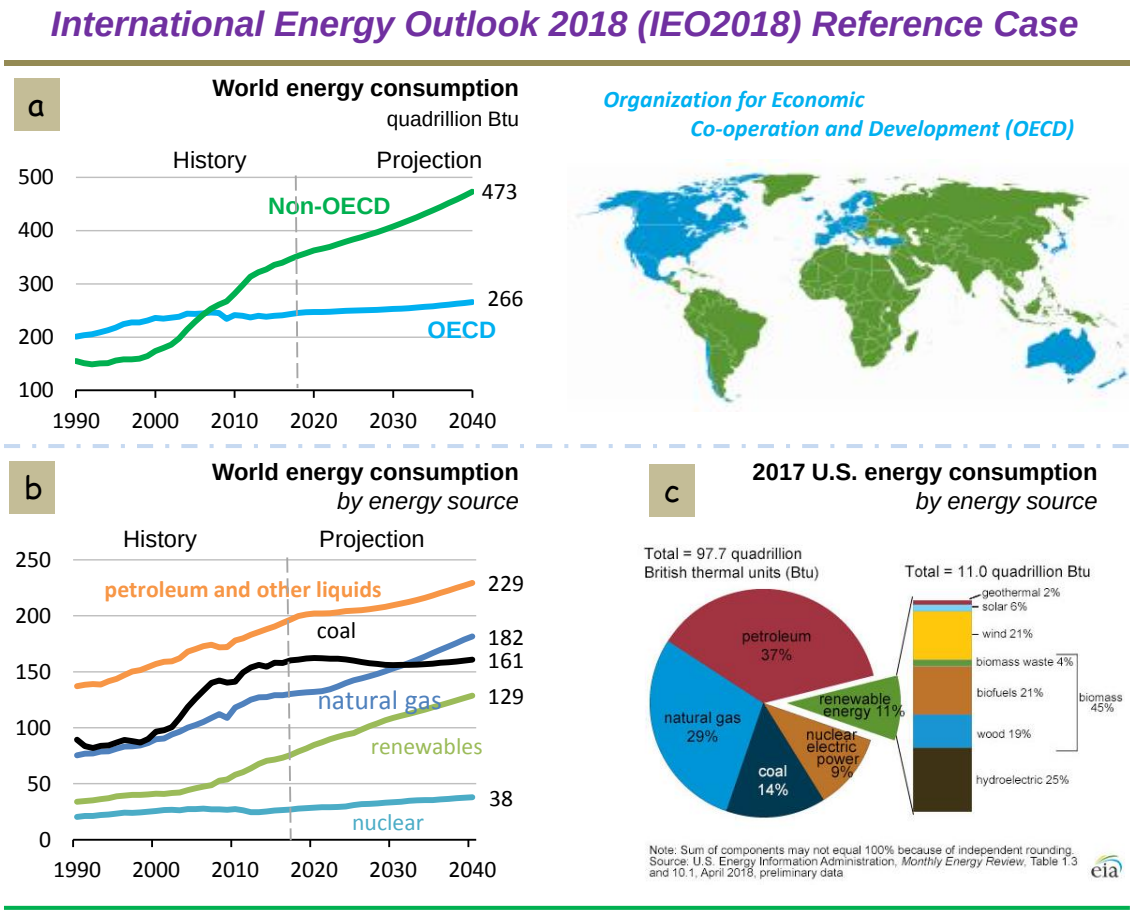

Figure 1.1. a) World energy consumption history vs. projection in the OECD and non-OCED countries. b) World energy consumption history vs. projection by energy source. c) U.S. energy consumption by energy source in 2017. Quadrillion Btu = 293 billion kWh. Source: U.S. Energy Information Administration, International Energy Outlook 2018. Reproduced from reference.[4]

The development and use of renewable energy is varying widely. Taking U.S. as an example, as presented in Figure 1.1c, in 2017 renewable energy accounted for up to 11% of its total energy consumption. Hydroelectric, wind, solar and geothermal source accounted for 25%, 21%, 6% and 2% of the 3.2 trillion kWh of renewable energy consumed, respectively. The largest share of this renewable energy was biomass, specifically 19%, 21% and 4% of the total energy consumption was obtained from wood, biofuels and biomass waste respectively. [4]

1.2 Energy conversion and storage

The energy produced or collected either in renewable or nonrenewable is largely consumed directly or immediately in the field of transportation.[5–7] However, the produced energy that is not used immediately needs to be stored for its future use, which generally involves an additional energy conversion step.[8–11] As shown in Figure 1.2, the energy can be mainly stored electrochemically, electrically, mechanically, thermally, biologically and chemically.[12]

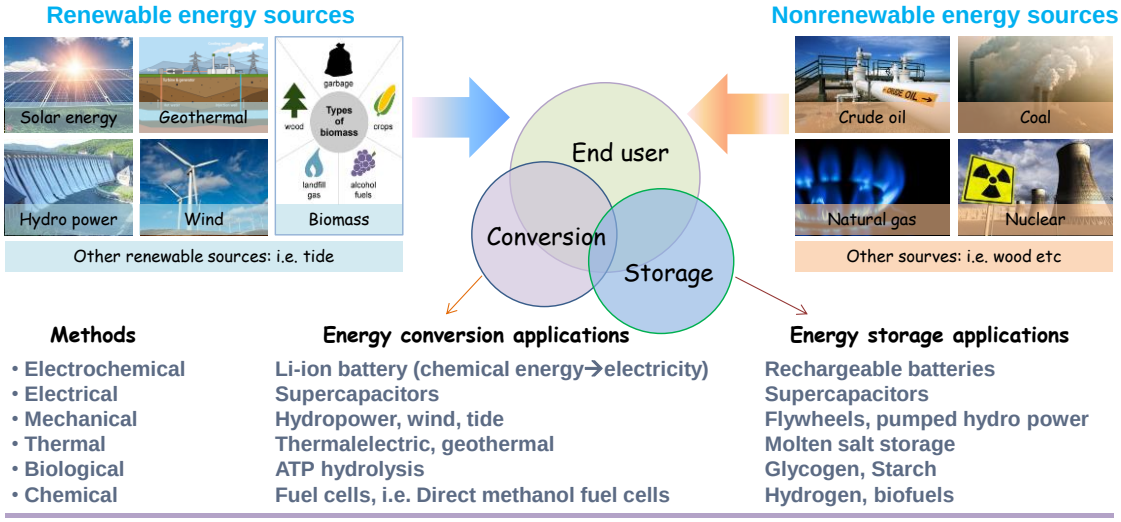

Figure 2.2. Energy conversion and storage: main methods and applications.

In this framework, the optimization of current energy conversion and storage systems is becoming critical. For this optimization, the development of breakthrough materials is required. Main target features of electrochemical energy management technologies, i.e. batteries, supercapacitors, and fuel cells, are safety, high efficiencies, lifetime, manufacturing cost, environmental impact and powder density. These features are largely depending on the materials used.

1.2.1 Fuel Cells-Direct Methanol Fuel Cells

Recent decades have seen unprecedented motivation for the cost-effective development of electrochemical energy technologies. Fuel cells have been known for over a century. Fuel cells directly convert chemical energy into electricity using hydrogen and biofuels as renewable energy sources.[10,13–15] The variation of operating temperatures, electrolytes, membranes and electrodes upon fuel types is presented in Figure 1.3a. Among the different types of fuel cell, direct methanol fuel cells (DMFCs) provide several advantages, including high energy density (the energy density of methanol is an order of magnitude greater than even highly compressed hydrogen, and 15 times higher than LIBs), high efficiency, low emissions, fast mechanical

refueling and simple operation.[16–18] Moreover, easy storage and distribution of methanol makes it one of the most interesting fuels. As one of the most appealing applications, Toshiba recently launched a DMFC in Japan as external power source for mobile electronic devices (Figure 1.3b).[19]

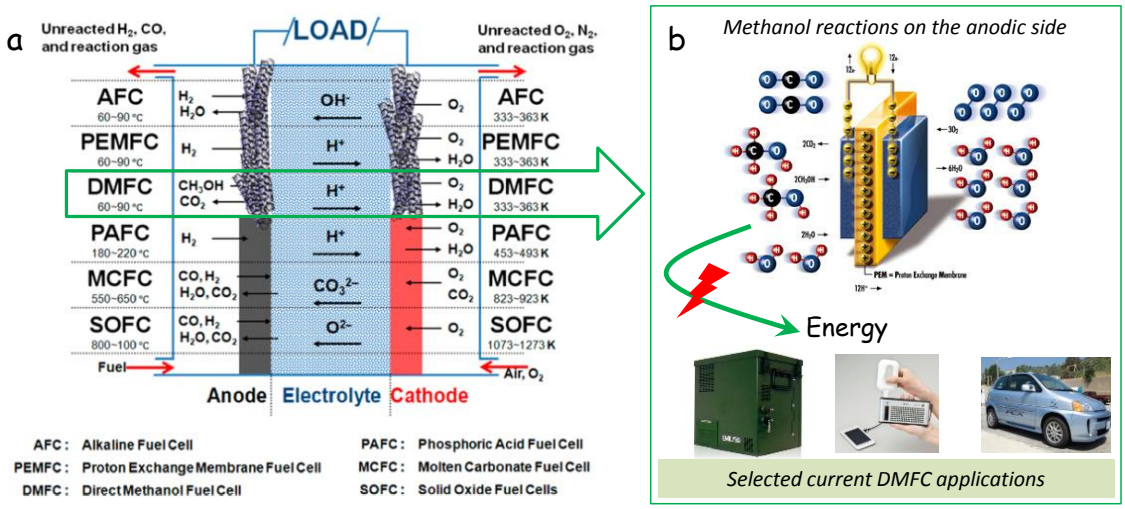

Figure 1.3. a) Schematic representation showing the versatile nature of fuel cells. b) Highlight of the direct methanol fuel cells: methanol oxidation reactions on the anodic side and the applications in the present commercial market.

The DMFC relies upon the oxidation of methanol on a catalyst layer to form carbon dioxide, where the MOR occurs on the anodic side and the oxygen reduction reaction (ORR) takes place on the cathode (Figure 1.3b). State-of-the-art electrocatalysts for the MOR are generally based on noble metals and their alloys, e.g. Pt,[20–22] PtNi,[23–25] PtCo,[26,27] PuCu,[28] PtPd,[29,30] and PtSn[31,32] etc. However, the low tolerance to CO and the high cost and scarcity of these materials have strongly limited the commercialization of DMFCs. Usually, the methanol electrooxidation is carried out in acidic electrolytes. However reports, the catalytic activity toward MOR in alkaline electrolyte is typically higher than in acidic electrolyte.

To this end, the development of cheap and efficient electrocatalysts for MOR has become a very dynamic research field. Among various Pt-free non-noble metal catalysts, Ni is considered to be a promising alternative due to its good surface oxidation properties, moderate cost, and abundant content in the earth. Thus, a great deal of research on Ni-based catalysts toward MOR has been reported. However, the catalytic performance and durability of the reported Ni-based electrocatalysts is not satisfactory. Therefore, the exploration of novel Ni-based catalysts with both high conductivity and excellent catalytic activity is of great importance in this field. According to previous reports, one of the approaches is to add a second metal to Ni-based electrocatalysts, such as early transition metals Co, Cu, and Mn etc. The enhanced activity of

the resulting bimetallic electrocatalysts can be ascribed to both the change in the electronic band structure with the alloy formation and the additional catalytic sites introduced. In addition, tuning the facets of Ni NCs is another option.

1.2.2 Rechargeable devices-Lithium/Sodium ion batteries

Energy storage is an essential component in our society. Among the different energy storage technologies, batteries have been widely used with satisfactory energy density and power density (Figure 1.4a).[34] LIBs in particular have aided the revolution in microelectronics and have become the choice of power source for portable electronic devices since its first commercialization in 1991 by Sony Corporation (Figure 1.4c).[35–37] While safety is the most important factor for portable electronics, cost, cycle life, and energy density are also critical parameters .[38–42]

The energy density, charging rate, and stability of LIBs are still critical performance parameters that has plenty of room for improvement by optimizing both anode and cathode materials.[43–45] At the anode, actual commercial LIBs use graphite (Figure 1.4b), which has a relatively low maximum theoretical capacity (372 mAh g^{-1} to form LiC_6).[46] Alternatively, anode materials such as Sn, Ge and Si provide platforms with potentially higher lithium storage capacities.[47] Among these candidate materials, Sn and Sn-based compounds are particularly appealing owing to their abundance, low cost and high electrical conductivity.[38,48–50]

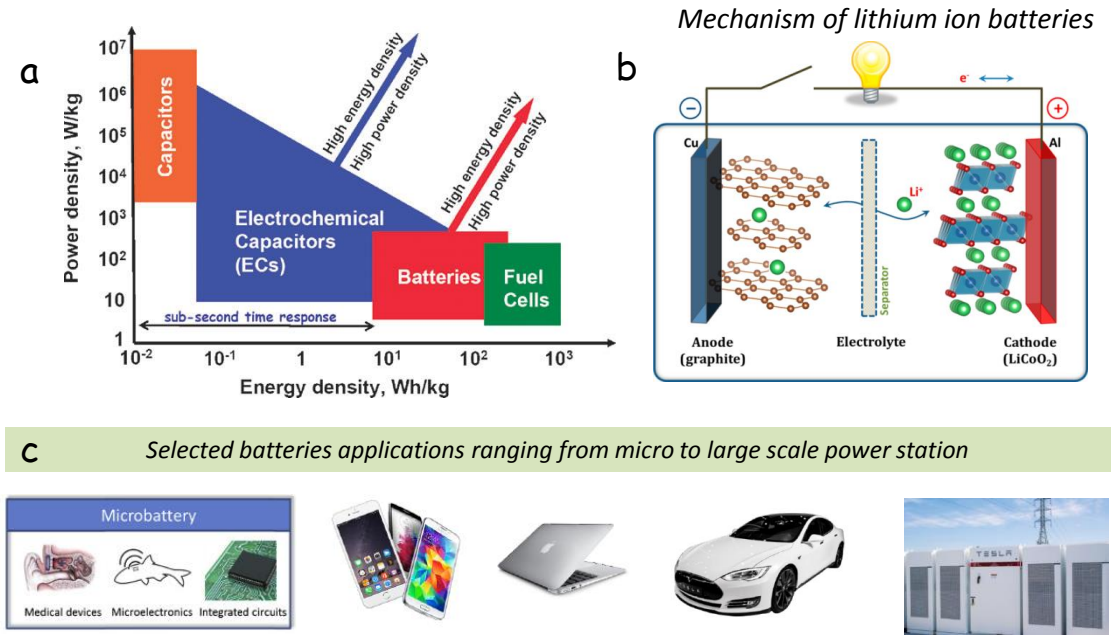

Figure 1.4. a) Energy and power density comparison between existing electrochemical energy storage technologies. Lithium ion batteries: b) the mechanism of lithium ion batteries and c) different commercial applications.

1.2.3 Materials for energy conversion and storage: Alloy NPs

Alloys have been used since ancient times, primarily in the bronze age.[60] Currently, we manufacture and use a large range of alloys in a wide variety of applications, such as steel, solder, brass, pewter, duralumin, bronze and amalgams. In some cases, a combination of metals may reduce the overall cost of the material while preserving important properties. In other cases, the combination of metals imparts improved properties with respect to the constituent elements, such as corrosion resistance or mechanical strength.

Alloys are classified into two categories depending on the atomic organization: solid-solution alloys and intermetallic compounds.[60] The former is typically classified as substitutional or interstitial solid-solution alloys. If the sized of mixed elements are similar, the final phase would be identical to that of the parent metal with random atomic arrangements (Figure 1.5a).[60] Interstitial solid-solution alloys can be formed if the atoms of one element are sufficiently small to fit within the lattice void of the counterpart element. The latter comprises the formation of a distinct crystal structures with ordered atomic arrangements of the two elements (Figure 1.5a).[60]

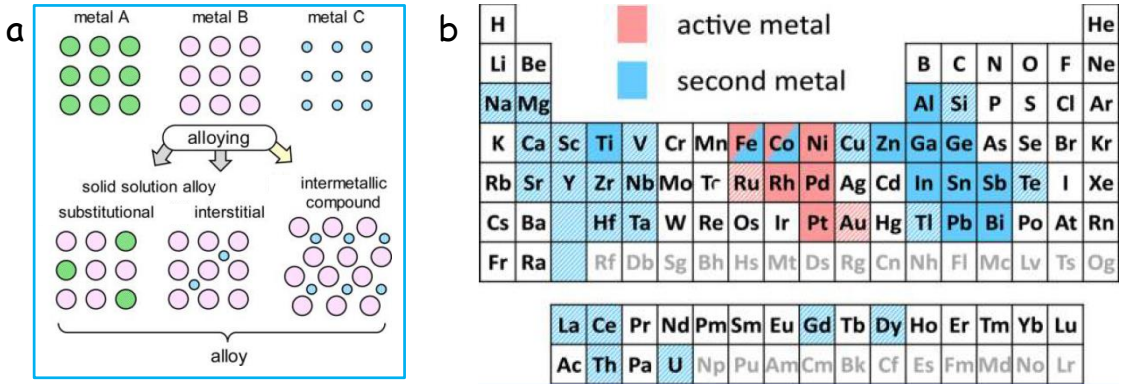

Figure. 1.5. a) Structure of bimetallic alloys: substitutional and interstitial solid-solution alloys and intermetallic compound. b) Active and second metal components of catalytically active intermetallic compounds represented in the periodic table. Lightly colored elements indicate those that are rarely used. Reproduced from the reference.[60]

In general, an alloy should contain a catalytically active element, such as one of the late transition metals (Au, Pt, Pd, Ni, Rh, Co, Ru, and Fe). Therefore, the counterpart metal should be an early transition metal or an usual metallic element, which is well-separated from the active metals in the periodic table (Figure 1.5).[60] The combination of a later transition metal and a typical metal or a half metal (Al, Si, Zn, Ga, Ge, In, Sn, Sb, Te, Tl, Pb, or Bi) is commonly employed, whereas combinations containing an early transition metal (Sc, Ti, V, Y, Zr, Nb, La, Hf, or Ta) have been less frequently reported. [60]

Overall, breakthroughs in alloy materials are urgently required to improve the stability of current battery electrodes and to replace and improve noble metals as (reversible) catalysts in fuel cells. These breakthroughs, which hold the key to new generations of cost-effective and durable products, will be only reached through the control of material properties and understanding of mechanisms and phenomena at the atomic level.

All in all, it is urgent to produce energy (or energy carriers) from renewable sources and then convert them to work as efficiently and cleanly as possible. The design and engineering of functional materials is the key step to fulfill our goal and future perspectives. As an emerging dynamic field, nanoscience and nanotechnology provide us many more possibilities to optimize materials by tuning their parameters nanoscale. In the past several decades have witnessed the huge success of nanomaterials with the motivation of *Cheaper, Smaller and Faster*.

For all this, will nanoscience and nanotechnology pave a path for a sustainable future?

1.3 Nanoscience and nanotechnology

Date back to the year 1959, Nobel laureate Richard P. Feynman, in his famous speech to the American Physicist Society, said "*in the year 2000, when they look back at this age, they will wonder why it was not until the year 1960 that anybody began seriously to move in this direction*" in a lecture *There's Plenty of Room at the Bottom: An Invitation to Enter a New Field of Physics*.[61] Later in 1979, the term "nano-technology" was first used by Norio Taniguchi.[62] Thus, nanotechnology as a new field in the early 1980s has been booming with the invention of advanced microscope. Since this new century, the field garnered increased scientific, political, and commercial attention that led to both controversy and progress. Meanwhile, commercialization of products based on advancements in nanoscale technologies began emerging.

1.3.1 What are nanomaterials and why are they interesting

Nanomaterials are defined as materials that have at least one dimension in the range between 1 and 100 nm.[63] Nanomaterials are often categorized as to how many of their dimensions fall in the nanoscale.[64] Following the sorting criteria, 0D, 1D, 2D and 3D of carbon based fullerene, nanotube, graphene and graphite respectively are presented in Figure 1.6a.[65]

If the materials are downsized to the nanoscale range, new properties arise. For 30 nm Au NPs, lower melting point, different color and better conductivities were observed compared to bulk Au.[65] In addition the more atoms are located on the surface of NPs, the more active sites would

be formed, i.e. nanostructuring, supports or well-defined shapes were introduced (as shown in Figure 1.6b).[66] In the same picture, another advantage of nanomaterials is to increase the intrinsic properties, by forming a core-shell structure, alloy or other confinements. For example on ferric hydroxides on nanoparticle size, the band gap decreases from 2.95 to 2.18 eV with increasing NP size from 7 nm to 120 nm.[67]

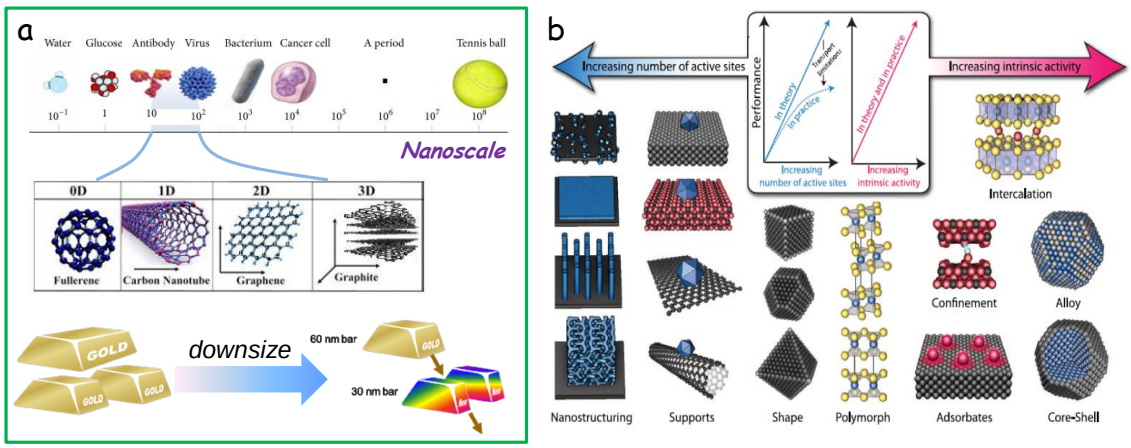

Figure 1.6. a) Materials in the nanoscale range: examples of the scales, classification and new properties arising from the downsized Au. b) Schematic of various nanomaterials development strategies, which aim to increase the number of active sites and/or increase the intrinsic activity of each active site. Reproduced from the reference.[65,66]

Today's scientists and engineers are finding a wide variety of ways to deliberately make materials at the nanoscale to take advantage of their enhanced properties such as higher strength, lighter weight, increased control of light spectrum, and greater chemical reactivity than their larger-scale counterparts. A large number of nanomaterials are currently at the laboratory stage of manufacture, many of them already are being commercialized.

1.3.2 The nanotechnology applications and outlook

Attracting worldwide attention, nanomaterials and nanotechnology have been widely used in the environmental protection, healthcare, energy, medicine, food, cosmetics, military, aerospace and devices as well as many other fields in our daily life and in industry.[68] A selection of fields where nanotechnology applications are being explored is listed in Figure 1.7a. This fantastic science has largely changed the quality of our life and brought revolutionary progress of human beings.

Owing to its wide range of uses, the global nanotechnology market is expected to grow at a compound annual growth rate (CAGR) of around 20% during the forecasted period of 2015-2020. The global market for nanotechnology products was valued at $120 billion in 2015 and

increased to about $530 billion in 2020.[69] Thus, there lies a great opportunity for industry participants to tap the fast growing market, which would garner huge revenue on the back of commercialization of the technology.

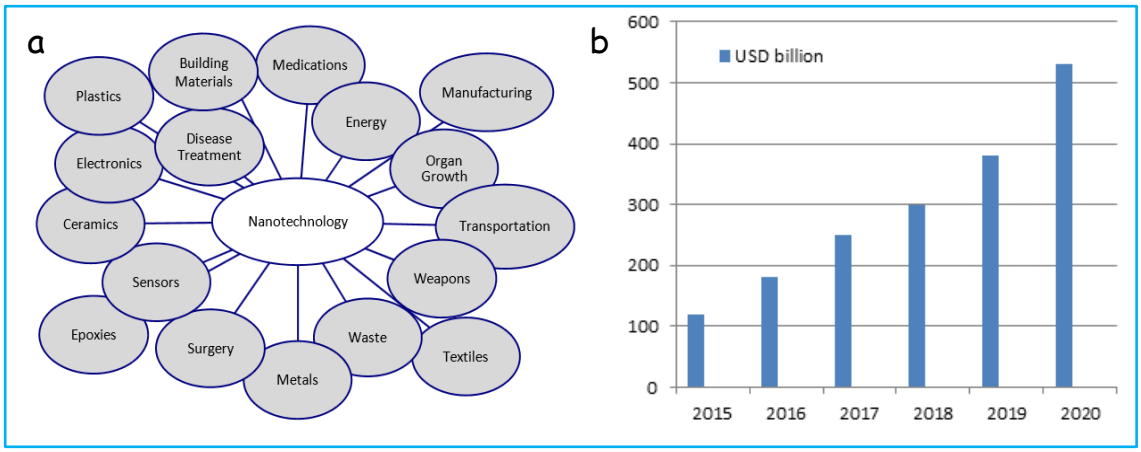

Figure 1.7. a) Selected fields where nanotechnology applications are being explored. b) Nanotechnology market in the year 2015-2020. Reproduced from the reference.[69]

This appealing technology largely depends on the development of new nanomaterials, and the synthetic method is the core point.

1.3.3 Nanomaterials synthesis

Various synthetic techniques/methods have been developed with efforts from all over the world. Generally, two approaches have been known in the preparation of ultrafine particles in industry and/or in laboratory. As shown in Figure 1.8, the first is the breakdown (top-down) method by which an external force is applied to a solid of micrometer or larger range that leads to its break-up into smaller particles.[70] The second is the bottom-up (build-up) method that produces nanoparticles starting from ions or molecules within a gas or liquid based on atomic bonding or molecular condensations.

For many years, liquid phase methods have been the major preparation methods of NPs. And the principal advantage is the facile fabrication of NPs of various shapes, such as nanorods, nanowires, nanoprisms, and nanoplates. Based on the phase of materials involved into the reaction, the bottom-up approach is roughly divided into gaseous phase methods and liquid phase methods. The detailed introduction of these methods can be found in various sources.

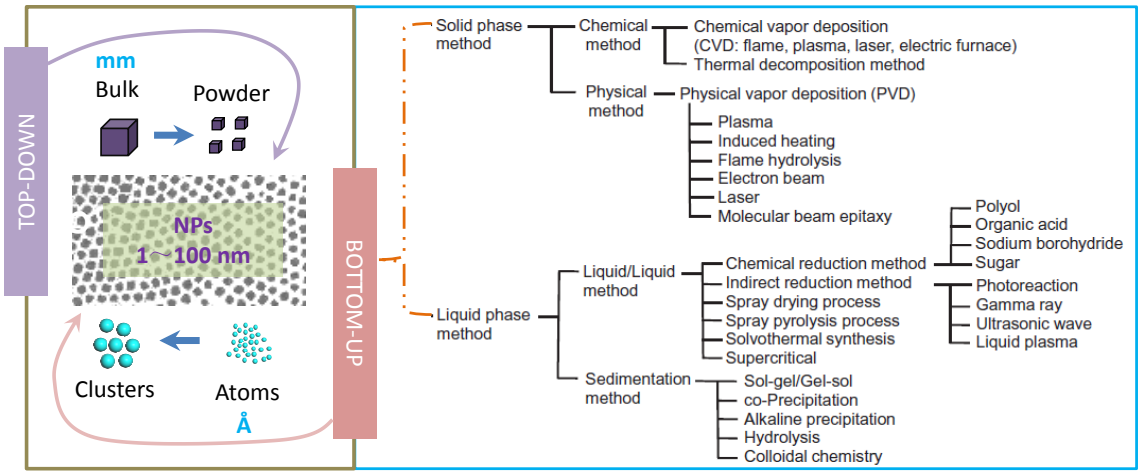

Figure 1.8. Schematic drawing of bottom-down and bottom-up approaches for NPs and detailed bottom-up synthetic methods, reproduced from the book.[70]

1.4 Solution-based NPs synthesis

Liquid phase methods have been the major preparation methods of NPs and they can be sub-divided into liquid/liquid methods, and sedimentation methods. In solution synthesis of nanomaterials, the synthetic process can be generally divided into nucleation and growth process. The nucleation can be recognized as the precursors are firstly dissolved or dispersed in the solvent and subsequently produce the nuclei or clusters, which are new-phase materials generated from the solution.[71] It is of great importance to understand the mechanism and principles of nucleation. The process of nucleation is fast and sub-nano species are involved. This process is the birth of NCs and is very important to the parameters of the final products, such as crystal structure, morphology, size, surface composition and electrical structure.[71]

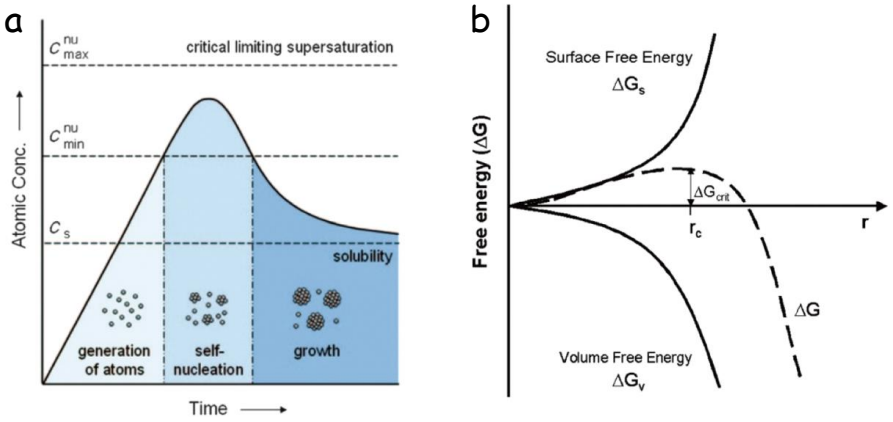

Figure 1.9. a) Plot of atomic concentration against time, illustrating the classical nucleation process and subsequent growth. b) Free energy diagram for classical nucleation process. Reproduced from the reference.[71]

As described in Figure 1.9.a, the nuclei generates when the supersaturation reaches a certain value above the solubility. After the initial nucleation, the process would not stop until the growth species reached the equilibrium concentration or solubility. When the concentration of metal atoms is below the minimum supersaturation, the metal atoms cannot be supplied by the decomposition of metal salts and the nuclei will readily grow to form NCs, which can be defined as the growth step.

From the viewpoint of thermodynamic description, as shown in Fig. 1.9.b, LaMer's group proposed this classical nucleation theory with the free energy change (ΔG).[72] The sum of ΔG can be divided into ΔG_v and ΔG_s which are related to the phase transformation and the formation of new surface in the solution system respectively. As the liquid is less stable than the solid one, the ΔG_v is negative in the crystallization from solution and facilitates the nucleation. In contrast, the ΔG_s is positive due to the new interface of solid/liquid and benefits for the dissolution. Fig. 1b illustrates the competition between the decrease in ΔG_v and increase in ΔG_s in the classical nucleation process. So, the rate of generation of nuclei generated from each unit volume can be defined as in the Arrhenius reaction rate equation.

Actually, the nucleation process from the solution to generate nuclei may follow more complex routes rather than the above-mentioned classical pathway. Wolde and Frenkel adopted the Monte Carlo technique to study the nucleation process in a Lennard-Jones system and reported a two-step mechanism.[73]

1.4.1 Colloidal synthesis

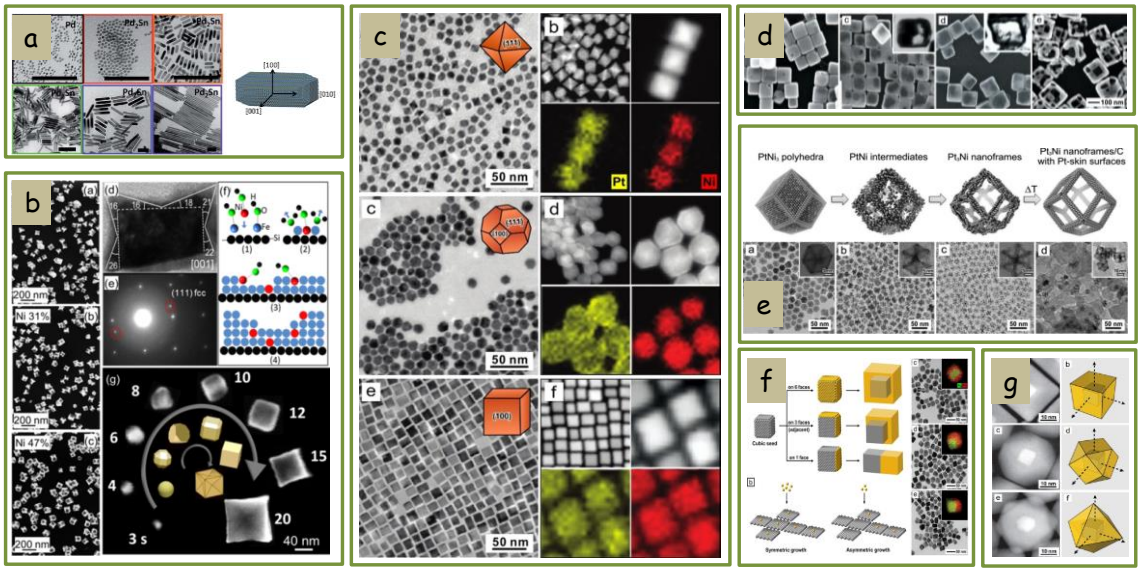

Figure 1.10. Selected alloy NPs developed in colloidal synthesis. a) Pd_2Sn NPs and nanorods.[74] b) FeNi concave nanocubes with different Ni content.[75] c) $PtNi_2$ octahedra, truncated octahedra and nanocubes.[76] d) Ag nanocubes and its hollow interior by galvanic replacement with $HAuCl_4$.[77] e) $PtNi_3$ from polyhedra to nanoframes.[78] f) PdAg core-shell nanocrystals.[79,80] g) Pt@Pd core-shell nanocrystals from cubes to cuboctahedra and octahedra.[81]

Among these techniques, solution-based colloidal synthesis has long been used to fine-tune the form (shape) and size of the NPs by changing the reducing agent, the dispersing agent, the reaction time and the temperature etc. Following this versatile synthetic protocols, well-defined alloy NPs are selected to present in Figure 1.10. As one of the examples in our research group, Luo et. al. produced colloidal Pd_2Sn NRs grown in the [010] direction with tuned size simply by adjusting the amount of foreign Cl^- precursors.[74]

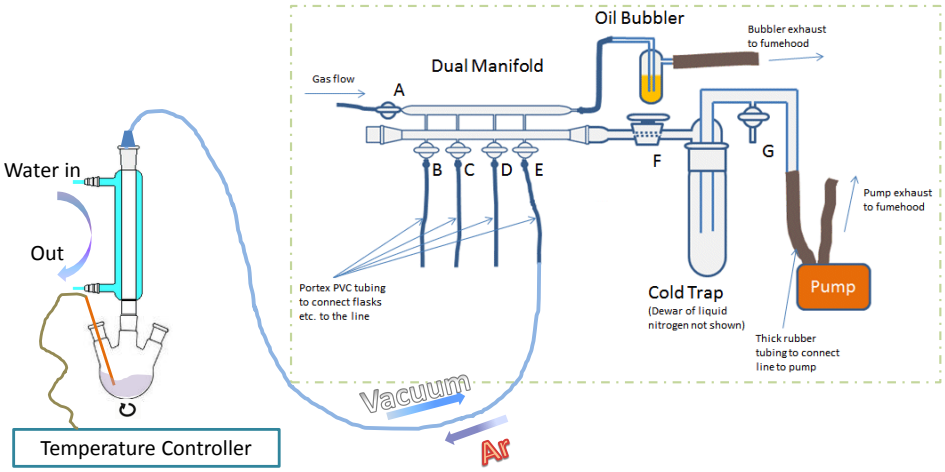

Figure 1.11. Colloidal synthesis setup used in FN lab. Reproduced from the reference.[82]

The colloidal setup is simple and low-cost. As shown in Figure 1.11, the typical colloidal synthesis setup used in our laboratory consists of Schlenk line, pump, condenser, and thermal mantle (compatible with a temperature controller) and reaction flask. This method produces monodisperse NPs with narrow size distribution, well-defined morphology and tuned composition based on the mid-to-high-temperature thermal decomposition/reaction of metal-organic or metal salt precursors in high-boiling non-polar solvent and/or in the presence of surfactant agents. In addition, the technique is beneficial for controlling concentrations of precursors and surfactants, reaction temperature, heating rate, reaction time, and exotic species etc. The obtained NPs are generally stable in solution in nonpolar solvent due to the hydrophobic surfactant used. The presence of organic ligands at the surface of nanoparticle building blocks strongly limits both, the material electrical properties and its ability to interact with the media.[83] Therefore the use of NPs for any application where charge transfer or transport is involved, organic ligands used in the synthesis need to be removed or exchanged.

1.5 Present research interests and challenges

To produce non-precious metallic NPs, various synthetic methods have been proposed, including ball milling, sol-gel, co-precipitation, chemical reduction, sputtering deposition, colloidal route etc. Among these, colloidal method is very simple process, providing a platform to control the particle size and tune the surface composition at the nanoscale range. All in all, searching for non-precious alloy NPs using the available colloidal setup is of great interests and challenges.

In recent decades, platinum or platinum alloys were the most studied catalysts used in DMFC. The utilization of low-cost nickel for the electrocatalytic oxidation of alcohol molecules has received increasing interest. Nickel-based materials, such as metallic nickel, nickel oxides, and hydroxides, as well as oxy-hydroxides, exhibit an excellent electrocatalytic oxidation performance toward many small organic molecules.[84] Generally, three main strategies have been used to design and tune the catalysts: a) the modification of the catalyst using carbon supports, i.e. carbon nanofiber, carbon nanotubes and graphene have been incorporated in many recently reported Ni based catalysts; b) the control of the catalyst morphology, which is mainly of the consideration of the increasing active sites; c) due to the bi-functional mechanism and the ligand/electronic effect, Ni-based alloys were largely explored and it is found that the alloy strategy was an effective way to promote the activity and stability.[85] Previous results, for example, Co, Ti, Mn, Cu with little catalytic activity could significantly improve the elcetro-activity of Ni when forming alloy.[84,86–90] For example, X. Cui et. al investigated the promoting effect of Co on Ni and the role of Co in promoting MOR with the help of electrochemical

experiments and density functional theory (DFT) study.[90] In addition, the rapid development of nanotechnology, especially in the area of synthesis of nanomaterials facilitates the exploration of the relationship between morphologies/structures and catalytic performance for Ni-based catalysts for MOR. For instance, highly porous branched NiCu networks and one dimensional NiCu structure showed better activity than that of NPs with several nanometers in diameter.[85] However, even in alkaline electrolytes, they lack of a satisfactory activity and durability. Therefore, the exploration of novel Ni-based compounds presenting improved stabilities is required.

For the energy storage field, current commercial LIBs use graphite, which has a relatively low maximum theoretical capacity (372 mAh g^{-1} to form LiC_6).[91] Alternatively, anode materials such as Sn, Ge and Si provide platforms with potentially higher lithium storage capacities: $Li_{22}Sn_5$ (994 mAh g^{-1}), $Li_{22}Ge_5$ (1600 mAh g^{-1}), and $Li_{22}Si_5$ (3000 mAh g^{-1}) respectively.[47] Sn and Sn-based compounds are particularly appealing owing to their relatively high abundance, low cost and high electrical conductivity.[36,41,48] However, the charging/discharging process cause expansion and contraction, with 300% for $Sn/Li_{4.4}Sn$ in volume change.[92] Thus, Sn-based intermetallic compounds (with Ni,[93,94] Co,[95–99] Fe,[92,100,101] Cu,[49,100] Sb[38,102–104]) show superior cycling performance than that of bare Sn anode. The inactive metal can act as a matrix, buffering volume changes and preventing electrochemical aggregation of Sn on the surface of NPs.[92] Moreover, nanosized materials present other advantages: a) high reversible capacity due to the high surface volume ratio; b) fast rate capability because of its shorter Li-ion diffusion paths. Thus, it is desirable to prepare alloy NPs with a uniform size with controlled composition, and further, to study how these properties affect anode performance.

1.6 Objectives

Taking all the aspects mentioned above into consideration, the overall goal of the thesis is to develop alloy NPs not based on Pt or Pt group metals for electrochemical energy technologies. In particular, I will develop Ni- and Sn-base metallic NPs and I will test them as electrodes in two fundamental electrochemical energy technologies: ion intercalation batteries and direct methanol fuel cells. The general aim in each field is to obtain materials able to improve stability of ion intercallation batteries and to enhance catalytic activity and thus current density and efficiency in direct methanol fuel cells. With these overall goals in mind I will:

- Develop solution-based synthesis methods able to produce alloy NPs with controlled size, shape and especially composition and element distribution within each NP. These NPs will be based on earth-abundant and low-cost elements, particularly transition metals such as Ni and Co and other non-noble metals such as Sn.
- Remove long-chain insulating ligands from the surface of the NPs or exchange/replace them with short molecules.
- Prepare inks using the obtained alloy NPs and test their performance as anode materials for methanol oxidation reaction for further application in direct methanol fuel cells. Additional DFT calculations will be carried out the further understand the methanol reaction mechanism.
- Fabricate and assemble the alloy NPs within coin-type cells to test the performance as anode materials in lithium and sodium ion batteries.

There's Plenty of Room at the Bottom:

An Invitation to Enter a New Field of Physics

Richard Feynman
Cal Tech, 1959

"People tell me about miniaturization, and how far it has progressed today. They tell me about electric motors that are the size of the nail on your small finger. And there is a device on the market, they tell me, by which you can write the Lord's Prayer on the head of a pin. But that's nothing; that's the most primitive, halting step in the direction I intend to discuss. It is a staggeringly small world that is below. In the year 2000, when they look back at this age, they will wonder why it was not until the year 1960 that anybody began seriously to move in this direction. *Why cannot we write the entire 24 volumes of the Encyclopedia Britannica on the head of a pin?"*

There's Plenty of Room at the Bottom-Yes, a lot of room for fun indeed!!!

1.7 Reference

1 R. E. Smalley, *MRS Bull.*, 2005, **30**, 412–417.

2 D. J. Nelson and M. Strano, *Nat. Nanotechnol.*, 2006, **1**, 96–97.

3 W. W. Adams and R. H. Baughman, *Science*, 2005, **310**, 1916.

4 U. S. E. I. Administration, International Energy Outlook 2018, https://www.eia.gov/outlooks/ieo/.

5 A. S. ARICÒ, P. BRUCE, B. SCROSATI, J.-M. TARASCON and W. VAN SCHALKWIJK, in *Materials for Sustainable Energy*, Co-Published with Macmillan Publishers Ltd, UK, 2010, pp. 148–159.

6 Q. Zhang, E. Uchaker, S. L. Candelaria and G. Cao, *Chem. Soc. Rev.*, 2013, **42**, 3127.

7 Y. Huang, M. Zhu, Y. Huang, Z. Pei, H. Li, Z. Wang, Q. Xue and C. Zhi, *Adv. Mater.*, 2016, **28**, 8344–8364.

8 W. E. Winsche, K. C. Hoffman and F. J. Salzano, *Science (80-.).*, 1973, **180**, 1325–1332.

9 A. J. Appleby, *Sci. Am.*, 1999, **281**, 74–79.

10 T. Schultz, S. Zhou and K. Sundmacher, *Chem. Eng. Technol.*, 2001, **24**, 1223–1233.

11 N. Demirdöven and J. Deutch, *Science (80-.).*, 2004, **305**, 974–976.

12 B. Peng and J. Chen, *Coord. Chem. Rev.*, 2009, **253**, 2805–2813.

13 B. C. H. Steele and A. Heinzel, *Nature*, 2001, **414**, 345–352.

14 J. R. Selman, *Science (80-.).*, 2009, **326**, 52–53.

15 J. R. McKone, S. C. Marinescu, B. S. Brunschwig, J. R. Winkler and H. B. Gray, *Chem. Sci.*, 2014, **5**, 865–878.

16 P. Kumar, K. Dutta, S. Das and P. P. Kundu, *Int. J. Energy Res.*, 2014, **38**, 1367–1390.

17 S. K. Kamarudin, F. Achmad and W. R. W. Daud, *Int. J. Hydrogen Energy*, 2009, **34**, 6902–6916.

18 M. F. Sgroi, F. Zedde, O. Barbera, A. Stassi, D. Sebastián, F. Lufrano, V. Baglio, A. S. Aricò, J. L. Bonde and M. Schuster, *Energies*, 2016, **9**, 1008.

19 Toshiba : News Release (22 Oct, 2009): Toshiba Launches Direct Methanol Fuel Cell in Japan as External Power Source for Mobile Electronic Devices, https://www.toshiba.co.jp/about/press/2009_10/pr2201.htm, (accessed 21 February 2019).

20 Z. Daşdelen, Y. Yıldız, S. Eriş and F. Şen, *Appl. Catal. B Environ.*, 2017, **219**, 511–516.

21 S. Wu, J. Liu, D. Liang, H. Sun, Y. Ye, Z. Tian and C. Liang, *Nano Energy*, 2016, **26**, 699–707.

22 X. Q. Wu, J. Zhao, Y. P. Wu, W. W. Dong, D. S. Li, J. R. Li and Q. Zhang, *ACS Appl. Mater. Interfaces*, 2018, **10**, 12740–12749.

23 S. Wang, G. Yang and S. Yang, *J. Phys. Chem. C*, 2015, **119**, 27938–27945.

24 Q. Jiang, L. Jiang, H. Hou, J. Qi, S. Wang and G. Sun, *J. Phys. Chem. C*, 2010, **114**, 19714–19722.

25 C. Cui, L. Gan, H. H. Li, S. H. Yu, M. Heggen and P. Strasser, *Nano Lett.*, 2012, **12**, 5885–5889.

26 K. D. Gilroy, A. Ruditskiy, H. C. Peng, D. Qin and Y. Xia, *Chem. Rev.*, 2016, **116**, 10414–10472.

27 S. Chen, P. J. Ferreira, W. Sheng, N. Yabuuchi, L. F. Allard and Y. Shao-Horn, *J. Am. Chem. Soc.*, 2008, **130**, 13818–13819.

28 Y. Liao, G. Yu, Y. Zhang, T. Guo, F. Chang and C. J. Zhong, *J. Phys. Chem. C*, 2016, **120**, 10476–10484.

29 C. H. Cui, H. H. Li, H. P. Cong, S. H. Yu and F. Tao, *Chem. Commun.*, 2012, **48**, 12062–12064.

30 G. You, J. Jiang, M. Li, L. Li, D. Tang, J. Zhang, X. C. Zeng and R. He, *ACS Catal.*, 2018, **8**, 132–143.

31 D.-H. Lim, D.-H. Choi, W.-D. Lee, D.-R. Park and H.-I. Lee, *Electrochem. Solid-State Lett.*, 2007, **10**, B87.

32 D. H. Lim, D. H. Choi, W. D. Lee and H. I. Lee, *Appl. Catal. B Environ.*, 2009, **89**, 484–493.

33 M. C. L. Santos, J. Nandenha, J. M. S. Ayoub, M. H. M. T. Assumpção and A. O. Neto, *J. Fuel Chem. Technol.*, 2018, **46**, 1462–1471.

34 M. Winter and R. J. Brodd, *Chem. Rev.*, 2004, **104**, 4245–4270.

35 N. Nitta, F. Wu, J. T. Lee and G. Yushin, *Mater. Today*, 2015, **18**, 252–264.

36 J. B. Goodenough and K. S. Park, *J. Am. Chem. Soc.*, 2013, **135**, 1167–1176.

37 M. R. Palacín, *Chem. Soc. Rev.*, 2009, **38**, 2565–2575.

38 Z. Liu, T. Song and U. Paik, *J. Mater. Chem. A*, 2018, **6**, 8159–8193.

39 A. Magasinski, P. Dixon, B. Hertzberg, A. Kvit, J. Ayala and G. Yushin, *Nat. Mater.*, 2010, **9**, 353–358.

40 M. F. Oszajca, M. I. Bodnarchuk and M. V. Kovalenko, *Chem. Mater.*, 2014, **26**, 5422–5432.

41 R. Marom, S. F. Amalraj, N. Leifer, D. Jacob and D. Aurbach, *J. Mater. Chem.*, 2011, **21**, 9938–9954.

42 C. M. Park, J. H. Kim, H. Kim and H. J. Sohn, *Chem. Soc. Rev.*, 2010, **39**, 3115–3141.

43 J. Wen, Y. Yu and C. Chen, *Mater. Express*, 2012, **2**, 197–212.

44 H. Huang and X. Wang, *J. Mater. Chem. A*, 2014, **2**, 6266–6291.

45 A. Mauger and C. M. Julien, *Ionics (Kiel).*, 2017, **23**, 1933–1947.

46 A. R. Kamali and D. J. Fray, *Rev. Adv. Mater. Sci.*, 2011, **27**, 14–24.

47 H. Tian, F. Xin, X. Wang, W. He and W. Han, *J. Mater.*, 2015, **1**, 153–169.

48 B. Wang, B. Luo, X. Li and L. Zhi, *Mater. Today*, 2012, **15**, 544–552.

49 W. X. Lei, Y. Pan, Y. C. Zhou, W. Zhou, M. L. Peng and Z. S. Ma, *RSC Adv.*, 2014, **4**, 3233–3237.

50 G. Zeb, P. Gaskell, K. Hu, Y. N. Kim, X. Xiao, T. Szkopek and M. Cerruti, *J. Phys. Chem. C*, 2017, **121**, 16682–16692.

51 X. Yang, C. Cheng, Y. Wang, L. Qiu, D. Li, P. L. Taberna, M. Naguib, P. Simon, M. W. Barsoum, Y. Gogotsi and K. S. Novoselov, *Science*, 2013, **341**, 534–7.

52 C. Liu, F. Li, L.-P. Ma and H.-M. Cheng, *Adv. Mater.*, 2010, **22**, E28–E62.

53 D. R. Rolison, J. W. Long, J. C. Lytle, A. E. Fischer, C. P. Rhodes, T. M. McEvoy, M. E. Bourg and A. M. Lubers, *Chem. Soc. Rev.*, 2009, **38**, 226–252.

54 A. Manthiram, A. Vadivel Murugan, A. Sarkar and T. Muraliganth, *Energy Environ. Sci.*, 2008, **1**, 621.

55 D. E. Scaife, *Sol. Energy*, 1980, **25**, 41–54.

56 Z.-S. Wu, G. Zhou, L.-C. Yin, W. Ren, F. Li and H.-M. Cheng, *Nano Energy*, 2012, **1**, 107–131.

57 Y. Zhong, X. Xia, F. Shi, J. Zhan, J. Tu and H. J. Fan, *Adv. Sci.*, 2016, **3**, 1500286.

58 Y. Yan, J. S. Du, K. D. Gilroy, D. Yang, Y. Xia and H. Zhang, *Adv. Mater.*, 2017, **29**, 1605997.

59 D. Wang and Y. Li, *Adv. Mater.*, 2011, **23**, 1044–1060.

60 S. Furukawa and T. Komatsu, *American Chemical Society*, 2017, vol. 7.

61 W. a Goddard, *Handbook of NANOSCIENCE and TECHNOLOGY*, CRC Press, 2003.

62 A. Sandhu, *Nat. Nanotechnol.*, 2006, **1**, 87–87.

63 G. L. Hornyak, *Introduction to Nanoscience and Nanotechnology*, CRC Press, 2018.

64 G. M. Whitesides, *Small*, 2005, **1**, 172–179.

65 E. F. Mohamed, *Environ. Manag. Sustain. Dev.*, 2017, **6**, 429.

66 Z. W. She, J. Kibsgaard, C. F. Dickens, I. Chorkendorff, J. K. Nørskov and T. F. Jaramillo, *Science (80-.).*, 2017, **355**, eaad4998.

67 I. V. Chernyshova, S. Ponnurangam and P. Somasundaran, *Phys. Chem. Chem. Phys.*, 2010, **12**, 14045.

68 The Royal Society and The Royal Academy of Engineering, *Nanoscience and nanotechnologies: opportunities and uncertainties*, 2004, vol. 46.

69 Nanoscience Congress 2019, Perth, Australia, https://nanoscience.conferenceseries.com/, (accessed 21 February 2019).

70 S. Horikoshi and N. Serpone, *Microwaves in Nanoparticle Synthesis*, Wiley-VCH, 2013.

71 Y. Wu, D. Wang and Y. Li, *Sci. China Mater.*, 2016, **59**, 938–996.

72 V. K. Lamer and R. H. Dinegar, *J. Am. Chem. Soc.*, 1950, **72**, 4847–4854.

73 P. R. Ten Wolde, M. J. Ruiz-Montero and D. Frenkel, *J. Chem. Phys.*, 1999, **110**, 1591–

1599.

74 Z. Luo, J. Lu, C. Flox, R. Nafria, A. Genç, J. Arbiol, J. Llorca, M. Ibáñez, J. R. Morante and A. Cabot, *J. Mater. Chem. A*, 2016, **4**, 16706–16713.

75 N. Moghimi, M. Abdellah, J. P. Thomas, M. Mohapatra and K. T. Leung, *J. Am. Chem. Soc.*, 2013, **135**, 10958–10961.

76 W. He, Y. Li, S. Cai, D. Wang and Y. Wu, *J. Am. Chem. Soc.*, 2012, **134**, 8975–8981.

77 C. M. Cobley and Y. Xia, *Mater. Sci. Eng. R Reports*, 2010, **70**, 44–62.

78 C. Chen, Y. Kang, Z. Huo, Z. Zhu, W. Huang, H. L. Xin, J. D. Snyder, D. Li, J. A. Herron, M. Mavrikakis, M. Chi, K. L. More, Y. Li, N. M. Markovic, G. A. Somorjai, P. Yang and V. R. Stamenkovic, *Science*, 2014, **343**, 1339–43.

79 Y. Xia, X. Xia and H.-C. Peng, *J. Am. Chem. Soc.*, 2015, **137**, 7947–7966.

80 J. Zeng, C. Zhu, J. Tao, M. Jin, H. Zhang, Z.-Y. Li, Y. Zhu and Y. Xia, *Angew. Chemie Int. Ed.*, 2012, **51**, 2354–2358.

81 S. E. Habas, H. Lee, V. Radmilovic, G. A. Somorjai and P. Yang, *Nat. Mater.*, 2007, **6**, 692–697.

82 Tips and Tricks for the Lab: Air-Sensitive Techniques: Education: ChemistryViews, https://www.chemistryviews.org/details/education/3728881/Tips_and_Tricks_for_the_Lab_Air-Sensitive_Techniques_1.html, (accessed 22 February 2019).

83 S. Mourdikoudis and L. M. Liz-Marzán, *Chem. Mater.*, 2013, **25**, 1465–1476.

84 Y. Yu, Q. Yang, X. Li, M. Guo and J. Hu, *Green Chem.*, 2016, **18**, 2827–2833.

85 X. Cui, P. Xiao, J. Wang, M. Zhou, W. Guo, Y. Yang, Y. He, Z. Wang, Y. Yang, Y. Zhang and Z. Lin, *Angew. Chemie - Int. Ed.*, 2017, **56**, 4488–4493.

86 I. Danaee, M. Jafarian, F. Forouzandeh, F. Gobal and M. G. Mahjani, *Int. J. Hydrogen Energy*, 2009, **34**, 859–869.

87 I. Danaee, M. Jafarian, F. Forouzandeh, F. Gobal and M. G. Mahjani, *Int. J. Hydrogen Energy*, 2008, **33**, 4367–4376.

88 M. Jafarian, R. B. Moghaddam, M. G. Mahjani and F. Gobal, *J. Appl. Electrochem.*, 2006, **36**, 913–918.

89 R. Ding, J. Liu, J. Jiang, F. Wu, J. Zhu and X. Huang, *Catal. Sci. Technol.*, 2011, **1**, 1406–1411.

90 X. Cui, W. Guo, M. Zhou, Y. Yang, Y. Li, P. Xiao, Y. Zhang and X. Zhang, *ACS Appl. Mater. Interfaces*, 2015, **7**, 493–503.

91 X. Xu, J. Liu, J. Liu, L. Ouyang, R. Hu, H. Wang, L. Yang and M. Zhu, *Adv. Funct. Mater.*, 2018, **28**, 1707573.

92 S. Wang, M. He, M. Walter, F. Krumeich, K. V. Kravchyk and M. V. Kovalenko, *Nanoscale*, 2018, **10**, 6827–6831.

93 X. Fan, P. Dou, A. Jiang, D. Ma and X. Xu, *ACS Appl. Mater. Interfaces*, 2014, **6**,

22282–22288.

94 J. Liu, Y. Wen, P. A. Van Aken, J. Maier and Y. Yu, *Nano Lett.*, 2014, **14**, 6387–6392.

95 J. He, H. Zhao, J. Wang, J. Wang and J. Chen, *J. Alloys Compd.*, 2010, **508**, 629–635.

96 P. Chen, L. Guo and Y. Wang, *J. Power Sources*, 2013, **222**, 526–532.

97 Z. Du and S. Zhang, *J. Phys. Chem. C*, 2011, **115**, 23603–23609.

98 B. O. Jang, S. H. Park and W. J. Lee, *J. Alloys Compd.*, 2013, **574**, 325–330.

99 N. Mahmood, C. Zhang, F. Liu, J. Zhu and Y. Hou, *ACS Nano*, 2013, **7**, 10307–10318.

100 X. L. Wang, W. Q. Han, J. Chen and J. Graetz, *ACS Appl. Mater. Interfaces*, 2010, **2**, 1548–1551.

101 L. O. Vogt and C. Villevieille, *J. Mater. Chem. A*, 2017, **5**, 3865–3874.

102 M. He, M. Walter, K. V. Kravchyk, R. Erni, R. Widmer and M. V. Kovalenko, *Nanoscale*, 2015, **7**, 455–459.

103 M. Walter, S. Doswald and M. V. Kovalenko, *J. Mater. Chem. A*, 2016, **4**, 7053–7059.

104 M. He, K. Kravchyk, M. Walter and M. V. Kovalenko, *Nano Lett.*, 2014, **14**, 1255–1262.

Chapter 2

Superior Methanol Electrooxidation Performance of (110)-Faceted Nickel Polyhedral Nanocrystals

We present the synthesis of (110)-faceted nickel polyhedral nanocrystals (NCs) and their characterization as electrocatalysts for the methanol oxidation reaction (MOR). Ni NCs were produced at 180 ºC through the reduction in solution of a Ni salt. They were combined with carbon black and Nafion and deposited over glassy carbon to study their electrocatalytic properties. Electrodes based on (110)-faceted Ni NCs displayed a first order reaction with KOH in the concentration range from 0.1 M to 1.0 M. These electrodes were characterized by higher coverages of active species, but lower rate limiting diffusion coefficients when compared with electrodes prepared from spherical Ni NCs. Overall, electrodes based on faceted Ni NCs displayed excellent performance with very high current densities, up to 61 mA cm^{-2} and unprecedented mass activities up to 2016 mA mg^{-1} at 0.6 V *vs.* Hg/HgO in 1.0 M KOH containing 1.0 M methanol. These electrodes also displayed a notable stability. While they suffered an initial activity loss of ca. 30% during the first 10000 s operation, activity stabilized at very high current densities, ~35 mA cm^{-2}, and mass activities, ~1200 mA mg^{-1}, with only a 0.5% decrease during operation from 20000 to 30000 s.

Keywords:
Nanocrystals
Collidal Nanoparticles
Electrocatalyst
Methanol oxidation reaction
Direct methanol fuel cell

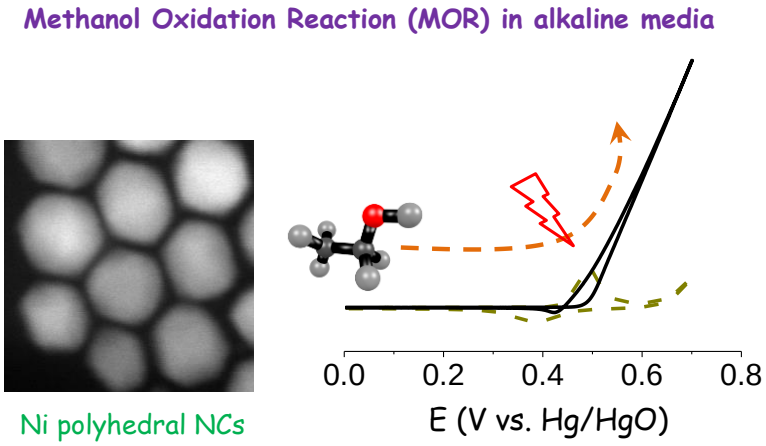

2.1 Introduction

Direct methanol fuel cells (DMFCs) are characterized by low operating temperatures, a relatively simple architecture, high energy efficiencies, a high fuel energy density and convenient fuel storage and transportation.[1–5] In spite of their advantages over competing fuel cell technologies, the requirement of Pt-based electrocatalysts restricts their commercialization to niche markets where cost-efficiency limitations are not a major concern.[5–8]

The widespread implementation of DMFCs requires the development of cost-effective electrocatalysts for the methanol oxidation reaction (MOR).[9] In this direction, Ni is considered a main alternative to noble metals, exhibiting excellent performance towards MOR in alkaline media.[10–12] To optimize its performance, Ni has been alloyed with different elements and it has been combined or grown on a variety of conductive supports.[13–16] Additionally, Ni particles with sizes in the nanometer scale have been produced to maximize the catalyst surface area and thus the density of surface site.[17–20] Besides composition and size, another fundamental catalyst parameter that strongly influence electrocatalytic activity are the exposed facets.[21–23] In related Pt catalyst, which has been more thoroughly studied, single crystal Pt(110) electrodes with more open atomic structures generally exhibit the highest electrocatalytic activities.[24–27] However, (110) facets of single crystals are also generally considered more prone to poisoning and thus to provide lower stabilities. We hypothesize that using small and highly faceted NCs, one can exploit the high activity of a preferential facet, while at the same time take advantage of the large density of interfaces and vertices to catalytically remove poisoning species.

We produced polyhedral Ni NCs with predominant (110) facets with the aim of taking advantage of an *a priori* high activity facet and to characterize how stability could be affected by this geometry. After removing the insulating ligands, these Ni NCs were mixed with carbon black and Nafion and deposited on a glassy carbon support. The activity and stability of such electrocatalysts toward MOR was subsequently analyzed by means of cyclic voltammetry (CV) and chronoamperometry (CA).

2.2 Experimental

2.2.1 Chemicals

Nickel(II) acetylacetonate ($Ni(acac)_2 \cdot xH_2O$ (x~2), 95%, Sigma-Aldrich), tri-n-octylphosphine (TOP, 97%, Strem), oleylamine (OAm, 80-90%, TCI), borane tert-butylamine complex (TBAB, 97%, Sigma-Aldrich), oleic acid (OAc, Sigma-Aldrich), Nafion (10 wt. %, perfluorinated ion-exchange resin, dispersion in water), methanol (anhydrous, 99.8%, Sigma-Aldrich), carbon

black (CB, Vulcan XC72), potassium hydroxide (KOH, 85%, Sigma-Aldrich), trioctylphosphine oxide (TOPO, 99%, Sigma-Aldrich) and ammonium thiocyanate (NH_4SCN, ACS reagent, ≥ 97.5%, Sigma-Aldrich) were used as received without further purification. Hexane, acetone and ethanol were of analytical grade and purchased from various sources. An argon-filled glove-box was used for storing and dealing with sensitive chemicals.

2.2.2 Ni polyhedral NCs

All syntheses were conducted using standard airless techniques. To prepare Ni polyhedral NCs, a solution of 10 mL OAm and 0.5 mL OAc together with 0.4 mmol $Ni(acac)_2 \cdot xH_2O$ were loaded into a 25 mL three-necked flask connected a vacuum/dry argon gas Schlenk line and containing a magnetic bar. The reaction was strongly stirred and degassed under vacuum at 80 °C for 1 hour to remove water, air, and other low-boiling point impurities. Then, a gentle flow of argon was introduced. Meanwhile, 0.5 mmol TBAB was dissolved in 0.5 mL OAm and them the mixture was sonicated for half an hour and degassed for an additional hour. Subsequently, the reaction flask was heated to 180 °C within a ramp of 5 °C/min. At this temperature, the prepared reductant mixture was injected. Upon injection, a visible color change, from deep green to black was immediately observed. The reaction was maintained at this temperature for 1 hour, followed by a rapid cool down to room temperature using a water bath. The content of the reaction mixture were centrifuged at 6000 rpm for 3 min with help of acetone as polar solvent. The isolated powder was suspended using hexane and acetone and then centrifuged again. This entire process was repeated twice. Finally, the NCs were suspended in 5 mL hexane in a vial for further use.

2.2.3 Ni spherical NCs

13 nm *fcc*-Ni NCs were prepared following the procedure described by Y. Chen et al.[28] In a typical synthesis, 1 mmol $Ni(acac)_2$, 7 ml OAm, 0.4 mmol TOP and 0.25 mmol TOPO were loaded in a three-neck flask and stirred under a gentle flow of argon. Temperature was raised to 130 °C and kept for 20 min. Then, the solution was quickly heated to 215 °C and maintained at this temperature for 45 min. Subsequently, the flask was cooled down to room temperature using a water bath. The black precipitate was separated through centrifugation after adding ethanol. NCs were re-dispersed and precipitated three times using hexane and ethanol as solvent and non-solvent, respectively. The product was finally dispersed in hexane.

2.2.4 Characterization

Powder X-ray diffraction (XRD) was measured on a Bruker AXS D8 Advance X-ray diffractometer with Cu K radiation (λ = 1.5106 Å) operating at 40 kV and 40 mA. Scanning electron microscopy (SEM) analyses were performed on a ZEISS Auriga SEM with an energy dispersive X-ray spectroscopy (EDS) detector at 20 kV. Transmission electron microscopy (TEM) analyses were carried out on a ZEISS LIBRA 120, operating at 120 kV, using a 200 mesh Carbon-coated grid from Ted-Pella as substrate. High-resolution TEM (HRTEM) and scanning TEM (STEM) studies were carried out using a field emission gun FEI Tecnai F20 microscope at 200 kV with a point-to-point resolution of 0.19 nm. High angle annular dark-field (HAADF) STEM was combined with electron energy loss spectroscopy (EELS) in the Tecnai microscope by using a GATAN QUANTUM filter. The Fourier transform infrared spectrometer (FTIR) data were recorded on an Alpha Bruker spectrometer before and after ligand exchange.

2.2.5 Ligand exchange

Native organic ligands were displaced from the NC surface using a NH_4SCN solution according to previously published reports.[31] In a typical procedure, 5 mL of a 0.13 M (1.0 g NH_4SCN in 100 mL acetone) NH_4SCN solution in acetone was added to 5 mL as-synthesized NCs in hexanes and the resulting solution agitated for 2 min and maintained unperturbed for another 10 min. The, the solution was centrifuged at low speed and the supernatant was discarded. Further washing process was repeated by centrifuging with equal volume of acetone and hexane. Finally, the precipitated NCs were dried under vacuum overnight.

2.2.6 Electrochemical characterization

Electrochemical measurements were conducted at room temperature on workstation (AutoLab, Metrohm) using conventional three-electrode system: a counter electrode (Pt mesh), a working electrode (Glassy Carbon Electrode) and a reference electrode (Hg/HgO). Catalytic ink was prepared by mixing 2 mg NCs together with 4 mg of CB were added to 1.6 mL MilliQ water/ethanol (v/v = 1:1) and 100 μL of 10 wt% Nafion solution. The working electrode was prepared by a drop-casting method, specifically, 5 μL ink was pipetted onto the polishing and carefully washing the working electrode, and then it was allowed to dry naturally in open air. The Hg/HgO was placed in a salt bridge of 1.0 M KOH. Prior to each experiment, the alkaline electrolyte was purged with high-purity N_2 gas for 30 min. All potential values presented in this paper were referred to the reference electrode, *vs.* Hg/HgO. Cyclic voltammetry (CV) and chronoamperometry (CA) measurements were performed to investigate the activity and stability

for MOR. The current densities were modified by the geometric surface area of the GC electrode (0.196 cm^{-2}) or the metal mass loading (~ 5.9 μg NCs).

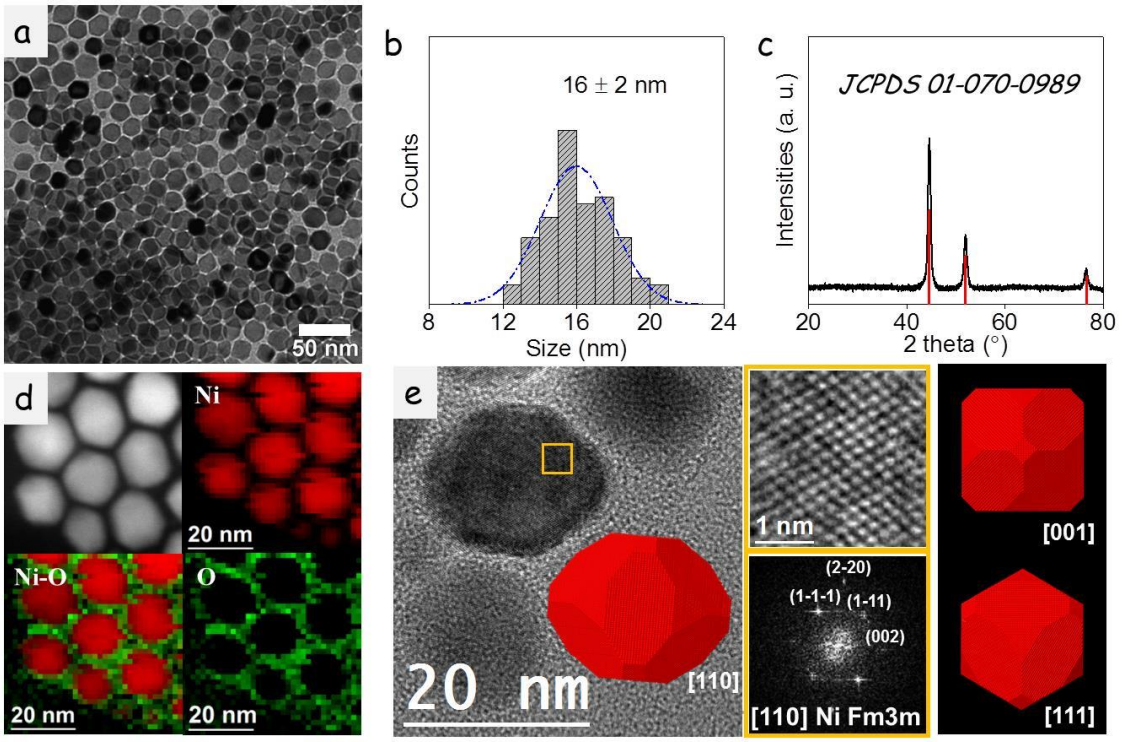

Figure 2.1. a) Representative TEM micrograph of Ni polyhedral NCs. (b) Size distribution histogram. c) XRD pattern of Ni NCs including the JCPDS 01-070-0989 reference corresponding to the Ni *fcc*-phase. d)) ADF-STEM image of several Ni NCs and EELS compositional maps for Ni (red) and O (green). e) Representative HRTEM micrograph of a Ni NC, detail of the orange squared region and its corresponding indexed power spectrum, and 3D atomic models of a NC visualized along two different orientations and displaying a multifaceted morphology with predominant (110) facets. The inset of the HRTEM micrograph displays the same 3D atomic model visualized from its [110] zone axis. The modeled NC is similar to the one observed experimentally. It presents 6{100}, 8{111} and 12{110} facets (the expansion relationship of the cell is 36{110} vs 64{200} vs 48{111}) and is composed by 374,769 Ni atoms.

2.3 Results and Discussion

Ni NCs were produced at 180 °C from the reaction of nickel acetylacetonate with TBAB in the presence of oleylamine and oleic acid (see experimental section for details). Figure 2.1a shows a representative TEM micrograph of the produced material. Ni NCs displayed highly faceted polyhedral geometries and had an average size of 16 ± 2 nm, as shown in Figure 2.1b. XRDanalysis proved the Ni NCs to have the *fcc* crystal phase and displayed no peaks corresponding to any additional crystalline phase (Figure 2.1c).

HAADF-STEM characterization and EELS chemical composition maps showed the Ni NCs to have a homogeneous composition, although a thin oxygen-rich shell could be discerned on its surface (Figure S1). This shell was related both to the presence of oxygen and oxygen-containing species bond to the NC surface and to a slight oxidation of the material during manipulation and transportation before TEM analysis. Extensive HRTEM characterization confirmed the Ni NCs to display a cubic crystal phase (space group = Fm3m) with a = b = c = 3.5157 Å (Figure 2.1e).

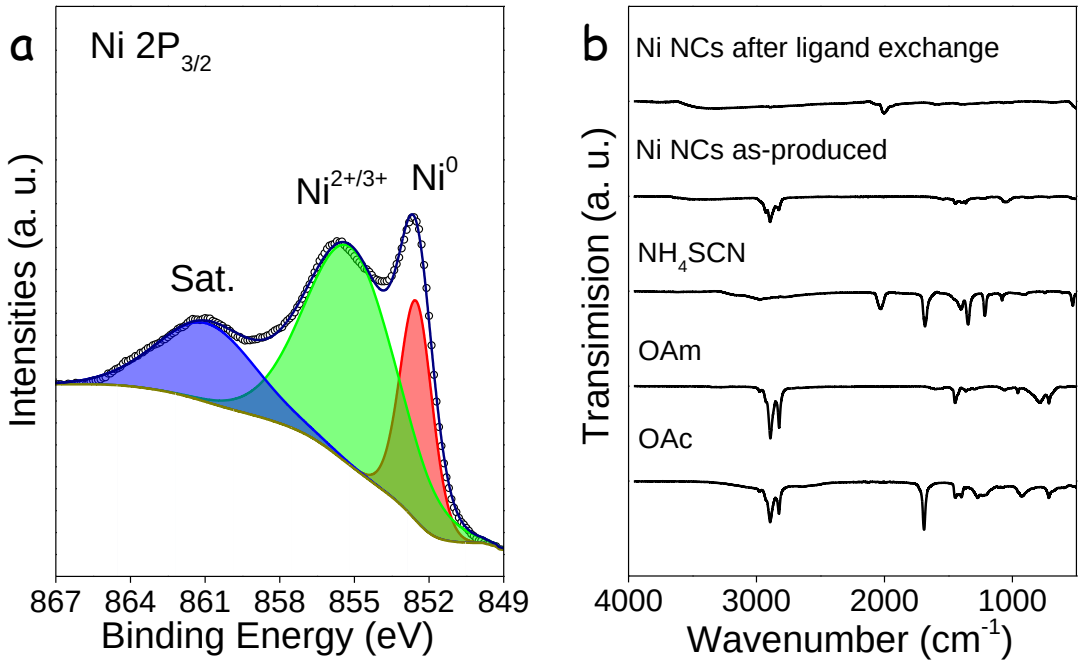

Figure 2.2. a) XPS spectra of the Ni $2P_{3/2}$ region of Ni NCs. b) FTIR spectra of the Ni NCs before and after ligand exchange. Experimental reference spectra of OAc, OAm and NH_4SCN are also included.

XPS analysis showed that the surface of Ni NCs exposed to air presented no less than two different Ni chemical states: Ni^0 and at least one oxidized Ni phase which accounted for 70% of the Ni observed (Figure 2.2a). Taking into account the reduced thickness probed by XPS, we estimate the oxidation layer on the surface of the air-exposed NCs to extend around 1-2 nm.[32,33]

While the formation of these faceted Ni NCs relied on the use of organic ligands to adjust surface energy and provide suitable crystal growth environment, the presence of these organic molecules could strongly limit their electrical properties and ability to interact with the media. Therefore, before their application as electrocatalysts, organic ligands were removed using a 0.13 M NH_4SCN solution (see experimental section for details).[31] After ligand removal, NCs could not be re-dispersed in organic solvents such as hexane. Additionally, IR absorption bands corresponding to the C–H vibration modes (2851-2923 cm^{-1}) completely disappeared from the

FTIR spectrum (Figure 2.2b). These two experimental observations proved the effective removal of organics from the Ni NC surface.[34]

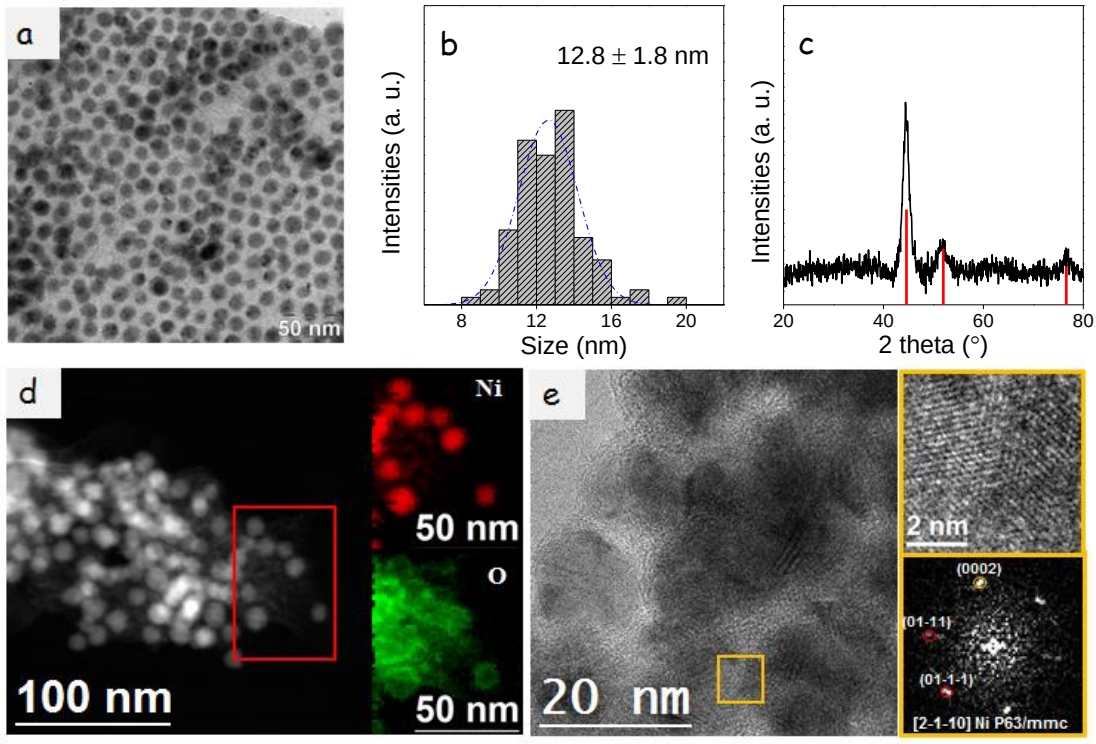

Figure 2.3. a) Representative TEM micrograph of Ni spherical NCs. b) Their size distribution histogram. c) XRD pattern of Ni spherical NCs including the JCPDS 01-070-0989 reference. d) ADF-STEM image of several Ni spherical NCs and EELS compositional maps for Ni (red) and O (green). e) HRTEM image of Ni spherical NCs and power spectrum fitting with the Ni *fcc*-phase.

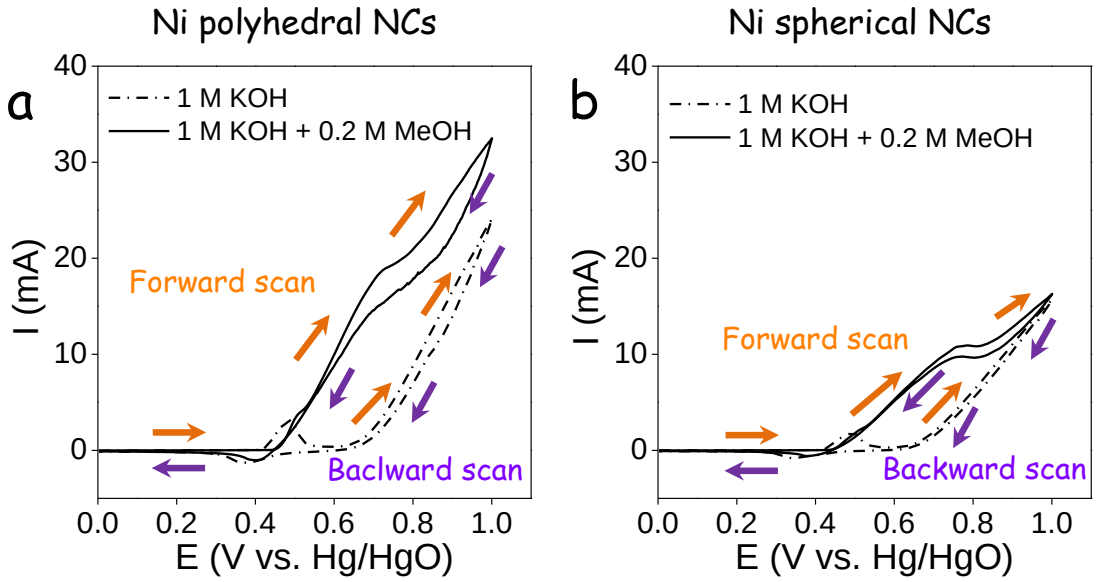

Figure 2.4. Cyclic voltammograms of Ni electrodes in 1.0 M KOH solution in the absence and presences of 0.2 M methanol at a scan rate of 50 mV s^{-1}: a) Polyhedral NCs; b) spherical NCs.

Subsequently, NCs were mixed with carbon black and Nafion in a mixture of water/isopropanol (1:1). The obtained ink was drop-casted on a glassy carbon electrode (see experimental section for details) to produce the electrocatalysts to be tested toward MOR. For the sake of comparison, 13 nm spherical Ni NCs were prepared according to previously published works (see experimental section and Figures 2.3) and treated in the same manner as the Ni polyhedrons to produce the corresponding electrocatalysts.

The electrocatalytic activity of the electrodes prepared from polyhedral and spherical Ni NCs was initially investigated by CV within the potential range 0-1.0 V *vs.* Hg/HgO, in the presence and absence of 0.2 M methanol in a 1.0 M KOH solution (Figure 2.4). The current density of polyhedral NC-based electrodes was systematically and significantly higher than that of electrodes prepared from spherical NCs.

In alkaline media, Ni is oxidized to $Ni(OH)_2$. When increasing the applied voltage, an anodic peak at ca. 0.43 V *vs.* Hg/HgO is ascribed to the oxidation of $Ni(OH)_2$ to NiOOH.[6] In the absence of methanol, at higher potential values, > 0.75 V vs. Hg/HgO, a rise in current density associated with the oxygen evolution from water (OER) is clearly observed.[35] In the reverse scan, NiOOH is reduced back to $Ni(OH)_2$ at ca. 0.35 V *vs.* Hg/HgO.

In the presence of methanol, the oxidation of $Ni(OH)_2$ to NiOOH triggers the electrocatalytic oxidation of methanol, fusing the increase of current density of the two chemical reactions together:

$$Ni(OH)_2 + OH^- \rightarrow NiOOH + H_2O + e^-$$

$$NiOOH + CH_3OH \rightarrow Ni(OH)_2 + \text{products}$$

being the possible products/intermediates of the methanol electrooxidation mainly formic acid, carbonate, formaldehyde, CO and CO_2. At higher applied voltages, the large increase of current corresponding to the OER adds on.

We investigated the kinetics of the $Ni(OH)_2$ oxidation to NiOOH as a function of the KOH concentration for the polyhedral Ni NCs by CV (Figure 2.5a and Table 2.1). We observed the anodic peak current (I_{pa}) to significantly increase and shift to lower potentials (E_{pa}) with the KOH concentration, while the cathodic peak current (I_{pc}) just moderately raised at a similar potential (E_{pc}). Accordingly, the potential difference between the two redox peaks (ΔE) was strongly reduced when increasing the KOH concentration, indicating enhanced electron transfer kinetics between the electrode surface and the electrolyte. The linear fit of the log j vs log $[OH^-]$ plot gave a OH^- reaction order of 1.2 for the $Ni(OH)_2$ to NiOOH reaction, which was consistent with previous literature reports displaying a reaction order of 1.[36]

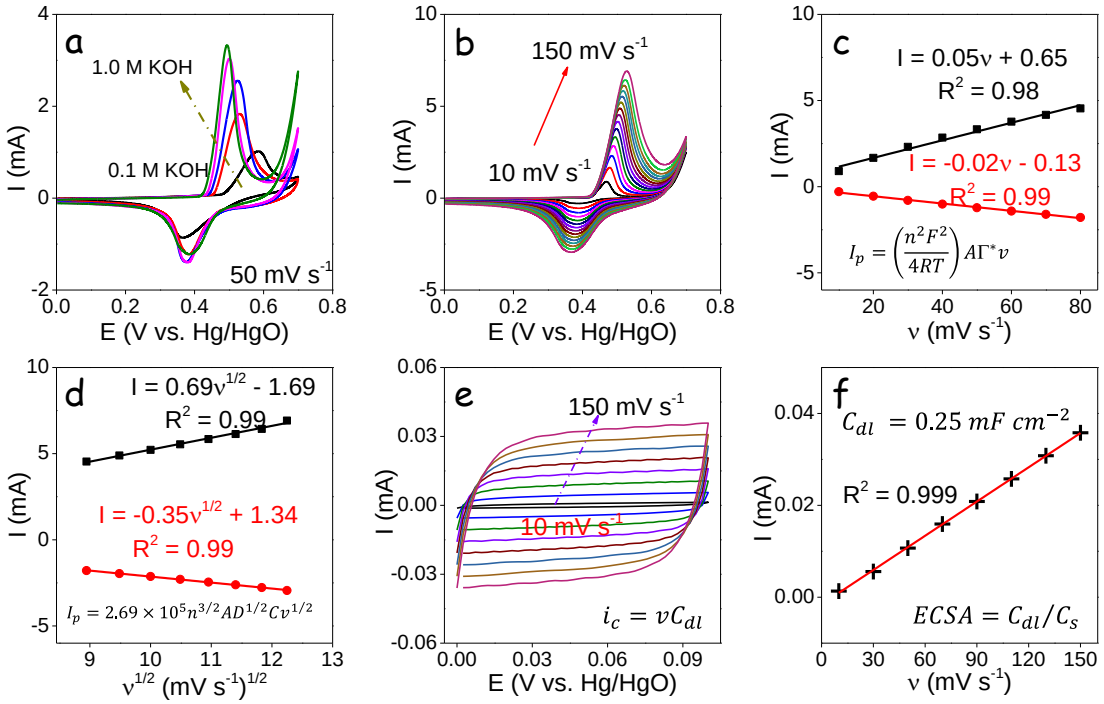

Figure 2.5. a) CV curves from electrodes based on polyhedral Ni NCs in 0.1 M, 0.3 M, 0.5 M, 0.7 M and 1.0 M KOH solution at a scan rate of 50 mV s^{-1}. b) CV curves from electrodes based on polyhedral Ni NCs in 1.0 M KOH solution at increasingly higher potentials sweep rates: 10, 20, 30, 40, 50, 60, 70, 80, 90, 100, 110, 120, 130, 140, 150 mV s^{-1}. c) Linear fitting of anodic and cathodic peak current densities with the scan rate in the low scan rate range (10-80 mV s^{-1}) for polyhedral Ni NCs. d) Linear fitting of anodic and cathodic peak current densities to the square roots of the scan rates in the high scan rate range (80-150 mV s^{-1}) for polyhedral Ni NCs. (e) CVs in the double layer region for electrodes based on polyhedral Ni NCs at scan rates of 10, 30, 50, 70, 90, 110, 130, 150 mV s^{-1} in the non-faradaic range of 0-0.1 V vs. Hg/HgO. f) Corresponding linear fit of the capacitive current vs. scan rates to calculate C_{dl} and ECSA.

When increasing the sweep rate, the position of the anodic peak shifted to higher potential values and the cathodic peak moved to lower potentials (Figures 2.5c and 2.6). The current densities of both anodic and cathodic peaks rose with increasing scan rate. In the low scan rate range ($\nu < 80$ mV s^{-1}), both peak currents were linearly proportional to the scan rate. From the average slope of the anodic and cathodic peaks *vs.* ν, the surface coverage of redox species (Γ*) was estimated (Table 1):[37]

$$I_p = \left(\frac{n^2F^2}{4RT}\right) A\Gamma^* \nu$$

where n, F, R, T and A are the number of transferred electrons (assumed to be 1), the Faraday constant (96845 C mol^{-1}), the gas constant (8.314 J K^{-1} mol^{-1}), temperature and the geometric surface area of the glassy carbon electrodes (0.196 cm^2), respectively. From this equation, the surface coverage of redox species was found to slightly increase with the KOH concentration, from 5.7×10^{-8} mol cm^{-2} in 0.1 M KOH to 1.93×10^{-7} mol cm^{-2} in 1.0 M KOH.

In the high scan rate range (80-150 mV s^{-1}), a linear relationship could be fitted to the dependence of the peak current density with the square root of the voltage scan rate. This dependence is generally related with a diffusion-limited $Ni(OH)_2 \leftrightarrow NiOOH$ redox reaction, where the proton diffusion within the particle is considered the diffusion process that limits the reaction rate: [37]

$$I_p = 2.69 \times 10^5 n^{3/2} A D^{1/2} C v^{1/2}$$

where *C* is the initial concentration of redox species. This equation is valid for a semi-infinite layer. In the case of 16 nm NCs, the related proton diffusion lengths are comparatively very small. Still, using the above equation, rate limiting diffusion coefficients at different KOH concentrations were estimated at 1.19×10^{-10}, 0.45×10^{-10}, 0.81×10^{-10}, 1.20×10^{-10} and 2.02×10^{-10} cm^2 s^{-1} in 0.1, 0.3, 0.5, 0.7 and 1.0 M KOH solution, respectively. When calculating these parameters for spherical NCs (Figure S7), we realized that the coverage Γ* in spherical Ni NCs was much lower than in polyhedral NCs, 3.19×10^{-8} mol cm^{-2} in 1.0 M KOH. On the other hand, the rate limiting diffusion coefficients was higher, 1.45×10^{-9} cm^2 s^{-1} in 1.0 M KOH.

Electrochemically active surface areas (ECSA) were estimated from the electrochemical double-layer capacitance (C_{dl}) on the basis of CVs recorded at different scan rates in the non-faradaic potential range 0-0.1 V vs. Hg/HgO (Figure 3.e).[38] Plotting the capacitive current (I_c) vs. the scan rate (v) yielded a straight line with a slope equal to C_{dl} (Figure 3f). ECSA was calculated by dividing C_{dl} by the specific capacitance (C_s):[39]

$$ECSA = C_{dl}/C_s$$

where C_s is 0.04 mF cm^{-2} based on values reported for metal electrodes in aqueous NaOH solution.[40] For polyhedral Ni NC electrodes in 1.0 M KOH solution, the calculated value of C_{dl} was 0.25 mF cm^{-2}, and ECSA was 6.5 cm^{-2}.

Table 2.1. Summary of the electrocatalytic performance of Ni polyhedral NCs based electrodes in variable concentration of KOH.

C_{KOH} (M)	I_{pa} (mA)	E_{pa} (V *vs.* Hg/HgO)	I_{pc} (mA)	E_{pc} (V *vs.* Hg/HgO)	ΔE (V)	Γ^* mol cm^{-2} ($\times 10^{-7}$)	D cm^2 s^{-1} ($\times 10^{-9}$)
0.1	1.021	0.583	-0.862	0.366	0.217	0.57	0.12
0.3	1.833	0.532	-1.225	0.383	0.149	1.09	0.45
0.5	2.556	0.525	-1.395	0.378	0.146	1.47	0.81
0.7	3.040	0.500	-1.400	0.381	0.120	1.71	1.20
1.0	3.331	0.493	-1.222	0.383	0.110	1.93	2.02

Note: I_{pa}, E_{pa}, I_{pc}, E_{pc} and ΔE were measured from the CVs in solution at a scan rate of 50 mV s^{-1} in 0.1 M, 0.3 M, 0.5 M, 0.7 M and 1.0 M KOH solution.

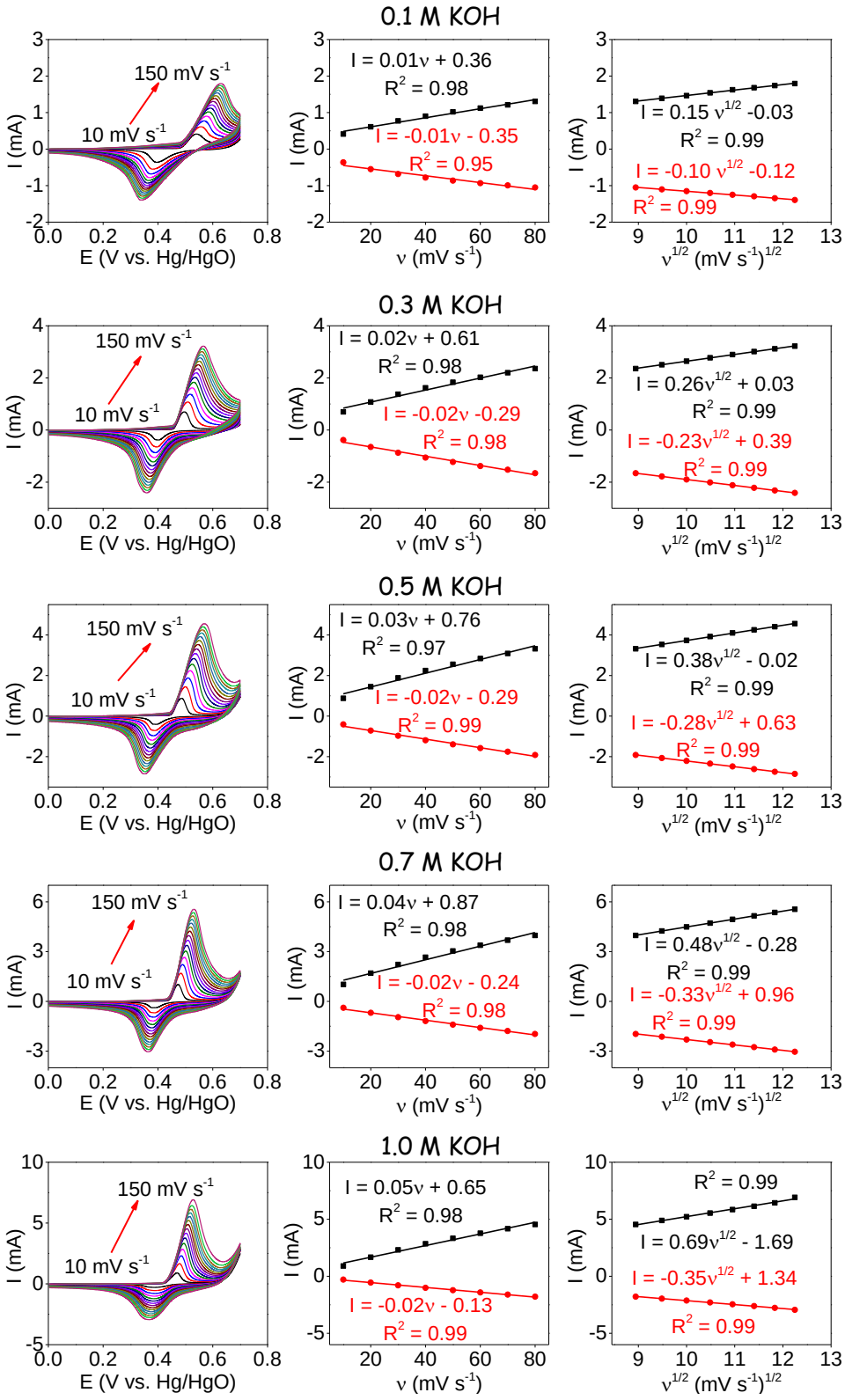

Figure 2.6. Cyclic voltammograms at increasingly higher potentials sweep rates: 10, 20, 30, 40, 50, 60, 70, 80, 90, 100, 110, 120, 130, 140, 150 mV s^{-1} and the linear fitting of anodic and cathodic peak current densities to the scan rates (10-80 mV s^{-1}) and linear fitting of anodic and cathodic peak current densities to the square roots of the scan rates (80-150 mV s^{-1}) of Ni polyhedral NPs in a solution containing 0.1 M KOH, 0.3 M KOH, 0.5 M KOH, 0.7 M KOH and 1.0 M KOH (spherical Ni NCs measured in this solution).

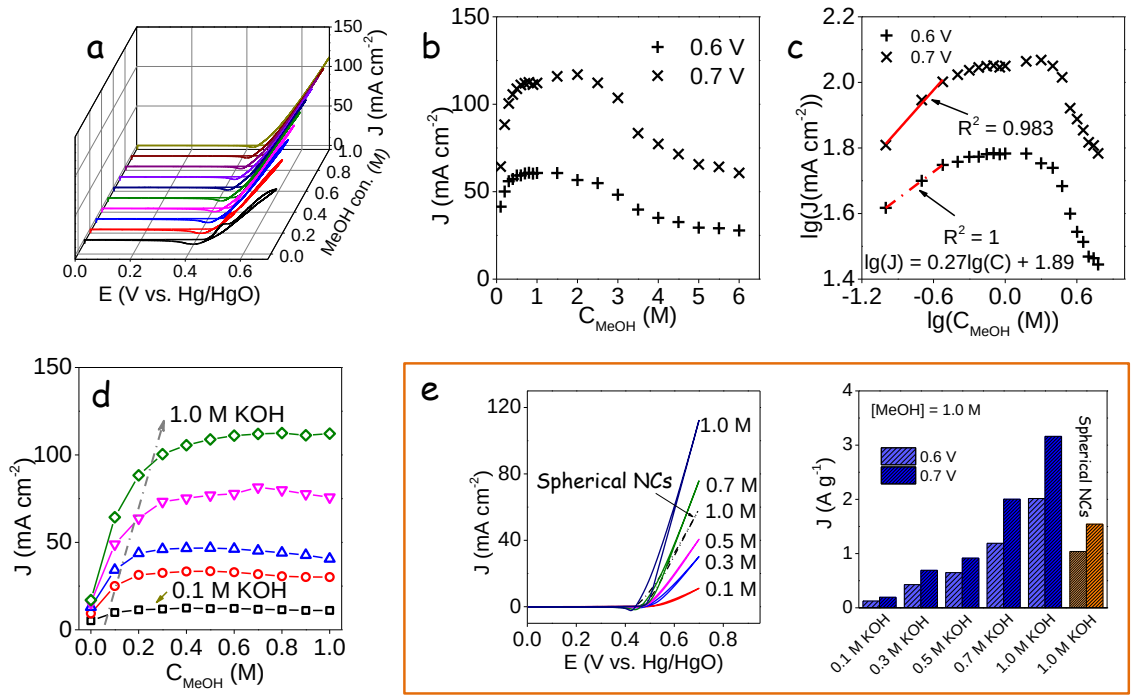

Figure 2.7. a) CVs of an electrode based on polyhedral Ni NCs in 1.0 M KOH solution with different methanol concentrations, from 0.1 M to 1.0 M, at a scan rate of 50 mV s^{-1}. b) Comparison of the current density at 0.6 V and 0.7 V *vs.* Hg/HgO of Ni polyhedral NCs based electrodes as a function of methanol concentrations from 0.1 M to 6.0 M. c) logarithmic dependence of the current density (0.6 V and 0.7 V vs. Hg/HgO) with the methanol concentration. d) CVs of an electrode based on Ni polyhedral NCs in 0.1 M, 0.3 M, 0.5 M, 0.7 M and 1.0 M KOH containing 1.0 M methanol at a scan rate of 50 mV s^{-1}. Data for an electrode based on Ni spherical NPs measured in 1.0 M KOH with 1.0 M methanol is also plotted for comparison. e) The mass current density of an electrode based on Ni polyhedral NCs in 0.1 M, 0.3 M, 0.5 M, 0.7 M, 1.0 M KOH and of an electrode based on Ni spherical NCs in 1.0 M KOH, both in 1.0 M methanol at 0.6 V and 0.7 V. Note: the mass current density at 0.7 V was corrected by subtracting the OER contribution (obtained from measurements in the absence of methanol) to the current densities measured in the presence of KOH and methanol.

Figure 2.7a display CV (50 mV s^{-1}) curves of the Ni polyhedral NCs electrocatalyts in a 1.0 M KOH media containing different methanol concentrations, from 0.1 M to 1.0 M. In addition, the electrochemical response towards methanol concentration for spherical Ni NCs in 1.0 M KOH containing 1.0 M methanol is also studied. It can be observed that the $Ni(OH)_2$ oxidation peak gradually disappeared within the large current density increase related to the MOR when the methanol concentration increased. Figure 2.7b summarizes the current density (0.6 V and 0.7 V *vs.* Hg/HgO) as a function of methanol concentration in 0.1-1.0 M KOH media. The current density monotonically increased with the concentration of KOH. At the same time, it rose gradually with the methanol concentration until 0.3 M of methanol was reached, followed by a rather lazy variation. Specifically, current densities around 110 mA cm^{-2} were measured in 1.0 M KOH solution containing 0.5 M methanol. As shown in Figure 2.7c, a linear fit of the

logarithmic plot of the current density versus the methanol concentration for electrodes based on Ni polyhedral NCs pointed toward an apparent methanol reaction order of around 0.3 at 0.6 V.

Figure 2.7d displays the CVs of electrodes based on polyhedral Ni NCs in 0.1 M, 0.3 M, 0.5 M, 0.7 M and 1.0 M KOH and of an electrode based on spherical Ni NCs in 1.0 M KOH. For these measurements, methanol concentration was set at 1.0 M. The current density in the vertical axis was normalized by the surface area of the electrode. As expected, MOR performances were strongly dependent on the alkaline media concentration. At equal KOH and methanol concentrations, polyhedral NCs provided close to twofold higher current densities than spherical NCs.

Mass current densities obtained in the presence of variable KOH concentrations and 1.0 M methanol from Ni polyhedral NCs based electrodes are compared. Our results are compared with literature values. At 1.0 M KOH, mass current densities up to 2016.2 mA mg^{-1} at 0.6 V and 3162 mA mg^{-1} and 0.7 V were obtained for electrodes based on Ni polyhedral NCs. These values are twofold higher than those obtained for spherical NCs and well above values previously reported in literature.

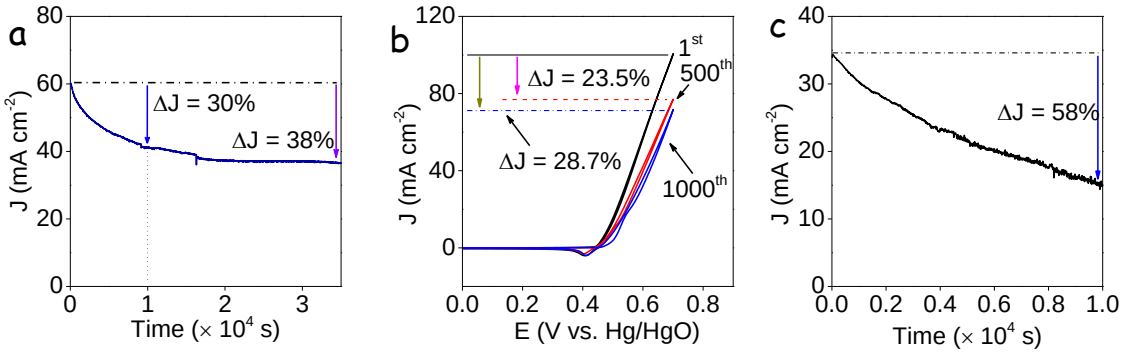

Figure 2.8. a) CA response of Ni polyhedral NCs based electrodes in 1.0 M KOH and 1.0 M methanol at 0.6 V for 35000 s. b) CVs of the Ni polyhedral NCs based electrode in 1.0 M KOH electrolyte with 1.0 M methanol at a scan rate of 100 mV s^{-1} in the potential range 0-0.7 V at cycles 1st, 500th, 1000th. c) CA response of Ni spherical NCs based electrodes in 1.0 M KOH and 1.0 M methanol at 0.6 V for 10000 s.

The long-term stability of Ni-based electrodes were evaluated by chronoamperometry (CA) in a 1.0 M KOH solution containing 1.0 M methanol at 0.6 V *vs.* Hg/HgO for 35000 s (Figure 2.8a). The current density of electrodes based on Ni polyhedral NCs suffered a relatively important decrease during the first few hours of operation (30% loss after 10000 s). A similar current density decrease was obtained after 1000 CV cycles (Figure 2.8b). After this initial lose, the current density quasi-stabilized at a value of ca. 37 mA cm^{-2}. During the last hours of operation tested, from t = 20000 s to t = 30000 s, a current density decrease of just a 0.5% was obtained. Notice that the mass current density at which the electrode stabilized, ~1,200 mA mg^{-1}, was still

significantly higher than the maximum current densities measured for Ni-based electrodes in previous reports. The initial current density decay was probably ascribed to the blocking of active sites by reaction products that moderately strongly bonded to the Ni surface. We hypothesize that after some hours of operation, the coverage of these species stabilized either because of having reached an equilibrium adsorption/desorption or because of the complete blocking of certain preferential sites. In any case, the density of surface reaction sites apparently decreased in around a 35% before the catalyst stabilizes.

Electrodes based on Ni polyhedral NCs displayed significantly improved stabilities over those based on Ni spherical NCs, which suffered a 58% loss after 10000 s in 1.0 M KOH with 1.0 M methanol at 0.6 V vs. Hg/HgO (Figure 2.8c). This experimental observation, which was unexpected taking into account previous reports on Pt(110) single crystals, could be explained by the different surface sites of polyhedral and spherical NCs, but additional work is required to exactly asses the mechanism of stability improvement in electrodes based on Ni polyhedral NCs with predominant (110) facets.

2.4 Conclusions

Colloidal Ni polyhedral NCs (16 ± 2 nm) with predominant (110) facets were synthesized and tested as electrodes for methanol electrooxidation. Results obtained from electrodes based on Ni polyhedral NCs were compared with those obtained for electrodes based on Ni spherical NCs. Electrocatalytic properties were first investigated in variable concentrations of KOH. We found the $Ni(OH)_2 \leftrightarrow NiOOH$ redox reaction rate was first order with the KOH concentration. The surface coverage of active species was much higher in electrodes based on polyhedral Ni NCs than in spherical ones. On the other hand, the rate limiting diffusion coefficient was higher in electrodes based on spherical NCs. Electrodes based on Ni polyhedral NCs displayed impressive current densities (59.4 mA cm^{-2}) and mass activities (2016 mA mg^{-1}) at 0.6 V *vs.* Hg/HgO in the presence of 1.0 M methanol and 1.0 M KOH, which corresponded to a twofold increase over electrodes based on spherical Ni NCs and over most Ni-based electrocatalyts previously reported. Such superior catalytic performance should be ascribed to the proper facets of Ni polyhedral NCs, which provided abundant active sites to promote the oxidation of methanol in alkaline media. Electrodes based on faceted polyhedral NCs displayed a 30% loss of activity during the first few operation hours, but activity stabilized to around a 65% of the initial value after ca. 20000 s operation. These results suggest Ni polyhedral NCs with predominant (110) facets to be among the best candidate electrocatalysts for MOR.

2.5 Reference

1 R. G. Minet, *Science (80-.).*, 1967, **157**, 1373.

2 X. Zhao, M. Yin, L. Ma, L. Liang, C. Liu, J. Liao, T. Lu and W. Xing, *Energy Environ. Sci.*, 2011, **4**, 2736.

3 J. N. Tiwari, R. N. Tiwari, G. Singh and K. S. Kim, *Nano Energy*, 2013, **2**, 553–578.

4 N. Kakati, J. Maiti, S. H. Lee, S. H. Jee, B. Viswanathan and Y. S. Yoon, *Chem. Rev.*, 2014, **114**, 12397–12429.

5 A. Serov and C. Kwak, *Appl. Catal. B Environ.*, 2009, **90**, 313–320.

6 X. Cui, W. Guo, M. Zhou, Y. Yang, Y. Li, P. Xiao, Y. Zhang and X. Zhang, *ACS Appl. Mater. Interfaces*, 2015, **7**, 493–503.

7 Y. Qin, Y. Liu, F. Liang and L. Wang, *ChemSusChem*, 2015, **8**, 260–263.

8 Z. Daşdelen, Y. Yıldız, S. Eriş and F. Şen, *Appl. Catal. B Environ.*, 2017, **219**, 511–516.

9 X. Cui, P. Xiao, J. Wang, M. Zhou, W. Guo, Y. Yang, Y. He, Z. Wang, Y. Yang, Y. Zhang and Z. Lin, *Angew. Chemie - Int. Ed.*, 2017, **56**, 4488–4493.

10 R. M. Abdel Hameed and R. M. El-Sherif, *Appl. Catal. B Environ.*, 2015, **162**, 217–226.

11 H. Sun, Y. Ye, J. Liu, Z. Tian, Y. Cai, P. Li and C. Liang, *Chem. Commun.*, 2018, **54**, 1563–1566.

12 G. S. Ferdowsi, S. A. Seyedsadjadi and A. Ghaffarinejad, *J. Nanostructure Chem.*, 2015, **5**, 17–23.

13 J. Li, Z. Luo, Y. Zuo, J. Liu, T. Zhang, P. Tang, J. Arbiol, J. Llorca and A. Cabot, *Appl. Catal. B Environ.*, 2018, **234**, 10–18.

14 J. Li, Z. Luo, F. He, Y. Zuo, C. Zhang, J. Liu, X. Yu, R. Du, T. Zhang, M. F. Infante-Carrió, P. Tang, J. Arbiol, J. Llorca and A. Cabot, *J. Mater. Chem. A*, 2018, **6**, 22915–22924.

15 N. A. M. Barakat, M. Motlak, B. S. Kim, A. G. El-Deen, S. S. Al-Deyab and A. M. Hamza, *J. Mol. Catal. A Chem.*, 2014, **394**, 177–187.

16 I. S. Pieta, A. Rathi, P. Pieta, R. Nowakowski, M. Hołdynski, M. Pisarek, A. Kaminska, M. B. Gawande and R. Zboril, *Appl. Catal. B Environ.*, 2019, **244**, 272–283.

17 Y. Yu, Q. Yang, X. Li, M. Guo and J. Hu, *Green Chem.*, 2016, **18**, 2827–2833.

18 A. Roy, H. S. Jadhav, G. M. Thorat and J. G. Seo, *New J. Chem.*, 2017, **41**, 9546–9553.

19 X. Li, X. Niu, W. Zhang, Y. He, J. Pan, Y. Yan and F. Qiu, *ChemSusChem*, 2017, **10**, 976–983.

20 L. Yang, Y. Tang, S. Luo, C. Liu, H. Song and D. Yan, *ChemSusChem*, 2014, **7**, 2907–2913.

21 S.-L. Yau, F.-R. F. Fan, T. P. Moffat and A. J. Bard, *J. Phys. Chem.*, 1994, **98**, 5493–5499.

22 Z. Luo, J. Lu, C. Flox, R. Nafria, A. Genç, J. Arbiol, J. Llorca, M. Ibáñez, J. R. Morante and A. Cabot, *J. Mater. Chem. A*, 2016, **4**, 16706–16713.

23 G. You, J. Jiang, M. Li, L. Li, D. Tang, J. Zhang, X. C. Zeng and R. He, *ACS Catal.*, 2018, **8**, 132–143.

24 H. Kita, Y. Gao, S. Ye and K. Shimazu, *Bull. Chem. Soc. Jpn.*, 2006, **66**, 2877–2882.

25 J. C. Davies, B. E. Hayden and D. J. Pegg, *Surf. Sci.*, 2000, **467**, 118–130.

26 J. Clavilier, A. Rodes, K. El Achi and M. Zamakhchari, *J. Chim. Phys.*, 2017, **88**, 1291–1337.

27 C. F. Mai, C. H. Shue, Y. C. Yang, L. Y. O. Yang, S. L. Yau and K. Itaya, *Langmuir*, 2005, **21**, 4964–4970.

28 Y. Chen, X. Luo, H. She, G.-H. Yue and D.-L. Peng, *J. Nanosci. Nanotechnol.*, 2009, **9**, 5157–5163.

29 J. Arbiol, A. Cirera, F. Peiró, A. Cornet, J. R. Morante, J. J. Delgado and J. J. Calvino, *Appl. Phys. Lett.*, 2002, **80**, 329–331.

30 S. Bernal, F. J. Botana, J. J. Calvino, C. López-Cartes, J. A. Pérez-Omil and J. M. Rodríguez-Izquierdo, *Ultramicroscopy*, 1998, **72**, 135–164.

31 A. T. Fafarman, W. K. Koh, B. T. Diroll, D. K. Kim, D. K. Ko, S. J. Oh, X. Ye, V. Doan-Nguyen, M. R. Crump, D. C. Reifsnyder, C. B. Murray and C. R. Kagan, *J. Am. Chem. Soc.*, 2011, **133**, 15753–15761.

32 J. Li, X. Xu, Z. Luo, C. Zhang, Y. Zuo, T. Zhang, P. Tang, M. F. Infante-Carrió, J. Arbiol, J. Llorca, J. Liu and A. Cabot, *ChemSusChem*, 2019, **12**, 1451–1458.

33 J. Li, X. Xu, Z. Luo, C. Zhang, X. Yu, Y. Zuo, T. Zhang, P. Tang, J. Arbiol, J. Llorca, J. Liu and A. Cabot, *Electrochim. Acta*, 2019, **304**, 246–254.

34 J. Liu, Z. Luo, J. Li, X. Yu, J. Llorca, D. Nasiou, J. Arbiol, M. Meyns and A. Cabot, *Appl. Catal. B Environ.*, 2019, **242**, 258–266.

35 D. Wu, W. Zhang and D. Cheng, *ACS Appl. Mater. Interfaces*, 2017, **9**, 19843–19851.

36 P. Oliva, J. Leonardi, J. F. Laurent, C. Delmas, J. J. Braconnier, M. Figlarz, F. Fievet and A. de Guibert, *J. Power Sources*, 1982, **8**, 229–255.

37 A. J. Bard and L. R. Faulkner, *Electrochemical Methods: Fundamentals and Applications*, 2nd edn., 2001.

38 J. D. Benck, Z. Chen, L. Y. Kuritzky, A. J. Forman and T. F. Jaramillo, *ACS Catal.*, 2012, **2**, 1916–1923.

39 C. C. L. McCrory, S. Jung, I. M. Ferrer, S. M. Chatman, J. C. Peters and T. F. Jaramillo, *J. Am. Chem. Soc.*, 2015, **137**, 4347–4357.

40 C. C. L. McCrory, S. Jung, J. C. Peters and T. F. Jaramillo, *J. Am. Chem. Soc.*, 2013, **135**, 16977–16987.

Chapter 3

NiSn Bimetallic Nanoparticles as Stable Electrocatalysts for Methanol Oxidation Reaction

Nickel is an excellent alternative catalyst to high cost Pt and Pt-group metals as anode material in direct methanol fuel cells. However, nickel presents a relatively low stability under operation conditions, even in alkaline media. In this work, a synthetic route to produce bimetallic NiSn nanoparticles (NPs) with tuned composition is presented. Through co-reduction of the two metals in the presence of appropriate surfactants, 3-5 nm NiSn NPs with tuned Ni/Sn ratios were produced. Such NPs were subsequently supported on carbon black and tested for methanol electro-oxidation in alkaline media. Among the different stoichiometries tested, the most Ni-rich alloy exhibited the highest electrocatalytic activity, with mass current density of 820 mA mg^{-1} at 0.70 V (*vs.* Hg/HgO). While this activity was comparable to that of pure nickel NPs, NiSn alloys showed highly improved stabilities over periods of 10000 s at 0.70 V. We hypothesize this experimental fact to be associated to the collaborative oxidation of the byproducts of methanol which poison the Ni surface or to the prevention of the tight adsorption of these species on the Ni surface by modifying its surface chemistry or electronic density of states.

Keywords:

Electrocatalysis,
Methanol oxidation
Colloidal synthesis
Bimetallic nanoparticles

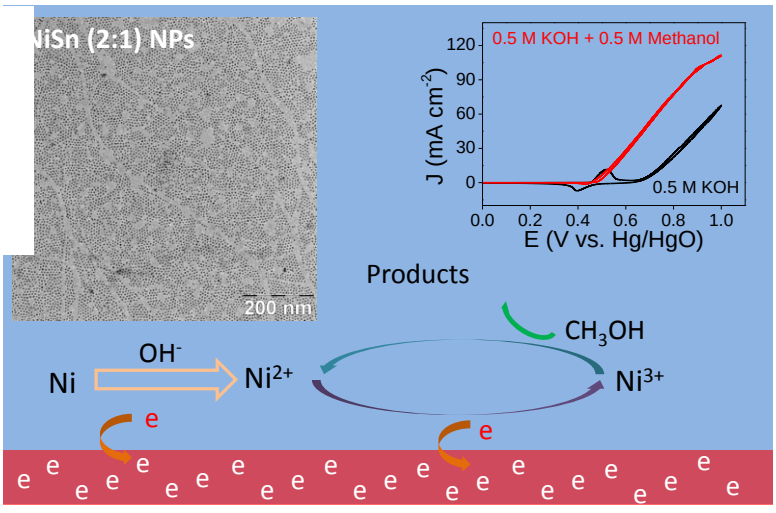

Monodisperse bimetallic NiSn nanoparticles towards methanol oxidation reaction.

3.1 Introduction

Fuel cells have raised increasing interest as a high efficiency and environmental friendly energy conversion technology. Among the different cell architectures and fuels proposed, direct methanol fuel cells (DMFCs) are the best positioned toward widespread commercialization and the most viable alternative to lithium-ion batteries for portable applications.[1,2] Methanol provides numerous advantages as a fuel, including safe handling, storage and transportation, solubility in aqueous electrolytes, availability and potential generation from renewable energies, high power and energy density (6100 Wh kg^{-1}) with high oxidation rates that do not require C-C bond breaking, low emissions and fast recharging and cell startup at low temperature.[3,4] However, a major drawback of this technology, currently delaying its extensive commercialization, is its high manufacturing cost, which is in large part related to the dependence on Pt-based electrocatalysts for both methanol oxidation at the anode and oxygen reduction at the cathode.[1,5,6] The development of Pt-free electrocatalysts is thus a key challenge to be urgently overcome for DMFCs to become cost-effective.

Nickel, a relatively abundant element in the earth's crust, is among the best candidate materials to replace Pt in the anode, where the methanol oxidation reaction (MOR) takes place. Ni [7–10] and Ni-based alloys reported to date, such as NiCu,[11–14] NiFe,[15] NiCo,[16] NiMn,[17] and NiTi[18,19] show excellent catalytic activities, but even in alkaline electrolytes, they lack of a satisfactory durability. Therefore, the exploration of novel Ni-based compounds presenting improved stabilities is required.

Among the possible alternative alloys, NiSn is a potentially excellent candidate for the MOR. Actually, Sn has been demonstrated to improve Pt performance in this reaction.[20–22] However, surprisingly, NiSn has yet to be tested as anode material in DMFCs. This anomaly is in part associated to the lack of reliable synthetic routes to produce NiSn alloys. Among the very few examples in the literature, J. Liu et al. produced porous Ni_3Sn_2 intermetallic microcages through a solvothermal method which were tested for lithium and sodium storage.[23] Recently, Y. Liu et al. reported a colloidal synthesis approach that made use of a strong Brønsted base, n-butylithium, to produce Ni_3Sn_2 NPs for the semi-hydrogenation of alkynes.[24]

To overcome these challenges, we present here a new synthetic route to produce NiSn NPs with controlled stoichiometry. We further demonstrated these NPs to show high electrocatalytic activities towards methanol electroxidation and at the same time significantly improved stabilities when compared with nickel.

3.2 Experimental

3.2.1 Chemicals

Nickel(II) acetylacetonate ($Ni(acac)_2 \cdot xH_2O$ (x~2), 95%, Sigma-Aldrich), tin(II) acetate ($Sn(oac)_2$, 95%, Fluka), tri-n-octylphosphine (TOP, 97%, Strem), oleylamine (OAm, 80-90%, TCI), borane tert-butylamine complex (TBAB, 97%, Sigma-Aldrich), oleic acid (OAc, Sigma-Aldrich), hydrazine monohydrate (N_2H_4 64-65%, reagent grade, 98%, Sigma-Aldrich), Nafion (10 wt. %, perfluorinated ion-exchange resin, dispersion in water), carbon black (CB, VULCAN XC72), potassium hydroxide (KOH, 85%, Sigma-Aldrich), acetonitrile (CH_3CN, extra dry, Fisher), methanol (anhydrous, 99.8%, Sigma-Aldrich), trioctylphosphine oxide (TOPO, 99%, Sigma-Aldrich), diisobutylaluminium hydride solution (DIBAH, 1.0 M in tetrahydrofuran (THF), Aldrich), tin(II) chloride ($SnCl_2$, anhydrous, 98%, Strem), and lithium bis(trimethylsilyl)amide ($LiN(SiME_3)_2$, 97%, Aldrich) were used as received without any further purification. Chloroform, hexane, acetone, toluene, and ethanol were of analytical grade and purchased from various sources. MilliQ water was obtained from a PURELAB flex from ELGA. All the syntheses were performed using standard airless techniques: a vacuum/dry argon gas Schlenk line was used for the synthesis and an argon-filled glove-box was used for storing and dealing with sensitive chemicals.

3.2.2 Synthesis of NiSn NPs

In a typical synthesis, 7 mL OAm, 0.1 mmol $Ni(acac)_2$, 0.1 mmol $Sn(oac)_2$ and 0.15 mL OAc were loaded into a 25 mL three-necked flask and degassed under vacuum at 80 °C for 1 hour while being strongly stirred using a magnetic bar. Afterward, a gentle flow of argon was introduced, and 1 mL of TOP was injected into the solution. Subsequently, the reaction flask was heated to 180 °C within 20 min, followed by quick injection of a solution containing 1 mmol TBAB in 1 mL degassed OAm. A visible color change, from light blue to black was observed immediately. The reaction was maintained at this temperature for 1 hour before it was quenched using a water bath. NiSn NPs were collected by centrifuging and washing the solid product with acetone and chloroform 3 times. The as-prepared NPs were finally dispersed in chloroform and stored for their posterior use. NPs were colloidally stable in chloroform for over two months. Different nominal Ni/Sn ratios were used to prepare NPs with different stoichiometries following the same procedure above detailed.

3.2.3 Synthesis of Sn NPs

13 nm Sn NPs were produced according to the method developed by K. Kravchyk et al.[25] Briefly, 16 ml OAm was loaded into a 25 ml three-necked flask and maintained under vacuum at 140 °C for 60 min under stirring. After cooling to 50 °C, 0.5 mmol $SnCl_2$ was added to the flask and kept under vacuum at 140 °C for 30 min. Then temperature was increased to 180 °C under argon and 2 ml of toluene containing 0.6 g of $LiN(SiME_3)_2$ was injected. Immediately afterward, 0.6 ml of a 1M DIBAH solution in THF was also injected. Upon injection of DIBAH, the solution immediately turned dark brown. After 10 min reaction, the solution was cooled down using a water bath. Acetone was added to the final mixture and NPs were collected by centrifugation. The obtained precipitate was re-dispersed in hexane for further use.

3.2.4 Synthesis of Ni NPs

12 nm *fcc*-Ni NPs were prepared following the procedure described by Y. Chen et al.[26] In a typical synthesis, 1 mmol $Ni(acac)_2$, 7 ml OAm, 0.4 mmol TOP and 0.25 mmol TOPO were loaded in a three-neck flask and stirred under a gentle flow of argon. Temperature was raised to 130 °C and kept for 20 min. Then, the solution was quickly heated to 215 °C and maintained at this temperature for 45 min. Subsequently, the flask was cooled down to room temperature using a water bath. The black precipitate was separated through centrifugation after adding ethanol. NPs were re-dispersed and precipitated three times using hexane and ethanol as solvent and non-solvent, respectively. The product was finally dispersed in hexane.

3.2.5 Ligand removal

NiSn, Sn and Ni NPs dispersed in chloroform were precipitated through addition of ethanol and centrifugation. Then, they were dispersed in a mixture containing 28 mL acetonitrile and 0.8 mL hydrazine hydrate and stirred for 4 hours. NPs were then collected by centrifugation and washed with acetonitrile for 3 times. Finally, the NiSn NPs were dried under vacuum.

3.2.6 Characterization

Powder X-ray diffraction (XRD) patterns were recorded from the as-synthesized NPs dropped on a Si(501) substrate on a Bruker AXS D8 Advance X-ray diffractometer with Ni-filtered (2 um thickness) Cu K radiation (1.5106) operating at 40 kV and 40 mA. Specimens for transmission electron microscopy (TEM) characterization were prepared by drop casting the dispersions of NPs onto a 200 mesh Cu grids with ultrathin carbon and formvar support films. TEM analyses were carried out on a ZEISS LIBRA 120, operating at 120 kV. High-resolution

TEM (HRTEM) and scanning TEM (STEM) studies were carried out using a field emission gun FEI Tecnai F20 microscope at 200 kV with a point-to-point resolution of 0.19 nm. High angle annular dark-field (HAADF) STEM was combined with electron energy loss spectroscopy (EELS) in the Tecnai microscope by using a GATAN QUANTUM filter. The composition of NPs was confirmed by scanning electron microscopy (SEM) on a ZEISS Auriga SEM with an energy dispersive X-ray spectroscopy (EDS) detector at 20 kV. Values were averaged from 3 measurements of each composition. X-ray photoelectron spectroscopy (XPS) was done on a SPECS system equipped with an Al anode XR50 source operating at 150 mW and a Phoibos 150 MCD-9 detector. The pressure in the analysis chamber was kept below 10^{-7} Pa. The area analyzed was about 2 mm x 2 mm. The pass energy of the hemispherical analyzer was set at 25 eV and the energy step was maintained at 1.0 eV. Data processing was performed with the Casa XPS program (Casa Software Ltd., UK). Binding energies were shifted according to the reference C 1s peak that was located at 284.8 eV. Fourier transform infrared spectrometer (FTIR) data were recorded on an Alpha Bruker FTIR spectrometer with a platinum attenuated total reflectance (ATR) single reflection module.

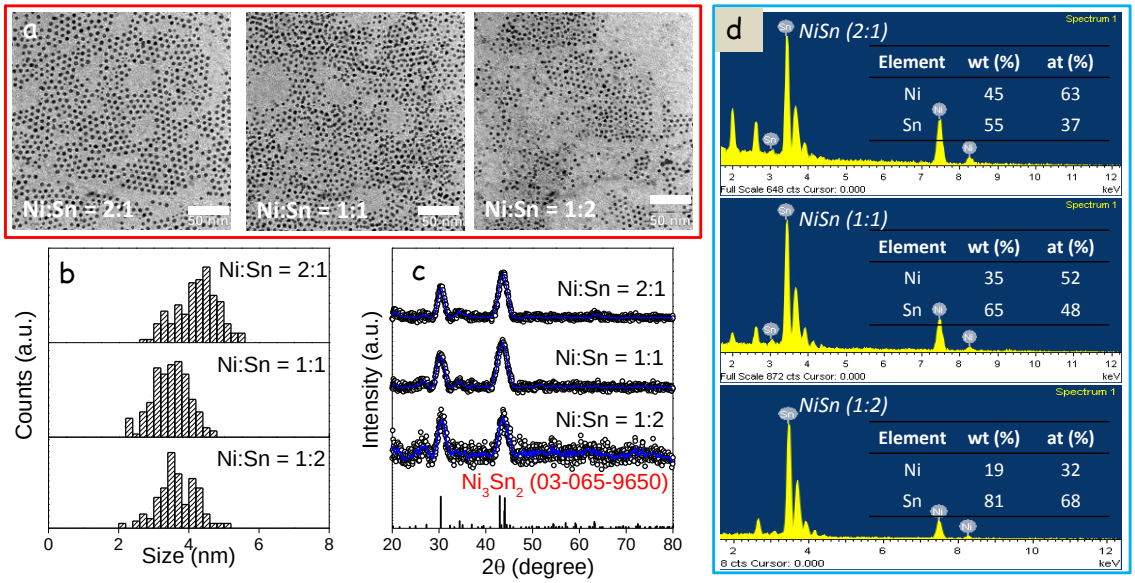

Figure 3.1. a) Representative TEM micrographs of NiSn NPs with different nominal Ni:Sn ratios: 2:1, 1:1 and 1:2. b) Corresponding size distribution histograms. c) XRD patterns of NiSn NPs with the same nominal stoichiometries. d) Actual Ni/Sn ratio obtained from SEM-EDS.

3.2.7 Electrochemical characterization

Electrochemical measurements were carried out at room temperature (25 ± 2 ºC) in an electrochemical workstation (AutoLab, Metrohm). The three electrode system consisted of a counter electrode (Pt mesh), a working electrode (glassy carbon (GC) electrode with diameter of 5 mm) and a reference electrode (Hg/HgO). The Hg/HgO was placed in a salt bridge of 1.0 M

KOH. 5 mg of NPs, 50 μL of 10 wt% Nafion solution together with 10 mg of CB were added to 1 mL ethanol and 1 mL MilliQ water which was vigorously sonicated for 1 hour to obtain a homogeneous solution. Then, 5 μL of the freshly prepared ink (around 0.012 mg catalyst) was evenly loaded onto the polished glassy carbon electrode and dried naturally in air at room temperature. All the measurements were performed in N_2-bubled 0.5 M KOH solution in the absence or presence of variable concentrations of methanol with magnetic bar stirring, except where noted. Current densities were calculated taking into account the geometric surface area of the GC electrode (0.196 cm^{-2}).

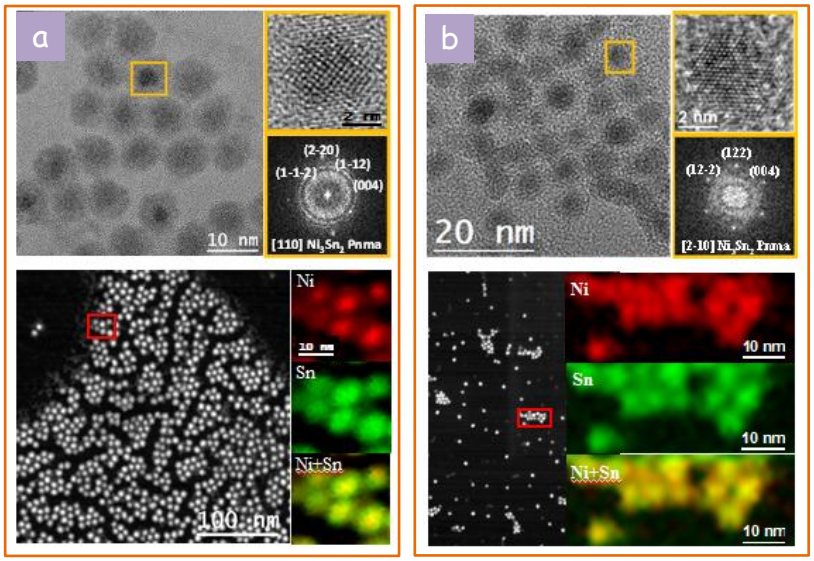

Figure 3.2. HRTEM micrograph of (a) NiSn (2:1) and (b) NiSn (1:1) NPs and detail of the yellow squared region with its corresponding power spectrum and its STEM-HAADF micrographs and EELS elemental maps of Ni and Sn radial gradient. Ni_3Sn_2 lattice fringe distances measured were 0.210 nm (2-20), 0.296 nm (-1-12) at 46° vs (2-20) and 0.204 nm (004) at 90° vs (2-20), which matched with the orthorhombic Ni_3Sn_2 phase visualized along its [110] zone axis.

3.3 Results and Discussion

A co-reduction strategy was developed to produce NiSn NPs with low size dispersion and tuned composition (see experimental section for details). Briefly, proper amounts of $Ni(acac)_2$ and $Sn(oac)_2$ were reduced at 180 ºC and in the presence of OAc, OAm and TOP by injection of a TBAB/OAm solution. Figures 3.1a-c show representative TEM macrographs of the quasi-spherical NiSn NPs produced with three different nominal Ni:Sn ratios (2:1; 1:1; 1:2). The average size of the NPs measured by TEM analysis fluctuated in the range from 3.5 ± 0.5 nm to 4.2 ± 0.6 nm, depending on the nominal composition (Figure 3.1a-b and Table 3.1). Figure 3.1c displays the XRD patterns of the NiSn NPs produced following the above detailed

procedure. As corresponding to small NPs, XRD patterns from all samples displayed broad diffraction peaks, which could be ascribed to the orthorhombic Ni_3Sn_2 or the monoclinic Ni_3Sn_4 crystal phases. Additional Ni_3Sn or even Ni or Sn phases could not be discarded from the XRD analysis. Previous works already reported the formation of these phases in the composition range here analyzed, 33-67% of each metal.[27,28]

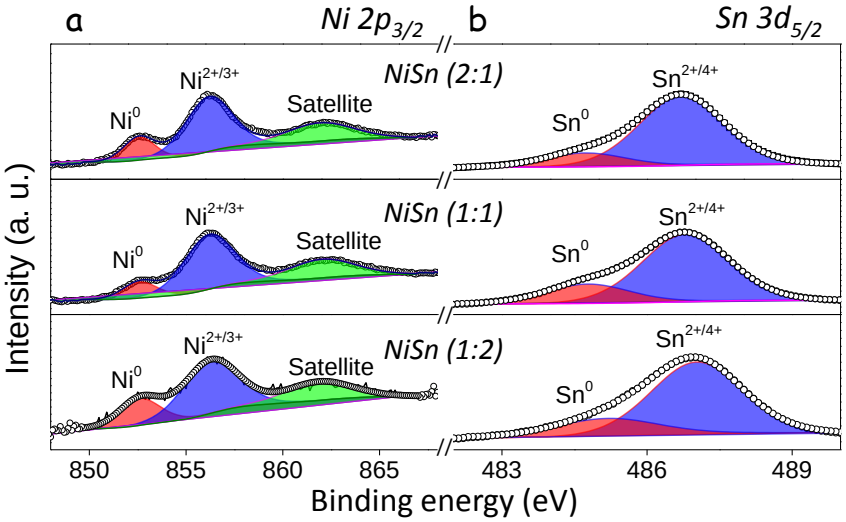

Figure 3.3. XPS spectra of (a) the Ni $2P_{3/2}$ region and (b) the Sn $3P_{5/2}$ region of NiSn (2:1), NiSn (1:1) and NiSn (1:2) NPs.

Extensive HRTEM and EELS analysis found all NiSn NPs to contain both elements, Ni and Sn, in a similar ratio within each sample. No independent Ni or Sn elemental NP was identified in any of the samples analyzed. Figure 3.2a shows HRTEM micrographs of the NiSn (2:1) NPs that had been exposed to air. NiSn NPs had average sizes of ca. 7.2 nm and displayed a core-shell structure. The core, with a diameter of ca. 3.5 nm, was crystalline and its structure matched that of a Ni_3Sn_2 orthorhombic phase (space group = *Pnma*) with a = 7.110 Å, b = 5.210 Å, c = 8.230 Å (Figure 3.2a). The shell was amorphous and it was attributed to an oxide layer formed during the NP exposure to the ambient atmosphere. STEM-HAADF micrographs and EELS chemical compositional maps revealed the NiSn (2:1) core to be Ni-rich and the shell to be Sn-rich (Figure 3.2a). The same crystal phase and compositional organization was observed for NiSn (1:1) NPS (Figure 3.2b). This composition inhomogeneity could be created during the synthesis due to a differential reduction rate of the two precursors, or during oxidation, being Sn atoms potentially more prone to react with ambient oxygen.

EDX analysis showed the composition on the NiSn NPs to match relatively well with the nominal Ni/Sn ratios (Table 3.1 and Figure 3.1d). Specifically Ni/Sn ratios of 1.7, 1.1 and 0.46 were obtained for NiSn NPs produced with nominal Ni:Sn stoichiometries 2:1; 1:1 and 1:2, respectively.

Table. 3.1 Average particle size measured from TEM micrographs, summary of the atomic ratios of Ni to Sn nominally introduced and experimentally measured from EDX and XPS analysis, and ratio of the chemical states obtained from XPS measurements.

Catalysts	TEM average NP size (nm)	Ni/Sn molar ratio			Chemical states (XPS)	
		Nominal	EDX	XPS	Ni(0)/Ni(II/III)	Sn(0)/Sn(IV)
NiSn-2:1	4.2 ± 0.6	2	1.7	0.41	0.14	0.28
NiSn-1:1	3.5 ± 0.5	1	1.1	0.20	0.20	0.19
NiSn-1:2	3.7 ± 0.5	0.5	0.46	0.10	0.27	0.29

XPS analysis was used to characterize the chemical environment of atoms at the surface of NiSn NCs that had been exposed to the ambient atmosphere. For these analyses, purified NiSn NPs with no surface ligands were used (see below for ligand removal details). XPS analysis confirmed the surface of these NPs to be Sn-rich and oxidized (Figure 3.3). The surface Ni/Sn ratios were 0.41, 0.20 and 0.10 for NiSn NPs produced with nominal Ni:Sn stoichiometries 2:1; 1:1 and 1:2, respectively. Ni $2p_{3/2}$ electronic states were found at binding energies of 856.3 eV, corresponding to a Ni^{2+} chemical environment, and 852.6 eV, which was associated to a Ni^{0} state.[29] The $Ni^{2+/3+}$ oxidized component was clearly majoritarian, with a ratio over Ni^{0}: $Ni^{0}/Ni^{2+/3+}$ = 0.14 for the NiSn (2:1) sample. Similar ratios were obtained for NiSn NPs with other Ni/Sn nominal compositions, with an increase of the Ni^{0} component with the Sn ratio (see Table 3.1). The main contribution to the Sn $3d_{5/2}$ electronic states were found at a binding energy of 486.8 eV, which was attributed to a Sn^{2+} or Sn^{4+} chemical environment.[29] A minor component was found at 484.7 eV, which was associated to metallic Sn. The ratio of the two chemical states was $Sn^{0}/Sn^{2+/4+}$ = 0.28 for the NiSn (2:1) NPs and fluctuated with the nominal composition of the samples (Table 1). This fluctuation may be associated to a different amount of time the samples were exposed to air before XPS analysis. Sn was more strongly affected by this experimental parameter as the NPs surface was rich in Sn and poor in Ni. Probably, the relative amount of Ni on the NP surface also decreased when increasing the Sn composition.

The presence of OAm, OAc and TOP in the reaction mixture was essential to produce monodisperse and colloidally stable NiSn NPs with the orthorhombic Ni_3Sn_2 crystal phase. Keeping all the synthetic parameters constant, but removing OAc, large spherical aggregates of NiSn NPs with the Ni_3Sn_4 crystal phase were produced (Figure 3.4a). On the other hand, in the absence of TOP, NiSn NPs aggregated in chains and with the Ni_3Sn_4 crystal phase were obtained (Figure 3.4b).

However, the presence of organic ligands at the NP surface strongly limits both their ability to interact with the media and the charge transport between NPs and between NPs and surrounding materials. Thus, we removed the native organic ligands from the NiSn NP surface by

suspending them in a mixture of acetonitrile and a small amount of hydrazine hydrate. The mixture was stirred for some hours and then the precipitated NPs were collected. Additional purification steps with acetonitrile were carried out to remove all the unbounded or loosely bond organics. FTIR analysis confirmed the absence of organic ligands at the NiSn NP surface after the ligand removal step, as observed from the disappearing of peaks at 2890 cm^{-1} and 2822 cm^{-1} that correspond to C-H stretching modes (Figure 3.4c).

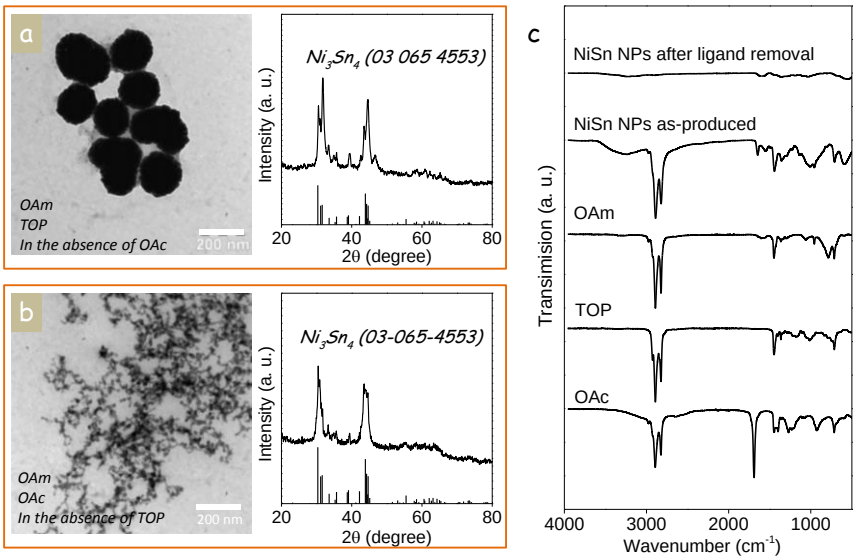

Figure 3.4. TEM micrograph and XRD of as-synthesized NiSn NPs using the same synthesis condition but in the absence of a) OAc and b) TOP. c) FTIR spectra of OAm, OAc, TOP and NiSn (2:1) NPs as produced and after ligand removal.

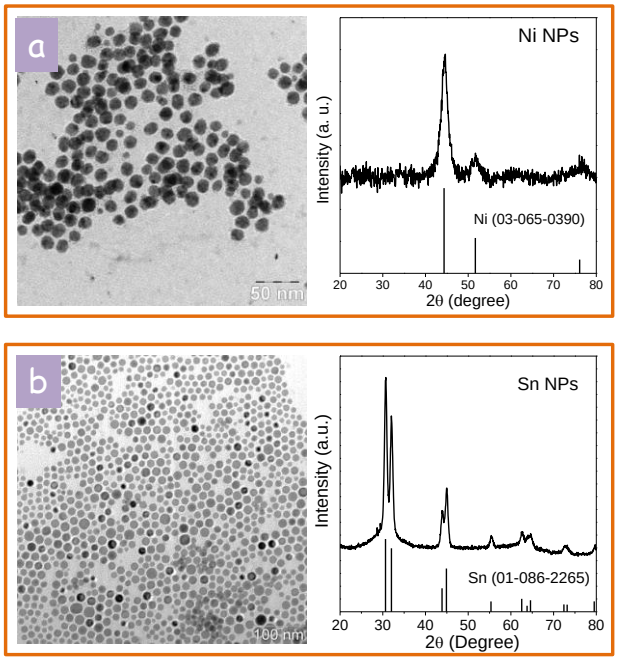

Figure 3.5. Representative TEM macrograph and XRD of colloidal a) Ni and b) Sn NPs.

Electrocatalysts were prepared by mixing NPs with CB and Nafion and supporting this composite onto a glassy carbon electrode (see experimental section for details). As reference materials, 12 nm Ni NPs and 13 nm Sn NPs produced following previously published synthetic routes (see experimental section for details) were used. Figures 3.5ab display representative TEM micrographs and the corresponding XRD patterns of these reference materials. Surface ligands of these NPs were removed following the same procedure used to displace ligands from NiSn NPs.

The electrocatalytic activity toward the MOR of NiSn NPs with different compositions was initially tested using cyclic voltammetry. Figure 3.6 presents cyclic voltammograms of the five different electrocatalysts tested in 0.5 M KOH medium without (Figure 3.6a) or with (Figure 3.6b) 0.5 M methanol. The scan rate was set at 50 mV s^{-1} and the potential window measured extended from 0 V to 1.0 V *vs.* Hg/HgO. Cyclic voltammograms in the absence of methanol were conducted to determine the potential range for Ni oxidation and oxygen evolution from water (OER).

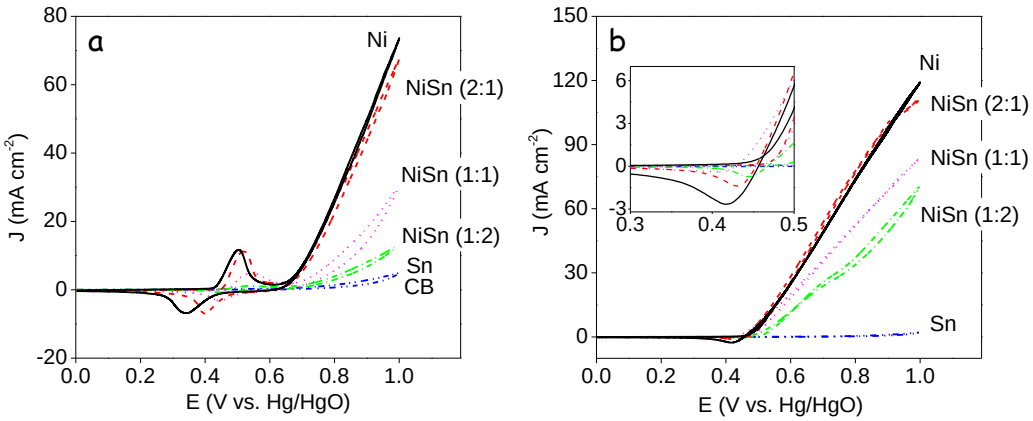

Figure 3.6. a) Cyclic voltammograms of Ni-Sn, Ni, Sn NPs in 0.5 M KOH solution at a scan rate of 50 mV s^{-1}. b) Cyclic voltammograms of NiSn NPs, Ni NPs and Sn NPs for methanol electrooxidation in 0.5 M KOH containing 0.5 M methanol solution at a scan rate of 50 mV s^{-1}.

The anodic oxidation of nickel in alkaline media has been extensively investigated. It is generally accepted that in alkaline medium, Ni undergoes oxidation to $Ni(OH)_2$.[11,30–32] In the absence of methanol, for the Ni electrocatalyst, we measured the first anodic peak at ca. 0.50 V *vs.* Hg/HgO and ascribed it to the oxidation of $Ni(OH)_2$ to NiOOH. Still during the forward scan, a second increase in the current density at 0.75 V *vs.* Hg/HgO was attributed to OER. Subsequently, the formed NiOOH was reduced in the backward direction at a potential value of ca. 0.50 V *vs.* Hg/HgO.

Using NiSn bimetallic NPs, the current densities of the first anodic and cathodic peaks decreased as the Sn content increased (Figure 3.6a). The current densities at the first oxidation

peak were 10.5 mA cm^{-2} for Ni, 10.8 mA cm^{2} for NiSn (2:1), 4.7 mA cm^{-2} for NiSn (1:1) and 1.7 mA cm^{-2} for NiSn (1:2) electrodes. In parallel, the corresponding oxidation and reduction onset potentials shifted with increasing Sn contents. The onset oxidation potential of Ni was 0.468 V *vs.* Hg/HgO and that of NiSn was 0.482 V, 0.483 V and 0.516 V for (2:1), (1:1) and (1:2) compositions, respectively. Sn electrodes displayed no redox peaks in the measured potential window and showed an OER activity comparable to that of carbon black. Consistently, in spite of the non-homogeneous Ni and Sn distribution within each particle, only one oxidation and reduction peak was observed for each sample.

Figure 3.6b shows cyclic voltammograms measured in the presence of methanol. The MOR onset was at ca. 0.43 V vs Hg/HgO, the same voltage at which $Ni(OH)_2$ undergoes oxidation to NiOOH. This is consistent with the proposed mechanisms of electrocatalytic MOR on Ni-based anodes, which involves the participation of the nickel oxyhydroxide in the methanol oxidation:[9,19,33]

$$Ni(OH)_2 + OH^- \leftrightarrow NiOOH + H_2O + e^-$$

$$NiOOH + CH_3OH \rightarrow Ni(OH)_2 + \text{products}$$

with carbonate, formaldehyde, formic acid, CO, and CO_2 as the possible products/intermediates of the MOR. Notice also in this direction, that the cathode peak, associated to the reduction of NiOOH to $Ni(OH)_2$ decreased or fully disappeared with the introduction of methanol, confirming the consumption of this compound during the MOR.

Figure 3.6b shows how the activity toward the MOR of the NiSn electrodes decreased with the amount of Sn. The activity of the Sn electrode was very low, confirming that elemental Sn did not catalyze the OER and MOR reactions in the voltage range studied. Activity of NiSn electrocatalysts was generally lower than that of Ni, except for the NiSn with the higher Ni content (2:1), which provided higher current densities up to a certain voltage when the OER reaction kicked in. In this regard, note also that MOR and OER reactions occurred simultaneously at voltages above 0.75 V. Thus, to further test the activity toward MOR without influence of the OER, we limited the analyzed potential to the range from 0 to 0.70 V *vs.* Hg/HgO.

Figure 3.7 displays the cyclic voltammograms in the 0 V-0.7 V *vs.* Hg/HgO range and at various scan rates of the Ni and NiSn electrodes within 0.5 KOH media and with no methanol. The anodic and cathodic peaks increased and shifted to higher and lower potentials respectively when increasing the scan rate. For all electrocatalysts, the ratio of the current densities at the anodic and cathodic peaks indicated the nickel redox reaction to be mostly reversible.

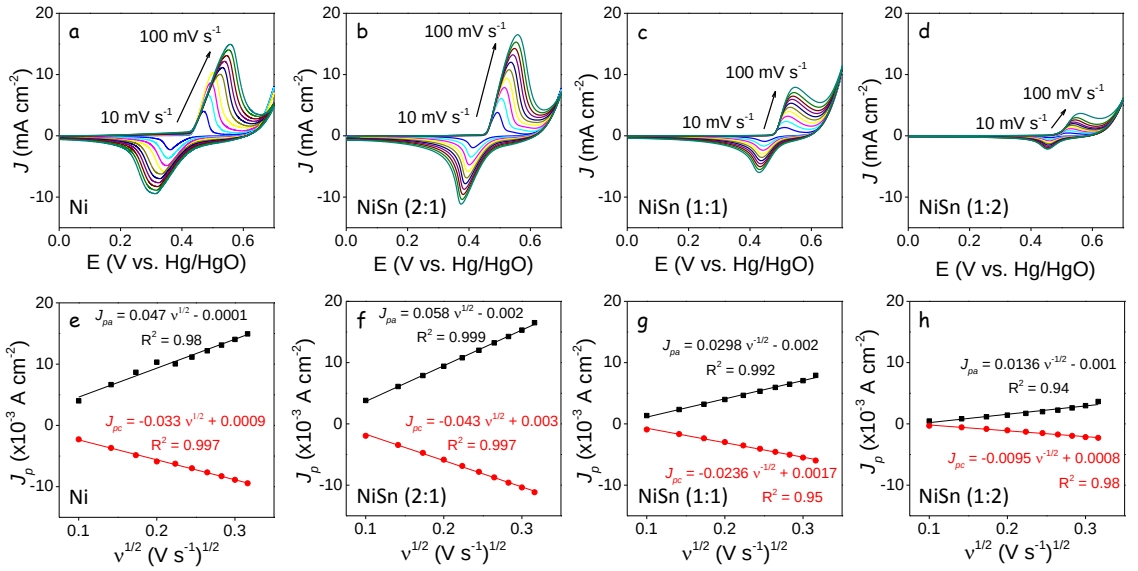

Figure 3.7. a-d) Cyclic voltammograms of Ni and NiSn electrocatalysts in 0.5 KOH at increasingly higher potentials sweep rates: 10, 20, 30, 40, 50, 60, 70, 80, 90, 100 mV s^{-1}. e-h) linear fitting of the anodic and cathodic peak current densities to the square roots of the scan rates.

To quantify the redox $Ni(OH)_2 \leftrightarrow NiOOH$ reaction, the peak anodic (J_{pa}) and cathodic (J_{pc}) current densities, the half wave redox potential ($E_{1/2}$), the redox potential difference (ΔE_p), the NiOOH surface coverage (Γ) and the proton diffusion coefficient (D), of the different electrocatalysts tested were determined (Table 2). Peak current densities were higher for NiSn (2:1) than for Ni-based electrodes, but decreased with the Sn content. Sharper oxidation and reduction peaks were obtained for all the NiSn-based electrodes compared with Ni, which could be related to the smaller size of the NiSn NPs. While $E_{1/2}$ increased with the Sn content, ΔE_p decreased with the incorporation of Sn, suggesting faster electron transfer kinetics. The surface coverage of $Ni(OH)_2$/NiOOH redox pairs participating in the reaction at each Ni-Sn electrode was calculated using the following equation:[34,35]

$$\Gamma = \frac{Q}{nFA}$$

where Q is the charge under the reduction/oxidation peak, which we averaged from forward and reverse scans, A is the geometrical electrode surface area, n is the number of transferred electron per reaction, i.e. 1, and F is the Faraday constant.

The calculated NiOOH surface coverages were independent of the scan rate in the low scan rate range (υ<50 mV s^{-1}). The coverage of electroactive species decreased as the amount of Sn in the NiSn NPs increased (Table 3.2). However, the coverage obtained from NiSn (2:1) electrocatalysts was very close to that of Ni. This experimental result was at first view surprising taking into account the lower overall amount of metal in NiSn catalysts due to the higher atomic mass of Sn, the lower content of Ni in the NiSn NPs compared with elemental Ni

NPs and the Sn-rich surface of NiSn NPs. However, it could be in part explained by the smaller size of the NiSn NPs compared with the Ni NPs. Overall, the surface coverages obtained from the Ni and NiSn electrodes in the present work were almost an order of magnitude higher than values usually reported, which we associated to the large surface area of the NPs used here.

Table 3.2. Summary of the electrocatalytic performance.

Catalyst	J_{pa} mA cm^{-2}	J_{pc} mA cm^{-2}	$E_{1/2}$ V *vs.* Hg/HgO	ΔE_p V	Γ mol cm^{-2}	D cm^2 s^{-1}
Ni	10.5	-6.8	0.47	0.190	2.5 x10^{-7}	1.2 x10^{-11}
NiSn (2:1)	10.8	-6.9	0.49	0.139	2.1 x10^{-7}	1.9 x10^{-11}
NiSn (1:1)	4.7	-3.5	0.50	0.090	1.1 x10^{-7}	5.3 x10^{-12}
NiSn (1:2)	1.7	-1.3	0.51	0.076	4.5 x10^{-8}	1.0 x10^{-13}

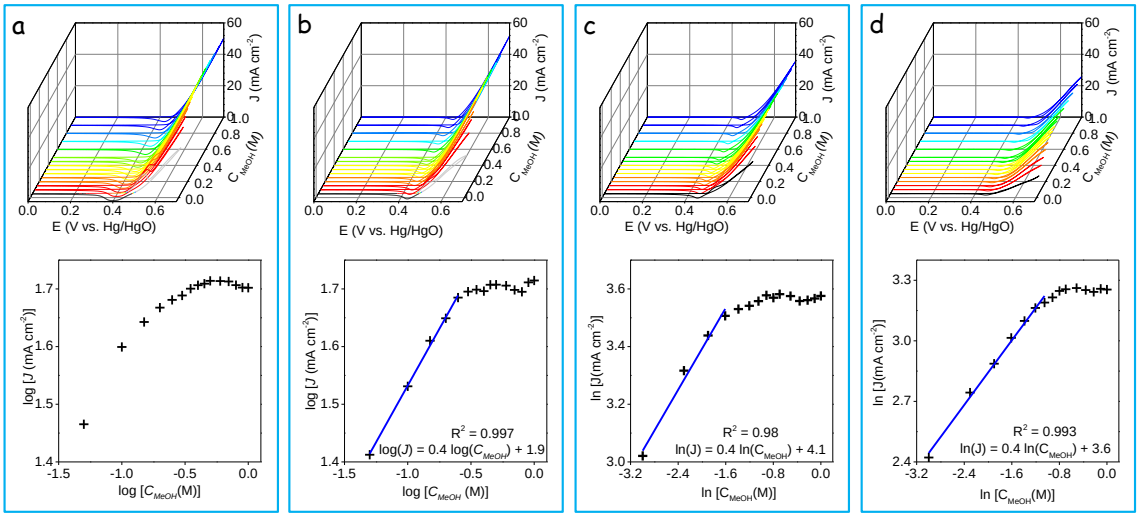

Figure 3.8. Cyclic voltammograms of a) Ni, b) NiSn-2:1, c) NiSn-1:1 and d) NiSn-1:2 electrodes and in 0.5 M KOH solution with various methanol concentrations from 0.05 M to 1.0 M at a scan rate of 50 mV s^{-1}and its corresponding logarithmic dependence of the current density (0.70 V *vs.* Hg/HgO).

In the high scan rate range, a linear relationship could be fitted to the dependence of the peak current density with the square root of the voltage scan rate, pointing toward a diffusion-limited $Ni(OH)_2 \leftrightarrow NiOOH$ redox reaction.[30,36] In this regard, it is generally accepted that the proton diffusion is the rate limiting step in the oxidation of $Ni(OH)_2$ to NiOOH. Therefore, the proton diffusion coefficient (D) can be determined from equation:[34]

$$I_p = 2.69 \times 10^5 n^{3/2} A D^{1/2} C v^{1/2}$$

where I_p is the peak current and C is the initial concentration of redox species that, taking into account a $Ni(OH)_2$ density of 3.97 g cm^{-3}, we estimated at 0.043 mol cm^{-3}.

The proton diffusion coefficient obtained from Ni nanoparticles was 1.2 x 10^{-11} cm^2 s^{-1}, consistent with previous works [36]. Remarkably, the diffusion coefficient for NiSn (2:1) was slightly higher, 1.9 x 10^{-11} cm^2 s^{-1}, but as Sn concentration increased, this apparent diffusion coefficient decreased (Table 3.2).

Figures 3.8a-d display cyclic voltammograms (50 mV s^{-1}) of the Ni and the NiSn electrocatalyts in a media containing different methanol concentrations, from 0.05 M to 1.0 M. It can be observed that the $Ni(OH)_2$ oxidation peak gradually disappears within the large current density increase related to the MOR when the methanol concentration increases. Figures 8a-d displays the dependence of the current density measured at 0.70 V *vs.* Hg/HgO with the methanol concentration. The current density at 0.70 V *vs.* Hg/HgO rapidly increased in the low methanol concentration range and stabilized at methanol concentrations around 0.3 M. A linear fit of the logarithmic plot of the current density of MOR versus the methanol concentration for the NiSn (2:1) electrode pointed toward an apparent methanol reaction order of around 0.4. A similar reaction orders was obtained for Ni-based electrodes (Figure 3.8a). No clear linear relationship could be fitted to the Ni electrode.

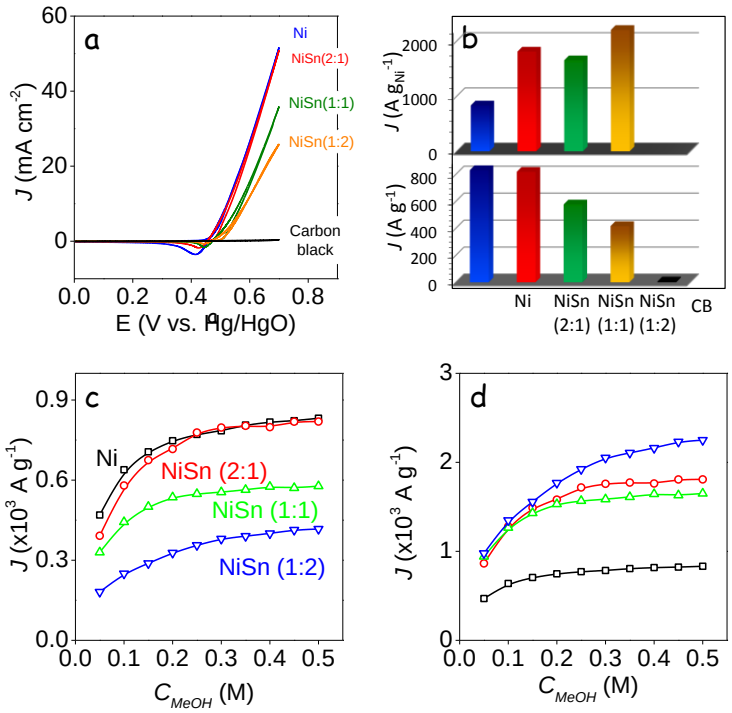

Figure 3.9. a) Cyclic voltammograms of CB, Ni, and NiSn-based electrodes in 0.5 M KOH with 0.5 M methanol at a sweep rate of 50 mV s^{-1}. b) Mass current densities considering the whole mass and only the mass of Ni for Ni, and NiSn-based electrodes in 0.5 M KOH containing 0.5 M methanol at 0.7 V vs. Hg/HgO. c) Mass current densities considering the mass for Ni, and NiSn-based electrodes 0.5 M KOH solution with various methanol concentrations ranging from 0.05 to 0.5 M at the same voltage. d) Mass current densities considering the mass of Ni for Ni, and NiSn-based electrodes in the same condition.

While saturating at relatively low methanol concentrations, very high current densities and mass current densities were obtained for Ni and NiSn NP-based electrodes (Figures 3.9a-b). Figure 3.9a displays the cyclic voltammograms of the electrocatalysts based on Ni NPs, Sn NPs, CB, and Ni-Sn NPs in 0.5 M KOH with 0.5 M methanol. Mass current densities were calculated taking into account the mass of metal in each electrode (Figure 3.9b). The calculated mass current density was 830 A g^{-1} for Ni and 820 A g^{-1} for NiSn (2:1)-based electrodes. When we increase the amount of Sn, the mass current densities decreased to 580 A g^{-1} and 420 A g^{-1} for NiSn (1:1) and NiSn (1:2), respectively. When only considering the mass of Ni as the active element to evaluate the mass current density (Figure 3.9c-d), all NiSn NP-based electrodes showed similar performances, all much higher than that of elemental Ni NPs: 830 A g^{-1} for Ni, 1800 A g_{Ni}^{-1} for NiSn (2:1), 1650 A g_{Ni}^{-1} for NiSn (1:1) and 2250 A g_{Ni}^{-1}, for NiSn (1:2). A comparison of catalytic performance was listed between our results and previously reported Ni-based catalysts towards MOR. From this comparison, we conclude that NiSn NPs are excellent candidates for the electro-oxidation of methanol in alkaline medium.

Chronoamperometric measurements were used to determine the electrocatalysts stability. Figure 3.10.a displays the chronoamperograms obtained from the different electrodes in a magnetically stirred 0.5 M KOH solution containing 0.5 M methanol at 0.70 V vs Hg/HgO. In this case, no methanol depletion layer is formed and current densities do not suffer any initial drop. Figure 3.10.b shows a representative STEM micrograph of the NiSn (2:1) electrocatalyst after a 10000 s stability test. A broader size distribution of the NCs was observed, which could be related to a partial aggregation during electrocatalyst formulation. In the same figure, the EELS chemical compositional maps of the NPs are displayed. While signal and resolution were not optimal due to the presence of the electrocatalyst additives, i.e. CB and Nafion, compositional maps showed the existence of Ni and Sn in all the nanoparticles and no clear phase segregation could be identified. On the contrary, they increased in the first minutes to later decrease over the 10000 seconds studied.

Figure 3.10c shows the chronoamperograms of NiSn (2:1) and Ni electrodes in a 0.5 M KOH solution containing 0.5 M methanol at 0.70 V *vs.* Hg/HgO. The current densities largely dropped in the first minutes and then relatively stabilized. Similarly fast initial drops were previously observed and are generally attributed to the fact that initially active sites are free of adsorbed methanol molecules and no methanol depletion layer around the electrode exist, allowing a very fast initial reaction.[14] In the first minutes, an equilibrium coverage of methanol at the catalyst surface and an equilibrium gradient of methanol around the electrode are stablished, dropping the current density to a lower value. The posterior progressive drop of current density is most likely related to the poisoning of the active sites at the electrode with reaction products. Figure 3.10d displays the Nyquist plot of the impedance spectra of methanol

oxidation on Ni, NiSn (2:1), NiSn (1:1) and NiSn (1:2) electrodes. The measurements were made in a 0.5 M KOH + 0.5 M methanol solution at 0.7 V *vs.* Hg/HgO. We observed the impedance associated to the charge transfer for methanol electrochemical oxidation to increase with the amount of Sn.

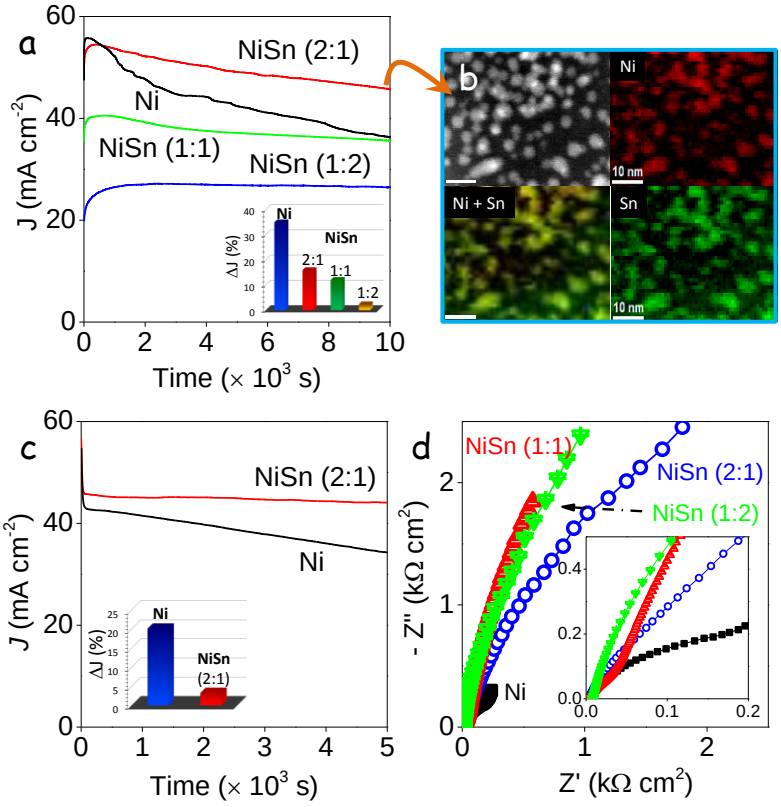

Figure 3.10. a) Chronoamperometric responses of NiSn and Ni electrodes at 0.70 V vs. Hg/HgO in 0.5 M KOH containing 0.5 M methanol with magnetic bar stirring during measurements. b) EELS chemical composition maps of a NiSn (2:1) electrocatalyst after 10000s CA stability test: Individual Ni $L_{2,3}$-edges at 855 eV (red), Sn $M_{4,5}$-edges at 485 eV (green) and composite Ni-Sn map. c) Chronoamperometry of NiSn (2:1) and Ni electrodes at 0.70 V *vs.* Hg/HgO in quiescent solution of 0.5 M KOH containing 0.5 M methanol. d) Nyquist plot of the methanol oxidation on Ni- and NiSn-based electrodes in a 0.5 M KOH + 0.5 M methanol solution at 0.7 V *vs.* Hg/HgO.

Overall, NiSn-based electrodes clearly displayed improved stabilities over Ni-based electrocatalysts. This experimental fact could have two different explanations: i) The presence of Sn can contribute to the oxidation of the MOR products that poisons the Ni surface sites. In this direction, lattice or adsorbed oxygen or OH^- groups on Sn metal, oxide or hydroxide could further oxidize MOR products that strongly adsorb onto the Ni sites poisoning its surface. ii) Alternatively, the presence of Sn atoms within the Ni structure, forming a Ni_3Sn_2 phase, certainly modifies the electronic density of states of Ni, thus affecting its chemistry, which could prevent strong binding of particular poisoning species. Additional work would be required

to exactly asses the mechanism of improvement of the electrode stability with the Sn incorporation.

3.4 Conclusion

In summary, a new synthetic route to produce NiSn intermetallic NPs with composition control was developed. Detailed electrochemical measurements showed that these NPs exhibited excellent performance for MOR in alkaline solution. Ni-rich NiSn-based electrocatalysts displayed slightly improved performances than Ni-based electrocatalysts. Most notorious was the significantly improved stability of NiSn catalysts compared with that of Ni. This work represents a significant advance in developing cost-effective electrocatalysts with high activity and stability for MOR in DMFCs.

3.5 References

1 M. F. Sgroi, F. Zedde, O. Barbera, A. Stassi, D. Sebastián, F. Lufrano, V. Baglio, A. S. Aricò, J. L. Bonde and M. Schuster, *Energies*, 2016, **9**, 1008.

2 T. Schultz, S. Zhou and K. Sundmacher, *Chem. Eng. Technol.*, 2001, **24**, 1223–1233.

3 S. S. Munjewar, S. B. Thombre and R. K. Mallick, *Ionics (Kiel).*, 2017, **23**, 1–18.

4 P. Kumar, K. Dutta, S. Das and P. P. Kundu, *Int. J. Energy Res.*, 2014, **38**, 1367–1390.

5 Z. Daşdelen, Y. Yıldız, S. Eriş and F. Şen, *Appl. Catal. B Environ.*, 2017, **219**, 511–516.

6 G. fa Long, X. hua Li, K. Wan, Z. xing Liang, J. hua Piao and P. Tsiakaras, *Appl. Catal. B Environ.*, 2017, **203**, 541–548.

7 M. A. A. Rahim, R. M. A. Hameed and M. W. Khalil, *J. Power Sources*, 2004, **134**, 160–169.

8 M. Zhou, P. Xiao, W. Guo, J. Deng, F. Liu and Y. Zhang, *J. Electrochem. Soc.*, 2014, **161**, H133–H137.

9 R. M. Abdel Hameed and R. M. El-Sherif, *Appl. Catal. B Environ.*, 2015, **162**, 217–226.

10 M. W. Khalil, M. A. Abdel Rahim, A. Zimmer, H. B. Hassan and R. M. Abdel Hameed, *J. Power Sources*, 2005, **144**, 35–41.

11 D. Wu, W. Zhang and D. Cheng, *ACS Appl. Mater. Interfaces*, 2017, **9**, 19843–19851.

12 I. Danaee, M. Jafarian, F. Forouzandeh, F. Gobal and M. G. Mahjani, *Int. J. Hydrogen Energy*, 2008, **33**, 4367–4376.

13 R. Ding, J. Liu, J. Jiang, F. Wu, J. Zhu and X. Huang, *Catal. Sci. Technol.*, 2011, **1**, 1406–1411.

14 X. Cui, P. Xiao, J. Wang, M. Zhou, W. Guo, Y. Yang, Y. He, Z. Wang, Y. Yang, Y.

Zhang and Z. Lin, *Angew. Chemie - Int. Ed.*, 2017, **56**, 4488–4493.

15 S. L. Candelaria, N. M. Bedford, T. J. Woehl, N. S. Rentz, A. R. Showalter, S. Pylypenko, B. A. Bunker, S. Lee, B. Reinhart, Y. Ren, S. P. Ertem, E. B. Coughlin, N. A. Sather, J. L. Horan, A. M. Herring and L. F. Greenlee, *ACS Catal.*, 2017, **7**, 365–379.

16 X. Cui, W. Guo, M. Zhou, Y. Yang, Y. Li, P. Xiao, Y. Zhang and X. Zhang, *ACS Appl. Mater. Interfaces*, 2015, **7**, 493–503.

17 I. Danaee, M. Jafarian, A. Mirzapoor, F. Gobal and M. G. Mahjani, *Electrochim. Acta*, 2010, **55**, 2093–2100.

18 Y. Yu, Q. Yang, X. Li, M. Guo and J. Hu, *Green Chem.*, 2016, **18**, 2827–2833.

19 Q. Yi, W. Huang, J. Zhang, X. Liu and L. Li, *Catal. Commun.*, 2008, **9**, 2053–2058.

20 Y. Wang, X. Wang, Y. Wang and J. Li, *Int. J. Hydrogen Energy*, 2015, **40**, 990–997.

21 X. Wang, J. Lian and Y. Wang, *Int. J. Hydrogen Energy*, 2014, **39**, 14288–14295.

22 D.-H. Lim, D.-H. Choi, W.-D. Lee, D.-R. Park and H.-I. Lee, *Electrochem. Solid-State Lett.*, 2007, **10**, B87.

23 J. Liu, Y. Wen, P. A. Van Aken, J. Maier and Y. Yu, *Nano Lett.*, 2014, **14**, 6387–6392.

24 Y. Liu, X. Liu, Q. Feng, D. He, L. Zhang, C. Lian, R. Shen, G. Zhao, Y. Ji, D. Wang, G. Zhou and Y. Li, *Adv. Mater.*, 2016, **28**, 4747–4754.

25 K. Kravchyk, L. Protesescu, M. I. Bodnarchuk, F. Krumeich, M. Yarema, M. Walter, C. Guntlin and M. V. Kovalenko, *J. Am. Chem. Soc.*, 2013, **135**, 4199–4202.

26 Y. Chen, X. Luo, H. She, G.-H. Yue and D.-L. Peng, *J. Nanosci. Nanotechnol.*, 2009, **9**, 5157–5163.

27 A. Yakymovych and H. Ipser, *Nanoscale Res. Lett.*, 2017, **12**, 142.

28 C. Schmetterer, J. Vizdal and H. Ipser, *Intermetallics*, 2009, **17**, 826–834.

29 C. Serrano-Cinca, Y. Fuertes-Callén and C. Mar-Molinero, *Perkin-Elmer Corporation Physical Electronics Division*, 2005, vol. 38.

30 D. M. MacArthur, The Electrochemical Society, 1970, vol. 117.

31 P. Oliva, J. Leonardi, J. F. Laurent, C. Delmas, J. J. Braconnier, M. Figlarz, F. Fievet and A. de Guibert, *J. Power Sources*, 1982, **8**, 229–255.

32 R. Chang, *Elsevier*, 2006, vol. 316.

33 N. A. M. Barakat and M. Motlak, *Appl. Catal. B Environ.*, 2014, **154**–**155**, 221–231.

34 A. J. Bard and L. R. Faulkner, *Electrochemical methods.* 2001, 50, 1–850.

35 D. Chen and S. D. Minteer, *J. Power Sources*, 2015, **284**, 27–37.

36 C. Zhang, *The Electrochemical Society*, 1987, vol. 134.

Chapter 4

Colloidal Ni-Co-Sn Nanoparticles as Efficient Electrocatalysts for Methanol Oxidation Reaction

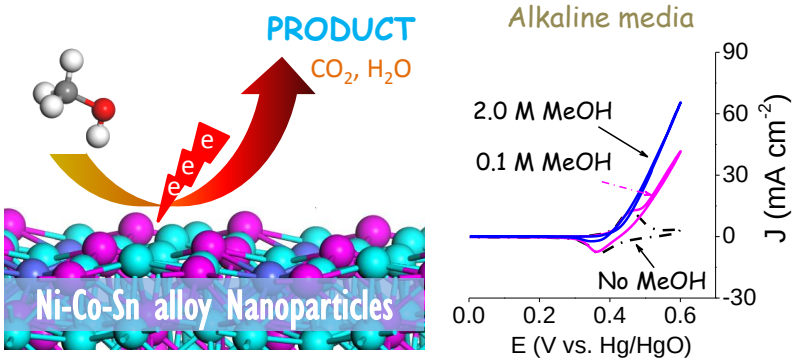

Methanol oxidation reaction in alkaline media and the activity

Key words:
Ni-based electrocatalyst
methanol oxidation
direct methanol fuel cells
electrocatalysis
colloidal synthesis
ternary nanoparticles

The deployment of direct methanol fuel cells requires engineering cost-effective and durable electrocatalyst for the methanol oxidation reaction (MOR). As an alternative to noble metals, Ni-based alloys have shown excellent performance and good stability toward MOR. Herein, we present a series of $Ni_{3-x}Co_xSn_2$ colloidal nanoparticles (NPs) with composition tuned over the entire Ni/Co range ($0 \leq x \leq 3$). We demonstrate electrodes based on these ternary NPs to provide improved catalytic performance toward MOR in alkaline medium when compared with binary Ni_3Sn_2 NPs. A preliminary composition optimization resulted in $Ni_{2.5}Co_{0.5}Sn_2$ NP-based electrodes exhibiting extraordinary mass current densities, up to 1050 mA mg^{-1}, at 0.6 V *vs.* Hg/HgO in 1.0 M KOH containing 1.0 M methanol. This current density was about two-fold higher than that of Ni_3Sn_2 electrodes (563 mA mg^{-1}). The excellent performance obtained with the substitution of small amounts of Ni by Co was concomitant to an increase of the surface overage of active species and an enhancement of the diffusivity of the reaction limiting species. Additionally, saturation of the catalytic activity at higher methanol

concentrations was measured for $Ni_{3-x}Co_xSn_2$ NP-based electrodes containing a small amount of Co when compared with binary Ni_3Sn_2 NPs. While the electrode stability was improved with respect to elemental Ni NP-based electrodes, the introduction of small amounts of Co slightly decreased the cycling performance. Additionally, Sn, a key element to improve stability with respect to elemental Ni NPs, was observed to slowly dissolve in the presence of KOH. Density functional theory calculations on metal alloy surfaces showed the incorporation of Co within the Ni_3Sn_2 structure to provide more effective sites for CO and CH_3OH adsorption. However, the relatively lower stability could not be related with CO or CH_3OH poisoning.

4.1 Introduction

The development of renewable energy technologies able to reduce the use of fossil fuels is one of the biggest challenges we face this 21st century. To this end, direct alcohol fuel cells able to convert chemical energy stored in alcohols into electricity, are regarded as a very promising energy conversion technology.[1–9] More particularly, direct methanol fuel cells (DMFCs) provide several advantages, including high energy density, high efficiency, low emissions, fast mechanical refueling and simple operation.[10–13] In addition, methanol not only provides a high energy density, but also an easy storage and distribution, which makes it one of the most interesting fuels.[10,14] In this scenario, the development of electrocatalyst for the methanol oxidation reaction (MOR) has become a very dynamic research field.[12,15]

State-of-the-art electrocatalysts for MOR are generally based on noble metals and their alloys, e.g. Pt,[16–21] PtNi,[22–28] PtCo,[29-32] PuCu,[33,34] PtPd,[34,35] and PtSn.[36–40] However, the low tolerance to CO and the high cost and scarcity of these materials have strongly limited the commercialization of DMFCs.[13,41–43] Therefore, over the past years, researchers have devoted increasing attention in searching for alternative earth-abundant and cost-efficient MOR electrocatalysts.

While no single metal has provided electrocatalytic properties comparable to Pt and Pt-group metals, particular bimetallic compositions have demonstrated very promising performances and stabilities. Among the earth-abundant elements, the most promising MOR catalysts under alkaline condition are bimetallic alloys based on Ni, e.g. Ni-Cu,[41,44–46] Ni-Mn,[47] Ni-Fe,[48,49] Ni-Co,[50–57] Ni-Sn.[58] In a previous study, we demonstrated NiSn NPs to present outstanding performance for electrocatalytically MOR in alkaline medium, and particularly an enhanced stability compared with state-of-the-art elemental Ni NPs.[58] We hypothesized this improvement to be related with an influence of Sn on the electronic properties of Ni or the introduction of additional adsorption sites that promoted electrocatalysis of poisoning species.

A main advantage of bimetallic catalysts over elemental compositions is their offering of additional degrees of freedom to control the surface electronic structure, to provide optimum active sites for one or various concatenated catalytic reaction, and to improve stability by combined catalytic reactions.[9,59–61] In the same direction, ternary compositions provide even larger opportunities to optimize electronic properties and provide suitable active sites for one or multiple reactions. However, few ternary alloy catalysts have been reported toward MOR and other electrocatalytic reactions. This is in large part due to the difficulty of producing ternary alloys with controlled composition. As an example, Hamza and coworkers demonstrated ternary oxide electrocatalysts $CuCoNiO_x$ supported on carbon nanotubes to have a notable activity toward MOR.[62] Recently, Rostami et al. demonstrated that NiCuCo on graphite electrodes enhanced activity and stability towards MOR.[53] However, in none of these previous works the full potential of ternary compositions to optimize catalytic properties could be demonstrated because no composition adjustment was attempted.

In this work, we detail a procedure to produce ternary $Ni_{3-x}Co_xSn_2$ NPs with tuned composition in all the Ni/Co ratio range ($0 \leq x \leq 3$). Subsequently, these NPs are supported on carbon black and tested as electrocatalysts toward MOR.

4.2 Experimental

4.2.1 Chemicals

Nickel(II) acetylacetonate ($Ni(acac)_2 \cdot xH_2O$ (x~2), 95%, Sigma-Aldrich), cobalt(II) acetylacetonate ($Co(acac)_2$, 97%, Sigma-Aldrich), tin(II) acetate ($Sn(oac)_2$, 95%, Fluka), tri-n-octylphosphine (TOP, 97%, Strem), oleylamine (OAm, 80-90%, TCI), borane tert-butylamine complex (TBAB, 97%, Sigma-Aldrich), oleic acid (OAc, Sigma-Aldrich), hydrazine monohydrate (N_2H_4, 64-65%, reagent grade, 98%, Sigma-Aldrich), Nafion (10 wt. %, perfluorinated ion-exchange resin, dispersion in water), methanol (anhydrous, 99.8%, Sigma-Aldrich), carbon black (CB, VULCAN XC72), potassium hydroxide (KOH, 85%, Sigma-Aldrich) and acetonitrile (CH_3CN, extra dry, Fisher) were used as received without any further treatment. Chloroform, hexane, acetone, and ethanol were of analytical grade and purchased from various sources. MilliQ water was obtained from a PURELAB flex from ELGA. An argon-filled glove-box was used for storing and handling sensitive chemicals.

4.2.3 Synthesis of colloidal $Ni_{3-x}Co_xSn_2$ NPs

All the syntheses were performed using standard airless techniques: a vacuum/dry argon gas Schlenk line was used for the synthesis. $Ni_{3-x}Co_xSn_2$ NPs were prepared following a similar protocol as the one we developed for the scale-up production of NiSn NPs.[58] In a typical synthesis of $Ni_{1.5}Co_{1.5}Sn_2$ NPs, 20 mL OAm, 0.3 mmol $Ni(acac)_2$, 0.3 mmol $Co(acac)_2$, 0.4 mmol $Sn(oac)_2$ and 1.0 mL OAc were loaded into a 50 mL three-necked flask and degassed under vacuum at 80 °C for 2 hours while being strongly stirred using a magnetic bar. Afterward, a gentle flow of argon was introduced, and then 5 mL of TOP was injected into the solution. Subsequently, the reaction flask was heated to 180 °C within 20 min, followed by quick injection of a solution containing 5 mmol TBAB in 5 mL degassed OAm. A visible color change, from deep pink to black was observed immediately. The reaction was maintained at this temperature for 1 hour before it was quenched using a water bath. The obtained NPs were collected by centrifuging and washing the solid product with acetone and chloroform 3 times. The as-prepared NPs were finally dispersed in chloroform and stored for further use. NPs were colloidally stable in chloroform for a couple of weeks. NPs with different nominal Ni/Co ratios, $Ni_{3-x}Co_xSn_2$ ($0 \leq x \leq 3$), were prepared following the same procedure (Scheme 4.1).

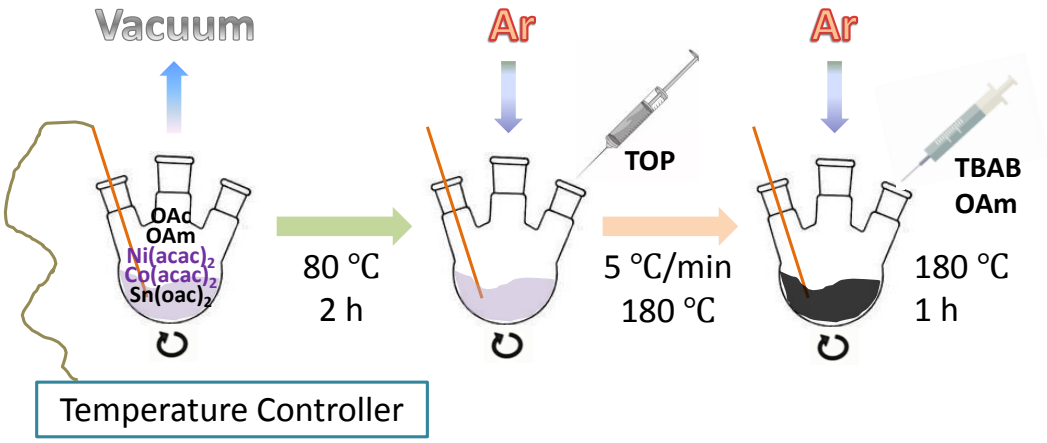

Scheme 4.1. Schematic drawing of the synthesis procedure to produce $Ni_{3-x}Co_xSn_2$ NPs.

4.2.4 Ligand removal

As-synthesized $Ni_{3-x}Co_xSn_2$ NPs dispersed in chloroform were precipitated through addition of ethanol and centrifugation. Then, they were dispersed in a mixture containing 25 mL acetonitrile and 0.8 mL hydrazine hydrate and stirred for 4 hours. NPs were then collected by centrifugation and washed with acetonitrile 3 additional times. Finally, NPs were dried under vacuum.

4.2.5 Characterization

The structural properties and chemical composition of the NPs was determined from a combination of characterization techniques. Powder x-ray diffraction (XRD) patterns were collected directly from the as-synthesized NPs on a Bruker AXS D8 Advance x-ray diffractometer with Ni-filtered (2 μm thickness) Cu K radiation (λ = 1.5106 Å) operating at 40 kV and 40 mA. 200 mesh carbon-coated transmission electron microscopy (TEM) grids from Ted-Pella were used as substrate. A drop of as-synthesized NPs dispersion was casted and dried on the grids before measurement. TEM analyses were carried out on a ZEISS LIBRA 120, operating at 120 kV. High-resolution TEM (HRTEM) and scanning TEM (STEM) studies were carried out using a field emission gun FEI Tecnai F20 microscope at 200 kV with a point-to-point resolution of 0.19 nm. High angle annular dark-field (HAADF) STEM was combined with electron energy loss spectroscopy (EELS) in the Tecnai microscope by using a GATAN QUANTUM filter. The Fourier transform infrared spectrometer (FTIR) data of the as-synthesized NPs before and after ligand removal were recorded on an Alpha Bruker FTIR spectrometer with a platinum attenuated total reflectance (ATR) single reflection module. Scanning electron microscopy (SEM) analyses were performed on a ZEISS Auriga SEM with an energy dispersive X-ray spectroscopy (EDS) detector at 20 kV. X-ray photoelectron spectroscopy (XPS) was done on a SPECS system equipped with an Al anode XR50 source operating at 150 mW and a Phoibos 150 MCD-9 detector. The pressure in the analysis chamber was kept below 10^{-7} Pa. The area analyzed was about 2 mm x 2 mm. The pass energy of the hemispherical analyzer was set at 25 eV and the energy step was maintained at 0.1 eV. Data processing was performed with the Casa XPS program (Casa Software Ltd., UK). Binding energies were shifted according to the reference C 1s peak that was located at 284.8 eV.

4.2.6 Preparation of Catalysts inks

In a typical preparation of a catalysts ink, 5 mg of purified NPs together with 5 mg of CB were added to 2 mL MilliQ water/ethanol solution (v/v = 1:1) containing 50 μL of a 10 wt% Nafion solution. Then the mixture was vigorously sonicated for 1 hour to obtain a homogeneous mixture. A glassy carbon (GC, 5 mm in diameter) electrode was polished using diamond paper and 0.05 μm alumina slurry, followed by water flush with MilliQ water. Subsequently, the electrode was ultra-sonicated in ethanol and MilliQ water separately for ~20 s before it was flushed with MilliQ water again and dried under argon flow at room temperature. Finally, 5 μL of the prepared ink was evenly loaded onto the GC electrode and was allowed to dry naturally in air at room temperature.

4.2.7 Electrochemical characterization

An electrochemical workstation (AutoLab, Metrohm) was employed for the electrochemical measurements in open air at room temperature. The conventional three-electrode system consisted of a counter electrode (Pt mesh), a working electrode and a reference electrode (*vs.* Hg/HgO). The Hg/HgO was placed in a salt bridge of 1.0 M KOH. All the measurements were performed in N_2-bubled 1.0 M KOH solution with and without addition of variable concentrations of methanol with magnetic bar stirring. All potential values presented in this paper were referred to the reference electrode, *vs.* Hg/HgO. Cyclic voltammetry (CV) and chronoamperometry (CA) measurements were performed to investigate the activity and stability for MOR. The current densities were calculated taking into account the geometric surface area of the GC electrode (0.196 cm^{-2}) or the metal mass loading (~ 0.012 mg NPs). The CO poisoning experiments were conducted in 1.0 M KOH containing 1.0 M CH_3OH using CA at 0.6 V simply by introducing a gentle gas (10% CO + 90% He) flow into the solution.

4.2.8 DFT calculations

To figure out the change of activity of Ni_3Sn_2 surface with the introduction of Co atoms, the adsorption of CH_3OH on the Ni_3Sn_2 and $Ni_{2.5}Co_{0.5}Sn_2$ surfaces was investigated using the Vienna ab-initio simulation package (VASP) based on the density functional theory (DFT).[63–66] An eight-layers slab was constructed in our models. During the structural optimization calculations, the atoms in the two bottom layers were fixed in their bulk positions, and those in the other six layers were allowed to relax. The (001) and (110) surfaces of both Ni_3Sn_2 and $Ni_{2.5}Co_{0.5}Sn_2$ were employed in our DFT calculations. The adsorption energies of CH_3OH on the surfaces, ΔE_{ads}, was defined as follows

$$\Delta E_{ads} = E_{adsorbate/slab} - E_{slab} - E_{adsorbates}$$

where $E_{adsorbate/slab}$ is the total energy of CH_3OH on the surfaces, E_{slab} is the total energy of the isolate surfaces and $E_{adsorbate/slab}$ is the total energy of isolate CH_3OH molecule. The first two terms were calculated with the same parameters. The third term was calculated by setting the isolated adsorbate in a box of 20 Å × 20 Å × 20 Å. Thus, negative ΔE_{ads} indicates exothermic chemisorption and positive values indicate an endothermic process.

4.3 Results and discussion

4.3.1 Synthesis of $Ni_{3-x}Co_xSn_2$ colloidal NPs

$Ni_{3-x}Co_xSn_2$ ($0 \leq x \leq 3$) colloidal NPs were produced from the reduction of proper amounts of the different metal salts in the presence of TOP, OAm and OAc (see experimental section and Scheme 4.1 for details). Figure 4.1a displays representative TEM micrographs of the quasi-spherical $Ni_{3-x}Co_xSn_2$ NPs produced. Table 4.1 displays the average diameter of NPs with different compositions. For the ternary compositions, a slight increase of size was obtained when increasing the amount of Co, from 4.2 ± 0.7 to 5.4 ± 0.8 nm. The size of the binary Co_3Sn_2 NPs was slightly larger, 7.5 ± 1.0 nm (Table 4.1).

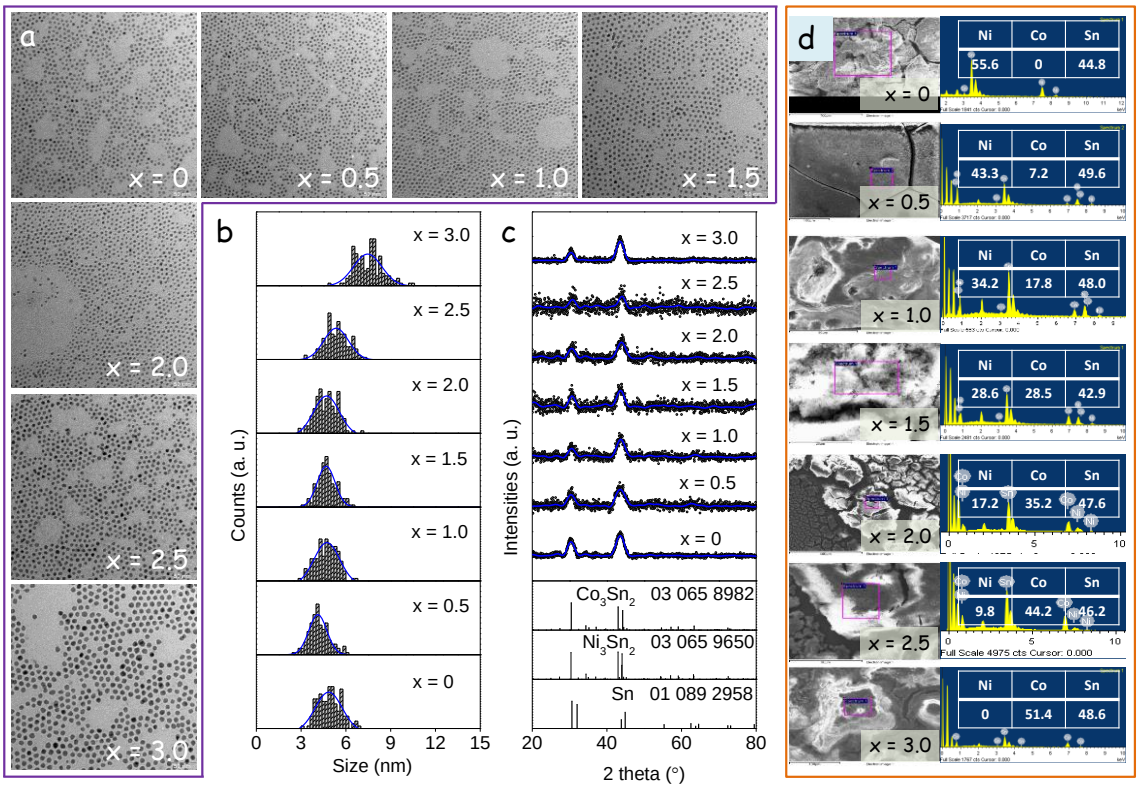

Figure 4.1. a) Representative TEM micrographs of $Ni_{3-x}Co_xSn_2$ NPs with different Co contents: x = 0, x = 1.5, x = 3.0. Scale bars: 50 nm. b) Size distribution histograms obtained from TEM images of $Ni_{3-x}Co_xSn_2$ ($0 \leq x \leq 3$) NPs. c) XRD patterns of $Ni_{3-x}Co_xSn_2$ ($0 \leq x \leq 3$) NPs. d) SEM-EDX characterization of the NPs of $Ni_{3-x}Co_xSn_2$, weight percentage (%) for each metal was presented in the table.

Ni_3Sn_2 and Co_3Sn_2 share the same orthorhombic crystal phase (*Pnma* space group) and have very similar lattice parameters, owing to their virtually equal ionic radius (0.135 nm).[67,68] Thus, very similar XRD patterns were obtained for all compositions, although the more noisy XRD patterns of the ternary structures pointed at slightly more defective crystals (Figure 4.1c).

Table 4.1. Average NPs size (TEM) and Ni:Co:Sn composition of $Ni_{3-x}Co_xSn_2$ NPs.

x $Ni_{3-x}Co_xSn_2$	Average Size (nm)	EDX			
		Ni	Co	Sn*	(Ni+Co)/Sn
0.0	4.9 ± 0.8	2.5	0.0	2.0	1.25
0.5	4.2 ± 0.7	1.8	0.3	2.0	1.05
1.0	4.7 ± 0.7	1.4	0.7	2.0	1.05
1.5	4.7 ± 0.7	1.3	1.3	2.0	1.30
2.0	4.7 ± 0.7	0.8	1.4	2.0	1.10
2.5	5.4 ± 0.8	0.4	1.9	2.0	1.15
3.0	7.5 ± 1.0	0.0	2.1	2.0	1.05

Note: *The amount of Sn was fixed to 2.0 to calculate the Ni and Co composition.

EDX analyses showed all compositions to be Sn-rich (Figure 4.1.d and Table 4.1), i.e. (Ni+Co)/Sn < 1.5. The Ni/Co ratio obtained by EDX analyses matched relatively well the nominal composition. This match was not surprising taking into account the resemblance of the two elements, with similar standard reduction potentials, Ni^{2+} (-0.25 V) and Co^{2+} (-0.28 V).[68]

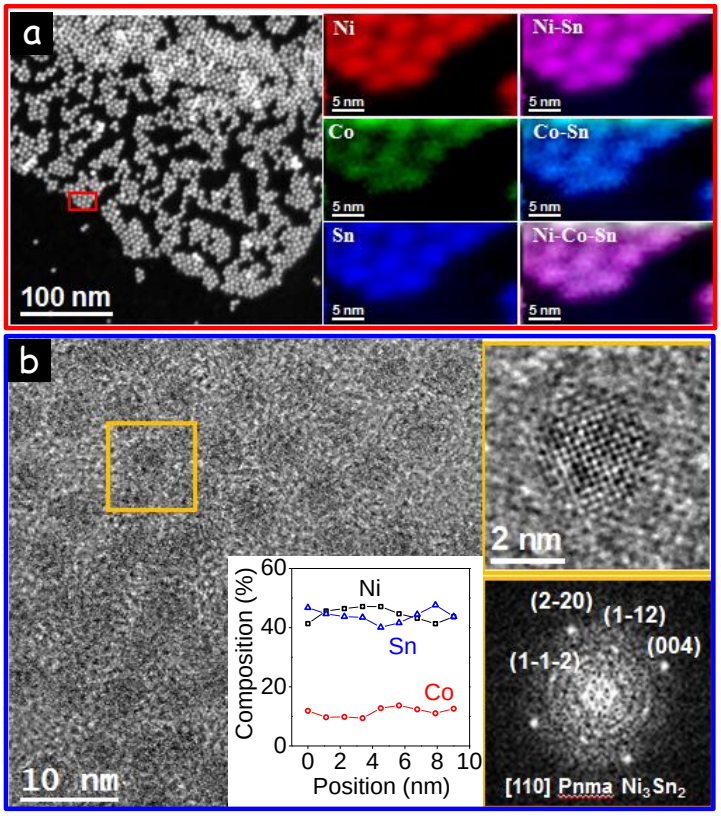

Figure 4.2. a) STEM micrograph, EELS chemical composition maps and a single NP line scan obtained from $Ni_{2.5}Co_{0.5}Sn_2$ NPs. Mappings correspond to the individual Ni $L_{2,3}$-edges at 855 eV (red), Co $L_{2,3}$-edges at 779 eV (green) and Sn M-edge at 485 eV (blue) as well as composites of Ni-Sn, Co-Sn and Ni-Co-Sn. b) HRTEM micrograph of a single $Ni_{2.5}Co_{0.5}Sn_2$ NP and its corresponding power spectrum. Lattice fringe distances were measured to be 0.211 nm, 0.205 nm, 0.306 nm and 0.302 nm, at 89.14º, 44.38º and 50.22º which could be interpreted as the orthorhombic Ni_3Sn_2 phase visualized along its [110] zone axis.

Figure 4.2a shows HAADF-STEM, EELS compositional mappings and a single NP line scan and a HRTEM micrograph from $Ni_{2.5}Co_{0.5}Sn_2$ NPs (see Figure 4.3 for additional compositions). All NPs within each sample contained the three elements in similar ratios. Within each NP, the three elements were found to be homogeneous distributed as shown from the compositional maps and the line scan of a single NP (Figure 4.2b). HRTEM micrographs revealed NPs to have a crystal structure compatible with that of Ni_3Sn_2 orthorhombic phase (space group = *Pnma*) with a = 7.1100 Å, b = 5.2100 Å and c = 8.2300 Å.

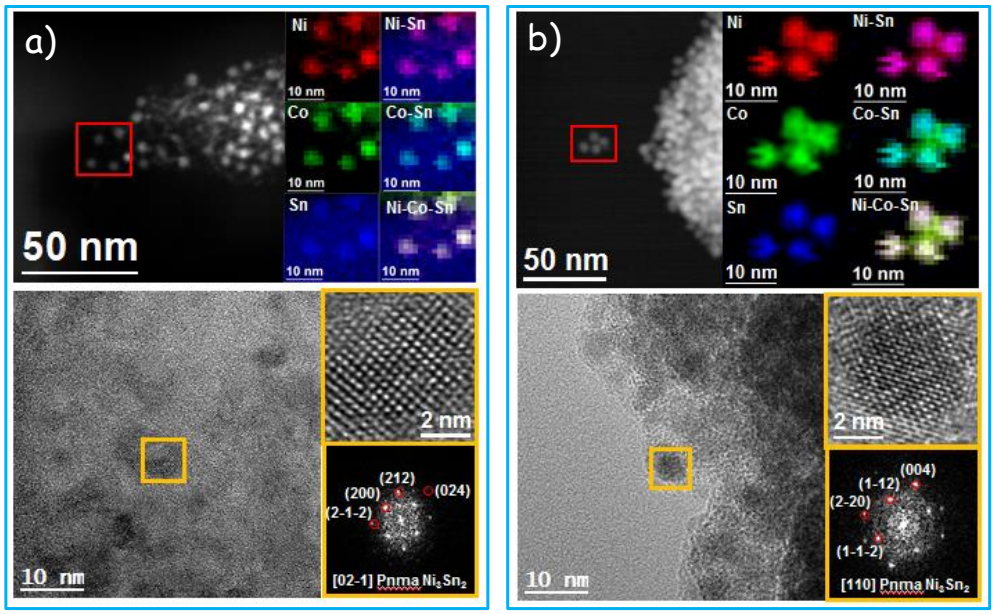

Figure 4.3. HRTEM micrograph and ADF-STEM image and EELS elemental mapping of $Ni_{3-x}Co_xSn_2$: a) x = 1.0, b) x = 1.5.

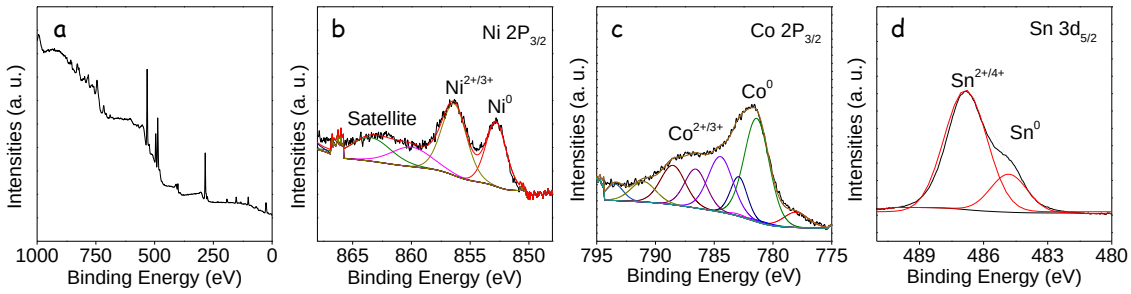

Figure 4.4. a) XPS spectra of $Ni_{3-x}Co_xSn_2$ (x = 1.5) NPs. b) Ni $2P_{3/2}$ region. c) Co $2P_{3/2}$ region. d) Sn $3P_{5/2}$ region.

XPS analyses of the $Ni_{1.5}Co_{1.5}Sn_2$ sample showed all elements to be present in two oxidation states: a minoritarian metallic state and a majoritarian oxidized phase (Figure 4.4). This result pointed at a partial surface oxidation of the NPs occurring due to their air exposure during purification, ligand removal and handling process.[58,69,70] Additionally, XPS analysis showed the surface of the $Ni_{1.5}Co_{1.5}Sn_2$ NPs to be slightly Sn rich compared with the global NP composition

measured by EDX, with (Ni + Co)/Sn = 0.91. The Sn-rich surface could be created during the NP surface oxidation.

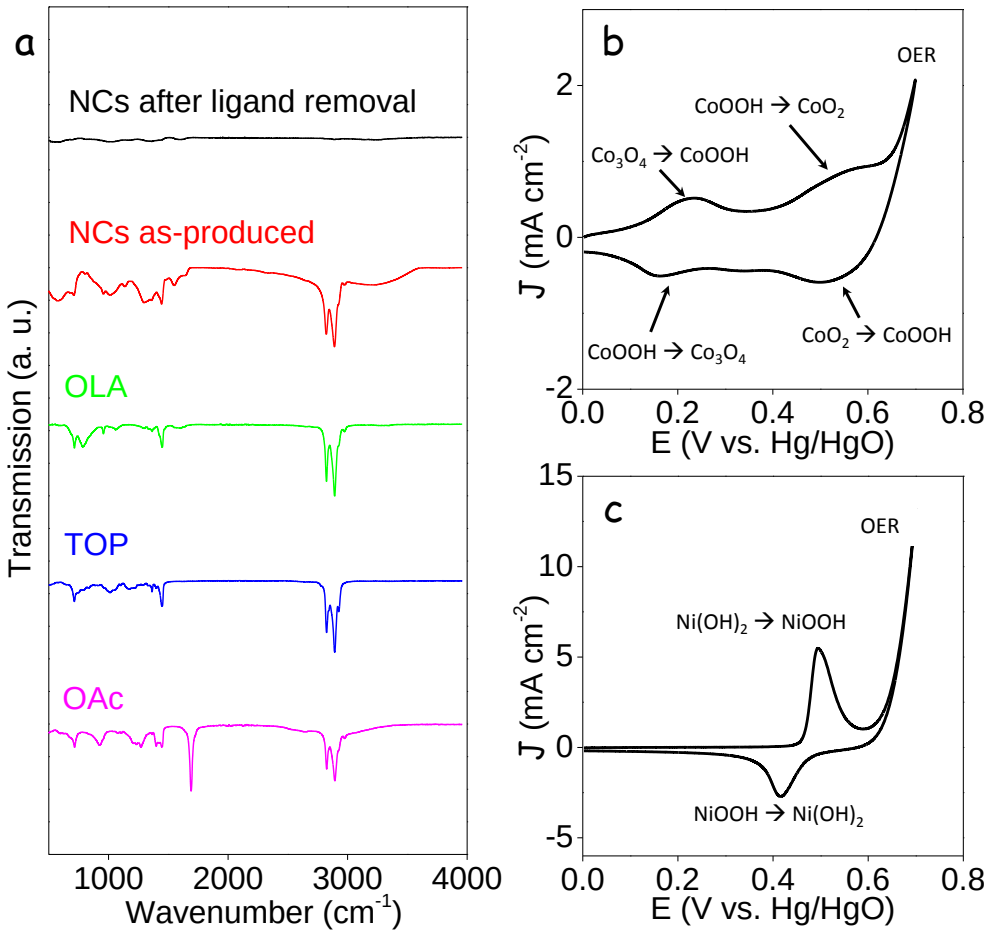

Figure 4.5. a) FTIR spectra of OAm, OAc, TOP and NiCoSn NCs as produced and after ligand removal. b) CV of Co_3Sn_2 electrodes in 1.0 M KOH solution at a scan rate of 50 mV s^{-1}. Tentative reduction and oxidation products are displayed. c) CV of Ni_3Sn_2 electrodes in 1.0 M KOH solution at a scan rate of 50 mV s^{-1}.

The presence of organic ligands at the surface of NPs strongly limits their electronic interaction and their ability to interact with the media.[37] Therefore, the use of NPs for applications where charge transfer or transport is involved requires the removal of the organic ligands used in the synthesis. Organic ligands were removed from the surface of $Ni_{3-x}Co_xSn_2$ NPs using a solution containing a 1.0 M hydrazine hydrate in acetonitrile.[71,72] After successive cleaning with acetonitrile, the disappearance of peaks at 2890 and 2822 cm^{-1} in the FTIR spectra, corresponding to C-H stretching modes, proved the effectiveness of the ligand removal (Figure 4.5a).

4.3.2 Electrochemical characterization

In our previous report, we showed electrodes based on Sn NPs to display no obvious oxidation and reduction peaks in the voltage range 0-0.6 V *vs.* Hg/HgO and to have a very limited performance toward MOR and OER in alkaline medium.[58] On the other hand, in alkaline medium, Co is generaly found in an oxidized form.[73–75] During the forward scan, at 0.15 V *vs.* Hg/HgO, cobalt is further oxidized probably to CoOOH and at ca. 0.55 V vs. Hg/HgO, CoOOH is further oxidized, possibly to CoO_2.[54,57,76,77] These phases are reduced during the reverse scan.

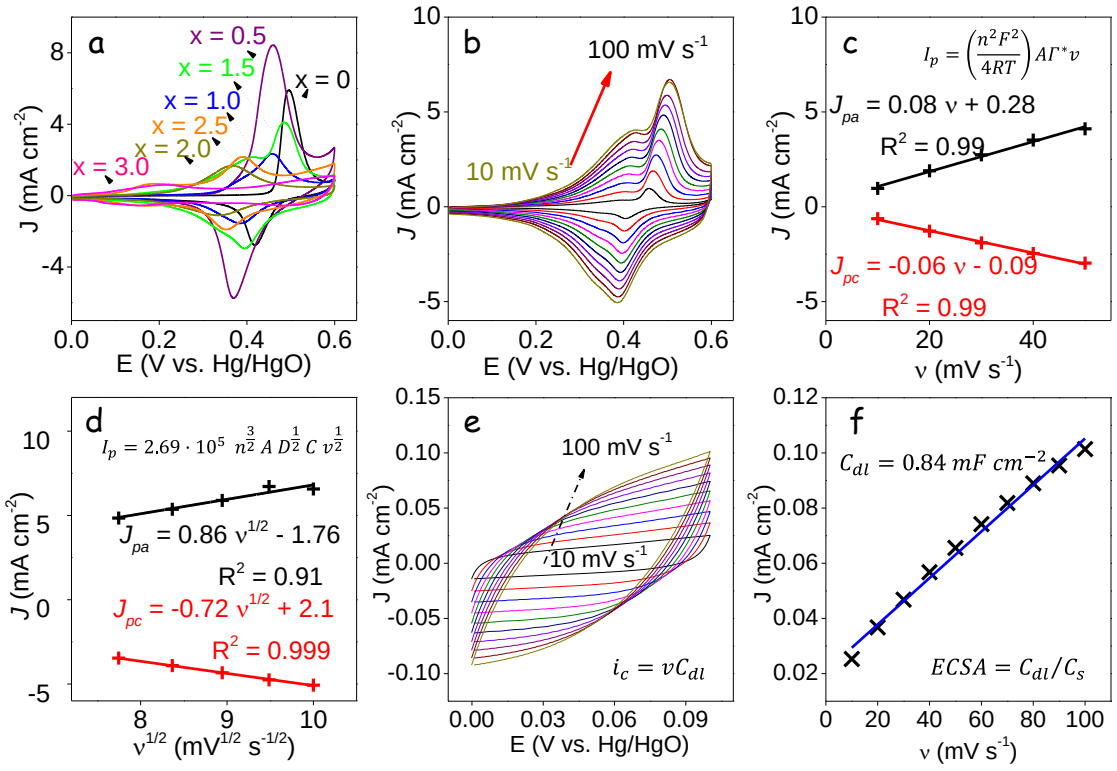

Figure 4.6. a) CVs of $Ni_{3-x}Co_xSn_2$ NP-based electrodes in 1.0 M KOH solution at a scan rate of 50 mV s^{-1}. b) CVs of electrodes based on $Ni_{1.5}Co_{1.5}Sn_2$ (x = 1.5) NPs in 1.0 M KOH solution at increasingly higher potential sweep rates: 10, 20, 30, 40, 50, 60, 70, 80, 90, 100 mV·s^{-1}. c) Linear fitting of the anodic and cathodic peak current densities with the scan rate in the low scan rate range (10-50 mV s^{-1}) for the $Ni_{1.5}Co_{1.5}Sn_2$ NP-based electrode. d) Linear fitting of the anodic and cathodic peak current densities with the square roots of the scan rate in the higher scan rate range (60-100 mV s^{-1}) for the $Ni_{1.5}Co_{1.5}Sn_2$ NP-based electrode. (e) CVs in the double layer region for the $Ni_{2.5}Co_{0.5}Sn_2$ electrode at scan rates of 10, 20, 30, 40, 50, 60, 70, 80, 90, 100 mV s^{-1} in the non-faradaic range of 0-0.1 V vs. Hg/HgO. (f) Corresponding linear fit of the capacitive current density vs. scan rates to estimate C_{dl} and calculate ECSA.

Figure 4.5b displays a CV of Co_3Sn_2 NPs in 1.0 M KOH at a scan rate of 50 mV s^{-1}. Co_3Sn_2 NPs show a low activity toward OER and small oxidation and reduction peaks during the positive and negative scans in the potential range 0-0.7 V *vs.* Hg/HgO, which correspond to the successive oxidation and reduction between cobalt oxide, hydroxide and/or oxyhydroxide phases.

In alkaline medium, Ni is generally found in the form of $Ni(OH)_2$, which is oxidized to NiOOH at 0.45 V vs. Hg/HgO.[58,78–81] The formation of the nickel oxyhydroxide is considered to be a key step in the electro-catalytic OER, which activates at E~0.65 V *vs.* Hg/HgO.[41,56] Figure 4.5b displays a CV of the electrode based on Ni_3Sn_2 NPs where the anodic peak corresponding to the oxidation of $Ni(OH)_2$ to NiOOH at 0.45 V *vs.* Hg/HgO is observed. In the reverse scan, a cathodic peak corresponding to the reduction of NiOOH to $Ni(OH)_2$ is clearly observed.

Figure 4.6a shows representative CVs of the $Ni_{3-x}Co_xSn_2$ electrodes in 1.0 M KOH solution at 50 mV s^{-1}. Compared with Ni_3Sn_2, when increasing the content of Co ($0 < x < 1.5$) the anodic peak broadened and shifted to lower potentials, denoting a clear influence of Co on the Ni_3Sn_2 surface properties. At higher amounts of Co ($x \geq 1.5$), a double peak was clearly observed, pointing at the occurrence of two differentiated oxidation reactions. Similar trends were observed for the cathodic peak. Simultaneously, the peak current densities increased when adding small amounts of Co, but decreased at higher Co loading (Table 4.2).

Figures 4.6b and 4.7a-g present the CV of $Ni_{3-x}Co_xSn_2$ in 1.0 M KOH solution at different scan rates, between 10 and 100 mV s^{-1}. When increasing the scan rate, current densities increased, the position of the anodic peak shifted to higher potentials, and the position of the cathodic peak shifted to lower potentials. The peak shift was attributed to a limitation of the reaction kinetics, which we further analyzed.[82] In the samples containing larger amounts of Co and presenting two redox peaks, we assumed the peak at higher potential values, related to a $Ni(OH)_2$ oxidation to NiOOH to be the relevant in the MOR. Therefore, we just considered the peak at the highest potential values in the following calculations.

The peak current (I_P) was proportional to the sweep rate (v) in the range 10-50 mV s^{-1}. From the slope of I_P vs. v (Figures 4.6c and 4.7f-j), the surface coverage of redox species (Γ^*) in the $Ni_{3-x}Co_xSn_2$ NPs was estimated[58,83]:

$$I_p = \left(\frac{n^2F^2}{4RT}\right) A\Gamma^* v$$

Where n, F, R, T and A are the number of transferred electrons (assumed to be 1), the Faraday constant (96845 C mol^{-1}), the gas constant (8.314 J K^{-1} mol^{-1}), temperature and the geometric surface area of the GC electrodes (0.196 cm^2), respectively.

Averaging results obtained from the forward and reverse scans, the surface coverage of redox species of Ni_3Sn_2 NPs-based electrodes was calculated to be 8.6×10^{-8} mol cm^{-2}. When introducing a small amount of Co, $Ni_{2.5}Co_{0.5}Sn_2$, this surface coverage increased to 1.4×10^{-7} mol cm^{-2}. Higher amounts of Co decreased this coverage to values below that of Ni_3Sn_2.

In the high scan rate range (Figures 4.6d and 4.7k-o),, 60-100 mV s^{-1}, the peak current increased linearly with the square root of the voltage scan rate, pointing toward a diffusion-limited redox reaction[58,83]:

$$I_p = 2.69 \times 10^5 n^{3/2} A D^{1/2} C v^{1/2}$$

where *D* is the diffusion coefficient of the reaction limiting specie and *C* is the initial concentration of redox species. Qualitatively, we observed the slope of I_P vs. $v^{1/2}$ obtained from Ni_3Sn_2 NP-based electrodes to increase when adding small amounts of Co. This observation pointed out at a faster diffusion of the redox limiting specie with the incorporation of Co. For Ni-based electrodes, the proton diffusion is generally accepted to be the rate limiting step that controls the oxidation reaction $Ni(OH)_2 \leftrightarrow NiOOH$.[58,84] Therefore, using the above equation and taking into account a proton density of 0.043 mol cm^{-3} for all the electrodes, the proton diffusion coefficient of the different materials was estimated.[58] The proton diffusion coefficient of Ni_3Sn_2 NP-based electrodes was 8.4 × 10^{-9} cm^2 s^{-1}. As qualitatively noted before, the diffusivity increased when introducing a small amount of Co within the structure: 1.3 × 10^{-8} cm^2 s^{-1} for $Ni_{2.5}Co_{0.5}Sn_2$, but decreased at higher Co concentrations: 2.9 × 10^{-9} cm^2 s^{-1} for Ni_2CoSn_2, and 4.6 × 10^{-9} cm^2 s^{-1} for $Ni_{1.5}Co_{1.5}Sn_2$.

Table 4.2. Summary of the electrocatalytic performance of $Ni_{3-x}Co_xSn_2$ NP-based electrodes

x	E_{pa}	J_{pa}	E_{pc}	J_{pa}	ΔE	Γ^* (×10^{-8})	D (×10^{-9})	E_η	J	ΔJ
0	0.496	5.934	0.417	-2.765	0.079	8.6	8.4	0.525	34.4	-15.2%
0.5	0.461	8.436	0.369	-5.756	0.092	14.2	12.8	0.452	65.5	-23.5%
1.0	0.457	2.351	0.383	-1.564	0.074	4.1	2.9	0.479	51.8	-40.8%
1.5	0.486	3.921	0.393	-2.970	0.093	7.3	4.6	0.464	53.8	-31.7%
2.0	0.364	1.682	0.330	-1.125	0.034	3.1	2.2	0.483	39.4	-81.4%
2.5	0.391	2.187	0.356	-1.903	0.035	4.7	4.2	0.481	34.4	-64.2%
3.0	0.207	0.579	0.172	-0.541	0.035	-	-	-	-	-

Note: *In samples showing two anodic/cathodic peaks, J_{pa}, E_{pa}, J_{pc}, E_{pc} and ΔE were measured from the highest voltage peak. CVs were carried out in 1.0 M KOH solution at a scan rate of 50 mV s^{-1}. E_η (@10 mA cm^{-2}), J (@0.6 V vs. Hg/HgO), ΔJ (@0.6 V vs. Hg/HgO) were calculated from the CVs in 1.0 M KOH solution containing 2.0 M methanol at a scan rate of 50 mV s^{-1}.*

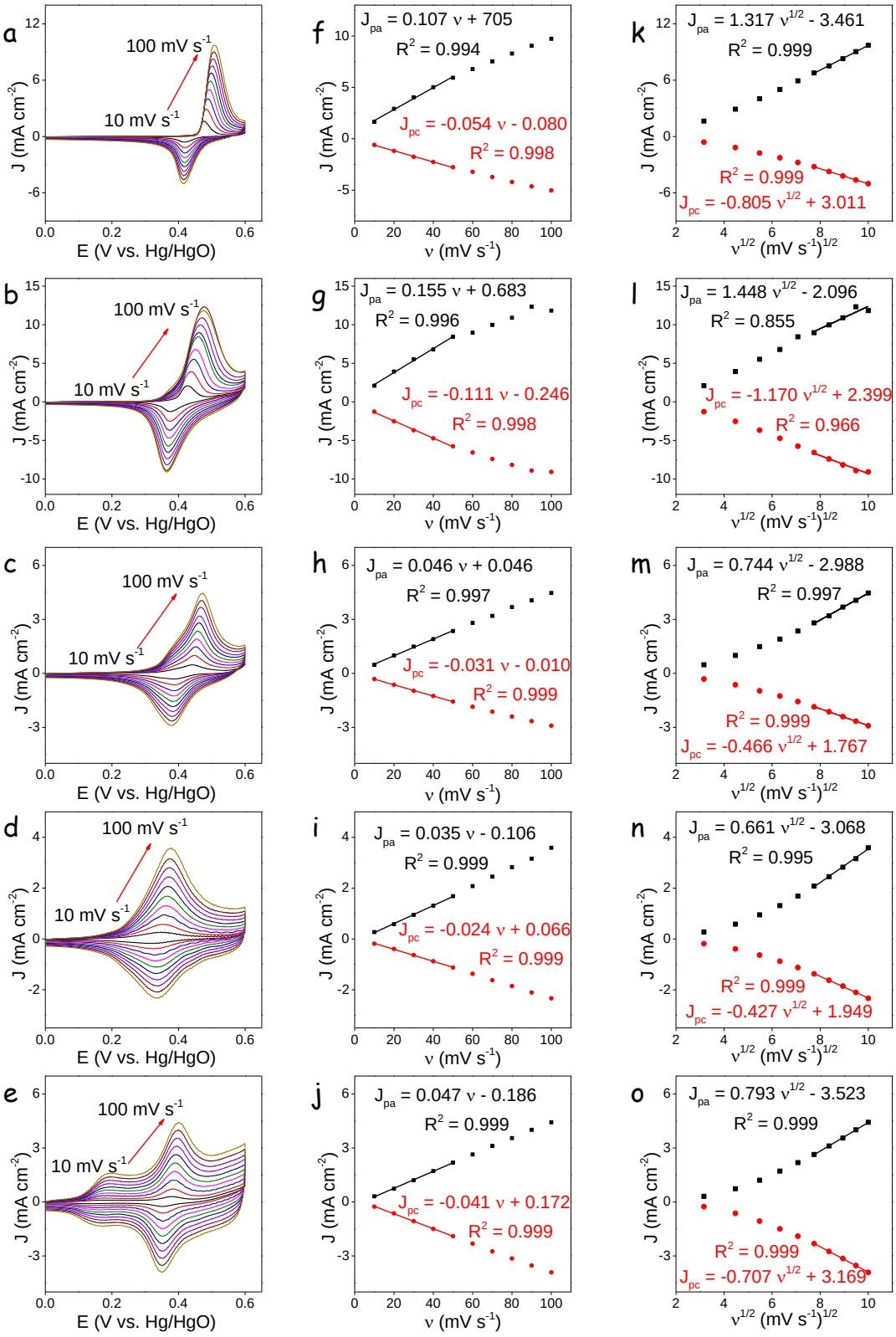

Figure 4.7. a-e) Cyclic voltammograms of $Ni_{3-x}Co_xSn_2$ (x = 0, 0.5, 1.0, 2.0, 2.5) NPs in 1 M KOH solution at increasingly higher potentials sweep rates: 10, 20, 30, 40, 50, 60, 70, 80, 90, 100 mVs^{-1}. f-j) Linear fitting of anodic and cathodic peak current densities to the scan rates of $Ni_{3-x}Co_xSn_2$ (x = 0, 0.5, 1.0, 2.0, 2.5) NPs. k-o) Linear fitting of anodic and cathodic peak current densities to the square roots of the scan rates of $Ni_{3-x}Co_xSn_2$ (x = 0, 0.5, 1.0, 2.0, 2.5) NPs.

The electrochemically active surface area (ECSA) was estimated by using the electrochemical double-layer capacitance (C_{dl}) on the basis of CVs recorded at different scan rates in the non-faradaic potential range (0-0.1 V vs. Hg/HgO).[85] Plotting i_c vs. yielded a straight line with a slope equal to C_{dl} (Figure 4.6e) and then ECSA was calculated by dividing C_{dl} by the specific capacitance:[86]

$$ECSA = C_{dl}/C_s$$

Where Cs is a general specific capacitance of 0.04 mF cm^{-2} based on typical value reported for metal electrodes in aqueous NaOH solution.[87] For $Ni_{2.5}Co_{0.5}Sn_2$, the calculated value of C_{dl} was 0.84 mF cm^{-2}, and the ECSA was 21 cm^{-2} (Figures 4.6f).

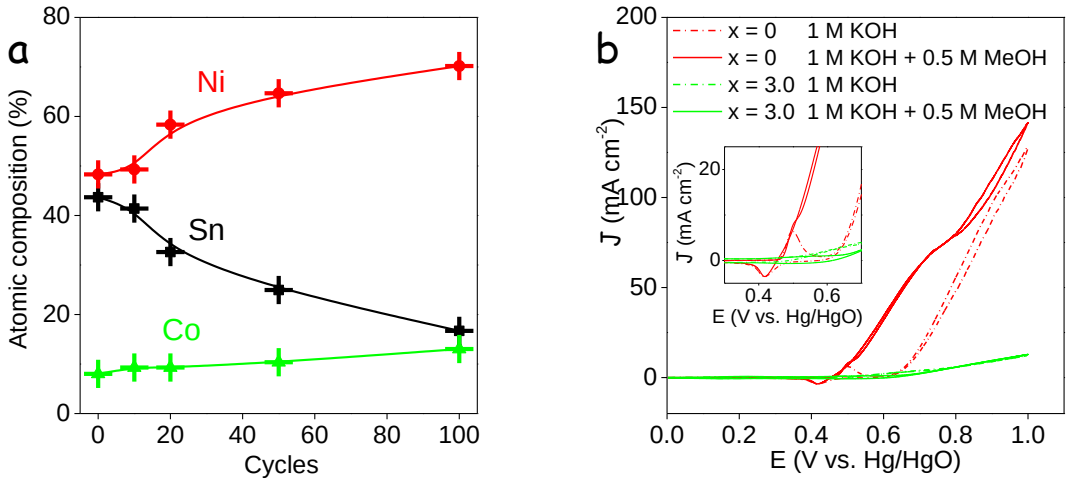

Figure 4.8. a) Atomic composition of the $Ni_{2.5}Co_{0.5}Sn_2$ material during CV (0-0.6 V vs Hg/HgO, 50 mV s^{-1}) in 1.0 M KOH. b) Cyclic voltammograms of $Ni_{3-x}Co_xSn_2$ (x = 0, 3.0) NPs in 1 M KOH solution at a scan rate of 50 mV s^{-1} in the presence and absence of 0.5 M methanol, inset shows an enlarged area of the current density with the applied potential of 0.35-0.65 V.

From the EDX analysis of the composition of the NPs during KOH cycling, we observed the amount of Sn to slowly decrease with the cycling number (Figure 4.8a) pointing at the partial dissolution of Sn from the $Ni_{3-x}Co_xSn_2$ alloy nanoparticles.

4.3.3 Electrocatalytic activity toward MOR

Figure 4.8b compares the cyclic voltammograms in 1.0 M KOH solution of electrodes based on Co_3Sn_2 and Ni_3Sn_2 NPs in absence and presence of a low concentration of methanol (0.5 M). Co_3Sn_2 showed much lower activities than the Ni_3Sn_2 catalyst toward both OER and MOR. The OER onset was found at ca. 0.65 V vs. Hg/HgO for both samples. While no significant MOR activity was appreciated in the Co_3Sn_2 electrode, MOR was activated at ca 0.45 V vs. Hg/HgO in Ni_3Sn_2-based electrodes. This voltage coincided with the formation of NiOOH. Indeed, it is

generally accepted that in Ni-based catalysts, MOR is activated by the formation of the NiOOH, which is believed to directly participate in the reaction.[41,46,58]

$$Ni(OH)_2 + OH^- \Rightarrow NiOOH + H_2O + e^-$$

$$NiOOH + CH_3OH \Rightarrow Ni(OH)_2 + products$$

To avoid the OER in the test of the MOR over $Ni_{3-x}Co_xSn_2$ NP-based electrodes, the potential range scanned was limited to 0-0.6 V *vs.* Hg/HgO.

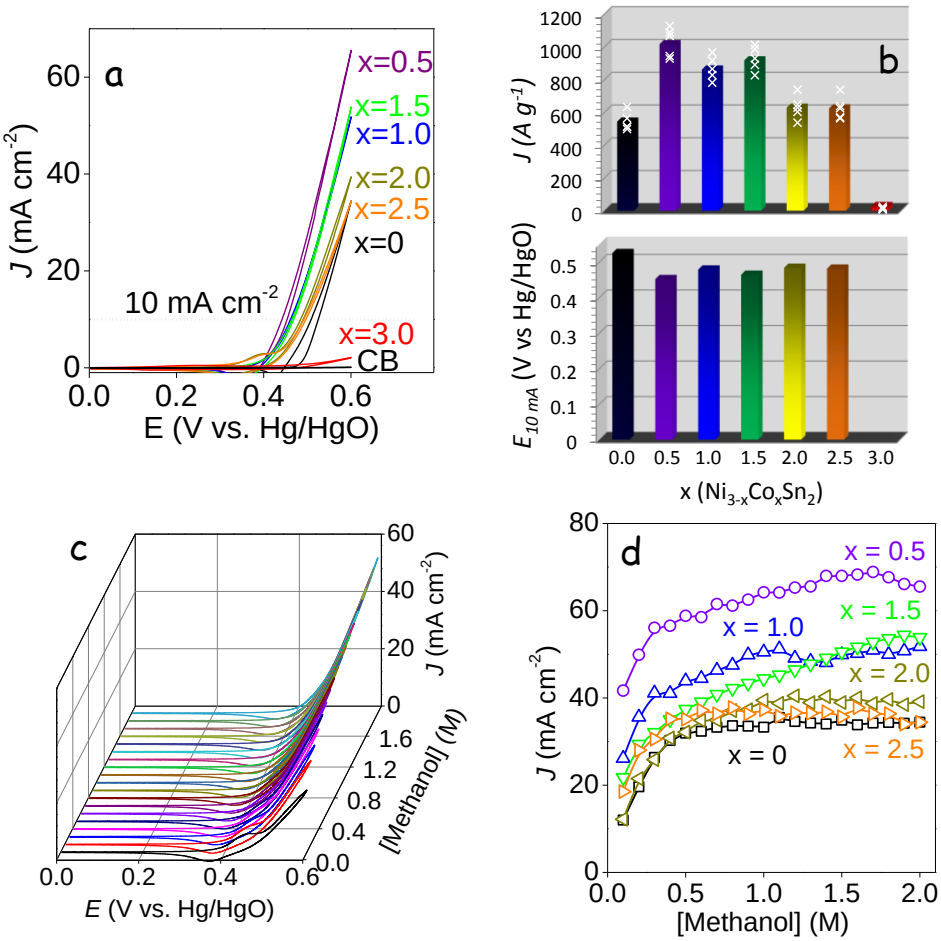

Figure 4.9. a) CVs of $Ni_{3-x}Co_xSn_2$ ($0 \leq x \leq 3$) and CB electrode in 1.0 M KOH containing 2.0 M methanol at a scan rate of 50 mV s^{-1}. b) Mass current density at 0.6 V and applied potential required to reach 10 mA cm^{-2} in $Ni_{3-x}Co_xSn_2$ ($0 \leq x \leq 3$) electrodes in 1.0 M KOH with 2.0 M methanol. Mass current densities measured from 5 electrodes with the same composition are presented. Bars reflect the average value of these 5 measurements. The standard deviations of the distributions were in the range from 7 % to 10 % for all the catalysts containing Ni and 20 % for the Co_3Sn_2 catalyst that showed a much lower activity. c) CVs of a $Ni_{1.5}Co_{1.5}Sn_2$ electrode in 1.0 M KOH solution with different methanol concentrations from 0.1 M to 2.0 M at a scan rate of 50 mV s^{-1}. d) Comparison of the current density at 0.6 V of $Ni_{3-x}Co_xSn_2$ ($0 \leq x \leq 2.5$) electrodes as a function of methanol concentrations from 0.1 M to 2.0 M.

Figure 4.9a shows representative CVs of a bare carbon black electrode and $Ni_{3-x}Co_xSn_2$ NP-based electrodes in 1.0 M KOH solution with 2.0 M methanol at a scan rate of 50 mV s^{-1}. Co_3Sn_2 presented very limited current densities toward MOR, similar to the carbon black electrode. However, surprisingly, all $Ni_{3-x}Co_xSn_2$ NP-based electrodes showed higher activity than the Ni_3Sn_2 NP-based electrode, including a lower onset potential and higher mass current densities. The onset potential (@ 10 mA cm^{-2}) was reduced from 0.53 V for Ni_3Sn_2 to 0.45 V for $Ni_{2.5}Co_{0.5}Sn_2$ and 0.46-0.48 V for the other Co-containing NP-based electrodes (Figure 4.9b). The mass current density, calculated from averaging results obtained from 5 different electrodes with the same composition, was found to increase with the incorporation of Co to the Ni_3Sn_2 alloy, from 543 A g^{-1} for Ni_3Sn_2 to 1016 A g^{-1} for the $Ni_{2.5}Co_{0.5}Sn_2$ electrode (Figure 4.9b). At higher Co/Ni ratios, the mass current density decreased with the Co content, but was kept above that of Ni_3Sn_2. In Table 4.3 a comparison of the performance toward MOR of the $Ni_{3-x}Co_xSn_2$ NP-based electrodes with other Ni-based electrodes and a commercial Pt/C composite is presented. The comparison demonstrated that $Ni_{3-x}Co_xSn_2$ NP-based electrodes with a preliminary optimized composition, $Ni_{2.5}Co_{0.5}Sn_2$, outperformed most previously developed catalysts.

Figure 4.9c shows the CVs of $Ni_{2.5}Co_{0.5}Sn_2$ NP-based electrodes in 1.0 M KOH solution with 0.1-2.0 M methanol at a scan rate of 50 mV s^{-1}. Figures 4.9d presents the current density at 0.6 V in 1.0 M KOH as a function of the methanol concentrations, from 0.1 to 2.0 M. For all electrodes, an initial rapid rise of the current density with the methanol concentration was observed. For Ni_3Sn_2, $Ni_{1.0}Co_{2.0}Sn_2$ and $Ni_{0.5}Co_{2.5}Sn_2$ electrodes, the current density stabilized at concentrations higher than 0.5 M methanol. However, the electrodes with a low Co loading still showed a slight increase of the current density above this concentration, which should be associated to a lower poisoning of the active sites by methanol adsorption in $Ni_{3-x}Co_xSn_2$ ($x \leq 1.5$) NPs compared with Ni_3Sn_2 NPs (Figure 4.9d). In particular, at 0.6 V *vs.* Hg/HgO, the $Ni_{2.5}Co_{0.5}Sn_2$ electrode displayed a current density of 41 mA cm^{-2} at 0.1 M, 59 mA cm^{-2} at 0.5 M and 65 mA cm^{-2} at 2.0 M. On the other hand, the Ni_3Sn_2 electrode was characterized by a current density of 12 mA cm^{-2} at 0.1 M, 32 mA cm^{-2} at 0.5 M and 34 mA cm^{-2} at 2.0 M at 0.6 V.

Table 4.3. Comparison of activity between catalysts in this work and recently reported Ni and Ni-based non-precious metal alloy catalyst

Catalysts	Morphology	Electrolyte	ECSA cm^{-2}	Applied potential V vs. RHE❶	Activity				Reference
					mA cm^{-2} Geometric area	mA cm^{-2} ECSA	mA mg_{metal}^{-1}	□J	
Cu/NiCu/C	Nanowires	1.0 M KOH + 1.0 MeOH		1.55	34.9		867.1	-12%@1000 cycles	[41]
$Ni_{0.75}Cu_{0.25}$	Branched 3D networks	1.0 M NaOH + 0.5 MeOH	112.5	1.69	84	0.75	168		[46]
Ni	NPs	0.4 M KOH + 1.0 MeOH		1.64	12				[88]
FeNi	NPs	0.1 M NaOH + 1.0 MeOH		1.56	50		1709		[48]
Ni@CNTs	Heterostructures	1.0 M KOH + 1.0 MeOH		1.62	~1.5		966		[80]
Ni_2Co_2	Cauliflower-like	1.0 M NaOH + 0.5 MeOH	72	1.74	~35	0.49			[57]
$Ni_{0.5}Co_{0.5}$	Porous alloy film	1.0 M NaOH + 0.5 MeOH		1.69	~35				[56]
Ni	Ti-supported flakes	1.0 M NaOH + 0.5 MeOH		1.74	39				[89]
Ni-Ti	NPs	0.1 M NaOH + 0.2 MeOH		1.62	0.5 mA				[81]
Ni	NPs@rGO	1.0 M KOH + 1.0 MeOH		1.64			1600		[90]
NiMn	Film	1.0 M NaOH + 0.5 MeOH		1.64	~80				[47]
$Ni_{1.7}Sn$	NPs	0.5 M KOH + 0.5 MeOH		1.65	50.9		819.3		[58]
$Ni_{2.5}Co_{0.5}Sn_2$	NPs	1.0 M KOH + 1.0 MeOH	21	1.57	65.5	3.12	1070.4	-35%@1500 cycles	This work
Ni_3Sn_2	NPs	1.0 M KOH + 1.0 MeOH		1.57	34.4		562.7		This work
Pt/C*	Commercial	1.0 M KOH + 1.0 MeOH		0.95			710		[41]

Note: *Commercial Pt/C was included here for comparison.

❶ For comparison, the applied potential was intended to convert to be vs. RHE using the following equation:

$$E_{RHE} = E^0_{Ref} + E_{Ref} + 0.059 \times PH$$

Where E^0_{Ref} is potential of the reference ($E^0_{Ag/AgCl}$ = 0.21 V, $E^0_{Hg/HgO}$ = 0.14 V), E_{Ref} is the potential that measured vs. reference, PH is simply converted from the electrolyte (PH = 14 + lg[OH^-], [OH^-] is the OH^- concentration of the alkaline media).

The long-term stability of $Ni_{3-x}Co_xSn_2$ NP-based electrodes was evaluated by CA measurements in 1.0 M KOH solution containing 2.0 M methanol at 0.60 V for 10000 s (Figure 4.10a). While an improved performance toward high methanol concentrations was obtained with the addition of small amounts of Co, the electrode stability decreased when adding increasingly higher amounts of Co, being the Ni_3Sn_2 electrode the most stable, followed by the $Ni_{2.5}Co_{0.5}Sn_2$. Compared with our previous work, the stability of the Ni_3Sn_2 and $Ni_{2.5}Co_{0.5}Sn_2$ electrodes was better than that of elemental Ni electrodes, what points at a beneficial role of Sn in this direction.[58] The improved stability with the presence of Sn could be related to a modification of the electronic structure or the promotion of the catalytic reaction of poisoning species, and could be limited by the partial dissolution of this element in the presence of KOH.

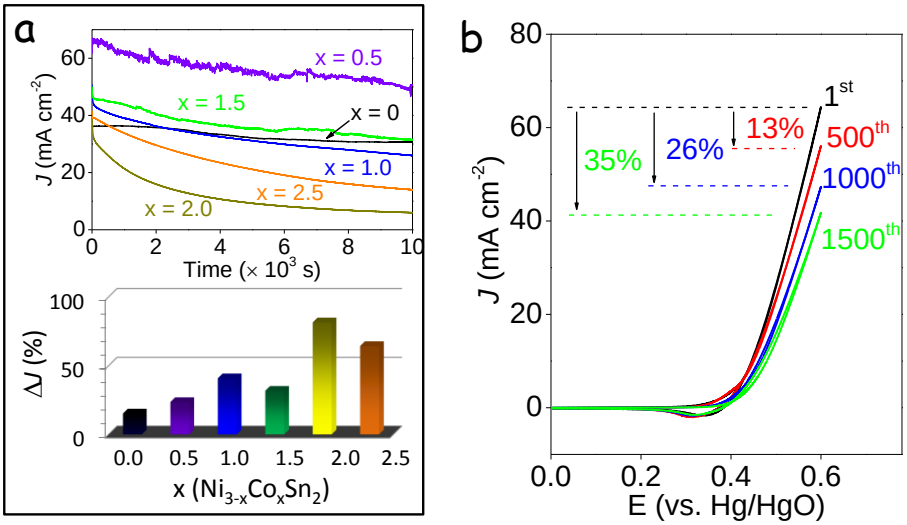

Figure 4.10. a) CA response of $Ni_{3-x}Co_xSn_2$ electrodes in 1.0 M KOH and 2.0 M methanol at 0.6 V for 10000 s. Current density change, $\Delta J = (J_1-J_2)/J_1$, during the 10000s tested, where J_1 and J_2 are the current densities measured at the 50th and 10000th s respectively. b) CVs of the $Ni_{2.5}Co_{0.5}Sn_2$ electrode in 1.0 M KOH electrolyte with 2.0 M methanol at a scan rate of 100 mV s^{-1} at cycles 1st, 500th, 1000th and 1500th.

The stability of the $Ni_{2.5}Co_{0.5}Sn_2$ electrode was also evaluated in the same concentration of methanol with continuous CV scanning with 100 mV s^{-1}. As shown in Figure 4.10b, the electrode lost 12.9% (500 circles), 21.5% (1000 circles) and 35.1% (1500 circles) of the current density of the 1st CV at 0.6 V. This performance decay could have its origin on: i) the progressive poisoning of the active sites by the reaction intermediates/products; ii) a restructuration of the alloy NPs or change of the NP electronic or chemical properties during the reaction, potentially related to the presence of cobalt; iii) the gradual dissolution of Sn, which presence was demonstrated to improve stability.

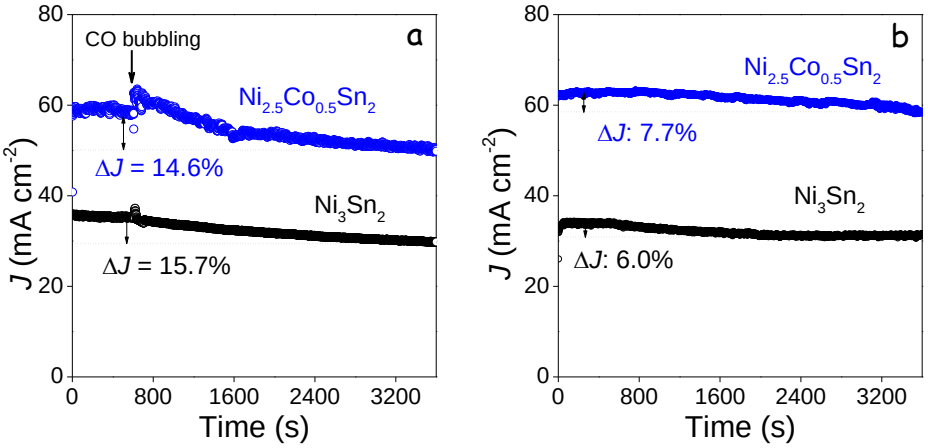

Figure 4.11. CA of Ni_3Sn_2 NPs and $Ni_{2.5}Co_{0.5}Sn_2$ NPs in 1.0 M KOH and 1.0 M methanol at 0.6 V: a) In the presence of a gentle CO flow (10% in He) added at t = 600 s. b) Without additional CO incorporation to the solution. $\Delta J = (J_1-J_2)/J_1$, where J_1 and J_2 is the current density measured at 600th and 3600th s respectively.

CO is generally considered as the most common intermediate/product degrading the catalyst performance over time through the blocking of its active sites.[34,40,42,55,57] Additional CA measurements were performed on the electrodes based on Ni_3Sn_2 NPs and $Ni_{2.5}Co_{0.5}Sn_2$ NPs in 1.0 M KOH and 1.0 M methanol at 0.6 V (Figure 4.11). At a certain time (t = 600 s), a gentle flow of CO was bubbled into the solution to determine its effect on the current density. With the presence of additional CO, both electrodes suffered a similar loss in the current density: 14.9% for $Ni_{2.5}Co_{0.5}Sn_2$ and 15.6% for Ni_3Sn_2. The same experiment in the absence of CO resulted in a significantly larger decrease of current density for the $Ni_{2.5}Co_{0.5}Sn_2$ electrode: 7.7% for $Ni_{2.5}Co_{0.5}Sn_2$ and 6.0% for Ni_3Sn_2. This result demonstrates the Co-containing electrode not to be specially sensitive to CO poisoning when compared with the Ni_3Sn_2-based one.

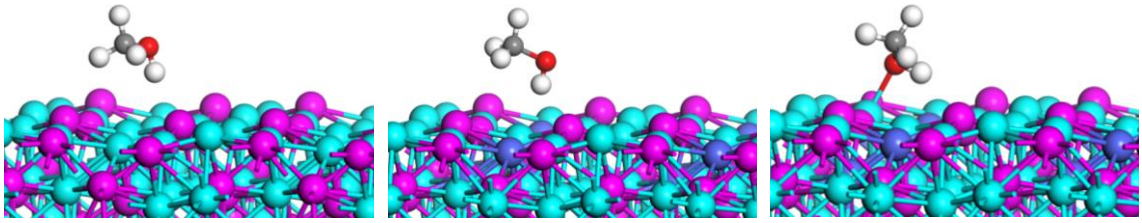

Figure 4.12. Side view of the absorption of methanol on different atom in (110) surface of Ni_3Sn_2 and $Ni_{2.5}Co_{0.5}Sn_2$ alloy. Green, pink and blue spheres represent Ni, Co and Sn, respectively.

4.3.4 DFT calculations

Complementary to the experimental work, to gain insight of the electronic effect that the Co incorporation had on the Ni_3Sn_2 alloy, DFT calculations of the surface of the metallic alloys were performed (see details in experimental section and Figure 4.12). DFT calculations showed

that the adsorption energies of methanol (E_{ads}) on Ni sites at Ni_3Sn_2 (001) and (110) facets were -0.57 eV and -0.49 eV. These values slightly increased for Ni sites at $Ni_{2.5}Co_{0.5}Sn_2$ surfaces: -0.59 eV and -0.74 eV for $Ni_{2.5}Co_{0.5}Sn_2$ (001) and (110), respectively. The adsorption energies of methanol on Co sites at $Ni_{2.5}Co_{0.5}Sn_2$ (001) and (110) surfaces were -0.63 eV and -0.52 eV, respectively. The higher absolute values of E_{ads} on Ni than Co in $Ni_{2.5}Co_{0.5}Sn_2$ surfaces pointed out at the preferential absorption of methanol molecules on the former. The higher E_{ads} obtained from the ternary alloy should imply a higher methanol poisoning not observed in the measurements of the current density as a function of the methanol concentration. On the other hand, the adsorption energies of CO on Ni sites at $Ni_{2.5}Co_{0.5}Sn_{2.0}$ (001) and (110) surfaces, -2.46 eV and -2.16 eV, were also higher than on Ni_3Sn_2 (001) and (110), -2.07 eV and -1.98 eV, which could result in a higher CO poisoning that was neither reflected in our experimental results. Further comprehensive DFT calculations including all the reaction steps and the proper alloy composition under reaction conditions would be required to evaluate the exact MOR mechanism.

4.4 Conclusions

In summary, a series of $Ni_{3-x}Co_xSn_2$ ($0 \leq x \leq 3$) quasi-spherical NPs with narrow size distribution were synthesized by a solution-based one-pot method. Detailed catalytic investigation of methanol oxidation showed that the introduction of small amounts of Co in the structure improved the electrocatalytic performance. A preliminary optimized catalyst composition, $Ni_{2.5}Co_{0.5}Sn_2$, showed 65.5 mA cm^{-2} and a mass current density of 1050 mA mg^{-1} at 0.6 V *vs.* Hg/HgO for MOR in 1.0 M KOH containing 1.0 M methanol. While the introduction of Co slightly decreased durability with respect to Ni_3Sn_2, $Ni_{2.5}Co_{0.5}Sn_2$ NP-based electrodes demonstrated a significant stability during continuous cycling and increased activity at high methanol concentrations. In any case, the presence of Sn was found to be essential to improve stability with respect elemental Ni, although Sn was observed to slowly dissolve in the presence of KOH. Overall, the excellent activity and stability towards MOR of ternary $Ni_{3-x}Co_xSn_2$ NPs suggested them as an attractive anode material for DMFCs.

4.5 References

1 X. Zhou, J. Qiao, L. Yang and J. Zhang, *Adv. Energy Mater.*, 2014, **4**, 1301523.

2 N. Demirdöven and J. Deutch, *Science (80-.).*, 2004, **305**, 974–976.

3 X. Zhao, M. Yin, L. Ma, L. Liang, C. Liu, J. Liao, T. Lu and W. Xing, *Energy Environ. Sci.*, 2011, **4**, 2736.

4 T. Schultz, S. Zhou and K. Sundmacher, *Chem. Eng. Technol.*, 2001, **24**, 1223–1233.
5 Y. Feng, H. Liu and J. Yang, *Sci. Adv.*, 2017, **3**, e1700580.
6 J. N. Tiwari, R. N. Tiwari, G. Singh and K. S. Kim, *Nano Energy*, 2013, **2**, 553–578.
7 H. Huang and X. Wang, *J. Mater. Chem. A*, 2014, **2**, 6266–6291.
8 S. Wasmus and A. Küver, *J. Electroanal. Chem.*, 1999, **461**, 14–31.
9 G. A. Tritsaris and J. Rossmeisl, *J. Phys. Chem. C*, 2012, **116**, 11980–11986.
10 N. Kakati, J. Maiti, S. H. Lee, S. H. Jee, B. Viswanathan and Y. S. Yoon, *Chem. Rev.*, 2014, **114**, 12397–12429.
11 S. P. S. Badwal, S. Giddey, A. Kulkarni, J. Goel and S. Basu, *Appl. Energy*, 2015, **145**, 80–103.
12 S. S. Munjewar, S. B. Thombre and R. K. Mallick, *Ionics (Kiel).*, 2017, **23**, 1–18.
13 S. K. Kamarudin, F. Achmad and W. R. W. Daud, *Int. J. Hydrogen Energy*, 2009, **34**, 6902–6916.
14 S. S. Munjewar, S. B. Thombre and R. K. Mallick, *Renew. Sustain. Energy Rev.*, 2017, **67**, 1087–1104.
15 P. Kumar, K. Dutta, S. Das and P. P. Kundu, *Int. J. Energy Res.*, 2014, **38**, 1367–1390.
16 L. R. Merte, M. Ahmadi, F. Behafarid, L. K. Ono, E. Lira, J. Matos, L. Li, J. C. Yang and B. R. Cuenya, *ACS Catal.*, 2013, **3**, 1460–1468.
17 K. Sasaki, H. Naohara, Y. Choi, Y. Cai, W. F. Chen, P. Liu and R. R. Adzic, *Nat. Commun.*, 2012, **3**, 1115.
18 Z. Daşdelen, Y. Yıldız, S. Eriş and F. Şen, *Appl. Catal. B Environ.*, 2017, **219**, 511–516.
19 C. Cui, L. Gan, M. Heggen, S. Rudi and P. Strasser, *Nat. Mater.*, 2013, **12**, 765–771.
20 S. Wu, J. Liu, D. Liang, H. Sun, Y. Ye, Z. Tian and C. Liang, *Nano Energy*, 2016, **26**, 699–707.
21 G. fa Long, X. hua Li, K. Wan, Z. xing Liang, J. hua Piao and P. Tsiakaras, *Appl. Catal. B Environ.*, 2017, **203**, 541–548.
22 J. Chen, Q. Niu, G. Chen, J. Nie and G. Ma, *J. Phys. Chem. C*, 2017, **121**, 1463–1471.
23 Q. Jiang, L. Jiang, H. Hou, J. Qi, S. Wang and G. Sun, *J. Phys. Chem. C*, 2010, **114**, 19714–19722.
24 K. W. Park, J. H. Choi, B. K. Kwon, S. A. Lee, Y. E. Sung, H. Y. Ha, S. A. Hong, H. Kim and A. Wieckowski, *J. Phys. Chem. B*, 2002, **106**, 1869–1877.
25 L. Li, Y. Wu, J. Lu, C. Nan and Y. Li, *Chem. Commun.*, 2013, **49**, 7486–7488.
26 K.-W. Park, J.-H. Choi and Y.-E. Sung, *J. Phys. Chem. B*, 2003, **107**, 5851–5856.
27 S. Wang, G. Yang and S. Yang, *J. Phys. Chem. C*, 2015, **119**, 27938–27945.
28 L. X. Ding, G. R. Li, Z. L. Wang, Z. Q. Liu, H. Liu and Y. X. Tong, *Chem. - A Eur. J.*, 2012, **18**, 8386–8391.
29 S. Papadimitriou, S. Armyanov, E. Valova, A. Hubin, O. Steenhaut, E. Pavlidou, G.

Kokkinidis and S. Sotiropoulos, *J. Phys. Chem. C*, 2010, **114**, 5217–5223.

30 S. Chen, P. J. Ferreira, W. Sheng, N. Yabuuchi, L. F. Allard and Y. Shao-Horn, *J. Am. Chem. Soc.*, 2008, **130**, 13818–13819.

31 Y. Ma, L. Yin, T. Yang, Q. Huang, M. He, H. Zhao, D. Zhang, M. Wang and Z. Tong, *ACS Appl. Mater. Interfaces*, 2017, **9**, 36164–36172.

32 Y. Liao, G. Yu, Y. Zhang, T. Guo, F. Chang and C. J. Zhong, *J. Phys. Chem. C*, 2016, **120**, 10476–10484.

33 H. J. Qiu, X. Shen, J. Q. Wang, A. Hirata, T. Fujita, Y. Wang and M. W. Chen, *ACS Catal.*, 2015, **5**, 3779–3785.

34 G. You, J. Jiang, M. Li, L. Li, D. Tang, J. Zhang, X. C. Zeng and R. He, *ACS Catal.*, 2018, **8**, 132–143.

35 Y. Liu, M. Chi, V. Mazumder, K. L. More, S. Soled, J. D. Henao and S. Sun, *Chem. Mater.*, 2011, **23**, 4199–4203.

36 Y. Liu, D. Li, V. R. Stamenkovic, S. Soled, J. D. Henao and S. Sun, *ACS Catal.*, 2011, **1**, 1719–1723.

37 Z. Luo, J. Lu, C. Flox, R. Nafria, A. Genç, J. Arbiol, J. Llorca, M. Ibáñez, J. R. Morante and A. Cabot, *J. Mater. Chem. A*, 2016, **4**, 16706–16713.

38 F. Han, X. Wang, J. Lian and Y. Wang, *Carbon N. Y.*, 2012, **50**, 5498–5504.

39 X. Wang, J. Lian and Y. Wang, *Int. J. Hydrogen Energy*, 2014, **39**, 14288–14295.

40 D. H. Lim, D. H. Choi, W. D. Lee and H. I. Lee, *Appl. Catal. B Environ.*, 2009, **89**, 484–493.

41 D. Wu, W. Zhang and D. Cheng, *ACS Appl. Mater. Interfaces*, 2017, **9**, 19843–19851.

42 W. Huang, H. Wang, J. Zhou, J. Wang, P. N. Duchesne, D. Muir, P. Zhang, N. Han, F. Zhao, M. Zeng, J. Zhong, C. Jin, Y. Li, S. T. Lee and H. Dai, *Nat. Commun.*, 2015, **6**, 10035.

43 A. Serov and C. Kwak, *Appl. Catal. B Environ.*, 2009, **90**, 313–320.

44 I. Danaee, M. Jafarian, F. Forouzandeh, F. Gobal and M. G. Mahjani, *Int. J. Hydrogen Energy*, 2009, **34**, 859–869.

45 I. Danaee, M. Jafarian, F. Forouzandeh, F. Gobal and M. G. Mahjani, *Int. J. Hydrogen Energy*, 2008, **33**, 4367–4376.

46 X. Cui, P. Xiao, J. Wang, M. Zhou, W. Guo, Y. Yang, Y. He, Z. Wang, Y. Yang, Y. Zhang and Z. Lin, *Angew. Chemie - Int. Ed.*, 2017, **56**, 4488–4493.

47 I. Danaee, M. Jafarian, A. Mirzapoor, F. Gobal and M. G. Mahjani, *Electrochim. Acta*, 2010, **55**, 2093–2100.

48 S. L. Candelaria, N. M. Bedford, T. J. Woehl, N. S. Rentz, A. R. Showalter, S. Pylypenko, B. A. Bunker, S. Lee, B. Reinhart, Y. Ren, S. P. Ertem, E. B. Coughlin, N. A. Sather, J. L. Horan, A. M. Herring and L. F. Greenlee, *ACS Catal.*, 2017, **7**, 365–379.

49 Y. Vlamidis, S. Fiorilli, M. Giorgetti, I. Gualandi, E. Scavetta and D. Tonelli, *RSC Adv.*, 2016, **6**, 110976–110985.

50 A. Roy, H. S. Jadhav, G. M. Thorat and J. G. Seo, *New J. Chem.*, 2017, **41**, 9546–9553.

51 S. Samanta, K. Bhunia, D. Pradhan, B. Satpati and R. Srivastava, *ACS Sustain. Chem. Eng.*, 2018, **6**, 2023–2036.

52 N. A. M. Barakat, M. Motlak, B. S. Kim, A. G. El-Deen, S. S. Al-Deyab and A. M. Hamza, *J. Mol. Catal. A Chem.*, 2014, **394**, 177–187.

53 T. Rostami, M. Jafarian, S. Miandari, M. G. Mahjani and F. Gobal, *Cuihua Xuebao/Chinese J. Catal.*, 2015, **36**, 1867–1874.

54 P. Manivasakan, P. Ramasamy and J. Kim, *Nanoscale*, 2014, **6**, 9665–9672.

55 E. Umeshbabu and G. Ranga Rao, *Electrochim. Acta*, 2016, **213**, 717–729.

56 X. Cui, Y. Yang, Y. Li, F. Liu, H. Peng, Y. Zhang and P. Xiao, *J. Electrochem. Soc.*, 2015, **162**, F1415–F1424.

57 X. Cui, W. Guo, M. Zhou, Y. Yang, Y. Li, P. Xiao, Y. Zhang and X. Zhang, *ACS Appl. Mater. Interfaces*, 2015, **7**, 493–503.

58 J. Li, Z. Luo, Y. Zuo, J. Liu, T. Zhang, P. Tang, J. Arbiol, J. Llorca and A. Cabot, *Appl. Catal. B Environ.*, 2018, **234**, 10–18.

59 Y. Gu, J. Luo, Y. Liu, H. Yang, R. Ouyang and Y. Miao, *J. Nanosci. Nanotechnol.*, 2015, **15**, 3743–3749.

60 K. D. Gilroy, A. Ruditskiy, H. C. Peng, D. Qin and Y. Xia, *Chem. Rev.*, 2016, **116**, 10414–10472.

61 P. Strasser, S. Koh, T. Anniyev, J. Greeley, K. More, C. Yu, Z. Liu, S. Kaya, D. Nordlund, H. Ogasawara, M. F. Toney and A. Nilsson, *Nat. Chem.*, 2010, **2**, 454–460.

62 A. Hamza, S. El-Refaei, A. Elzatahry and A. Abdullah, *Appl. Sci.*, 2017, **7**, 64.

63 G. Kresse and J. Furthmüller, *Phys. Rev. B - Condens. Matter Mater. Phys.*, 1996, **54**, 11169–11186.

64 G. Kresse and J. Hafner, *Phys. Rev. B*, 1994, **49**, 14251–14269.

65 G. Kresse and J. Hafner, *Phys. Rev. B*, 1993, **47**, 558–561.

66 G. Kresse and J. Furthmüller, *Comput. Mater. Sci.*, 1996, **6**, 15–50.

67 H. Fjellvåg, A. Kjekshus, R. Stomberg, R. Zingales, I. Vikholm, F. Urso, J. Weidlein and R. A. Zingaro, *Acta Chem. Scand.*, 1986, **40a**, 23–30.

68 S. Furukawa and T. Komatsu, *American Chemical Society*, 2017, vol. 7.

69 Y. Liu, X. Liu, Q. Feng, D. He, L. Zhang, C. Lian, R. Shen, G. Zhao, Y. Ji, D. Wang, G. Zhou and Y. Li, *Adv. Mater.*, 2016, **28**, 4747–4754.

70 M. He, L. Protesescu, R. Caputo, F. Krumeich and M. V. Kovalenko, *Chem. Mater.*, 2015, **27**, 635–647.

71 M. Walter, S. Doswald and M. V. Kovalenko, *J. Mater. Chem. A*, 2016, **4**, 7053–7059.

72 M. He, K. Kravchyk, M. Walter and M. V. Kovalenko, *Nano Lett.*, 2014, **14**, 1255–1262.

73 H. G. Meier, J. R. Vilche and A. J. Arvía, *J. Electroanal. Chem.*, 1982, **138**, 367–379.

74 E. B. Castro, C. A. Gervasi and J. R. Vilche, *J. Appl. Electrochem.*, 1998, **28**, 835–841.

75 I. G. Casella and M. Gatta, *J. Electroanal. Chem.*, 2002, **534**, 31–38.

76 I. G. Casella and M. Gatta, *J. Electroanal. Chem.*, 2002, **534**, 31–38.

77 M. Walter, S. Doswald, F. Krumeich, M. He, R. Widmer, N. P. Stadie and M. V. Kovalenko, *Nanoscale*, 2018, **10**, 3777–3783.

78 M. W. Khalil, M. A. Abdel Rahim, A. Zimmer, H. B. Hassan and R. M. Abdel Hameed, *J. Power Sources*, 2005, **144**, 35–41.

79 L. Wang, G. Zhang, Y. Liu, W. Li, W. Lu and H. Huang, *Nanoscale*, 2016, **8**, 11256–11263.

80 J. Wang, D. Teschner, Y. Yao, X. Huang, M. Willinger, L. Shao and R. Schlögl, *J. Mater. Chem. A*, 2017, **5**, 9946–9951.

81 Y. Yu, Q. Yang, X. Li, M. Guo and J. Hu, *Green Chem.*, 2016, **18**, 2827–2833.

82 D. Chen and S. D. Minteer, *J. Power Sources*, 2015, **284**, 27–37.

83 A. J. Bard and L. R. Faulkner, *Anti-Corrosion Methods Mater.*, 2001, 50, 1–850.

84 D. M. MacArthur, *The Electrochemical Society*, 1970, vol. 117.

85 J. D. Benck, Z. Chen, L. Y. Kuritzky, A. J. Forman and T. F. Jaramillo, *ACS Catal.*, 2012, **2**, 1916–1923.

86 C. C. L. McCrory, S. Jung, I. M. Ferrer, S. M. Chatman, J. C. Peters and T. F. Jaramillo, *J. Am. Chem. Soc.*, 2015, **137**, 4347–4357.

87 C. C. L. McCrory, S. Jung, J. C. Peters and T. F. Jaramillo, *J. Am. Chem. Soc.*, 2013, **135**, 16977–16987.

88 R. M. Abdel Hameed and R. M. El-Sherif, *Appl. Catal. B Environ.*, 2015, **162**, 217–226.

89 Q. Yi, W. Huang, J. Zhang, X. Liu and L. Li, *Catal. Commun.*, 2008, **9**, 2053–2058.

90 H. Sun, Y. Ye, J. Liu, Z. Tian, Y. Cai, P. Li and C. Liang, *Chem. Commun.*, 2018, **54**, 1563–1566.

Chapter 5

Compositionally tuned Ni_xSn alloys as anode materials for lithium-ion and sodium-ion batteries with a high pseudocapacitive contribution

Nickel tin alloy nanoparticles (NPs) with tuned composition Ni_xSn ($0.6 \leq x \leq 1.9$) were synthesized by a solution-based procedure and used as anode materials for Li-ion batteries (LIBs) and Na-ion batteries (SIBs). Among the compositions tested, $Ni_{0.9}Sn$-based electrodes exhibited the best performance in both LIBs and SIBs. As LIB anodes, $Ni_{0.9}Sn$-based electrodes delivered charge-discharge capacities of 980 mAh g^{-1} after 340 cycles at 0.2 A g^{-1} rate, which surpassed their maximum theoretical capacity considering that only Sn is lithiated. A kinetic characterization of the charge-discharge process demonstrated the electrode performance to be aided by a significant pseudocapacitive contribution that compensated for the loss of energy storage capacity associated to the solid-electrolyte interphase formation. This significant pseudocapacitive contribution, which not only translated into higher capacities but also longer durability, was associated to the small size of the crystal domains and the proper electrode composition. The performance of Ni_xSn-based electrodes toward Na-ion storage was also characterized, reaching significant capacities above 200 mAh g^{-1} at 0.1 A g^{-1} but with a relatively fast fade over 120 continuous cycles. A relatively larger pseudocapacitive contribution was obtained in Ni_xSn-based electrodes for SIBs when compared with LIBs, consistently with the lower contribution of the Na ion diffusion associated to its larger size.

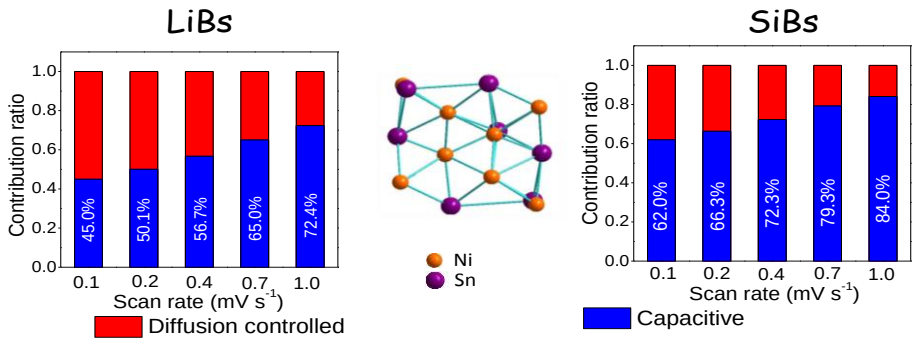

Keywords: colloidal bimetallic nanoparticles; nickel tin alloy; anode materials; lithium-ion batteries; sodium-ion batteries.

5.1 Introduction

Lithium ion batteries (LIBs) have become essential in portable electronic applications. However, while widely spread in the market, current LIBs are far from being optimized electrochemical energy storage devices.[1–5] LIBs still suffer from moderate durabilities and current densities, which are in large part associated to the limitations of actual electrode materials. Additionally, the availability of lithium poses middle-long term limitations to this technology.[6,7] Thus, the development of improved electrode materials for LIBs and alternative battery technologies based on more abundant ions, such as sodium, is a worthwhile endeavor.

Current commercial LIBs use graphite as anode material, what limits the theoretic maximum energy density to 375 mAh g^{-1}.[8–11] On the other hand, sodium ion batteries (SIBs) cannot make use of graphite due to the insignificant Na-insertion in this material.[12–14] As an alternative anode material for both LIBs and SIBs, Sn and Sn-based alloys have been extensively studied due to their abundance, low toxicity and high energy density, 992 mAh g^{-1} for LIBs and 847 mAh g^{-1} for SIBs, corresponding to the formation of $Li_{22}Sn_5$ and $Na_{15}Sn_4$, respectively.[15–18] However, Sn undergoes huge volume changes during charge-discharge cycles that shorten its usage time.[19–24] This drawback can be partially overcome by reducing the size of the crystal domains in the electrode. The use of nanostructured electrodes provides additional advantages in terms of increasing rate capability, because of the shorter Li-ion diffusion paths, and increasing the pseudocapacitive contribution associated with the larger surface/volume ratios.[25–30] An additional strategy to improve stability is to alloy tin with non-active elements, reducing in this way the volume changes and potentially increasing the pseudocapacitive contribution. In this direction, bimetallic Sn-based allows such as Cu-Sn,[31–33] FeSn,[33–35] Co-Sn,[34–53] and Ni-Sn[17,33,54–56] have been tested as base materials for LIB and/or SIB electrodes with excellent results.

Not considering pseudocapacitive effects, the main drawback of alloying Sn with non-active metals is the decrease of the maximum energy density potentially achieved with the amount on non-active metal introduced. Thus, the alloy composition needs to be finely and continuously tuned along the whole solid-solution range to find the optimal composition. However, most previous works have focused on studding the performance of intermetallic Sn-based alloys, with strongly constrained compositions. In the present work, we take advantage of the versatility of colloidal synthesis method to produce nanoparticles (NPs) of a range of Ni-Sn solid solutions with Ni:Sn ratios from 0.6 to 1.9. After removing surface ligands, we use these NPs to test the performance Ni-Sn solid solutions as anode materials for LIBs and SIBs.

5.2 Experimental

5.2.1 Chemicals

Nickel(II) acetylacetonate ($Ni(acac)_2 \cdot xH_2O$ (x~2), 95%, Sigma-Aldrich), tin(II) acetate ($Sn(oac)_2$, 95%, Fluka), oleic acid (OAc, Sigma-Aldrich), oleylamine (OAm, 80-90%, TCI), tri-*n*-octylphosphine (TOP, 97%, Strem), borane tert-butylamine complex (TBAB, 97%, Sigma-Aldrich), TIMCAL Graphite & Carbon Super P (Super P, KJ group), polyvinylidene fluoride (PVDF, KJ group), N-methy1-2-pyrrolidone (NMP, 99%, Aladdin), hydrazine monohydrate (N_2H_4 64-65%, reagent grade, 98%, Sigma-Aldrich) and acetonitrile (CH_3CN, extra dry, Fisher) were used as received without any further purification. Chloroform, acetone and ethanol were of analytical grade and purchased from various sources. An argon-filled glove-box was used for storing and dealing with sensitive chemicals.

5.2.2 Colloidal Synthesis of NiSn NPs

All the syntheses were carried out using standard airless techniques using a vacuum/dry argon gas Schlenk line. Ni-Sn NPs were prepared following the scaled-up version of a protocol we previously detailed.[57] Briefly, 20 mL OAm, 1.0 mL OAc, 0.9 mmol $Ni(acac)_2 \cdot xH_2O$ and 0.6 mmol $Sn(oac)_2$ were loaded into a 50 mL three-neck flask containing a magnetic stirring bar. The reaction was strongly stirred and degassed under vacuum at 80 °C for 2 hours to remove water, air, and low-boiling point impurities. Then, a gentle flow of argon was introduced, 5 mL of TOP were injected and the reaction flask was heated to 180 °C at 5 °C/min. Meanwhile, a reducing solution was prepared by dissolving 5 mmol TBAB in 5 mL OAm through sonication for 30 min, and subsequently degassed this mixture for 1 hour at ambient temperature. This reducing solution was injected into the reaction flask containing the Ni and Sn precursor at 180 °C. Upon injection, a visible color change, from deep green to black, was immediately observed. The reaction was maintained at 180 °C for 1 hour, followed by a rapid cool down to room temperature using a water bath. The content of the reaction mixture was transferred to two centrifuge tubes, followed by centrifuging at 9000 rpm for 3 min after introducing acetone as non-solvent. The precipitate was suspended in chloroform and centrifuged again after adding additional acetone. This process was repeated twice. Finally, the NPs were suspended in 10 mL chloroform.

5.2.3 Ligand removal

The native organic ligands were removed from the NP surface according to a previously published report.[28,58] Briefly, 25 mL acetonitrile and 0.8 mL hydrazine hydrate was introduced

into a vial containing the precipitated NPs. The mixture was stirred for 4 hours at room temperature and then collected by centrifuging at low speed. The product was further washed with acetonitrile and centrifuged at 2000 rpm for another 3 times. NPs were collected and stored in inert air atmosphere after drying under vacuum at room temperature.

5.2.4 Characterization

Powder x-ray diffraction (XRD) was measured on a Bruker AXS D8 Advance x-ray diffractometer with Cu K radiation (λ = 1.5106 Å) operating at 40 kV and 40 mA. Scanning electron microscopy (SEM) analyses were performed on a ZEISS Auriga SEM with an energy dispersive X-ray spectroscopy (EDS) detector at 20 kV. EDS analysis were performed after removing ligands from the NP surface. Transmission electron microscopy (TEM) analyses were carried out on a ZEISS LIBRA 120, operating at 120 kV, using a 200 mesh Carbon-coated grid from Ted-Pella as substrate. High-resolution TEM (HRTEM) and scanning TEM (STEM) studies were carried out using a field emission gun FEI Tecnai F20 microscope at 200 kV with a point-to-point resolution of 0.19 nm. High angle annular dark-field (HAADF) STEM was combined with electron energy loss spectroscopy (EELS) in the Tecnai microscope by using a GATAN QUANTUM filter. X-ray photoelectron spectroscopy (XPS) was done on a SPECS system equipped with an Al anode XR50 source operating at 150 mW and a Phoibos 150 MCD-9 detector. The pressure in the analysis chamber was kept below 10^{-7} Pa. The area analyzed was about 2 mm x 2 mm. The pass energy of the hemispherical analyzer was set at 25 eV and the energy step was maintained at 1.0 eV. Data processing was performed with the Casa XPS program (Casa Software Ltd., UK). Binding energies were shifted according to the reference C 1s peak that was located at 284.8 eV. The Fourier transform infrared spectrometer (FTIR) data were recorded on an Alpha Bruker spectrometer. Inductively coupled plasma optical emission spectrometry (ICP-OES) analyses were conducted on a Spectro Arcos FHS16 ICP-OES analyzer. Ni-Sn NPs (5 mg) were dissolved in 10 ml of aqua regia. Then, 0.5 ml of this dissolution was diluted in 24.5 ml of MilliQ water.

5.2.5 Electrochemical measurements

Ni-Sn NPs (80 wt%) were mixed with Super P (10 wt%), PVDF (10 wt%) and NMP. The obtained slurry was bladed onto a copper foil and dried at 80 ºC for 24 h in a vacuum oven. Working electrodes were obtained by cutting the printed foil into circular disk with a diameter of 12.0 mm. The mass loading of active materials was estimated to be 0.7-1.2 mg cm^{-2}. To test the performance of electrodes based on Ni-Sn NPs, half cells were assembled in the glove box (H_2O and O_2 < 0.1 ppm) using Celgard2400 as separator. As electrolyte for LIBs, a 1 M $LiPF_6$

solution in ethylene carbonate (EC)/diethyl carbonate (DEC) (1:1 in volume) with 5 vol% fluoroethylene carbonate (FEC) as additive was used. For SIBs, 1 M $NaClO_4$ in propylene carbonate (PC)/ EC (1:1 in volume) with 5 vol% FEC was used as the electrolyte. Galvanostatic charge-discharge were measured by a battery test system (CT2001A, LAND) with cutoff potentials from 0.01 V to 3.0 V. Cyclic voltammograms (CV) were obtained using an electrochemical workstation (Gamry Interface 1000) in the voltage range of 0–3.0 V at scan rates from 0.1 mV s^{-1} to 1 mV s^{-1}. Electrochemical impedance spectroscopy (EIS) tests were performed using a sinusoidal voltage with amplitude of 10 mV and a scanning frequency from 100 kHz to 10 mHz.

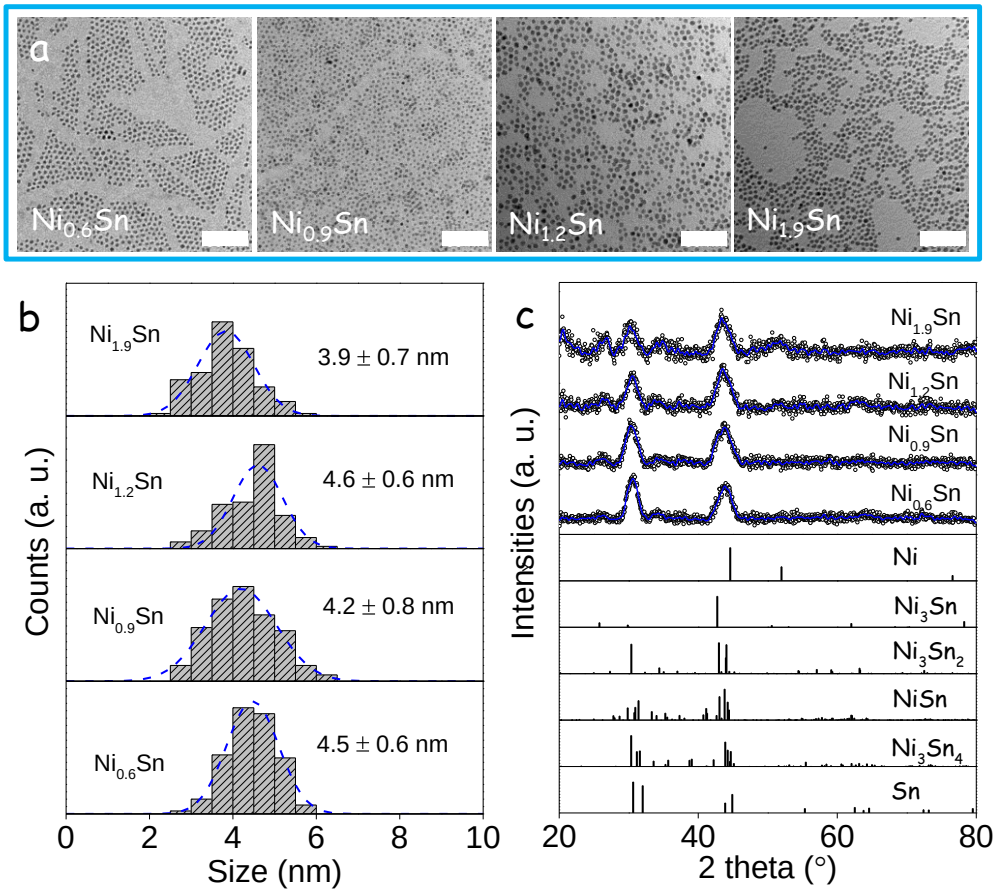

Figure 5.1. a) TEM micrographs of Ni-Sn NPs with different compositions, as obtained from EDX and displayed in each image. Scale bar: 50 nm. b) Size distribution histograms of the Ni-Sn NPs; c) XRD patterns of the Ni-Sn NPs with different compositions. Sn, Ni and different Ni-Sn intermetallic XRD patterns are displayed as reference.

5.3 Results and Discussion

Ni_xSn NPs with tuned composition ($0.6 < x < 1.9$) were prepared by the co-reduction of proper amounts of nickel(II) acetylacetonate and tin(II) acetate at 180 ºC by TBAB and in the presence

of OAm and OAc (see experimental section for details). Following this procedure, quasi-spherical NPs with sizes in the range from 3.9 ± 0.7 nm to 4.6 ± 0.6 nm were produced (Figure 5.1ab). ICP-OES and SEM-EDS analysis showed the Ni/Sn ratio of the Ni_xSn NPs to be 0.6, 0.9, 1.2 and 1.9 ± 0.1 for nominal Ni/Sn ratios of 0.75, 1.0, 1.5 and 2.0, respectively (Figure 5.1a). XRD analysis displayed the crystallographic phase of all the alloys to resemble that of Sn or orthorhombic Ni_3Sn_2 (Figure 5.1c). Main XRD peaks did not significantly shift with the introduction of different amounts of Ni. However, as the Ni amount increased, the material crystallinity decreased and additional peaks became visible, denoting the formation of a more complex crystal phase, which did not match well with any of the reported intermetallic Ni-Sn phases.

EELS chemical composition maps showed Ni and Sn to be present in all the NPs with similar ratio. Additionally, uniform distributions of Ni and Sn within each NP were observed (Figure 5.2a). HRTEM analysis revealed the NPs to have a good crystallinity with a crystallographic phase in agreement with the Ni_3Sn_2 orthorhombic phase (space group = Pnma) with a = 7.1100 Å, b = 5.2100 Å and c = 8.2300 Å (Figure 5.2b). [59]

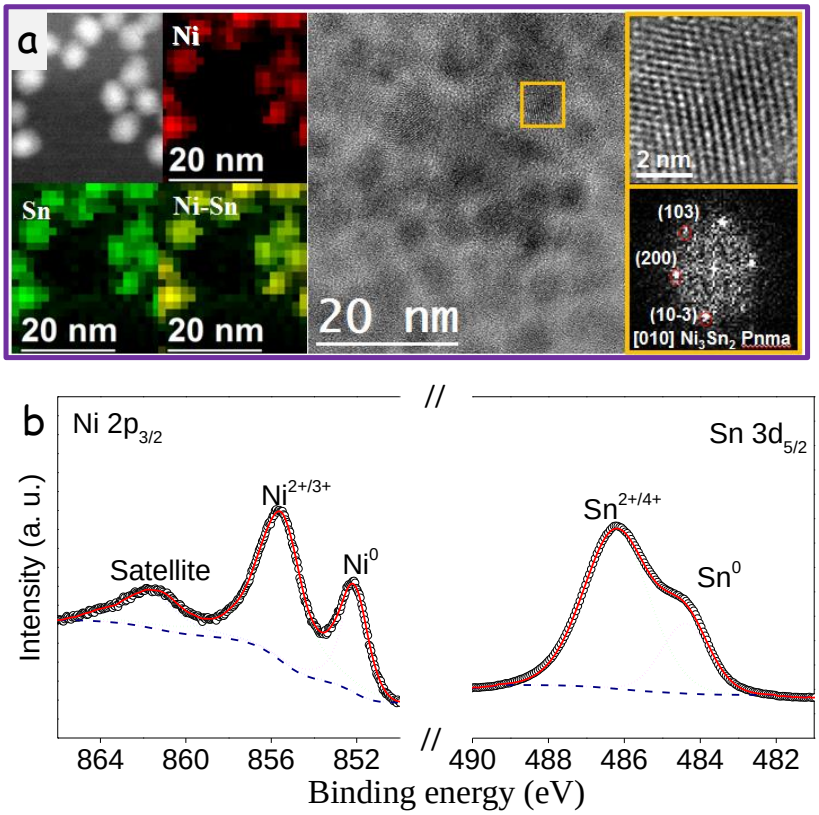

Figure 5.2 a) STEM and EELS compositional maps of $Ni_{0.6}Sn$ NPs and its HRTEM micrograph exposed to atmosphere and displaying a core-shell type structure. The Ni_3Sn_2 lattice fringe distances were measured to be 0.260 nm, 0.337 nm and 0.269 nm, at 69.40 and 134.54º which could be interpreted as the orthorhombic Ni_3Sn_2 phase, visualized along its [010] zone axis. b) XPS spectra of the Ni $2P_{3/2}$ region and the Sn $3d_{5/2}$ region of $Ni_{1.2}Sn$ NPs.

As displayed in Figure 5.2b, XPS analysis of the Ni_xSn NPs showed Ni to be present in two different chemical states, which we associated with metallic Ni^0 (Ni $2p_{3/2}$ at 852.3 eV) and $Ni^{2+/3+}$ oxidation states (Ni $2p_{3/2}$ at 855.6 eV).[60] The ratio of the two components was found to be $Ni^{2+/3+}/Ni^0$ = 2.5 for $Ni_{1.2}Sn$. Sn was also present in two chemical states, displaying a metallic (Sn $3d_{5/2}$ peak at 484.4 eV) and an oxidized component (Sn $3d_{5/2}$ peak at 486.2 eV) with a relative ratio $Sn^{2+/4+}/Sn^0$ = 3.2 for $Ni_{1.2}Sn$.[60] The relative amount of the oxidized component depended on the previous history of the sample, particularly on the time it had been exposed to air before XPS analysis. We associated the oxidized states to the presence of an oxide layer at the Ni_xSn NPs surface, which had been grown during their manipulation and transportation in ambient conditions. The ratio of metalsNi/Sn obtained from XPS analysis was systematically lower than values obtained from bulk chemical analysis techniques, e.g. in $Ni_{1.2}Sn$ NPs, was Ni/Sn = 0.46, which pointed at a segregation of Sn to the NP surface, also consistent with the higher relative oxidized component in Sn than Ni. We hypothesize that this surface segregation could have taken place during oxidation.[57,61,62]

Before testing the performance of Ni_xSn NPs as anode material in LIBs and SIBs, the organic ligands present at their surface were removed though a treatment with a mixture of hydrazine and acetonitrile. FTIR analysis confirmed the effectivity of this treatment through the disappearance of peaks at 2890 cm^{-1} and 2822 cm^{-1} that correspond to C-H stretching modes.[63]

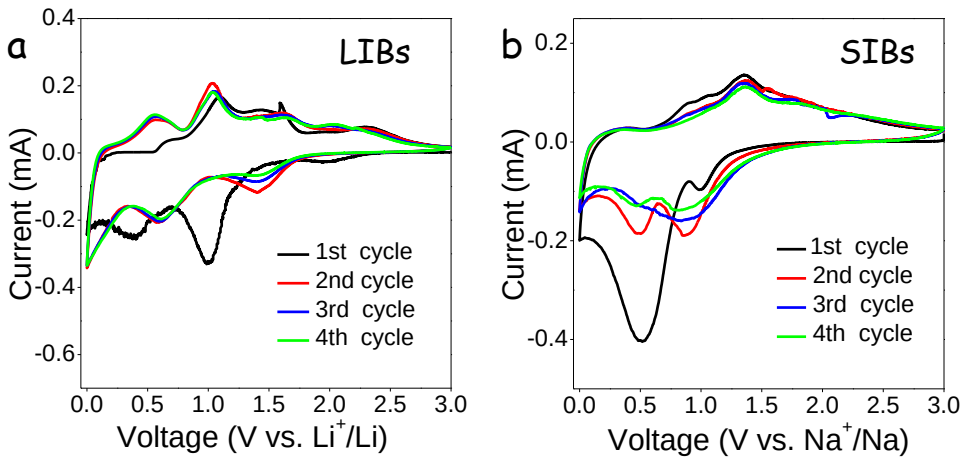

Figure 5.3. Initial CV curves obtained from the $Ni_{0.9}Sn$ NP-based electrode at 0.1 mV s^{-1} in the voltage window 0-3.0 V *vs.* a) Li^+/Li and b) Na^+/Na.

To evaluate the performance of Ni_xSn NPs as anode material in LIBs and SIBs, coin-type half-cells with metallic Li or Na foil as counter electrodes were assembled. Working electrodes were prepared by mixing Ni_xSn NPs with Super P, PVDF and NMP, and coating the resulting slurry onto Cu foil. Standard liquid electrolyte formulations were used: $LiPF_6$ in EC/DEC with FEC for LIBs and $NaClO_4$ in PC/EC with FEC for SIBs.

Figure 5.3ab shows representative initial CV profiles of the $Ni_{0.9}Sn$ NP-based electrode obtained at 0.1 mV s^{-1} in the applied potential region of 0-3.0 V vs. Li^+/Li and Na^+/Na, respectively. Significant differences were obtained between the 1st and following cycles, associated to the formation of the solid electrolyte interface (SEI) layer in both systems.[17]

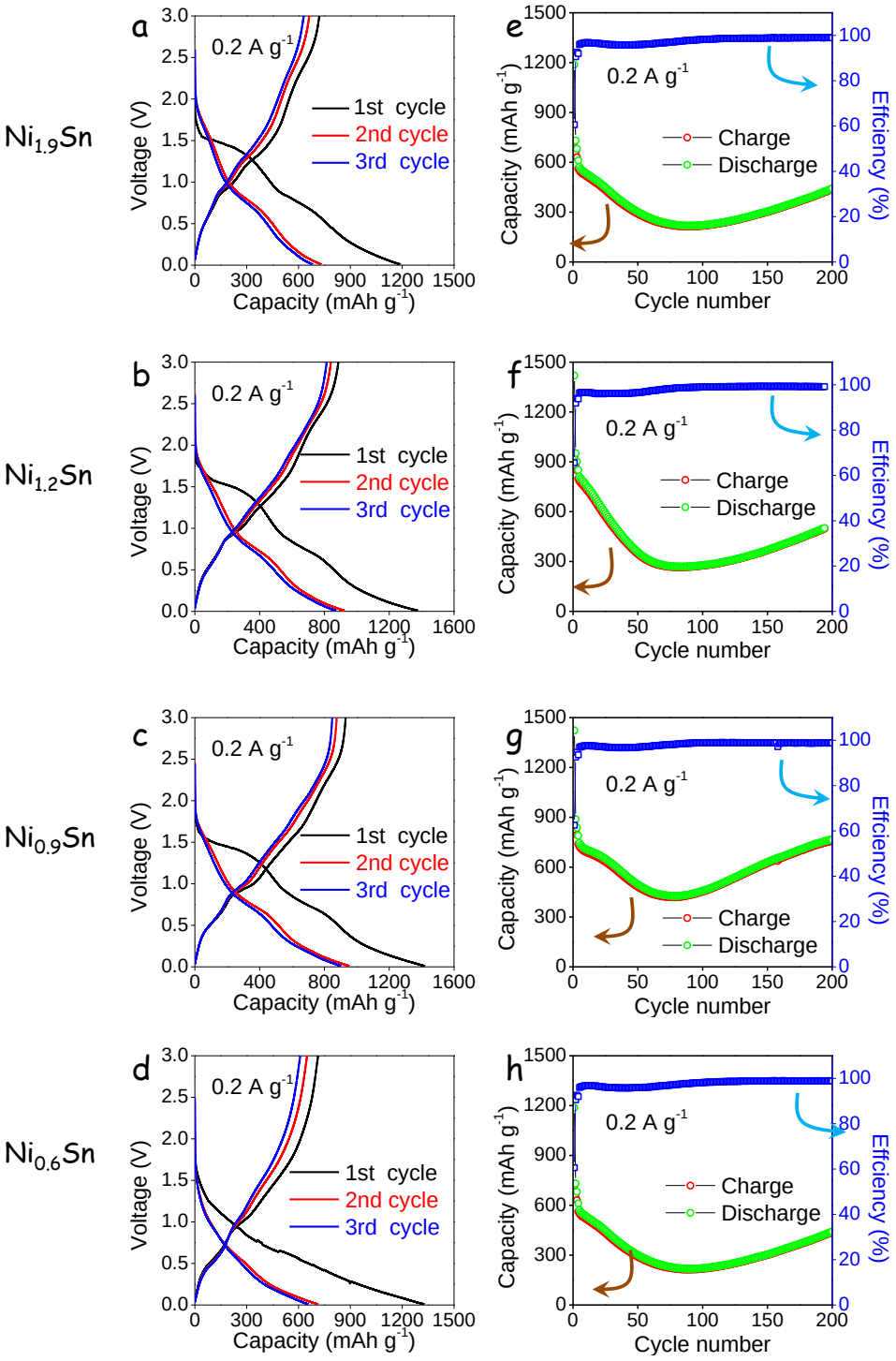

Figure 5.4. a-d) Initial charge-discharge curves at 0.2 A g^{-1} for the different electrode compositions as displayed on the left of each graph. e-h) Charge-discharge capacity and related efficiency over 200 cycles at a current density of 0.2 A g^{-1}.

Lithium reversibly interacts with Sn with a theoretical capacity of 992 mAh g^{-1}, corresponding to the alloying reaction: $Sn \rightarrow Li_{4.4}Sn$.[34] Lithium does not react with Ni. Thus, assuming no capacity contribution from Ni, the theoretical specific capacity of $Ni_{0.6}Sn$, $Ni_{0.9}Sn$, $Ni_{1.2}Sn$ and $Ni_{1.9}Sn$ electrodes was 765 mAh g^{-1}, 687 mAh g^{-1}, 623 mAh g^{-1}, and 511 mAh g^{-1}, respectively.

The cycling performance of Ni_xSn NP-based electrodes was measured by galvanostatic charging-discharging at 0.2 A g^{-1}, as shown in Figure 5.4a-h. Ni_xSn NP-based electrodes delivered very large initial capacities, over 1200 mAh g^{-1}, well above their theoretical maximum. These large values were ascribed to the decomposition of the electrolyte to form the SEI layer. However, in the first few cycles, a strong capacity loss in the form of a decreased current density was observed due to the formed SEI layer. Upon continuous cycling, the charge-discharge capability decreased during dozens of cycles, but recovered after some additional cycles up to values well above their theoretical maximum capacity, e.g. 980 mAh g^{-1} after 200 cycles for the $Ni_{0.9}Sn$ electrode (Figure 5.4c). On the other hand, the columbic efficiency was stabilized at ca. 99% after the first 10 cycles. Besides the SEI formation in the first few cycles, the phenomenon of a capacity decrease in the initial fifty cycles followed by an increase during subsequent cycling may be attributed to structural and compositional changes of the electrode material, resulting in a complex evolution of the electrical conductivity, the electrode porous volume and its surface area.[64] During cycling, a redistribution of Ni and Sn, and changes in the shape and size of the material domains take place, strongly influencing the electrical properties of the electrode, the amount of solid/electrolyte interphase accesible, the amount of material contributing to the storage capacity through ion diffusion and the amount of surface providing a pseudocapacitance contribution. Additionally, a capacity increase during repeated cycles is a common feature of Ni_xSn and other M_xSn (M = transition metal) alloys, which has been associated to the formation and dissolution of gel-like polymeric species in the SEI layer aided by the catalytic activity of the anode material.[65–67]

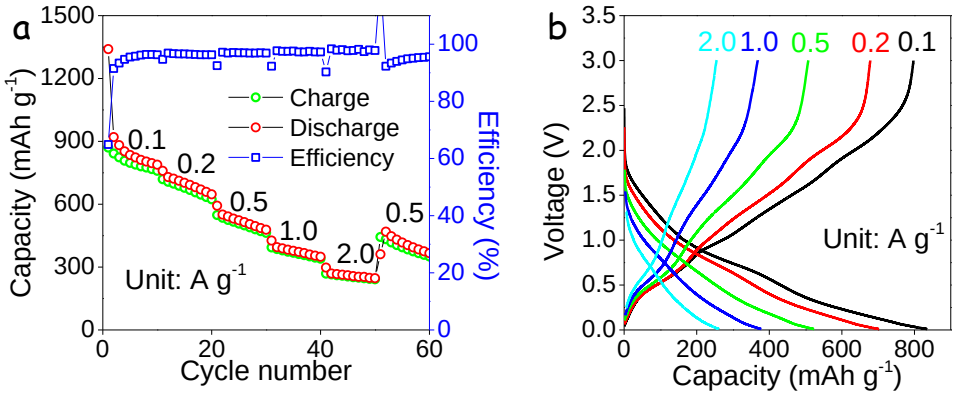

Figure 5.5. Li-ion storage performance of the $Ni_{0.9}Sn$ electrode: a) Rate performance at 0.1, 0.2, 0.5, 1.0, 2.0 A g^{-1}. b) Charge-discharge curves at rates: 0.1, 0.2, 0.5, 1.0, 2.0, 0.5 A g^{-1}.

Within this complex system, while the maximum theoretical capacity decreases with the amount of Ni introduced, $Ni_{0.9}Sn$ showed the highest capacity after several hundreds of cycles among the different Ni_xSn compositions tested in the present work. The extra-capacity of Ni_xSn alloys, compared with their theoretical maximum, should be attributed to the ultra-small particle size and the related high surface area, which provided additional active sites for Li-ion storage that translated into an increased pseudocapacitive contribution. The relative stable cycling performance and high capacity retention could be also ascribed to the ultra-small particle size and the presence of Ni as a conductive buffer substrate, both parameters moderating the variation of stress during the alloying/dealloying process.

To further evaluate the rate capability of the $Ni_{0.9}Sn$ NP-based electrodes, galvanostatic measurements were carried out at different current densities, between 0.1 and 2.0 A g^{-1} (Figure 5.5). $Ni_{0.9}Sn$ NP-based electrodes delivered average discharge capacities of 835, 702, 523, 378 and 261 mAh g^{-1} at 0.1, 0.2, 0.5, 1.0, 2.0 A g^{-1}, respectively. The notable rate capability of Ni_xSn-based electrodes was associated with their ultra-small particles size with high surface area shorting Li-ion diffusion paths and providing more channels for Li^+/electrons transporting. The inactive Ni as conductive part improved the electrical conductivity of the all Ni_xSn alloys also facilitating the diffusion of Li^+/electrons. A low charge transfer resistance of Ni_xSn-based electrodes was further confirmed by EIS measurements (Figure 5.7e).

The kinetics of $Ni_{0.9}Sn$ NP-based electrodes in LIBs was investigated by collecting CV curves at different scan rates: 0.1, 0.2, 0.4, 0.7, 1.0 mV s^{-1} in the potential range of 0-3.0 V vs. Li^+/Li (Figure 5.6). The anodic peaks at 0.62 V and 1.04 V, and the cathodic peak at 0.54 V were observed to increase with scan rate. Generally, a potential relationship between the measured current (i) and the scan rate (v) can be considered: [64–66]

$$i = av^b$$

where a, b are adjustable parameters. According to previous reports, an ideal capacitive behavior is characterized by b = 1. On the other hand, when b is close to 0.5 the capacity is dominated by the diffusion process.[65–67] From our experimental results, the b values of the current peaks at 0.62, 0.54, 1.04 V were calculated to be 0.83, 0.66 and 0.63, respectively. All calculated b values above 0.5 indicated the $Ni_{0.9}Sn$ NP-based electrodes to be characterized by a significant pseudocapacitive contribution (Figure 5.6).

At a certain potential, the current density at each scan rate can be divided into two parts, a diffusion-controlled ($k_1v^{1/2}$) fraction associated to the Li^+ insertion and a capacitor-like fraction (k_2v) :[65–67]

$$i(V) = k_1 v^{1/2} + k_2 v$$

Thus, k_1 and k_2 can be determined by plotting $i(V)/ v^{1/2}$ vs. $v^{1/2}$, distinguishing in this way the two contributions. Figure 5.6 shows a CV at different scan rates where the two components have been differentiated: the capacitive current as the blue shaded region and the diffusion component in red. Similarly, the two contributions are differentiated in the CVs at 0.1, 0.2, 0.7 and 1.0 mV s^{-1}. All these data are summarized in Figure 5.6. Overall, increasing capacitive contributions were obtained when increasing the scan rate, reaching a capacitive contribution up to 72% at 1.0 mV s^{-1}. This increased contribution with the scan rate is related to the slower Li^+ diffusion that translates into minor Li^+ in-depth alloying when compared with the faster and less rate-depended contribution of the surface reaction.

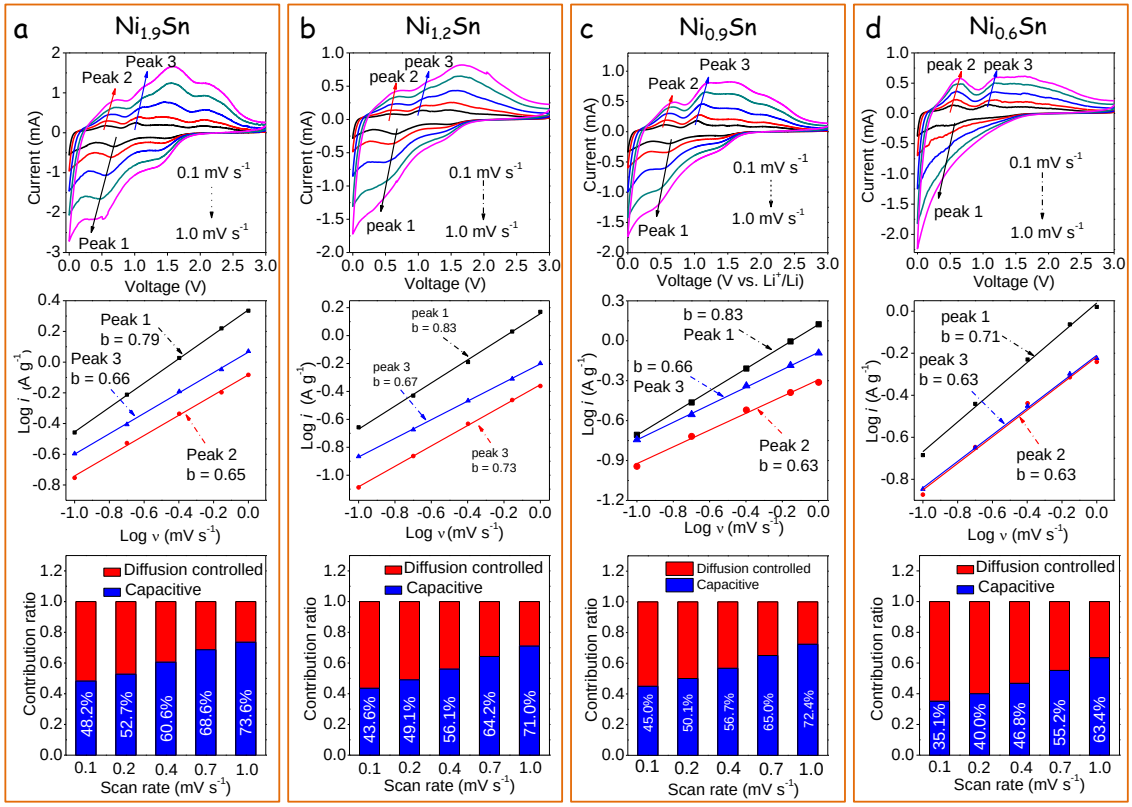

Figure 5.6. Kinetic analysis of the Li-ion storage performance of the electrode: a) $Ni_{1.9}Sn$, b) $Ni_{1.2}Sn$, c) $Ni_{0.9}Sn$, d) $Ni_{0.6}Sn$.

Similarly high capacitive contributions were obtained for all Ni_xSn NP-based electrodes electrodes except for $Ni_{0.6}Sn$, which showed a slightly lower, but still very significant contribution (Figure 5.6). We associated these large capacitive contributions to the small size of the Ni_xSn crystal domains. High capacitive contributions, such as the ones found for Ni_xSn alloys, are highly beneficial because surface processes are much faster and stable than diffusion-controlled alloying. The high capacitive contributions also illuminated the origin of the notable rate capability of Ni_xSn NP-based electrodes.

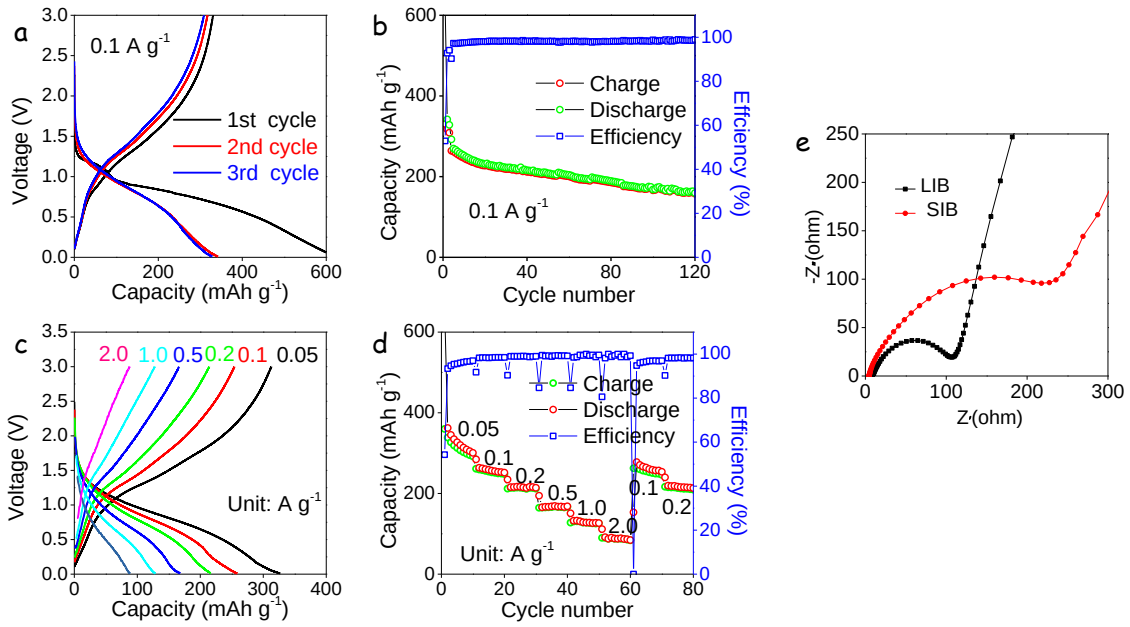

Figure 5.7. Na-ion storage performance of the $Ni_{0.9}Sn$ electrode: a) Typical first three charging-discharging curves at 0.1 A g^{-1}. b) Charge-discharge capacity and related efficiency over 120 cycles at a current density of 0.1 A g^{-1}. c) Selected charging-discharging curves at 0.05, 0.1, 0.2, 0.5, 1.0, 2.0, 0.1 and 0.2 A g^{-1} rates. d) Rate capabilities of $Ni_{0.9}Sn$ at 0.05, 0.1, 0.2, 0.5, 1.0 and 2.0 A g^{-1}.e) EIS plots in Li- and Na-ion batteries for the electrode $Ni_{0.9}Sn$.

Sodium is also reversibly stored in Sn, with a maximum theoretical capacity of 847 mAh g^{-1} corresponding to the reaction: $Sn \rightarrow Na_{3.75}Sn$.[17] Considering that Ni does not contribute to any Na-ion capacity, thus the theoretical capacity of $Ni_{0.6}Sn$, $Ni_{0.9}Sn$, $Ni_{1.2}Sn$ and $Ni_{1.9}Sn$ electrodes is 653 mAh g^{-1}, 586 mAh g^{-1}, 532 mAh g^{-1}, and 437 mAh g^{-1}, respectively.

Figures 5.7a-d and 5.8 present the Na-ion storage performance of Ni_xSn NP-based electrodes over 120 cycles at 0.1 A g^{-1}. Again, while capacity should decrease with the Ni content, $Ni_{0.9}Sn$ NPs exhibited the highest capacities among the different compositions tested. In the first cycles, Na-ion discharge-charge storage capacities above 300 mAh g^{-1} at 0.1 A g^{-1} were obtained for the $Ni_{0.9}Sn$ NP-based electrode. However, upon subsequent cycling, a monotonous capacity decrease was observed, decaying to 160 mAh g^{-1} at the 120th cycle. It is worth noting that the smaller Na-ion storage capacity, when compared with Li-ion, is ascribed to the larger radius of Na^+ than Li^+, causing less Na^+ in-depth alloying. EIS analysis further demonstrated a larger charge transfer resistance of Ni_xSn-based electrodes in SIBs than in LIBs (Figure 5.7e). Rate-capability tests in the window 0.1-2.0 A g^{-1} showed the $Ni_{0.9}Sn$ NP-based electrode to deliver average discharge capacities of 327, 258, 217, 168, 128, and 88 mAh g^{-1} at 0.05, 0.1, 0.2, 0.5, 1.0, and 2.0 A g^{-1}, respectively. In addition, $Ni_{0.9}Sn$ NP-based electrodes showed similar capacities at 0.1 and 0.2 A g^{-1} after 30-40 more cycles at higher discharging-charging rate (Figure 5.9d).

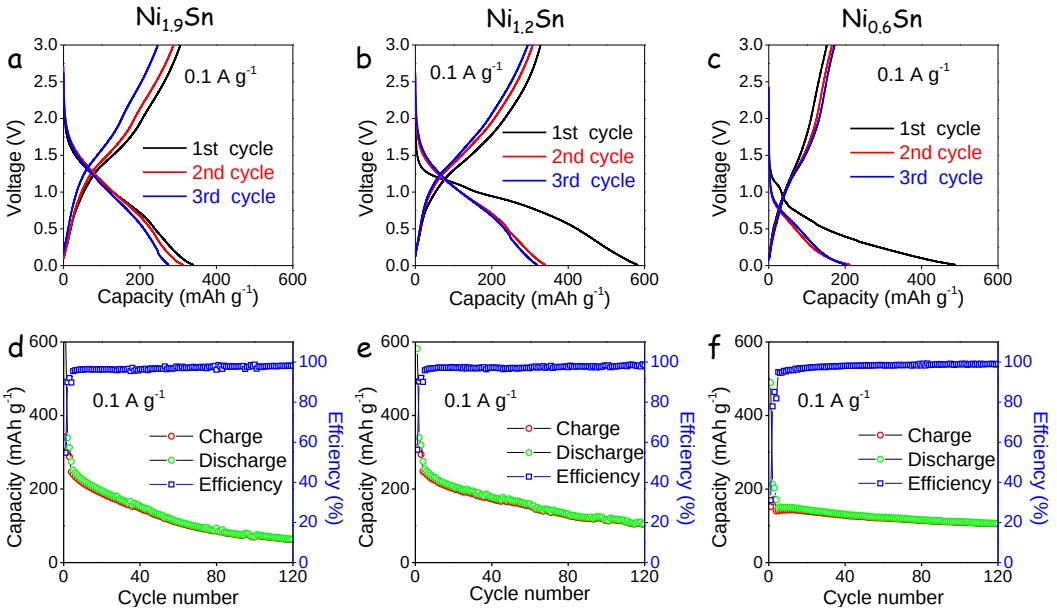

Figure 5.8 Li-ion storage performance of the Ni_xSn NPs electrode: a-c) Typical first three charge-discharge curves of different Ni:Sn ratio NPs at 0.2 A g^{-1} displayed on the top of each graph. d-f) Charge-discharge capacity and related efficiency over 200 cycles at a current density of 0.2 A g^{-1}.

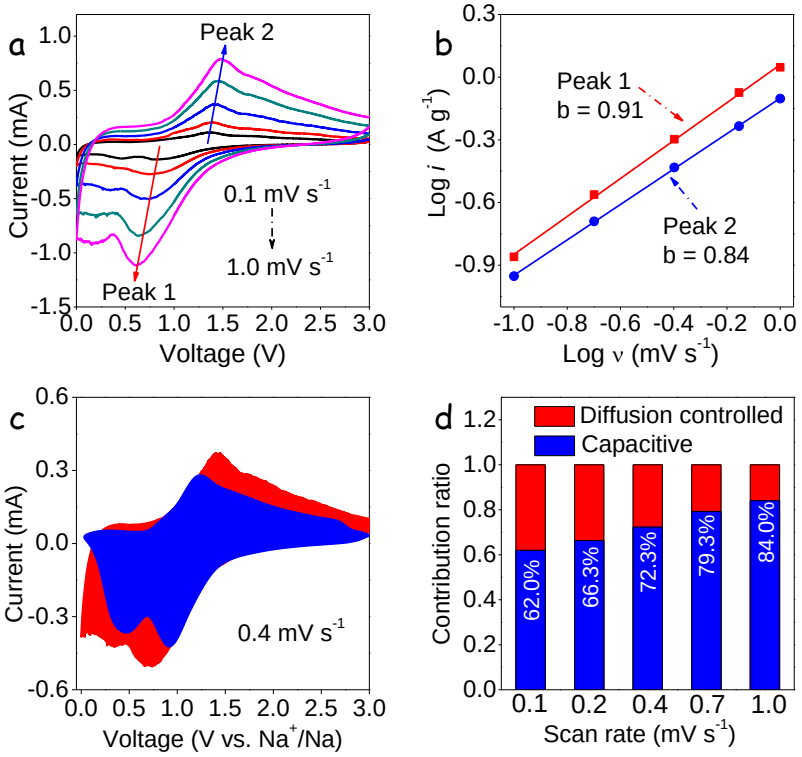

Figure 5.9. Na-ion storage performance of the $Ni_{0.9}Sn$ electrode: a) CV curve at the scan rates of 0.1, 0.2, 0.4, 0.7, 1.0 mV s^{-1}. b) Logarithmic dependence between peak current density and scan rate at the anodic peaks 0.62, 0.54, 1.04V. c) Capacitive contribution to the total current contribution at 0.4 mV s^{-1}. d) Normalize capacitive and diffusion-controlled contribution at the scan rates of 0.1, 0.2, 0.4, 0.7, 1.0 mV s^{-1}.

The kinetics of $Ni_{0.9}Sn$ NP-based electrodes in SIBs was investigated in a similar way as in LIBs, by collecting CV curves at different scan rates: 0.1, 0.2, 0.4, 0.7, 1.0 mV s^{-1}. $Ni_{0.9}Sn$ NP-based electrodes in SIBs were characterized with b values of 0.91 and 0.84 at 0.85 V and 1.36 V, respectively. Higher b values already pointed out at a relatively higher capacitance contribution in SIBs than LIBs. This phenomenon could be associated with the larger radius of Na^+, which increased the diffusion resistance into the interior of the materials and caused a larger fraction of Na^+ to exist on the surface, leading to higher capacitive contributions in SIBs than in LIBs. As shown in Figure 5.9, contributions up to 84% at 1.0 mV s^{-1} were measured from $Ni_{0.9}Sn$ NP-based electrodes in SIBs.

5.4 Conclusion

In summary, we reported the synthesis of Ni_xSn NPs with tuned composition ($0.6 \leq x \leq 1.9$) and their performance as anode material in LIBs and SIBs. Among the different compositions tested, best performances toward Li^+ ion and Na^+ ion insertion were obtained for $Ni_{0.9}Sn$ NP-based electrodes. This optimized cycling charge-discharge performance for LIBs provided 980 mAh g^{-1} at 0.2 A g^{-1} after 340 cycles. Additionally, $Ni_{0.9}Sn$ NP-based electrodes were tested in Na^+-ion half cells, exhibiting 160 mAh g^{-1} over 120 cycles at 0.1 A g^{-1}. From CV measurements at different current rates, it was found that the charging process was both capacitive and diffusion controlled, while the capacitive contribution was dominant in both LIBs and SIBs. The pseudocapacitive charge-storage accounted for a high portion of the whole energy storage capacity, which was associated to the small size and the composition of the Ni_xSn NPs used.

5.5 References

1 C. M. Park, J. H. Kim, H. Kim and H. J. Sohn, *Chem. Soc. Rev.*, 2010, **39**, 3115–3141.

2 D. Larcher and J. M. Tarascon, *Nat. Chem.*, 2015, **7**, 19–29.

3 J. B. Goodenough and K. S. Park, *J. Am. Chem. Soc.*, 2013, **135**, 1167–1176.

4 M. D. Slater, D. Kim, E. Lee and C. S. Johnson, *Adv. Funct. Mater.*, 2013, **23**, 947–958.

5 M. R. Palacín, *Chem. Soc. Rev.*, 2009, **38**, 2565–2575.

6 X. Liu, J. Zhang, W. Si, L. Xi, B. Eichler, C. Yan and O. G. Schmidt, *ACS Nano*, 2015, **9**, 1198–1205.

7 C. Yan, W. Xi, W. Si, J. Deng and O. G. Schmidt, *Adv. Mater.*, 2013, **25**, 539–544.

8 Y. Wen, K. He, Y. Zhu, F. Han, Y. Xu, I. Matsuda, Y. Ishii, J. Cumings and C. Wang, *Nat. Commun.*, 2014, **5**, 4033.

9 M. F. Oszajca, M. I. Bodnarchuk and M. V. Kovalenko, *Chem. Mater.*, 2014, **26**, 5422–

5432.

10 N. Liu, Z. Lu, J. Zhao, M. T. Mcdowell, H. W. Lee, W. Zhao and Y. Cui, *Nat. Nanotechnol.*, 2014, **9**, 187–192.

11 J. Deng, H. Ji, C. Yan, J. Zhang, W. Si, S. Baunack, S. Oswald, Y. Mei and O. G. Schmidt, *Angew. Chemie Int. Ed.*, 2013, **52**, 2326–2330.

12 F. Nacimiento, P. Lavela, J. L. Tirado and J. M. Jiménez-Mateos, *J. Solid State Electrochem.*, 2012, **16**, 953–962.

13 J.-Y. Hwang, S.-T. Myung and Y.-K. Sun, *Chem. Soc. Rev.*, 2017, **46**, 3529–3614.

14 M. Lao, Y. Zhang, W. Luo, Q. Yan, W. Sun and S. X. Dou, *Adv. Mater.*, , DOI:10.1002/adma.201700622.

15 P. G. Bruce, B. Scrosati and J. M. Tarascon, *Angew. Chemie - Int. Ed.*, 2008, **47**, 2930–2946.

16 H. Tian, F. Xin, X. Wang, W. He and W. Han, *J. Mater.*, 2015, **1**, 153–169.

17 J. Liu, Y. Wen, P. A. Van Aken, J. Maier and Y. Yu, *Nano Lett.*, 2014, **14**, 6387–6392.

18 R. Marom, S. F. Amalraj, N. Leifer, D. Jacob and D. Aurbach, *J. Mater. Chem.*, 2011, **21**, 9938–9954.

19 J. Wen, Y. Yu and C. Chen, *Mater. Express*, 2012, **2**, 197–212.

20 B. Wang, B. Luo, X. Li and L. Zhi, *Mater. Today*, 2012, **15**, 544–552.

21 C. Vaalma, D. Buchholz, M. Weil and S. Passerini, *Nat. Rev. Mater.*, 2018, **3**, 18013.

22 M. N. Obrovac and V. L. Chevrier, *Chem. Rev.*, 2014, **114**, 11444–11502.

23 N. Nitta, F. Wu, J. T. Lee and G. Yushin, *Mater. Today*, 2015, **18**, 252–264.

24 A. R. Kamali and D. J. Fray, *Rev. Adv. Mater. Sci.*, 2011, **27**, 14–24.

25 M. Walter, S. Doswald, F. Krumeich, M. He, R. Widmer, N. P. Stadie and M. V. Kovalenko, *Nanoscale*, 2018, **10**, 3777–3783.

26 M. F. Oszajca, M. I. Bodnarchuk and M. V. Kovalenko, *Chem. Mater.*, 2014, **26**, 5422–5432.

27 K. Kravchyk, L. Protesescu, M. I. Bodnarchuk, F. Krumeich, M. Yarema, M. Walter, C. Guntlin and M. V. Kovalenko, *J. Am. Chem. Soc.*, 2013, **135**, 4199–4202.

28 M. He, M. Walter, K. V. Kravchyk, R. Erni, R. Widmer and M. V. Kovalenko, *Nanoscale*, 2015, **7**, 455–459.

29 C. Chen, Y. Wen, X. Hu, X. Ji, M. Yan, L. Mai, P. Hu, B. Shan and Y. Huang, *Nat. Commun.*, 2015, **6**, 6929.

30 T. Brezesinski, J. Wang, S. H. Tolbert and B. Dunn, *Nat. Mater.*, 2010, **9**, 146–151.

31 W. X. Lei, Y. Pan, Y. C. Zhou, W. Zhou, M. L. Peng and Z. S. Ma, *RSC Adv.*, 2014, **4**, 3233–3237.

32 Y. M. Lin, P. R. Abel, A. Gupta, J. B. Goodenough, A. Heller and C. B. Mullins, *ACS Appl. Mater. Interfaces*, 2013, **5**, 8273–8277.

33 X. L. Wang, W. Q. Han, J. Chen and J. Graetz, *ACS Appl. Mater. Interfaces*, 2010, **2**, 1548–1551.

34 S. Wang, M. He, M. Walter, F. Krumeich, K. V. Kravchyk and M. V. Kovalenko, *Nanoscale*, 2018, **10**, 6827–6831.

35 L. O. Vogt and C. Villevieille, *J. Mater. Chem. A*, 2017, **5**, 3865–3874.

36 N. Tamura, Y. Kato, A. Mikami, M. Kamino, S. Matsuta and S. Fujitani, *J. Electrochem. Soc.*, 2006, **153**, A1626.

37 Z. Du and S. Zhang, *J. Phys. Chem. C*, 2011, **115**, 23603–23609.

38 C. M. Ionica-Bousquet, P. E. Lippens, L. Aldon, J. Olivier-Fourcade and J. C. Jumas, *Chem. Mater.*, 2006, **18**, 6442–6447.

39 J. Zhu, D. Wang, T. Liu and C. Guo, *Electrochim. Acta*, 2014, **125**, 347–353.

40 X. Shi, H. Song, A. Li, X. Chen, J. Zhou and Z. Ma, *J. Mater. Chem. A*, 2017, **5**, 5873–5879.

41 G. O. Park, J. Yoon, J. K. Shon, Y. S. Choi, J. G. Won, S. Bin Park, K. H. Kim, H. Kim, W. S. Yoon and J. M. Kim, *Adv. Funct. Mater.*, 2016, **26**, 2800–2808.

42 B. O. Jang, S. H. Park and W. J. Lee, *J. Alloys Compd.*, 2013, **574**, 325–330.

43 X. Liu, J. Xie, H. Zhao, P. Lv, K. Wang, Z. Feng and K. Świerczek, *Solid State Ionics*, 2015, **269**, 86–92.

44 J. R. González, F. Nacimiento, R. Alcántara, G. F. Ortiz and J. L. Tirado, *CrystEngComm*, 2013, **15**, 9196–9202.

45 R. Gnanamuthu, Y. N. Jo and C. W. Lee, *J. Alloys Compd.*, 2013, **564**, 95–99.

46 G. Ferrara, C. Arbizzani, L. Damen, M. Guidotti, M. Lazzari, F. G. Vergottini, R. Inguanta, S. Piazza, C. Sunseri and M. Mastragostino, *J. Power Sources*, 2012, **211**, 103–107.

47 P. P. Ferguson, A. D. W. Todd and J. R. Dahn, *Electrochem. commun.*, 2008, **10**, 25–31.

48 J. He, H. Zhao, J. Wang, J. Wang and J. Chen, *J. Alloys Compd.*, 2010, **508**, 629–635.

49 S. Il Lee, S. Yoon, C. M. Park, J. M. Lee, H. Kim, D. Im, S. G. Doo and H. J. Sohn, *Electrochim. Acta*, 2008, **54**, 364–369.

50 P. Chen, L. Guo and Y. Wang, *J. Power Sources*, 2013, **222**, 526–532.

51 J. Shin, W.-H. Ryu, K.-S. Park and I.-D. Kim, *ACS Nano*, 2013, **7**, 7330–7341.

52 J. Zhang and Y. Xia, *J. Electrochem. Soc.*, 2006, **153**, A1466.

53 N. Mahmood, C. Zhang, F. Liu, J. Zhu and Y. Hou, *ACS Nano*, 2013, **7**, 10307–10318.

54 D. wei ZHANG, C. ge YANG, J. DAI, J. wu WEN, L. WANG and C. hua CHEN, *Trans. Nonferrous Met. Soc. China (English Ed.*, 2009, **19**, 1489–1493.

55 M. Uysal, T. Cetinkaya, A. Alp and H. Akbulut, *J. Alloys Compd.*, 2015, **645**, 235–242.

56 X. Fan, P. Dou, A. Jiang, D. Ma and X. Xu, *ACS Appl. Mater. Interfaces*, 2014, **6**, 22282–22288.

57 J. Li, Z. Luo, Y. Zuo, J. Liu, T. Zhang, P. Tang, J. Arbiol, J. Llorca and A. Cabot, *Appl. Catal. B Environ.*, 2018, **234**, 10–18.

58 M. Walter, S. Doswald and M. V. Kovalenko, *J. Mater. Chem. A*, 2016, **4**, 7053–7059.

59 H. Fjellvåg, A. Kjekshus, R. Stomberg, R. Zingales, I. Vikholm, F. Urso, J. Weidlein and R. A. Zingaro, *Acta Chem. Scand.*, 1986, **40a**, 23–30.

60 C. Serrano-Cinca, Y. Fuertes-Callén and C. Mar-Molinero, *Measuring DEA efficiency in Internet companies*, Perkin-Elmer Corporation Physical Electronics Division, 2005, vol. 38.

61 Y. Liu, X. Liu, Q. Feng, D. He, L. Zhang, C. Lian, R. Shen, G. Zhao, Y. Ji, D. Wang, G. Zhou and Y. Li, *Adv. Mater.*, 2016, **28**, 4747–4754.

62 M. He, L. Protesescu, R. Caputo, F. Krumeich and M. V. Kovalenko, *Chem. Mater.*, 2015, **27**, 635–647.

63 J. Li, Z. Luo, F. He, Y. Zuo, C. Zhang, J. Liu, X. Yu, R. Du, T. Zhang, M. F. Infante-Carrió, P. Tang, J. Arbiol, J. Llorca and A. Cabot, *J. Mater. Chem. A*, , DOI:10.1039/C8TA08242A.

64 H.-S. Kim, J. B. Cook, S. H. Tolbert and B. Dunn, *J. Electrochem. Soc.*, 2015, **162**, A5083–A5090.

65 V. Augustyn, P. Simon and B. Dunn, *Energy Environ. Sci.*, 2014, **7**, 1597–1614.

66 X. Xu, S. Ji, M. Gu and J. Liu, *ACS Appl. Mater. Interfaces*, 2015, **7**, 20957–20964.

67 X. Xu, J. Liu, J. Liu, L. Ouyang, R. Hu, H. Wang, L. Yang and M. Zhu, *Adv. Funct. Mater.*, 2018, **28**, 1707573.

Chapter 6

Co-Sn nanocrystalline solid solutions as anode materials in lithium-ion batteries with high pseudocapacitive contribution

Key words:

Colloidal
Bimetallic
Nanoparticles
Tin
Tin cobalt alloy
Anode
Lithium-ion Batteries

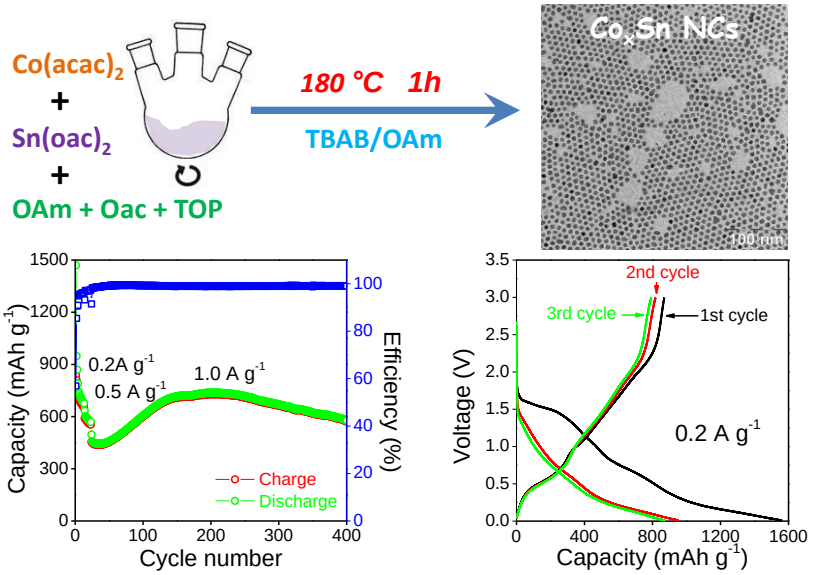

Cobalt-based solid-solution nanoparticles with the Sn crystal structure and tuned metal ratios were synthesized by a facile one-pot solution-based procedure involving the initial reduction of a Sn precursor and the posterior incorporation of Co within the Sn lattice. Such nanoparticles were used as anode materials for Li-ion batteries. Among the different compositions tested, $Co_{0.7}Sn$ and $Co_{0.9}Sn$ electrodes provided the highest capacities, with values above 1500 mAh g^{-1} at a current density of 0.2 A g^{-1} after 220 cycles and up to 800 mAh g^{-1} at 1.0 A g^{-1} after 400 cycles. Up to 81 % pseudocapacitance contribution at a sweep rate of 1.0 mV s^{-1} were measured for these electrodes, providing fast kinetics and long durability. The excellent performance of Co-Sn alloy nanoparticle-based electrodes was associated to both the small size of the crystal domains and their suitable composition, which buffered volume changes of Sn and contributed to a suitable electrode restructuration.

6.1 Introduction

Lithium-ion batteries (LIBs) have become the dominant energy storage technology in portable applications. However, their energy density, charging rate, and stability are still critical performance parameters that has plenty of room for improvement by optimizing both anode and cathode materials.[1–4] At the anode, current commercial LIBs use graphite, which has a relatively low maximum theoretical capacity (372 mAh g^{-1} to form LiC_6).[5] Alternatively, anode materials such as Sn, Ge and Si provide platforms with potentially higher lithium storage capacities: $Li_{22}Sn_5$ (994 mAh g^{-1}), $Li_{22}Ge_5$ (1600 mAh g^{-1}), and $Li_{22}Si_5$ (3000 mAh g^{-1}) respectively.[6–8] While Si is the most abundant element and has the highest potential storage capacity, Sn and Sn-based compounds are particularly appealing owing to their relatively high abundance, low cost and high electrical conductivity.[7,9]

In terms of stability, the huge lattice expansion and contraction of the anode material during cycling strongly reduces the battery performance due to a loss of electrical connection by electrode pulverization. In the case of Sn, the $Sn/Li_{22}Sn_5$ reaction has associated a 300% volume change, which inevitably leads to major structural rearrangements generally resulting in a loss of capacity.[10,11] Different strategies have been proposed to tackle down this major issue. One main approach is to alloy the active phase, Sn, with a second elements that buffers the volume changes.[12,13] In this direction, Sn-based alloys with Ni,[14–17] Co,[18–30] Fe,[31,32] Cu,[33,34] and Sb[35–37] have demonstrated superior cycling performance than bare Sn anodes. Among the different Sn-based alloys tested, CoSn electrodes have shown particularly promising performances as anode materials for LIBs.[31] Co-Sn-C composites have been even used in commercial batteries, what has motivated a notable interest in this system.[38–42] Most previous works have focused on the intermetallic Co-Sn alloys: Co_3Sn_2, CoSn, $CoSn_2$. Among these intermetallics, while some controversy remains, $CoSn_2$ has been considered as the optimum stoichiometry, due to its highest content of Sn. However, beyond intermetallic phases, a range of Co-Sn solid solutions exist that are yet to be explored.

Besides alloying the active material to improve cycling performance, the use of nanostructured electrodes can reduce the overall stress generated on the material domains during lithiation, thus diminishing mechanical disintegration and improving stability. Furthermore, nanosized materials present additional advantages, such as faster rate capabilities because of the shorter Li-ion diffusion paths and a potentially huge pseudocapacitive contribution associated with their very high surface/volume ratio.[43–46] This pseudocapacitive contribution is particularly appealing because it can significantly improve both the rate performance of LIBs and their stability.

In the present work, we take advantage of the versatility of colloidal synthesis methods to produce Co-Sn solid solution nanoparticles (NPs) with tuned Co:Sn atomic ratios, from 0.3 to

1.3. After removing surface ligands, we use these NPs to test the performance of Co-Sn solid solutions as anode materials for LIBs, defining an optimal composition and demonstrating this system to be characterized by a high energy storage capacity, with a high pseudocapacitive contribution and a notable stability.

6.2 Experimental

6.2.1 Colloidal synthesis of Sn and Co-Sn NPs

Syntheses were carried out using standard air-free techniques. All the reagents and solvent were analytical grade and used without further purification. In a typical synthesis of Co-Sn NPs with nominal composition Co:Sn = 3:2, 0.6 mmol cobalt(II) acetylacetonate ($Co(acac)_2$, 99%, Sigma-Aldrich) and 0.4 mmol tin(II) acetate ($Sn(OAc)_2$, 95%, Fluka) were added into a 50 mL three-neck round-bottomed flask. Subsequently, 20 mL of oleylamine (OAm, 80-90%, TCI) and 1.0 mL of oleic acid (OAc, Sigma-Aldrich) were loaded along with a magnetic bar in a three-neck flask connected with a thermometer, condenser and septum. The flask was heated to 80 °C and degassed under vacuum for 2 hours and then backfilled with Ar. Then, 5 mL of tri-n-octylphosphine (TOP, 97%, Strem) were injected, and afterward the solution was heated up to 180 °C at 5 °C min^{-1}. Right after reaching 180 °C, 5 mL of a degassed OAm solution containing 5 mmol of borane tert-butylamine (TBAB, 97%, Sigma-Aldrich) was injected. Upon injection of this reducing complex, the solution became black, but the reaction mixture was maintained at 180 °C for 1 additional hour to allow the NPs to grow. After 1 h reaction, the heating mantle was removed and the solution was cooled down to room temperature in approximately 3 min using a water bath. NPs were collected by centrifugation after adding an excess of acetone. The precipitate was dispersed in chloroform and centrifuged a second time with an excess of acetone. This washing process was repeated for three times. Finally, NPs were stored in chloroform.

6.2.2 Ligand removal

25 mL of acetonitrile containing 0.8 mL hydrazine hydrated were added into a vial containing about 100 mg of precipitated NPs. The solution was strongly stirred for 4 hours and centrifuged. The NPs were further washed with acetonitrile 3 more times, followed by vacuum-drying at room temperature. The product was kept in an Ar-filled glove box.

6.2.3 Characterization

X-ray diffraction (XRD) patterns were recorded at room temperature on a Bruker AXS D8 Advance X-ray diffractometer with Cu K radiation (λ = 1.5106 Å) operating at 40 kV and 40 mA. Transmission electron microscopy (TEM) analyses were performed on a ZEISS LIBRA 120, operating at 120 kV. High-resolution TEM (HRTEM) and scanning TEM (STEM) studies were carried out using a field emission gun FEI Tecnai F20 microscope at 200 kV with a point-to-point resolution of 0.19 nm. High angle annular dark-field (HAADF) STEM was combined with electron energy loss spectroscopy (EELS) in the Tecnai microscope by using a GATAN QUANTUM filter. Composition analysis was carried out using a ZEISS Auriga Scanning electron microscopy (SEM) equipped with an energy dispersive X-ray spectroscopy (EDS) detector operated at 20 kV. X-ray photoelectron spectroscopy (XPS) measurements were carried out in normal emission using an Al anode XR50 source operating at 150 mW and a Phoibos 150 MCD-9 detector. Fourier transform infrared spectrometer (FTIR) data was recorded on an Alpha Bruker spectrometer.

6.2.4 Electrochemical measurements

To evaluate the intrinsic electrochemical performance of Co-Sn NPs, the working electrode was prepared by mixing dried NPs, Super P and polyvinylidene fluoride (PVDF) with a weight ratio of 80:10:10 in an appropriate amount of N-methy1-2-pyrrolidone (NMP) to obtain a slurry. Then, the mixture was coated onto a Cu foil. Then, it was dried in a vacuum oven at 80 °C for 24 h. Subsequently, the foil was cut into disks with a diameter of 12 mm. The typical mass loading of active materials was estimated to be 0.7-1.2 mg cm^{-2}. To test the performance of electrodes based on Co-Sn NPs, half cells were assembled in the glove box (H_2O and O_2 < 0.1 ppm) using Celgard2400 as separator. As electrolyte, a 1 M $LiPF_6$ solution in ethylene carbonate (EC)/diethyl carbonate (DEC) (1:1 in volume) with 5 wt% fluoroethylene carbonate (FEC) as additive was used. Galvanostatic charge-discharge were measured by a battery test system (CT2001A, LAND) with cutoff potentials from 0.01 V to 3.0 V. Cyclic voltammetry (CV) curves were performed by an electrochemical workstation (Gamry Interface 1000) in the voltage range from 0–3.0 V and the scan rate from 0.1 mV s^{-1} to 1 mV s^{-1}.

6.3 Results and discussion

Colloidal Co-Sn NPs were produced by the reduction of tin(II) acetate and cobalt(II) acetylacetonate with borane tert-butylamine (TBAB) at 180 °C, in a solution containing oleylamine (OAm), oleic acid (OAc) and tri-n-octylphosphine (TOP, see details in experimental

section). Figures 1a-d show representative TEM micrographs and size distribution histograms of the quasi-spherical NPs produced. The average NP size was estimated to be 6 - 7 nm for all compositions except for the Sn-richest NPs, which had an average size of 10 nm. XRD analysis showed that, independently of the Co:Sn ratio, NPs conserved the Sn crystal structure. However, XRD peaks appeared shifted to lower angles, as it corresponds to the introduction of a slightly larger atom, Co, within the Sn lattice. The formation of CoSn solid solutions was somehow surprising when taking into account that previous works reported the formation of intermetallics, i.e. $CoSn_2$, CoSn and Co_3Sn_2, when co-reducing proper amounts of the two elements. We associate the differences in the products obtained between our synthesis protocol and previous works to the relatively low synthesis temperatures we used which prevented the crystallization of independent Co NPs and Co-Sn intermetallic phases.

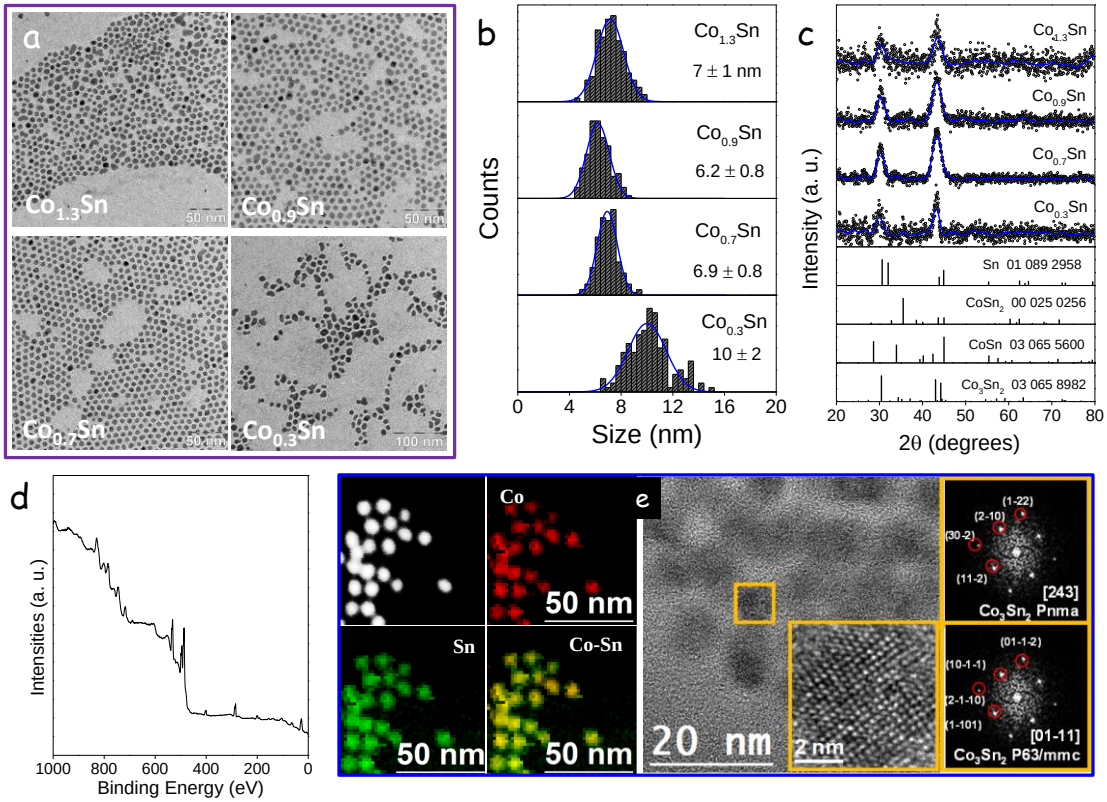

Figure 6.1. a) TEM micrographs of Co-Sn NPs with different compositions, as obtained from EDX and displayed in each image. b) Size distribution histograms of the Co-Sn NPs; c) XRD patterns of the NPs with different compositions. Sn and different Co-Sn intermetallic XRD patterns are shown as reference. d) Survey XPS spectra of $Co_{0.9}Sn$ NPs. e) STEM and EELS compositional maps of $Co_{0.9}Sn$ NPs and HRTEM micrograph exposed to atmosphere and displaying a core-shell structure.

EDX analysis showed the Co:Sn ratio in Co-Sn solid-solution NPs to be: 1.3, 0.9, 0.7 and 0.3 when produced from nominal Co:Sn precursor ratios of 2.0, 1.5, 1.0 and 0.5, respectively. The final Co-poor NP stoichiometry (with respect to the nominal) and the pink color of the

supernatant obtained after NP precipitation revealed that some of the cobalt precursor remained unreacted after 1h at 180 °C. We also observed that the same reaction conditions but in the absence of Sn precursor did not result in the formation of Co NPs. On the contrary, the same reaction in the absence of Co resulted in the formation of Sn NPs. We believe that in the reaction conditions used, the Sn precursor was first reduced to nucleate Sn NPs. Taking advantage of the lower energy for heterogeneous growth over homogeneous nucleation, during the 1h period at 180 °C Co ions within the solution incorporated to the initial Sn nuclei upon reduction with TBAB. Through this synthesis mechanism, the Sn crystal structure was conserved, which is in contrast to the results obtained in previous works that make use of higher reaction, alloying or annealing temperatures to produce Co-Sn intermetallic alloys.

XPS analysis (Figure 6.1d) showed the Co:Sn atomic ratio of the $Co_{0.9}Sn$ NPs to be 0.7, which pointed at a slightly Sn-rich surface. We hypothesize that this Sn-rich surface was related to a slight oxidation of the NPs exposed to ambient conditions. We believe air exposure resulted in a slight restructuration of the alloy due to the higher Sn affinity to oxygen that drove the diffusion of Sn to the surface.

Figure 6.1e shows STEM micrographs and EELS chemical composition maps of the $Co_{0.9}Sn$ NPs. All $Co_{0.9}Sn$ NPs contained the two elements in similar ratios. Within each NP, Co and Sn distributions were mostly homogeneous, but most NPs presented a Sn-rich shell, consistent with XPS analysis. HRTEM micrographs (Figure 6.1e) clearly displayed a core-shell structure of the NPs. From HRTEM analysis, the core crystal structure could be assigned to the $Co_{2.9}Sn_2$ orthorhombic phase (space group = Pnma) with a = 7.1450 Å, b = 5.2500 Å and c = 8.1730 Å, or to the Co_3Sn_2 hexagonal phase (space group = P63/mmc) with a = b = 4.1130 Å and c = 5.1850 Å (SI).[47] This result is in contradiction with XRD patterns and EDX and XPS analysis(Figure 6.1d). We hypothesize that solid-solution NPs with the $Co_{0.9}Sn$ composition and Sn structure were initially formed. With the exposition to air, these NPs developed a Sn-rich surface associated to a differential reactivity of the two elements with oxygen.[48–50] Within the electron beam during HRTEM analysis, the core, having a higher Co content due to the diffusion of Sn to the surface, crystallized to an intermetallic Co_3Sn_2 phase with potential additional Sn segregation to the surface.

Co-Sn solid solution NPs were explored as anode material in LIBs. Before testing their performance, the organic ligands used to control the growth of the NPs in solution were removed by treating them with a mixture of hydrazine and acetonitrile.[36,37] FTIR analysis confirmed the effectiveness of the ligand removal step. LIB anodes were prepared by casting a non-aqueous slurry containing 80 wt% of active material, polyvinylidene (PVDF, 10 wt%) as a polymer binder, and Super P as conductive additive (10 wt%). After vacuum drying, all anodes had similar mass loading of the active materials (ca. 0.79-1.36 mg). All electrodes were tested

under the same conditions, using coin type half-cells with metallic Li as counter electrodes (see details in experimental section).

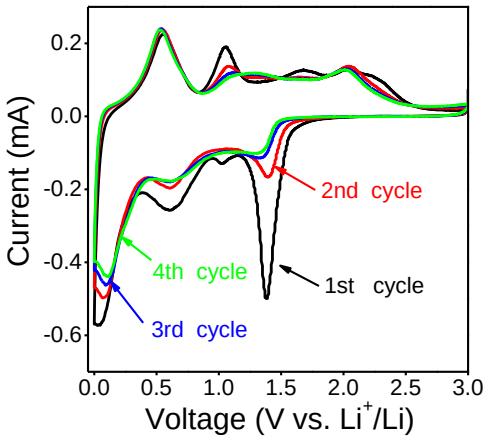

Figure 6.2. Initial cyclic voltammograms obtained from the $Co_{0.9}Sn$ electrode in the voltage window 0-3.0 V vs. Li^+/Li at 0.1 mV s^{-1}.

The electrochemical performance of Co-Sn NP-based electrodes was initially assessed through cyclic voltammetry (CV) with a scan rate of 0.1 mV s^{-1} in the potential window of 0-3.0 V (vs. Li^+/Li). As shown in Figure 6.2, all CV cycles showed a similar trend, but the initial two cycles displayed more pronounced peaks than following ones at 1.31 V and 2.05 V in the forward scan and 0.65 V and 1.45 V in the reverse one. Differences were ascribed to the formation of the solid electrolyte interphase (SEI) layer during the first cycles and the reduction of the surface SnO_x layer formed during NP manipulation and electrode preparation, in agreement with previous works.[51,52] The overlap of the 3rd and subsequent cycles indicated a reasonable stability of the electrode. The two obvious peaks around 0.65 and 0.05 V in the reverse scan were assigned to the reversible lithium insertion in the CoSn alloy to form $Li_{4.4}Sn$.[53] During the anodic sweep, peaks at 0.52V were related to the extraction of Li ions from the electrode. Qualitatively similar voltammograms were obtained for the four compositions tested.

Figures 6.3a-d display the first three charge-discharge cycles at a current density of 0.2 A g^{-1} of the electrodes containing Co-Sn NPs with different ratios. For all the compositions tested, small charging and discharging plateaus were observed at around 0.4 V and 1.6 V, respectively. The charge voltage at ca. 0.4 V was in good agreement with previous results.[29,54] Figure 4e-f shows the charge-discharge capacity and related efficiency over 400 cycles at a current density of 1.0 A g^{-1} (activated at 0.2 and 0.5 A g^{-1} for 10 cycles respectively). The low initial coulombic efficiency measured for all the electrodes, ca. 50%, was associated with the SEI formation. During the first few cycles, the coulombic efficiency increased to ca. 98% and it was stabilized at this value for several hundreds of cycles. All compositions showed a similar trend, with an initial very fast decrease of the capacity, attributed to the SEI formation, a following slower loss

of capacity, associated to a partial disintegration of the anode material, a capacity recover after a certain number of cycles and a moderate and sustained decrease of capacity at much larger cycle numbers. We hypothesize the reactivation to be in part associated to a rearrangement of the active material domains within the anode making a larger amount of electroactive material accessible to Li ions, although at the same time reducing electrical conductivity as observed from the EIS analysis below. This rearrangement of the active material could also provide larger surface areas and increase the pseudocapacitive contribution to the total energy storage capacity.[55] On the other hand, a restructuration of the active material at the atomic scale, and particularly its amorphisation, could facilitate lithium insertion.

$Co_{0.9}Sn$ and $Co_{0.7}Sn$ electrodes showed the highest Li storage capacities among the compositions tested. For the $Co_{0.9}Sn$ electrode at 0.2 A g^{-1}, as shown in Figure 6.3, during the first cycle, the coulombic efficiency was just 55.7%, with a high discharge (869 mAh g^{-1}) and charge capacity (1560 mAh g^{-1}). A strong capacity loss was observed during the first cycles, down to charge and discharge capacities of 629 mAh g^{-1} and 647 mAh g^{-1} with 97.2% coulombic efficiency at the 24th cycle. With continuous cycling, the coulombic efficiency remained stable and the capacity gradually increased up to charge and discharge capacities of 1534 mAh g^{-1} and 1555 mAh g^{-1} at the 220th cycle. The extraordinarily high capacities obtained, above the theoretical maximum not only for Co-Sn alloys, but also for pure Sn, may be attributed to the ultra-small particle size of the active anode material, which provided additional active sites for Li-ion storage and a larger density of diffusion channels for Li ions to access all the active material.[55–59]

To evaluate the rate capability of the Co-Sn electrodes, galvanostatic cycling was performed at current rates between 0.05 to 4 A g^{-1} (Figure 6.5a). Figure 6.5b presents the corresponding charge-discharge profiles from 0.05 to 4.0 A g^{-1}. For $Co_{0.9}Sn$, the electrode delivered a discharge capacity of 804, 702, 598, 532, 448, 365, 267 mAh g^{-1} at 0.05, 0.1, 0.2, 0.5, 1.0, 2.0, 4.0 A g^{-1}, respectively.

Figure 6.4 compares the EIS data obtained from electrodes with different Co-Sn compositions and from the $Co_{0.9}Sn$ electrode in the first and the 400th cycle, all at 1 A g^{-1}. From the Nyquist plots, not a straightforward dependence of the anode-electrolyte charge transfer resistance on the Co-Sn alloy composition was observed. However, the lowest resistances were obtained for the optimum compositions $Co_{0.7}Sn$ and $Co_{0.9}Sn$. With cycling, the electrode resistance increased and two semicircles evolved, one corresponding to the SEI layer impedance and the other to the charge-transfer impedance on the electrode-electrolyte interphase. In the low frequency region, slopes well above 1 for all compositions and both for the fresh and cycled samples indicated a significant capacitive behavior.

The kinetics of the Co-Sn electrodes was further investigated using CV at different scan rates, from 0.1 to 1 mV s^{-1}. Figure 5c presents the CV curves obtained from the $Co_{0.9}Sn$ electrode at the scan rates of 0.1, 0.2, 0.4, 0.7, 1.0 mV s^{-1} in the potential range 0-3.0 V vs Li^+/Li. Three anodic peak were observed at 0.52, 1.31, 2.05 V, all of them increasing with the scan rate.

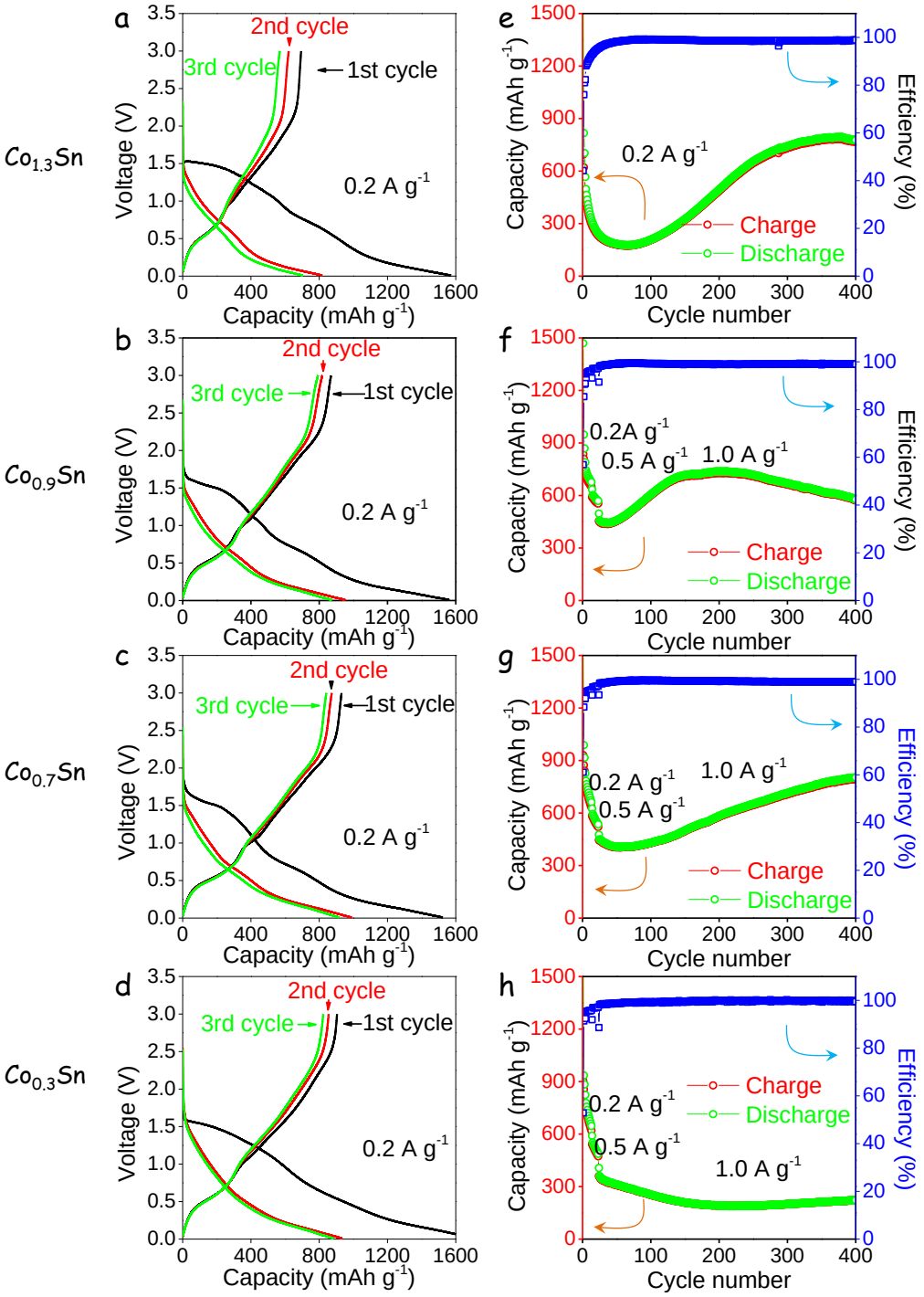

Figure 6.3. a-d) Initial charge-discharge curves at 0.2 A g^{-1} for the different electrode compositions as displayed on the top of each graph. e-h) Charge-discharge capacity and related efficiency over 400 cycles at a current density of 1.0 A g^{-1}: activated at 0.2 and 0.5 A g^{-1} for 10 cycles each. For the $Co_{1.3}Sn$ electrode only data at 0.2 A g^{-1} is shown.

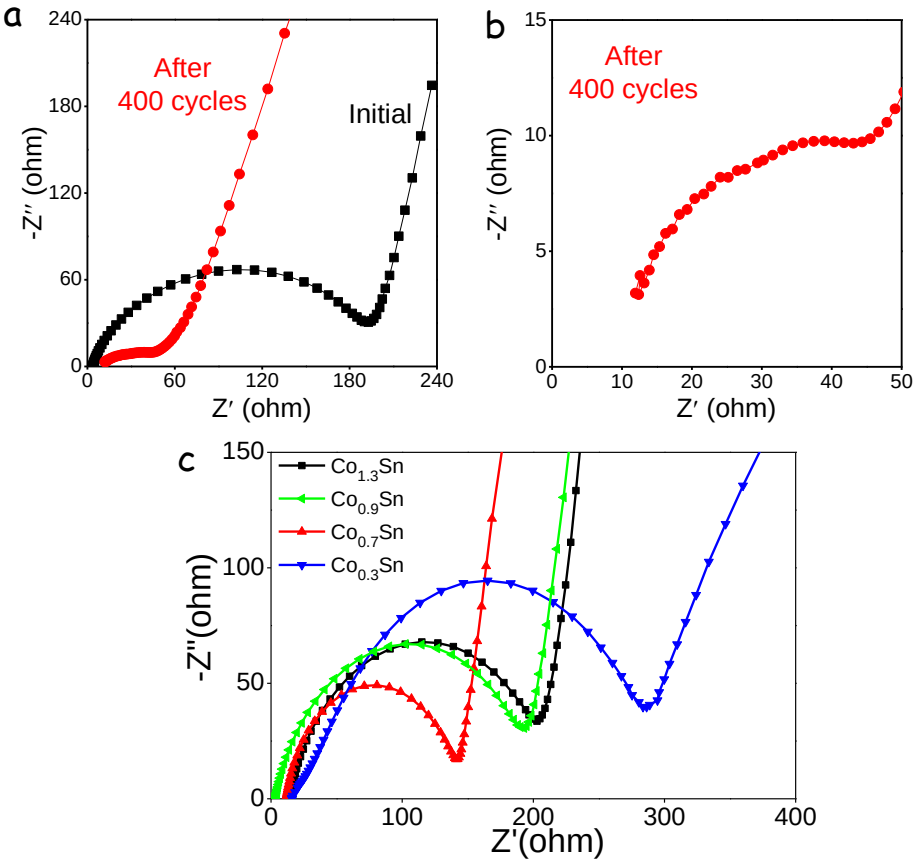

Figure 6.4. (a) EIS Nyquist plots of the $Co_{0.9}Sn$ before and after 400 cycles. (b) Zoomed Nyquist plot of the $Co_{0.9}Sn$ after 400 cycles. (c) EIS Nyquist plots of $Co_{0.3}Sn$, $Co_{0.7}Sn$ and $Co_{1.3}Sn$ anodes before cycles.

Two main charge-storage mechanisms determine the electrode storage capacity: i) a diffusion-controlled contribution associated to the $Li_{22}Sn_5$ alloy formation; and ii) a surface-related capacitive contribution known as the pseudocapacitive contribution.[60] The pseudocapacitive contribution is particularly attractive because it is a much faster and stable process, whereas the diffusion-controlled alloying is slower and generally provides relatively poor cycle life.

Generally, the relationship between the measured current (i) and the scan rate (v) can be expressed as:

$$i = av^b$$

where a, b was the adjustable constant parameters. According to previous reports, a diffusion controlled process is characterized by a scan rate dependence with b = 0.5, whereas an ideal capacitive behavior translates into b = 1.[61–63] From the linear fit of the logarithmic plot of the current vs. scan rate (Figure 6.5d), b values of 0.80, 0.93 and 0.84 were calculated at 0.52, 1.31, 2.05 V, respectively. These values indicated a fast kinetics resulting from a pseudocapacitive effect.

At each potential, the current density contribution at a given scan rate could be divided into two parts, a diffusion-controlled ($k_1v^{1/2}$) and a capacitor-like fraction (k_2v):

$$i(V) = k_1 v^{1/2} + k_2 v$$

To distinguish the fraction of the current arising from Li^+ insertion and that from a capacitive process at each specific potential, k_1 and k_2 were determined by plotting $i(V)/v^{1/2}$ vs. $v^{1/2}$.[44,61] Figure 5e shows the CV profiles at 0.4 mV s^{-1} and compares the capacitive current (blue shaded region) with that for the total measured current (red curve) for the $Co_{0.9}Sn$ electrode. The relative pseudocapacitive contributions at sweep rates of 0.1, 0.2, 0.4, 0.7 and 1.0 mV s^{-1} were 55%, 59%, 65%, 73% and 81%, respectively (Figure 6.5f). For comparison, the pseudocapacitive study of $Co_{0.3}Sn$ electrode is presented in Figure 6.6, the calculated contributions at sweep rates of 0.1-1.0 mV s^{-1} were lower than that of $Co_{0.9}Sn$. These results clearly suggest that the pseudocapacitive charge-storage amount does occupy a high portion of the whole energy storage capacity, which is associated to the small size of the Co-Sn NPs used and their Sn-rich and oxidized surface.

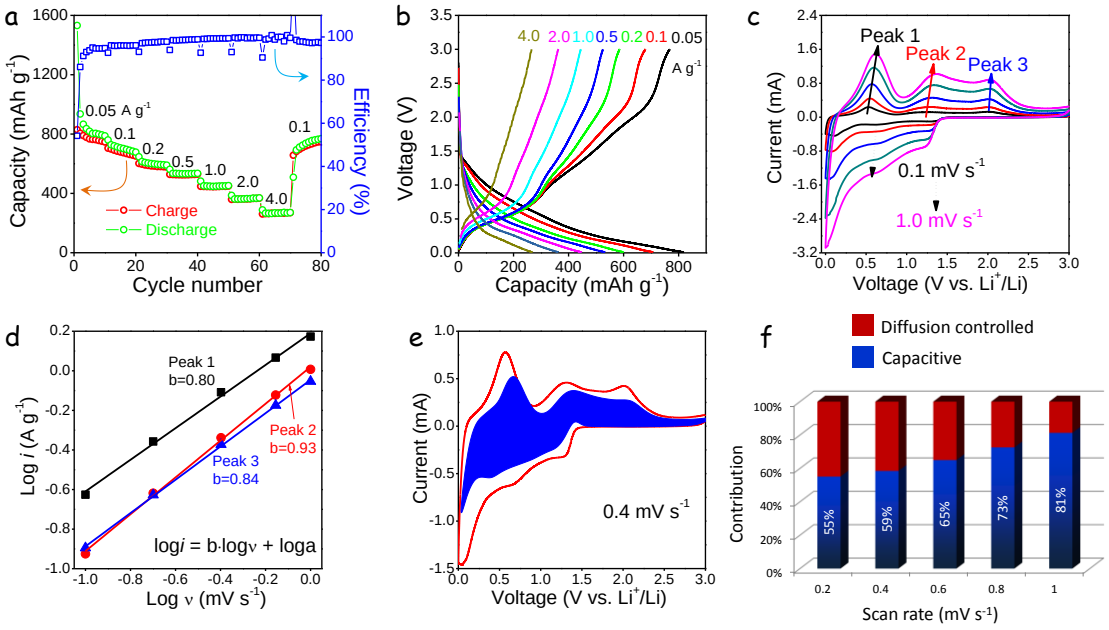

Figure 6.5. Li-ion storage performance of the $Co_{0.9}Sn$ electrode: a) Charge-discharge curves at rates: 0.05, 0.1, 0.2, 0.5, 1.0, 2.0, 4.0, 0.1 A g^{-1}. b) Rate performance at 0.05, 0.1, 0.2, 0.5, 1.0, 2.0, 4.0 A g^{-1}. c) CV curve at the scan rates of 0.1, 0.2, 0.4, 0.7, 1.0 mV s^{-1}. d) Logarithmic dependence between peak current density and scan rate at the anodic peaks 0.52, 1.31, 2.05 V. e) Capacitive contribution to the total current contribution at 0.4 mV s^{-1}. f) Normalize capacitive and diffusion-controlled contribution at the scan rates of 0.1, 0.2, 0.4, 0.7, 1.0 mV s^{-1}.

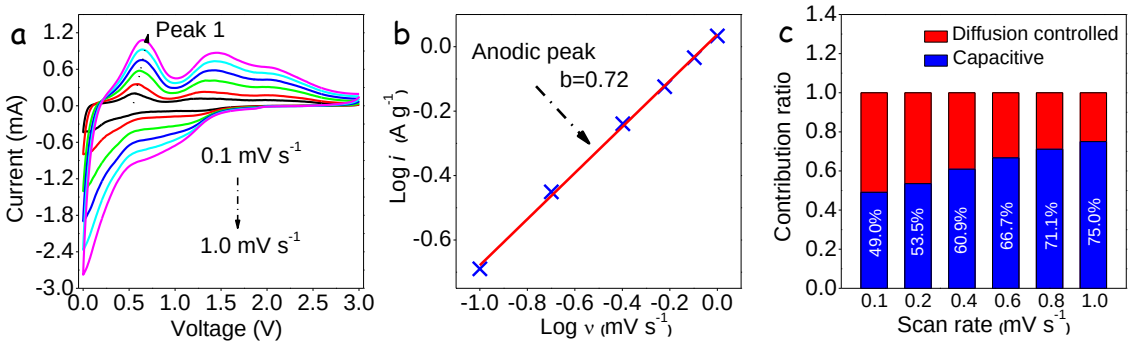

Figure 6.6. Li-ion storage performance of the $Co_{0.3}Sn$ electrode: a) CV curve at the scan rates of 0.1, 0.2, 0.4, 0.6, 0.8 and 1.0 mV s^{-1}. b) Logarithmic dependence between peak current density and scan rate at the anodic peaks 0.52 V. c) Normalize capacitive and diffusion-controlled contribution at the scan rates of 0.1, 0.2, 0.4, 0.6, 0.8 and 1.0 mV s^{-1}.

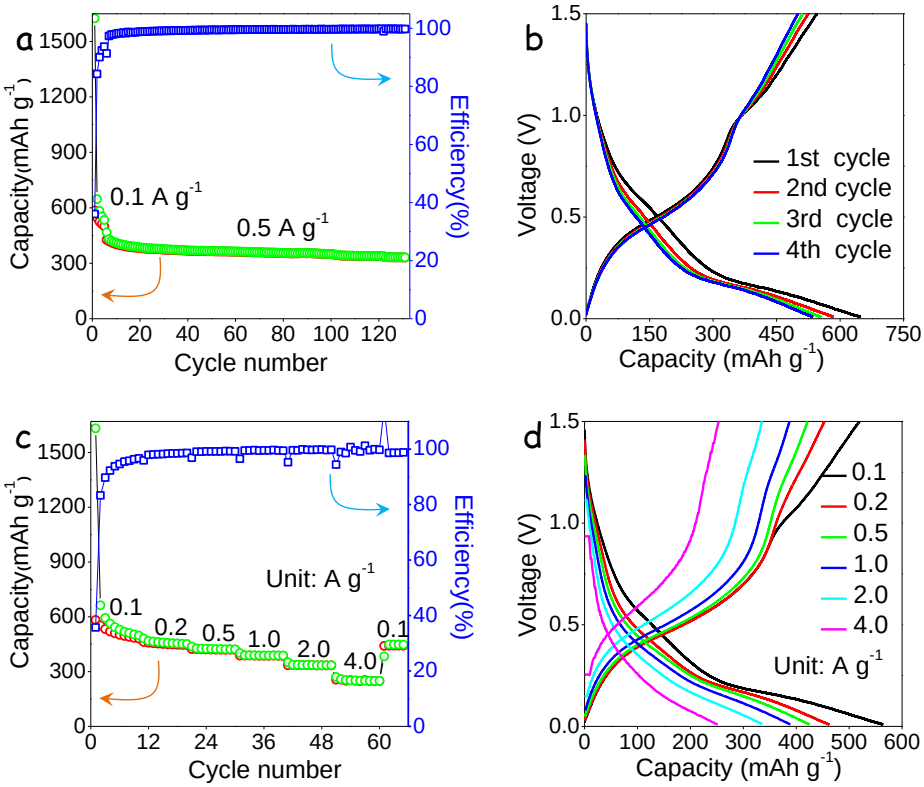

Figure 6.7. Li-ion storage performance of the $Co_{0.9}Sn$ electrode in the range 0-1.5 V vs. Li/Li^+: a) Charge-discharge curves at rates: 0.1, 0.2, 0.5, 1.0, 2.0, 4.0, 0.1 A g^{-1}. b) Rate performance at 0.1, 0.2, 0.5, 1.0, 2.0, 4.0 A g^{-1}. c) Charge-discharge capacity and related efficiency over 130 cycles at a current density of 0.5 A g^{-1}: activated at 0.1 A g^{-1} for 10 cycles. d) Initial charge-discharge curves at 0.1 A g^{-1}.

To estimate the practical application of Co-Sn NP-based anodes, they were tested in the range of 0.01-1.5 V vs. Li/Li^+. As shown in Figures 6.7a-b and Figure 6.8, over continuous charge-discharge cycles, $Co_{0.7}Sn$ and $Co_{0.9}Sn$ electrodes show the highest capacity and stability, stabilizing at 360 mAh g^{-1} at 0.5 A g^{-1}. This value is comparable to theoretical capacities of graphene-based electrodes. The rate capability of the $Co_{0.9}Sn$ electrode is also shown in Figure

6c-d. Specifically, the electrode delivered discharge capacities of 520, 453, 421, 388, 336, 253 mAh g^{-1} at 0.1, 0.2, 0.5, 1.0, 2.0, 4.0 A g^{-1}, respectively. Additionally, this electrode delivered a stable charge-discharge capacity at 0.1 A g^{-1} after continuous 60 cycles at variable charging rate.

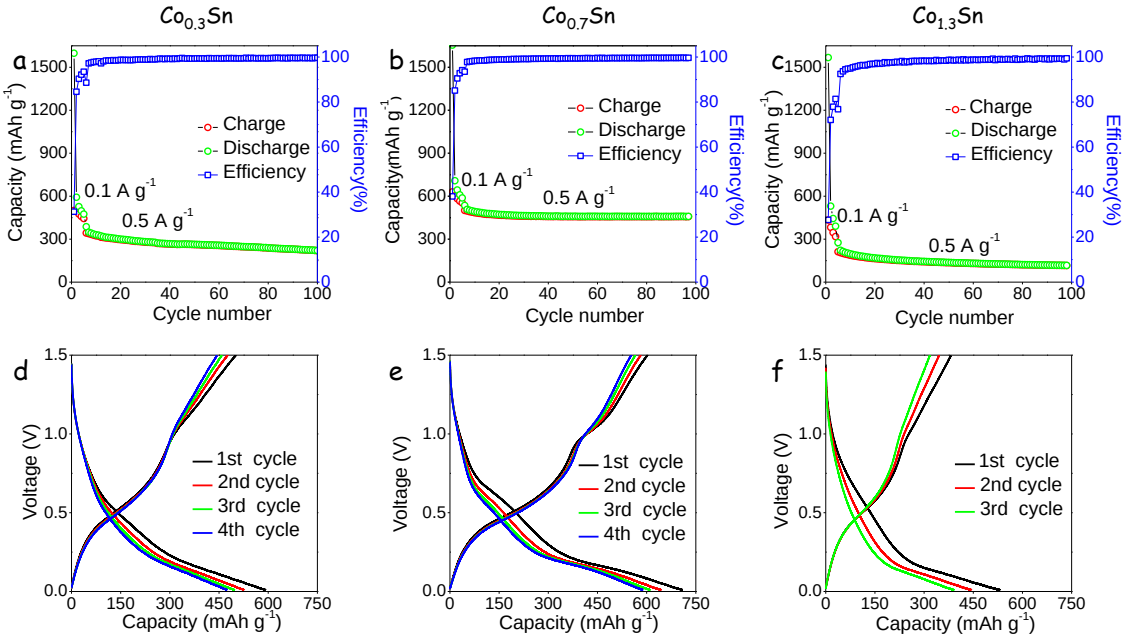

Figure 6.8. a-c) Charge-discharge capacity and related efficiency over 100 cycles at a current density of 0.5 A g^{-1}: activated at 0.1 A g^{-1} for 10 cycles each. d-f) Initial charge-discharge curves at 0.1 A g^{-1} for the different electrode compositions as displayed on the top of each graph.

6.4 Conclusions

In conclusion, Co-Sn solid-solution NPs with average size in the 6-10 nm range were synthesized via a simple one pot colloidal-based approach. The Co_xSn NP composition was adjusted, $1.3 \leq x \leq 0.3$, by tuning the ratio of the initial precursors. The low synthesis temperature favoured the nucleation of Sn NPs and the subsequent inclusion of Co to the Sn lattice, forming a solid solution with the Sn crystal phase, instead of an intermetallic compound. The same strategy could be used to produce a much more extended range of Co-Sn compositions. Co-Sn NPs presented a Sn-rich surface after exposure to air. These Co-Sn solid solutions were tested as anode materials in LIBs on a half-cell battery system. Among the different compositions tested, $Co_{0.9}Sn$ and $Co_{0.7}Sn$ NPs provided the best performance, with a charge-discharge capacity above 1500 mAh g^{-1} at a current density of 0.2 A g^{-1} after 220 cycles and up to 800 mAh g^{-1} at 1.0 A g^{-1} after 400 cycles in the range 0-3.0 V. When testing in the range 0-1.5 V, these two electrode delivered an average of 360 mAh g^{-1} at 0.5 A g^{-1}. These values were larger than that of graphite currently used in commercial devices and larger than the theoretical maximum for Co-Sn alloys and even for pure Sn. Through the kinetic analysis of

$Co_{0.9}Sn$ NPs by the CV measurement, we found these charge-discharge capacities to include a very large pseudocapacitive contribution, up to 81% at a sweep rate of 1 mV s^{-1}, which we related to the small size of the particles.

6.5 References

1 C. M. Park, J. H. Kim, H. Kim and H. J. Sohn, *Chem. Soc. Rev.*, 2010, **39**, 3115–3141.

2 M. N. Obrovac and V. L. Chevrier, *Chem. Rev.*, 2014, **114**, 11444–11502.

3 R. Marom, S. F. Amalraj, N. Leifer, D. Jacob and D. Aurbach, *J. Mater. Chem.*, 2011, **21**, 9938–9954.

4 P. G. Bruce, B. Scrosati and J. M. Tarascon, *Angew. Chemie - Int. Ed.*, 2008, **47**, 2930–2946.

5 L. X. Ding, G. R. Li, Z. L. Wang, Z. Q. Liu, H. Liu and Y. X. Tong, *Chem. - A Eur. J.*, 2012, **18**, 8386–8391.

6 H. Tian, F. Xin, X. Wang, W. He and W. Han, *J. Mater.*, 2015, **1**, 153–169.

7 B. Wang, B. Luo, X. Li and L. Zhi, *Mater. Today*, 2012, **15**, 544–552.

8 C. K. Chan, R. N. Patel, M. J. O'Connell, B. A. Korgel and Y. Cui, *ACS Nano*, 2010, **4**, 1443–1450.

9 H. Ying and W. Q. Han, *Adv. Sci.*, 2017, **4**, 1700298.

10 N. Nitta, F. Wu, J. T. Lee and G. Yushin, *Mater. Today*, 2015, **18**, 252–264.

11 J. B. Goodenough and K. S. Park, *J. Am. Chem. Soc.*, 2013, **135**, 1167–1176.

12 M. R. Palacín, *Chem. Soc. Rev.*, 2009, **38**, 2565–2575.

13 M. F. Oszajca, M. I. Bodnarchuk and M. V. Kovalenko, *Chem. Mater.*, 2014, **26**, 5422–5432.

14 D. wei ZHANG, C. ge YANG, J. DAI, J. wu WEN, L. WANG and C. hua CHEN, *Trans. Nonferrous Met. Soc. China (English Ed.*, 2009, **19**, 1489–1493.

15 J. Liu, Y. Wen, P. A. Van Aken, J. Maier and Y. Yu, *Nano Lett.*, 2014, **14**, 6387–6392.

16 X. Fan, P. Dou, A. Jiang, D. Ma and X. Xu, *ACS Appl. Mater. Interfaces*, 2014, **6**, 22282–22288.

17 M. Uysal, T. Cetinkaya, A. Alp and H. Akbulut, *J. Alloys Compd.*, 2015, **645**, 235–242.

18 N. Tamura, Y. Kato, A. Mikami, M. Kamino, S. Matsuta and S. Fujitani, *J. Electrochem. Soc.*, 2006, **153**, A1626.

19 Z. Du and S. Zhang, *J. Phys. Chem. C*, 2011, **115**, 23603–23609.

20 C. M. Ionica-Bousquet, P. E. Lippens, L. Aldon, J. Olivier-Fourcade and J. C. Jumas, *Chem. Mater.*, 2006, **18**, 6442–6447.

21 G. O. Park, J. Yoon, J. K. Shon, Y. S. Choi, J. G. Won, S. Bin Park, K. H. Kim, H. Kim,

W. S. Yoon and J. M. Kim, *Adv. Funct. Mater.*, 2016, **26**, 2800–2808.

22 B. O. Jang, S. H. Park and W. J. Lee, *J. Alloys Compd.*, 2013, **574**, 325–330.

23 J. R. González, F. Nacimiento, R. Alcántara, G. F. Ortiz and J. L. Tirado, *CrystEngComm*, 2013, **15**, 9196–9202.

24 R. Gnanamuthu, Y. N. Jo and C. W. Lee, *J. Alloys Compd.*, 2013, **564**, 95–99.

25 G. Ferrara, C. Arbizzani, L. Damen, M. Guidotti, M. Lazzari, F. G. Vergottini, R. Inguanta, S. Piazza, C. Sunseri and M. Mastragostino, *J. Power Sources*, 2012, **211**, 103–107.

26 J. He, H. Zhao, J. Wang, J. Wang and J. Chen, *J. Alloys Compd.*, 2010, **508**, 629–635.

27 J. Shin, W.-H. Ryu, K.-S. Park and I.-D. Kim, *ACS Nano*, 2013, **7**, 7330–7341.

28 J. Zhang and Y. Xia, *J. Electrochem. Soc.*, 2006, **153**, A1466.

29 S. Wang, M. He, M. Walter, F. Krumeich, K. V. Kravchyk and M. V. Kovalenko, *Nanoscale*, 2018, **10**, 6827–6831.

30 M. Walter, S. Doswald, F. Krumeich, M. He, R. Widmer, N. P. Stadie and M. V. Kovalenko, *Nanoscale*, 2018, **10**, 3777–3783.

31 X. L. Wang, W. Q. Han, J. Chen and J. Graetz, *ACS Appl. Mater. Interfaces*, 2010, **2**, 1548–1551.

32 L. O. Vogt and C. Villevieille, *J. Mater. Chem. A*, 2017, **5**, 3865–3874.

33 W. X. Lei, Y. Pan, Y. C. Zhou, W. Zhou, M. L. Peng and Z. S. Ma, *RSC Adv.*, 2014, **4**, 3233–3237.

34 Y. M. Lin, P. R. Abel, A. Gupta, J. B. Goodenough, A. Heller and C. B. Mullins, *ACS Appl. Mater. Interfaces*, 2013, **5**, 8273–8277.

35 Z. Liu, T. Song and U. Paik, *J. Mater. Chem. A*, 2018, **6**, 8159–8193.

36 M. Walter, S. Doswald and M. V. Kovalenko, *J. Mater. Chem. A*, 2016, **4**, 7053–7059.

37 M. He, M. Walter, K. V. Kravchyk, R. Erni, R. Widmer and M. V. Kovalenko, *Nanoscale*, 2015, **7**, 455–459.

38 J. Zhu, D. Wang, T. Liu and C. Guo, *Electrochim. Acta*, 2014, **125**, 347–353.

39 X. Liu, J. Xie, H. Zhao, P. Lv, K. Wang, Z. Feng and K. Świerczek, *Solid State Ionics*, 2015, **269**, 86–92.

40 F. Nacimiento, P. Lavela, J. L. Tirado and J. M. Jiménez-Mateos, *J. Solid State Electrochem.*, 2012, **16**, 953–962.

41 S. Il Lee, S. Yoon, C. M. Park, J. M. Lee, H. Kim, D. Im, S. G. Doo and H. J. Sohn, *Electrochim. Acta*, 2008, **54**, 364–369.

42 P. Chen, L. Guo and Y. Wang, *J. Power Sources*, 2013, **222**, 526–532.

43 H.-S. Kim, J. B. Cook, S. H. Tolbert and B. Dunn, *J. Electrochem. Soc.*, 2015, **162**, A5083–A5090.

44 V. Augustyn, P. Simon and B. Dunn, *Energy Environ. Sci.*, 2014, **7**, 1597–1614.

45 T. Brezesinski, J. Wang, S. H. Tolbert and B. Dunn, *Nat. Mater.*, 2010, **9**, 146–151.

46 L. Yang, X. Li, S. He, G. Du, X. Yu, J. Liu, Q. Gao, R. Hu and M. Zhu, *J. Mater. Chem. A*, 2016, **4**, 10842–10849.

47 H. Fjellvåg, A. Kjekshus, R. Stomberg, R. Zingales, I. Vikholm, F. Urso, J. Weidlein and R. A. Zingaro, *Acta Chem. Scand.*, 1986, **40a**, 23–30.

48 M. He, L. Protesescu, R. Caputo, F. Krumeich and M. V. Kovalenko, *Chem. Mater.*, 2015, **27**, 635–647.

49 J. Li, Z. Luo, Y. Zuo, J. Liu, T. Zhang, P. Tang, J. Arbiol, J. Llorca and A. Cabot, *Appl. Catal. B Environ.*, 2018, **234**, 10–18.

50 Y. Liu, X. Liu, Q. Feng, D. He, L. Zhang, C. Lian, R. Shen, G. Zhao, Y. Ji, D. Wang, G. Zhou and Y. Li, *Adv. Mater.*, 2016, **28**, 4747–4754.

51 C. H. Cui, X. J. Liu, H. H. Li, M. R. Gao, H. W. Liang, H. Bin Yao and S. H. Yu, *ChemCatChem*, 2012, **4**, 1560–1563.

52 N. Mahmood, C. Zhang, F. Liu, J. Zhu and Y. Hou, *ACS Nano*, 2013, **7**, 10307–10318.

53 C. Lupu, J. G. Mao, J. W. Rabalais, A. M. Guloy and J. W. Richardson, *Inorg. Chem.*, 2003, **42**, 3765–3771.

54 K. Kravchyk, L. Protesescu, M. I. Bodnarchuk, F. Krumeich, M. Yarema, M. Walter, C. Guntlin and M. V. Kovalenko, *J. Am. Chem. Soc.*, 2013, **135**, 4199–4202.

55 R. Hu, Y. Ouyang, T. Liang, H. Wang, J. Liu, J. Chen, C. Yang, L. Yang and M. Zhu, *Adv. Mater.*, 2017, **29**, 1605006.

56 Y. He, A. Li, C. Dong, C. Li and L. Xu, *Chem. - A Eur. J.*, 2017, **23**, 13724–13733.

57 J. Qin, X. Zhang, N. Zhao, C. Shi, E. Liu, J. Li and C. He, *RSC Adv.*, 2014, **4**, 49247–49256.

58 J. Qin, D. Liu, X. Zhang, N. Zhao, C. Shi, E. Z. Liu, F. He, L. Ma, Q. Li, J. Li and C. He, *Nanoscale*, 2017, **9**, 15856–15864.

59 Z. Wang, D. Wang, S. Luo, S. Bao, Y. Liu, X. Qi, C. He, C. Shi and N. Zhao, *New J. Chem.*, 2016, **41**, 393–402.

60 C. Chen, Y. Wen, X. Hu, X. Ji, M. Yan, L. Mai, P. Hu, B. Shan and Y. Huang, *Nat. Commun.*, 2015, **6**, 6929.

61 T.-C. Liu, *J. Electrochem. Soc.*, 1998, **145**, 1882.

62 X. Xu, S. Ji, M. Gu and J. Liu, *ACS Appl. Mater. Interfaces*, 2015, **7**, 20957–20964.

63 X. Xu, J. Liu, J. Liu, L. Ouyang, R. Hu, H. Wang, L. Yang and M. Zhu, *Adv. Funct. Mater.*, 2018, **28**, 1707573.

Conclusion

In this thesis, we developed new bottom-up production methods, primarily of colloidal alloy NPs and their electrochemical characterization with significantly enhanced performances for the field of energy conversion and storage. As for the MOR in alkaline media, the highlight is the development of monodisperse NPs towards significantly improved activities and durability, on the one hand, with alloy effect with new element, and on the other hand, with a further accurate control over facets of the produced NPs. For the energy storage area, Sn-based NPs with tuned compositions were assembled to test its Li-ion and/or Na-ion insertion/extraction as rechargeable batteries, and the pseudocapacitive study was conducted as well. The main conclusions reached are:

1) Colloidal Ni polyhedral NCs (16 ± 2 nm) were synthesized and tested as electrodes for methanol electrooxidation. The $Ni(OH)_2 \leftrightarrow NiOOH$ redox reaction rate was first order with the KOH concentration. The surface coverage of active species was much higher in electrodes based on polyhedral Ni NCs than in spherical ones. On the other hand, the rate limiting diffusion coefficient was higher in electrodes based on polyhedral NCs. Electrodes based on Ni polyhedral NCs displayed impressive current densities (59.4 mA cm^{-2}) and mass activities (2016 mA mg^{-1}) at 0.6 V *vs.* Hg/HgO in the presence of 1.0 M methanol and 1.0 M KOH, which corresponds to a twofold increase over electrodes based on spherical Ni NCs and over most previous Ni-based electrocatalyts previously reported.

2) We developed a new synthetic route to produce NiSn intermetallic NPs with narrow size distributions. In addition, the composition of the obtained NPs could be tuned simply by adjusting the precursor ration. These NPs exhibited excellent performance for MOR in alkaline solution. Ni-rich NiSn-based electrocatalysts displayed slightly improved performances than Ni-based electrocatalysts, especially the stability.

3) The NiSn colloidal synthetic techniques could be extended to produce ternary Ni-Co-Sn NPs with tuned composition over the entire range ($0 \leq x \leq 3$). Out of the optimized composition with small amounts of Co into the structure, $Ni_{2.5}Co_{0.5}Sn_2$, showed a current density of 65.5 mA cm^{-2} and a mass current density of 1050 mA mg^{-1} at 0.6 V *vs.* Hg/HgO for the MOR in 1.0 M KOH containing 1.0 M methanol. In any case, the presence of Sn was found to be essential to improve stability with respect to elemental Ni, although Sn was observed to slowly dissolve in the presence of KOH. Overall, the excellent activity and stability towards the MOR of ternary $Ni_{3-x}Co_xSn_2$ NPs suggested them to be attractive anode materials for DMFCs.

4) Ni_xSn NPs with tuned composition ($0.6 \leq x \leq 1.9$) displayed excellent performance as anode material in LIBs and SIBs. Among the different compositions tested, best performances toward Li^+ ion and Na^+ ion insertion were obtained for $Ni_{0.9}Sn$ NP-based electrodes. This optimized cycling charge-discharge performance for LIBs provided 980 mAh g^{-1} at 0.2 A g^{-1} after 340 cycles. Additionally, $Ni_{0.9}Sn$ NP-based electrodes were tested in Na^+-ion half cells, exhibiting 160 mAh g^{-1} over 120 cycles at 0.1 A g^{-1}. From CV measurements at different current rates, it was found that the charging process was both capacitive and diffusion controlled, while the capacitive contribution was dominant in both LIBs and SIBs. The pseudocapacitive charge-storage accounted for a high portion of the whole energy storage capacity, which was associated to the small size and the composition of the Ni_xSn NPs used.

5) Co-Sn solid-solution NPs with average size in the 6-10 nm range were synthesized via a simple one pot colloidal-based approach. The Co_xSn ($0.3 \leq x \leq 1.3$) NP composition could be adjusted by tuning the ratio of the initial precursors. The low synthesis temperature favoured the nucleation of Sn NPs and the subsequent inclusion of Co to the Sn lattice, forming a solid solution with the Sn crystal phase, instead of an intermetallic compound. Co-Sn solid solutions were tested as anode materials in LIBs on a half-cell battery system. Among the different compositions tested, $Co_{0.9}Sn$ and $Co_{0.7}Sn$ NPs provided the best performance, with a charge-discharge capacity above 1500 mAh g^{-1} at a current density of 0.2 A g^{-1} after 220 cycles and up to 800 mAh g^{-1} at 1.0 A g^{-1} after 400 cycles. These values were larger than that of graphite currently used in commercial devices and larger than the theoretical maximum for Co-Sn alloys and even for pure Sn. Through the kinetic analysis of $Co_{0.9}Sn$ NPs by the CV measurement, we found these charge-discharge capacities to include a very large pseudocapacitive contribution, up to 81% at a sweep rate of 1 mV s^{-1}, which we related to the small size of the particles.

Overall, different strategies toward improving the electrochemical performance for non-precious alloy NPs produced from bottom-up engineering were developed in this thesis. Additionally, it was proven that the solution-processed synthesis approach is simple, low-cost, scale-up and also compatible with control over the composition, morphology and other parameters for the optimization of the application as anode materials for the DMFCs, LIBs and SIBs.

Perspectives

One of the "rules" behind the modern science is that *the more we discovered, the more questions we have*. This is true for the work presented in this thesis as well, and in this final text I will try to contemplate on *where and how to go from here* based on *what has been achieved* in this project.

While the bottom-up engineering of electrochemical applications is a well-suited approach to reach high efficiencies, we still face critical challenges. As far as I am concerned, there is still a long way to continue based on the results I presented here.

To improve the performance of the methanol electrooxidation in alkaline media and better understand its mechanism, there are four main research directions to follow up:

i) Enhance the alloy effect. The NPs could be alloyed with new element, and the composition could be tuned as well. In addition, the obtained NPs could be supported with carbon materials, MOF etc.

ii) Control the morphologies of these NPs. Specific facets, highly porous/branched structure, core-shell, heterojunctions could be introduced.

iii) More advanced electrochemical characterization. *In-situ* spectroscopies including UV-vis, Raman, EPR and DEMS would advantageous to study the electrochemical interface, achieving a deep insight into the relationship between physico-chemical and electronic properties of the interfaces and electrochemical performance.

iv) Comprehensive DFT calculations including all the reaction steps and the proper alloy composition under reaction conditions would be required to evaluate the exact MOR mechanism.

For Sn-based anode electrode in LIBs and SIBs, three main tasks should be further pursuit.

i) To improve the batteries performance, controlling the size over the NiSn, CoSn NPs and supporting with carbon materials, MOF etc would be a plus.

ii) Other Sn-based alloys. FeSn, CuSn alloy NPs should be investigated.

iii) In-situ characterization of ion intercalation would be extremely helpful to futher optimize the intercalating materials.

Nothing in life is to be feared, it is only to be understood. Now is the time to understand more, so that we may fear less.

— *Marie Curie*

Curriculum Vitae

Junshan Li
Gender: Male
Date of birth: 28/08/1986
Birthplace: Sichuan, P. R. China
Nationality: Chinese
Tel.: +34 602540354 (Spain) / +86 18328586570 (China)
Present Address: Sant Marti, Barcelona, Spain
E-mail: lijunshan@foxmail.com / junshanli@irec.cat
ORCID: 0000-0002-1482-1972
Researcher ID: A-7834-2019
Scopus ID: 57201690175

Research Interests

Methanol oxidation reaction, colloidal synthesis, electrochemistry, lithium/sodium ion batteries, solid-state chemistry, materials science, energy storage and conversion

Education Background

2016.9- Now University of Barcelona
Catalonia Institute for Energy Research-IREC Barcelona, Spain
PhD candidate in *Nanoscience* program
Supervisor: Prof. Andreu Cabot
Research project: Ni- and Sn-based colloidal nanoparticles for electrochemical energy technologies.

2011.8-2013.11 University of Oslo Oslo, Norway
M.Sc. in Materials, Energy and Nanotechnology
Qualification Awarded: Master's Degree of Science
Thesis: Ruddlessden-Popper type phases in the Ln-Sr-Fe-O (Ln = La, Nd; n = 3) system-synthesis & characterization
Supervisor: Prof. Helmer Fjellvåg & Prof. Anja Olafson Sjåstad

2006.9-2010.7 Southwest University of Science and Technology Mianyang, China
B.Sc. in Materials Science and Engineering
Qualification Awarded: Graduation Certificate & Bachelor's Degree in Engineering
Thesis: Preparation and Characteristics of BZT-xBCT non-Pb Piezoelectric Ceramics
Supervisor: Prof. Linhong Cao

Working Experience

2014.2- 2016.3 Chengdu Hongming Electronics Co., Ltd Chengdu, China
Position title: Assistant to chief of Quality Control section
Responsibility: specifically, Murata manufacturing group transferred one product line (PTC thermistor pills for motor starters) to Hongming. For the first several months, I was responsible for the technique/engineering work as well as some experiments, and later especially for the quality control (QC).

2010.7-2011.7 Wuxi Murata Electronics Co., Ltd Wuxi, China
Position title: Assistant Engineer
Responsibility: In charge of *Electrode Printing, Chip Pressing and Cutting* in process of ***Multi-Layer Ceramic Capacitors (MLCCs)***, such as setting up and improving processing technique, improving product quality, increasing productivity, failure analysis, assessment of new products and cost down *etc*.

Professional Skills

Software: GSAS & Topas (Rietveld refinement), Diamond, FindIt, EVA, Origin, Office, JMP
Instrument: TEM, FT-IR, (Synchrotron Radiation) XRD, TGA-DSC, SEM-EDS, MS, Cerimetric titration, MPMS, PPMS, SQUID, Autolab
Language: Chinese (mother tongue) & English (fluent) & Japanese (basic)
Other skills: Driving

Conference/Seminar

2019.03.31-2019.04.05	MATRAC 2 School 2019: Application of Neutrons and Synchrotron Radiation in Materials Science with special focus on Fundamental Aspects of Materials		
	Poster contribution		Munich, Germany
2019.03.11-2019.03.15	6th International Conference on Multifunctional, Hybrid and Nanomaterials		
	Poster contribution		Sitges, Spain
2018.07.08-2018.07.14	FEMS Junior EUROMAT 2018	*Oral presentation*	Budapest, Hungary
2017.07.17-2017.07.21	WE-Heraeus Physics School		Badhonef, Gemany
2013.01.17-2013.01.19	SMN annual Winter Seminar		Oslo, Norway
2012.02.28-2012.02.29	NAFUMA strategy meeting		Oslo, Norway

Internships

2016.4-2016.6	University of Cadiz (Research stay)	Cadiz, Spain
2010.3-2010.4	Sichuan JinChuan Electronic Devices Co. Ltd	Yibing, China

Course Highlights

Master's level: Synthesis of inorganic materials, Condensed matter physics, Advanced inorganic chemistry, Energy physics-solar cells, Advanced structural chemistry & Nano chemistry.
Bachelor's level: Semiconductor physics, Solid-state physics, Dielectric physics, Fundamentals of materials science, Advanced ceramics, Piezoelectric and ferroelectric materials, Physics of thin films, Fundamentals of Quantum mechanics, Inorganic and analytic chemistry, Technology of materials measurement and analysis, Mordern electronic components etc.

Honors/Awards/Felloships

2016.9	CSC scholarship (China Scholarship Council)	Awarded by Chinese government
2010.6	Outstanding graduate of the School of Materials Science and Engineering	Awarded by SWUST
2007.9	Outstanding student of Academic grades	Awarded by SWUST

References

Prof. Andreu Cabot, *UB & IREC*, Spain, acabot@irec.cat
Prof. Helmer Fjellvåg, *UiO*, Norway helmer.fjellvag@kjemi.uio.no
Prof. Anja Olafson Sjåstad, *UiO*, Norway a.o.sjastad@kjemi.uio.no
Prof. Linhong Cao, *SWUST*, China hyclh@yeah.net
Prof. Hongtao Yu, *SWUST*, China yuhongtao@swust.edu.cn

Publications

1. **Junshan Li**, Yong Zuo, Junfeng Liu, Xiaoting Yu, Ruifeng Du, Ting Zhang, Maria F. Infante-Carrió, Pengyi Tang, Jordi Arbiol, Jordi Llorca, Zhishan Luo, Andreu Cabota. Superior Methanol Electrooxidation Performance of (110)-Faceted Nickel Polyhedral Nanocrystals. **Submitted (under review).**
2. **Junshan Li**, Xijun Xu, Zhishan Luo, Chaoqi Zhang, Xiaoting Yu, Yong Zuo, Ting Zhang, Pengyi Tang, Jordi Arbiol, Jordi Llorca, Jun Liu, Andreu Cabota. Compositionally tuned Ni_xSn alloys as anode materials for lithium-ion and sodium-ion batteries with a high pseudocapacitive contribution. Electrochim. Acta, 2019, 304, 246–254.
3. Yong Zuo, Yongpeng Liu, **Junshan Li**, Ruifeng Du, Xiaoting Yu, Ting Zhang, Jordi Arbiol, Jordi Llorca, Kevin Sivula, Néstor Guijarro, Andreu Cabot. Solution-processed ultrathin SnS_2-Pt

nanoplates for photoelectrochemical water splitting. ACS Appl. Mater. Interfaces, 2019, 11, 6918–6926.

4. **Junshan Li**, Xijun Xu, Zhishan Luo, Chaoqi Zhang, Ting Zhang, Maria Francisca Infante Carrió, Jordi Arbiol, Jordi Llorca, Jun Liu, Andreu Cabot. Co-Sn nanocrystalline solid solutions as anode materials in lithium-ion batteries with high pseudocapacitive contribution. ChemSusChem. 2019, 12, 1451–1458.
5. Mengyao Li, Yu Liu, Yu Zhang, Yong Zuo, **Junshan Li**, Khak Ho Lim, Doris Cadavid, Ka Ming Ng, Andreu Cabot. Crystallographically textured SnSe nanomaterials produced from the liquid phase sintering of nanocrystals. Dalton Trans. 2019, 48, 3641-3647.
6. Junfeng Liu, Zhishan Luo, **Junshan Li**, Xiaoting Yu, Jordi Llorca, Déspina Nasiou, Jordi Arbiol, Michaela Meyns, Andreu Cabot. Graphene-supported palladium phosphide PdP_2 nanocrystals for ethanol electrooxidation. Appl. Catal. B Environ., 2019, 242, 258–266.
7. **Junshan Li**, Yong Zuo, Ting Zhang, Chaoqi Zhang, Ruifeng Du, Junfeng Liu, Jordi Arbiol, Jordi Llorca, Zhishan Luo, Andreu Cabot. Colloidal Ni-Co-Sn Nanoparticles as Efficient Electrocatalysts for the Methanol Oxidation Reaction. J. Mater. Chem. A, 2018, 6, 22915-22924.
8. Junfeng Liu, Zhenxing Wang, Jeremy David, Jordi Llorca, **Junshan Li**, Xiaoting Yu, Alexey Shavel, Jordi Arbiol, Michaela Meyns, Andreu Cabot. Colloidal $Ni_{2-x}Co_xP$ nanocrystals for the hydrogen evolution reaction. J. Mater. Chem. A, 2018, 6, 11453-11462.
9. **Junshan Li**, Zhishan Luo, Yong Zuo, Junfeng Liu, Ting Zhang, Pengyi Tang, Jordi Arbiol, Jordi Llorca, Andreu Cabot**.** NiSn Bimetallic Nanoparticles as Stable Electrocatalysts for Methanol Oxidation Reaction. Appl. Catal. B Environ., 2018, 234, 10–18.
10. Ying-xiang Li, Zhen-jun Qin, Bin Tang, Shu-ren Zhang, Geng Chang, Hao Li, He-tuo Chen, Han Yang**, Junshan Li**. Microwave Dielectric Properties of TiO_2-Added $Li_2ZnTi_3O_8$ Ceramics Doped with Li_2O-Al_2O_3-B_2O_3 Glass. J. Electron. Mater., 2014, 44, 281–286.
11. Yingxiang Li, Hao Li, **Junshan Li**, Bin Tang, Shuren Zhang, Hetuo Chen, Ya Wei. Effect of TiO_2 Ratio on the Phase and Microwave Dielectric Properties of $Li_2ZnTi_{3+x}O_{8+2x}$Ceramics. Journal of Electronic Materials. J. Electron. Mater., 2014, 43, 1107–1111.
12. Yingxiang Li, **Junshan Li**, Bin Tang, Shuren Zhang, Hao Li, Zhenjun Qin, Hetuo Chen, Han Yang, Hong Tu. Low temperature sintering and dielectric properties of $Li_2ZnTi_3O_8$-TiO_2 composite ceramics doped with CaO-B_2O_3-SiO_2 glass. J. Mater. Sci. Mater. Electron., 2014, 25, 2780–2785.

Other contributions

Reviewer for Applied catalysis B: Environmental (Nov. 2018).

Hobbies

Hiking, biking, travelling, history, documentary, table tennis etc.

QR code on WeChat

QR code on Linkedln

To be good is no longer enough — excellence, by definition, must go beyond that!

Nature 554, 403-404 (2018)

Annex

Applied Catalysis B: Environmental 234 (2018) 10–18

Contents lists available at ScienceDirect

Applied Catalysis B: Environmental

journal homepage: www.elsevier.com/locate/apcatb

NiSn bimetallic nanoparticles as stable electrocatalysts for methanol oxidation reaction

Junshan Li[a,b,1], Zhishan Luo[a,1], Yong Zuo[a,b], Junfeng Liu[a,b], Ting Zhang[c], Pengyi Tang[c], Jordi Arbiol[c,e], Jordi Llorca[d], Andreu Cabot[a,e,*]

[a] Catalonia Institute for Energy Research – IREC, Sant Adrià del Besòs, Barcelona 08930, Spain
[b] Departament d'Electronica, Universitat de Barcelona, 08028 Barcelona, Spain
[c] Catalan Institute of Nanoscience and Nanotechnology (ICN2), CSIC and BIST, Campus UAB, Bellaterra, 08193 Barcelona, Spain
[d] Institute of Energy Technologies, Department of Chemical Engineering and Barcelona Research Center in Multiscale Science and Engineering, Universitat Politècnica de Catalunya, EEBE, 08019 Barcelona, Spain
[e] ICREA, Pg. Lluís Companys 23, 08010 Barcelona, Spain

ARTICLE INFO

Keywords:
Electrocatalysis
Methanol oxidation
Colloidal synthesis
Bimetallic nanoparticles

ABSTRACT

Nickel is an excellent alternative catalyst to high cost Pt and Pt-group metals as anode material in direct methanol fuel cells. However, nickel presents a relatively low stability under operation conditions, even in alkaline media. In this work, a synthetic route to produce bimetallic NiSn nanoparticles (NPs) with tuned composition is presented. Through co-reduction of the two metals in the presence of appropriate surfactants, 3–5 nm NiSn NPs with tuned Ni/Sn ratios were produced. Such NPs were subsequently supported on carbon black and tested for methanol electro-oxidation in alkaline media. Among the different stoichiometries tested, the most Ni-rich alloy exhibited the highest electrocatalytic activity, with mass current density of 820 mA mg^{-1} at 0.70 V (vs. Hg/HgO). While this activity was comparable to that of pure nickel NPs, NiSn alloys showed highly improved stabilities over periods of 10,000 s at 0.70 V. We hypothesize this experimental fact to be associated to the collaborative oxidation of the byproducts of methanol which poison the Ni surface or to the prevention of the tight adsorption of these species on the Ni surface by modifying its surface chemistry or electronic density of states.

1. Introduction

Fuel cells have raised increasing interest as a high efficiency and environmental friendly energy conversion technology. Among the different cell architectures and fuels proposed, direct methanol fuel cells (DMFCs) are the best positioned toward widespread commercialization and the most viable alternative to lithium-ion batteries for portable applications [1,2]. Methanol provides numerous advantages as a fuel, including safe handling, storage and transportation, solubility in aqueous electrolytes, availability and potential generation from renewable energies, high power and energy density (6100 W h kg^{-1}) with high oxidation rates that do not require C–C bond breaking, low emissions and fast recharging and cell startup at low temperature [3,4]. However, a major drawback of this technology, currently delaying its extensive commercialization, is its high manufacturing cost, which is in large part related to the dependence on Pt-based electrocatalysts for both methanol oxidation at the anode and oxygen reduction at the cathode [1,5,6]. The development of Pt-free electrocatalysts is thus a key challenge to be urgently overcome for DMFCs to become cost-effective.

Nickel, a relatively abundant element in the earth's crust, is among the best candidate materials to replace Pt in the anode, where the methanol oxidation reaction (MOR) takes place. Ni [7–10] and Ni-based alloys reported to date, such as NiCu [11–14], NiFe [15], NiCo [16], NiMn [17] and NiTi [18,19] show excellent catalytic activities, but even in alkaline electrolytes, they lack of a satisfactory durability. Therefore, the exploration of novel Ni-based compounds presenting improved stabilities is required.

Among the possible alternative alloys, NiSn is a potentially excellent candidate for the MOR. Actually, Sn has been demonstrated to improve Pt performance in this reaction [20–22]. However, surprisingly, NiSn has yet to be tested as anode material in DMFCs. This anomaly is in part associated to the lack of reliable synthetic routes to produce NiSn alloys. Among the very few examples in the literature, Liu et al. produced porous Ni_3Sn_2 intermetallic microcages through a solvothermal method

* Corresponding author at: Catalonia Institute for Energy Research – IREC, Sant Adrià del Besòs, Barcelona 08930, Spain.
E-mail address: acabot@irec.cat (A. Cabot).
[1] These authors contributed equally to this work.

https://doi.org/10.1016/j.apcatb.2018.04.017
Received 2 February 2018; Received in revised form 30 March 2018; Accepted 10 April 2018
Available online 14 April 2018
0926-3373/

which were tested for lithium and sodium storage [23]. Recently, Liu et al. reported a colloidal synthesis approach that made use of a strong Brønsted base, n-butylithium, to produce Ni_3Sn_2 NPs for the semi-hydrogenation of alkynes [24].

To overcome these challenges, we present here a new synthetic route to produce NiSn NPs with controlled stoichiometry. We further demonstrate these NPs to show high electrocatalytic activities towards methanol electroxidation and at the same time significantly improved stabilities when compared with nickel.

2. Experimental section

2.1. Chemicals

Nickel(II) acetylacetonate ($Ni(acac)_2{\cdot}xH_2O$ (x ~ 2), 95%, Sigma-Aldrich), tin(II) acetate ($Sn(oac)_2$, 95%, Fluka), tri-*n*-octylphosphine (TOP, 97%, Strem), oleylamine (OAm, 80–90%, TCI), borane tert-butylamine complex (TBAB, 97%, Sigma-Aldrich), oleic acid (OAc, Sigma-Aldrich), hydrazine monohydrate (N_2H_4 64–65%, reagent grade, 98%, Sigma-Aldrich), Nafion (10 wt. %, perfluorinated ion-exchange resin, dispersion in water), methanol (anhydrous, 99.8%, Sigma-Aldrich), carbon black (CB, VULCAN XC72), potassium hydroxide (KOH, 85%, Sigma-Aldrich), acetonitrile (CH_3CN, extra dry, Fisher), trioctylphosphine oxide (TOPO, 99%, Sigma-Aldrich), diisobutylaluminium hydride solution (DIBAH, 1.0 M in tetrahydrofuran (THF), Aldrich), tin(II) chloride ($SnCl_2$, anhydrous, 98%, Strem), and lithium bis(trimethylsilyl)amide ($LiN(SiME_3)_2$, 97%, Aldrich) were used as received without any further purification. Chloroform, hexane, acetone, toluene, and ethanol were of analytical grade and purchased from various sources. MilliQ water was obtained from a PURELAB flex from ELGA. All the syntheses were performed using standard airless techniques: a vacuum/dry argon gas Schlenk line was used for the synthesis and an argon-filled glove-box was used for storing and dealing with sensitive chemicals.

2.2. Synthesis of NiSn NPs

In a typical synthesis, 7 ml OAm, 0.1 mmol $Ni(acac)_2$, 0.1 mmol $Sn(oac)_2$ and 0.15 ml OAc were loaded into a 25 ml three-necked flask and degassed under vacuum at 80 °C for 1 h while being strongly stirred using a magnetic bar. Afterward, a gentle flow of argon was introduced, and 1 ml of TOP was injected into the solution. Subsequently, the reaction flask was heated to 180 °C within 20 min, followed by quick injection of a solution containing 1 mmol TBAB in 1 ml degassed OAm. A visible color change, from light blue to black was observed immediately. The reaction was maintained at this temperature for 1 h before it was quenched using a water bath. NiSn NPs were collected by centrifuging and washing the solid product with acetone and chloroform 3 times. The as-prepared NPs were finally dispersed in chloroform and stored for their posterior use. NPs were colloidally stable in chloroform for over two months. Different nominal Ni/Sn ratios were used to prepare NPs with different stoichiometries following the same procedure above detailed.

2.3. Synthesis of Sn NPs

13 nm Sn NPs were produced according to the method developed by Kravchyk et al. [25]. Briefly, 16 ml OAm was loaded into a 25 ml three-necked flask and maintained under vacuum at 140 °C for 60 min under stirring. After cooling to 50 °C, 0.5 mmol $SnCl_2$ was added to the flask and kept under vacuum at 140 °C for 30 min. Then temperature was increased to 180 °C under argon and 2 ml of toluene containing 0.6 g of $LiN(SiME_3)_2$ was injected. Immediately afterward, 0.6 ml of a 1 M DIBAH solution in THF was also injected. Upon injection of DIBAH, the solution immediately turned dark brown. After 10 min reaction, the solution was cooled down using a water bath. Acetone was added to the final mixture and NPs were collected by centrifugation. The obtained precipitate was re-dispersed in hexane for further use.

2.4. Synthesis of Ni NPs

12 nm *fcc*-Ni NPs were prepared following the procedure described by Chen et al. [26]. In a typical synthesis, 1 mmol $Ni(acac)_2$, 7 ml OAm, 0.4 mmol TOP and 0.25 mmol TOPO were loaded in a three-neck flask and stirred under a gentle flow of argon. Temperature was raised to 130 °C and kept for 20 min. Then, the solution was quickly heated to 215 °C and maintained at this temperature for 45 min. Subsequently, the flask was cooled down to room temperature using a water bath. The black precipitate was separated through centrifugation after adding ethanol. NPs were re-dispersed and precipitated three times using hexane and ethanol as solvent and non-solvent, respectively. The product was finally dispersed in hexane.

2.5. Ligand removal

NiSn, Sn and Ni NPs dispersed in chloroform were precipitated through addition of ethanol and centrifugation. Then, they were dispersed in a mixture containing 28 ml acetonitrile and 0.8 ml hydrazine hydrate and stirred for 4 h. NPs were then collected by centrifugation and washed with acetonitrile for 3 times. Finally, the NiSn NPs were dried under vacuum.

2.6. Characterization

Powder X-ray diffraction (XRD) patterns were recorded from the as-synthesized NPs dropped on a Si(501) substrate on a Bruker AXS D8 Advance X-ray diffractometer with Ni-filtered (2 u m thickness) Cu K radiation (1.5106) operating at 40 kV and 40 mA. Specimens for transmission electron microscopy (TEM) characterization were prepared by drop casting the dispersions of NPs onto a 200 mesh Cu grids with ultrathin carbon and formvar support films. TEM analyses were carried out on a ZEISS LIBRA 120, operating at 120 kV. High-resolution TEM (HRTEM) and scanning TEM (STEM) studies were carried out using a field emission gun FEI Tecnai F20 microscope at 200 kV with a point-to-point resolution of 0.19 nm. High angle annular dark-field (HAADF) STEM was combined with electron energy loss spectroscopy (EELS) in the Tecnai microscope by using a GATAN QUANTUM filter. The composition of NPs was confirmed by scanning electron microscopy (SEM) on a ZEISS Auriga SEM with an energy dispersive X-ray spectroscopy (EDS) detector at 20 kV. Values were averaged from 3 measurements of each composition. X-ray photoelectron spectroscopy (XPS) was done on a SPECS system equipped with an Al anode XR50 source operating at 150 mW and a Phoibos 150 MCD-9 detector. The pressure in the analysis chamber was kept below 10^{-7} Pa. The area analyzed was about 2 mm × 2 mm. The pass energy of the hemispherical analyzer was set at 25 eV and the energy step was maintained at 1.0 eV. Data processing was performed with the Casa XPS program (Casa Software Ltd., UK). Binding energies were shifted according to the reference C 1s peak that was located at 284.8 eV. Fourier transform infrared spectrometer (FTIR) data were recorded on an Alpha Bruker FTIR spectrometer with a platinum attenuated total reflectance (ATR) single reflection module.

2.7. Electrochemical characterization

Electrochemical measurements were carried out at room temperature (25 ± 2 °C) in an electrochemical workstation (AutoLab, Metrohm). The three electrode system consisted of a counter electrode (Pt mesh), a working electrode (glassy carbon (GC) electrode with diameter of 5 mm) and a reference electrode (Hg/HgO). The Hg/HgO was placed in a salt bridge of 1.0 M KOH. 5 mg of NPs, 50 μL of 10 wt% Nafion solution together with 10 mg of CB were added to 1 ml ethanol

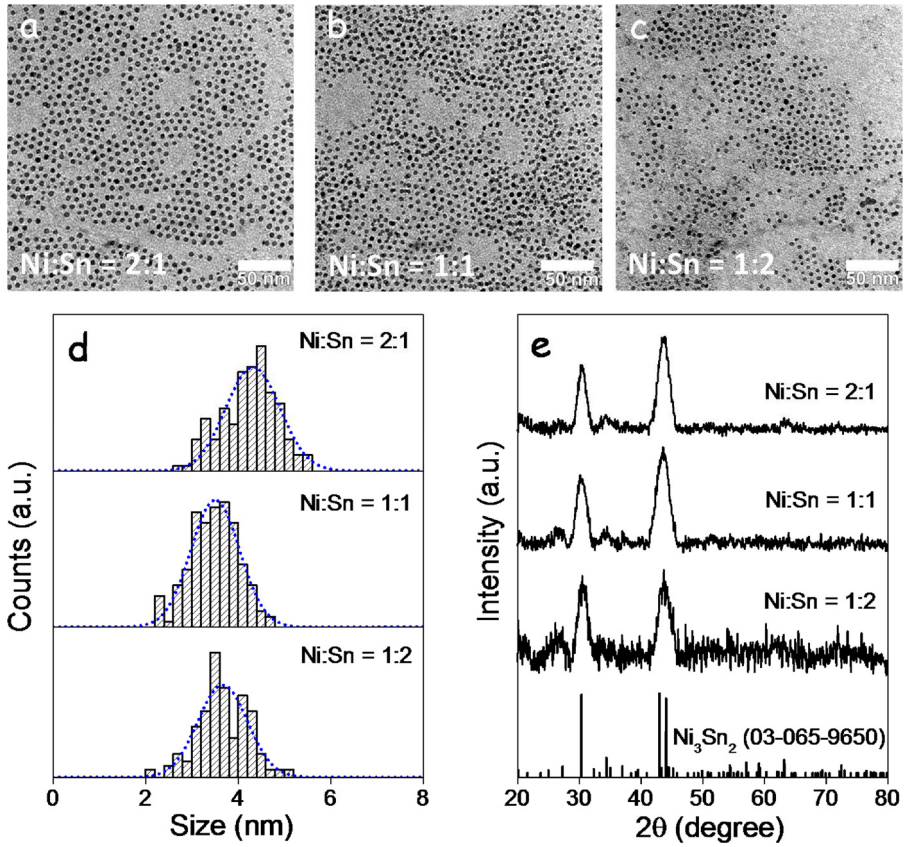

Fig. 1. (a–c) Representative TEM micrographs of NiSn NPs with different nominal Ni:Sn ratios: 2:1 (a); 1:1 (b); and 1:2 (c). (d) Corresponding size distribution histograms. (e) XRD patterns of NiSn NPs with the same nominal stoichiometries.

and 1 ml MilliQ water which was vigorously sonicated for 1 h to obtain a homogeneous solution. Then, 5 μL of the freshly prepared ink (around 0.012 mg catalyst) was evenly loaded onto the polished glassy carbon electrode and dried naturally in air at room temperature. All the measurements were performed in N_2-bubled 0.50 M KOH solution in the absence or presence of variable concentrations of methanol with magnetic bar stirring, except where noted. Current densities were calculated taking into account the geometric surface area of the GC electrode (0.196 cm^{-2}).

3. Results and discussion

A co-reduction strategy was developed to produce NiSn NPs with low size dispersion and tuned composition (see experimental section for details). Briefly, proper amounts of $Ni(acac)_2$ and $Sn(oac)_2$ were reduced at 180 °C and in the presence of OAc, OAm and TOP by injection of a TBAB/OAm solution. Fig. 1a–c shows representative TEM micrographs of the quasi-spherical NiSn NPs produced with three different nominal Ni:Sn ratios (2:1; 1:1; 1:2). The average size of the NPs measured by TEM analysis fluctuated in the range from 3.5 ± 0.5 nm to 4.2 ± 0.6 nm, depending on the nominal composition (Fig. 1d and Table 1). Fig. 1e displays the XRD patterns of the NiSn NPs produced following the above detailed procedure. As corresponding to small NPs, XRD patterns from all samples displayed broad diffraction peaks, which could be ascribed to the orthorhombic Ni_3Sn_2 or the monoclinic Ni_3Sn_4 crystal phases. Additional Ni_3Sn or even Ni or Sn phases could not be discarded from the XRD analysis. Previous works already reported the formation of these phases in the composition range here analyzed, 33–67% of each metal [27,28].

Extensive HRTEM and EELS analysis found all NiSn NPs to contain both elements, Ni and Sn, in a similar ratio within each sample. No independent Ni or Sn elemental NP was identified in any of the samples analyzed. Fig. 2a shows HRTEM micrographs of the NiSn (2:1) NPs that had been exposed to air. NiSn NPs had average sizes of ca. 7.2 nm and displayed a core-shell structure. The core, with a diameter of ca. 3.5 nm, was crystalline and its structure matched that of a Ni_3Sn_2 orthorhombic phase (space group = Pnma) with a = 7.110 Å, b = 5.210 Å, c = 8.230 Å (Fig. 2a). The shell was amorphous and it was attributed to an oxide layer formed during the NP exposure to the ambient atmosphere. STEM-HAADF micrographs and EELS chemical compositional maps revealed the NiSn (2:1) core to be Ni-rich and the shell to be Sn-rich (Fig. 2b). The same crystal phase and compositional organization was observed for NiSn (1:1) NPS. This composition inhomogeneity could be created during the synthesis due to a differential reduction rate of the two precursors, or during oxidation, being Sn atoms potentially more prone to react with ambient oxygen.

EDX analysis showed the composition on the NiSn NPs to match relatively well with the nominal Ni/Sn ratios (Table 1 and Fig. S4). Specifically Ni/Sn ratios of 1.7, 1.1 and 0.46 were obtained for NiSn NPs produced with nominal Ni:Sn stoichiometries 2:1; 1:1 and 1:2,

Table 1
Average particle size measured from TEM micrographs, summary of the atomic ratios of Ni to Sn nominally introduced and experimentally measured from EDX and XPS analysis, and ratio of the chemical states obtained from XPS measurements.

Catalysts	TEM average NP size (nm)	Ni/Sn molar ratio			Chemical states (XPS)	
		Nominal	EDX	XPS	Ni(0)/Ni (II)	Sn(0)/Sn (IV)
NiSn-2:1	4.2 ± 0.6	2	1.7	0.41	0.14	0.28
NiSn-1:1	3.5 ± 0.5	1	1.1	0.20	0.20	0.19
NiSn-1:2	3.7 ± 0.5	0.5	0.46	0.10	0.27	0.29

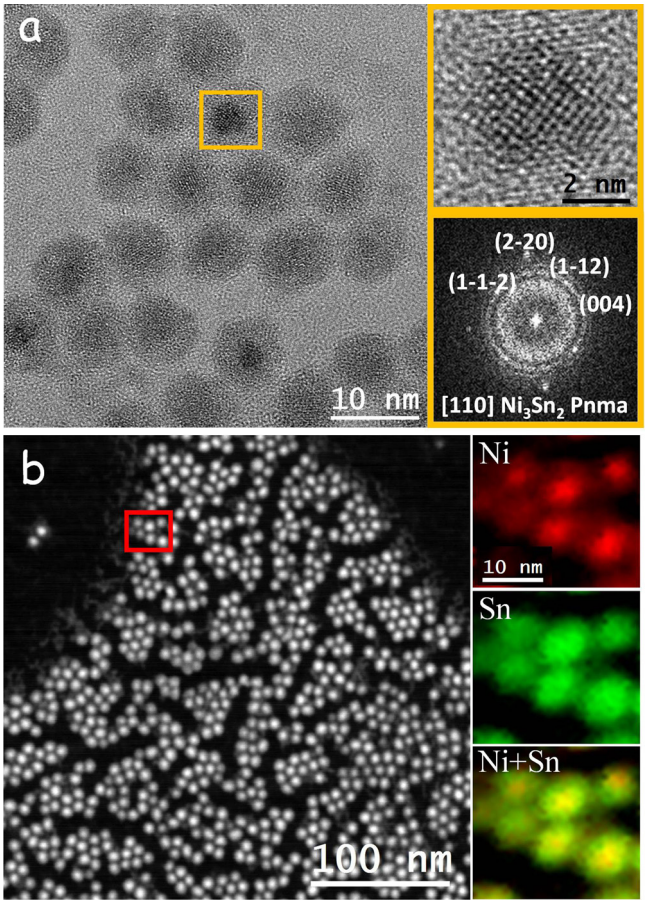

Fig. 2. (a) HRTEM micrograph of NiSn (2:1) NPs and detail of the yellow squared region with its corresponding power spectrum. Ni_3Sn_2 lattice fringe distances measured were 0.210 nm (2–20), 0.296 nm (-1-12) at 46° vs (2–20) and 0.204 nm (004) at 90° vs (2–20), which matched with the orthorhombic Ni_3Sn_2 phase visualized along its [110] zone axis. (b) STEM-HAADF micrographs and EELS elemental maps of several NiSn (2:1) NPs showing a Ni and Sn radial gradient. (For interpretation of the references to colour in this figure legend, the reader is referred to the web version of this article).

respectively.

XPS analysis was used to characterize the chemical environment of atoms at the surface of NiSn NCs that had been exposed to the ambient atmosphere. For these analyses, purified NiSn NPs with no surface ligands were used (see below for ligand removal details). XPS analysis confirmed the surface of these NPs to be Sn-rich and oxidized (Fig. 3).

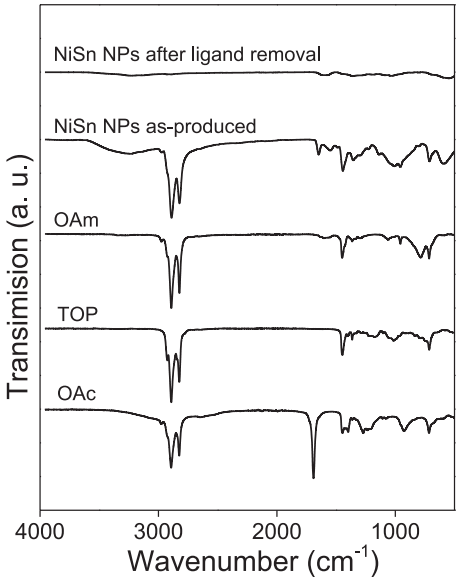

Fig. 4. FTIR spectra of OAm, OAc, TOP and NiSn (2:1) NPs as produced and after ligand removal.

The surface Ni/Sn ratios were 0.41, 0.20 and 0.10 for NiSn NPs produced with nominal Ni:Sn stoichiometries 2:1; 1:1 and 1:2, respectively. Ni $2p_{3/2}$ electronic states were found at binding energies of 856.3 eV, corresponding to a Ni^{2+} chemical environment, and 852.6 eV, which was associated to a Ni° state [29]. The Ni^{2+} oxidized component was clearly majoritarian, with a ratio over Ni°: $Ni°/Ni^{2+} = 0.14$ for the NiSn (2:1) sample. Similar ratios were obtained for NiSn NPs with other Ni/Sn nominal compositions, with an increase of the Ni° component with the Sn ratio (see Table 1). The main contribution to the Sn $3d_{5/2}$ electronic states were found at a binding energy of 486.8 eV, which was attributed to a Sn^{2+} or Sn^{4+} chemical environment [29]. A minor component was found at 484.7 eV, which was associated to metallic Sn. The ratio of the two chemical states was $Sn°/Sn^{2+/4+} = 0.28$ for the NiSn (2:1) NPs and fluctuated with the nominal composition of the samples (Table 1). This fluctuation may be associated to a different amount of time the samples were exposed to air before XPS analysis. Sn was more strongly affected by this experimental parameter as the NPs surface was rich in Sn and poor in Ni. Probably, the relative amount of Ni on the NP surface also decreased when increasing the Sn composition.

The presence of OAm, OAc and TOP in the reaction mixture was essential to produce monodisperse and colloidally stable NiSn NPs with the orthorhombic Ni_3Sn_2 crystal phase. Keeping all the synthetic

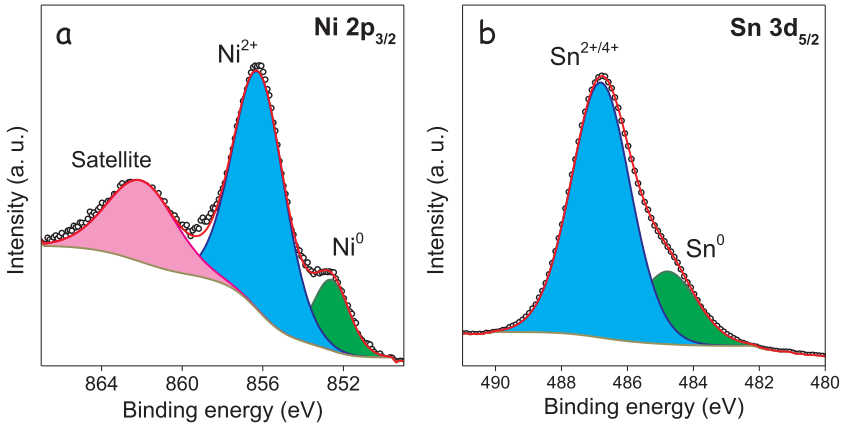

Fig. 3. XPS spectra of the Ni $2P_{3/2}$ region (a) and of the Sn $3P_{5/2}$ region (b) of NiSn (2:1) NPs.

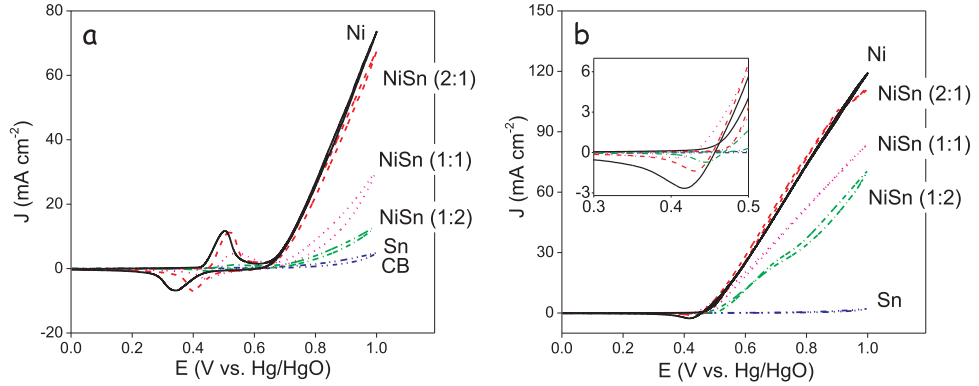

Fig. 5. (a) Cyclic voltammograms of Ni-Sn, Ni, Sn NPs in 0.50 M KOH solution at a scan rate of 50 mV s^{-1}. (b) Cyclic voltammograms of NiSn NPs, Ni NPs and Sn NPs for methanol electrooxidation in 0.50 M KOH containing 0.50 M methanol solution at a scan rate of 50 mV s^{-1}.

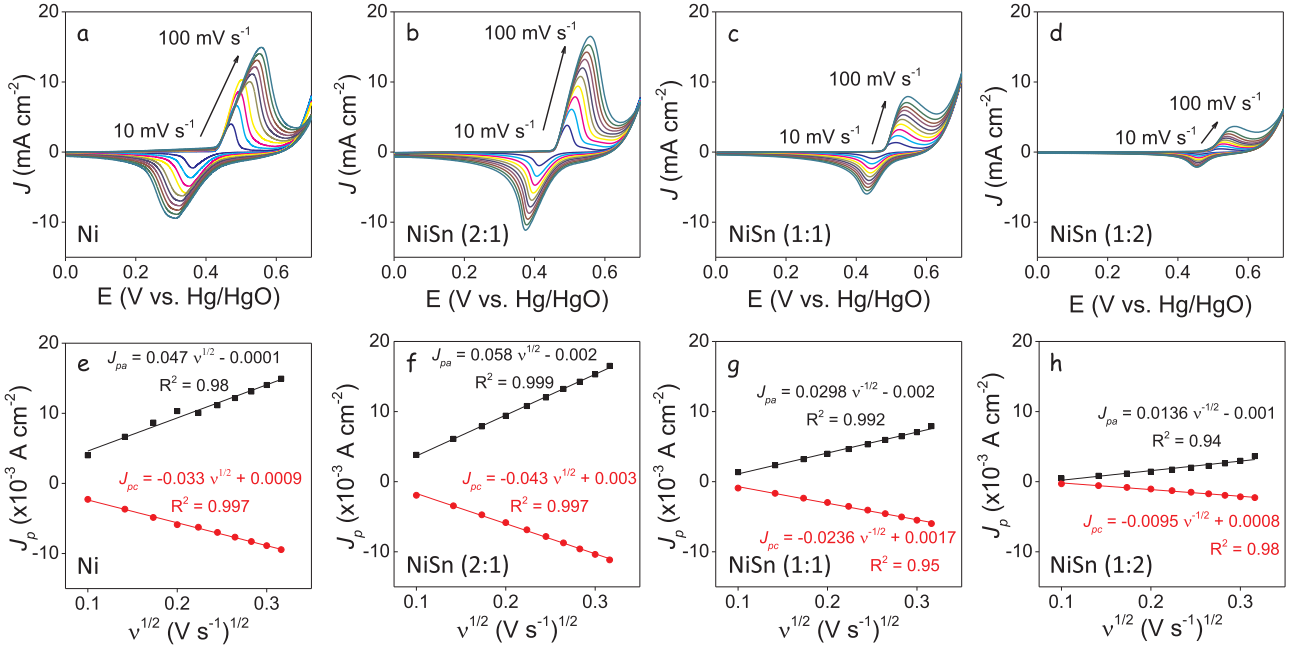

Fig. 6. (a–d) Cyclic voltammograms of Ni and NiSn electrocatalysts in 0.50 KOH at increasingly higher potentials sweep rates: 10, 20, 30, 40, 50, 60, 70, 80, 90, 100 mV s^{-1}. (e–h) linear fitting of the anodic and cathodic peak current densities to the square roots of the scan rates.

Table 2
Summary of the electrocatalytic performance.

Catalyst	J_{pa} mA cm^{-2}	J_{pc} mA cm^{-2}	$E_{1/2}$ V vs Hg/HgO	ΔE_p V	Γ mol cm^{-2}	D cm^2 s^{-1}
Ni	10.5	−6.8	0.47	0.190	2.5×10^{-7}	1.2×10^{-11}
NiSn (2:1)	10.8	−6.9	0.49	0.139	2.1×10^{-7}	1.9×10^{-11}
NiSn (1:1)	4.7	−3.5	0.50	0.090	1.1×10^{-7}	5.3×10^{-12}
NiSn (1:2)	1.7	−1.3	0.51	0.076	4.5×10^{-8}	1.0×10^{-13}

parameters constant, but removing OAc, large spherical aggregates of NiSn NPs with the Ni_3Sn_4 crystal phase were produced (Fig. S1). On the other hand, in the absence of TOP, NiSn NPs aggregated in chains and with the Ni_3Sn_4 crystal phase were obtained (Fig. S2).

However, the presence of organic ligands at the NP surface strongly limits both their ability to interact with the media and the charge transport between NPs and between NPs and surrounding materials. Thus, we removed the native organic ligands from the NiSn NP surface by suspending them in a mixture of acetonitrile and a small amount of hydrazine hydrate. The mixture was stirred for some hours and then the precipitated NPs were collected. Additional purification steps with acetonitrile were carried out to remove all the unbounded or loosely bond organics. FTIR analysis confirmed the absence of organic ligands at the NiSn NP surface after the ligand removal step, as observed from the disappearing of peaks at 2890 cm^{-1} and 2822 cm^{-1} that correspond to C—H stretching modes (Fig. 4).

Electrocatalysts were prepared by mixing NPs with CB and Nafion and supporting this composite onto a glassy carbon electrode (see experimental section for details). As reference materials, 12 nm Ni NPs and 13 nm Sn NPs produced following previously published synthetic routes (see experimental section for details) were used. Figs. S6 and S7 display representative TEM micrographs and the corresponding XRD patterns of these reference materials. Surface ligands of these NPs were removed following the same procedure used to displace ligands from

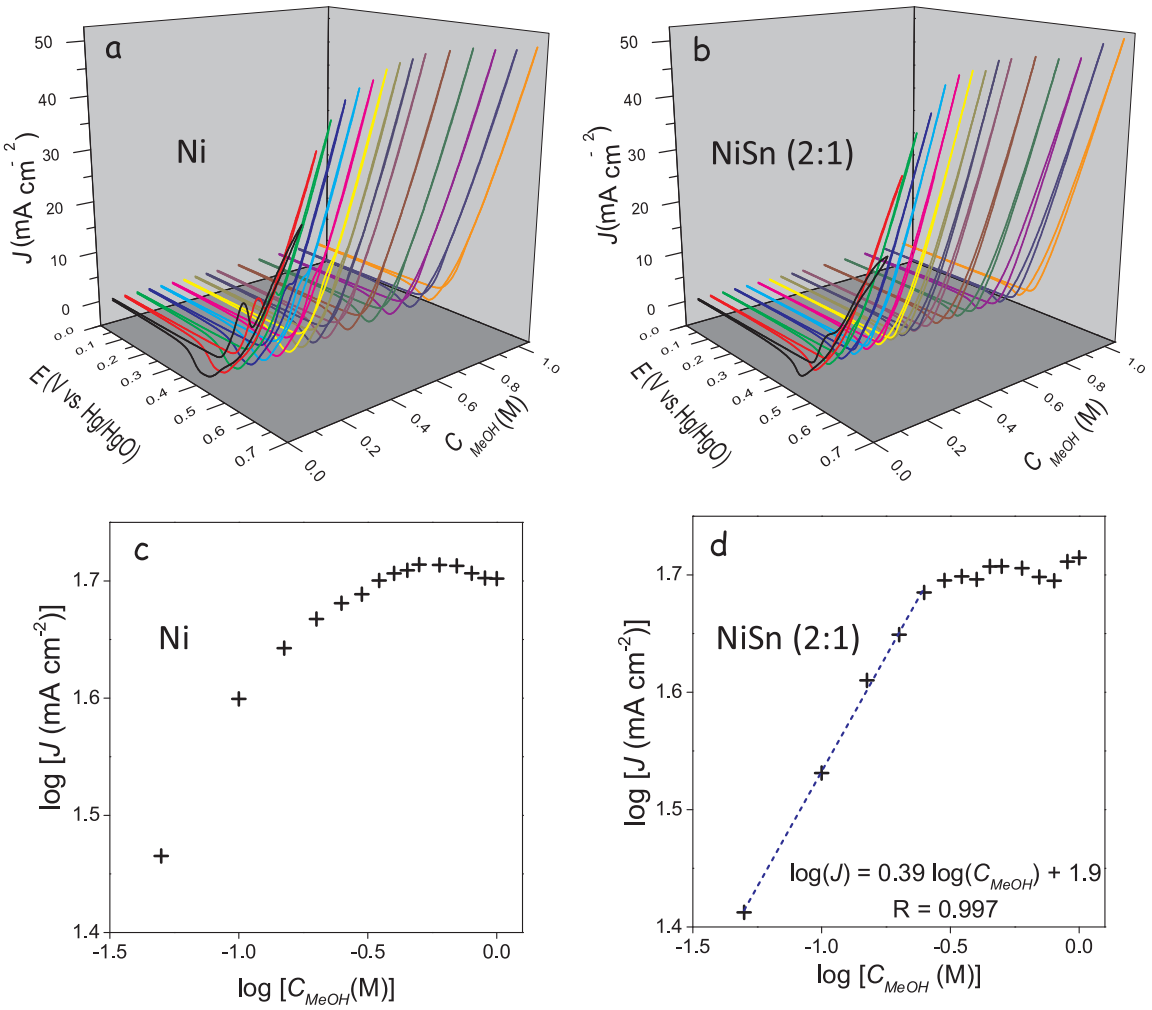

Fig. 7. Cyclic voltammograms (a,b) and logarithmic dependence of the current density (0.70 V vs Hg/HgO) with the methanol concentration (c,d) for a Ni electrode (a,c) and a NiSn (2:1) electrode (b,d) in 0.50 M KOH solution with various methanol concentrations from 0.05 M to 1.00 M at a scan rate of 50 mV s^{-1}.

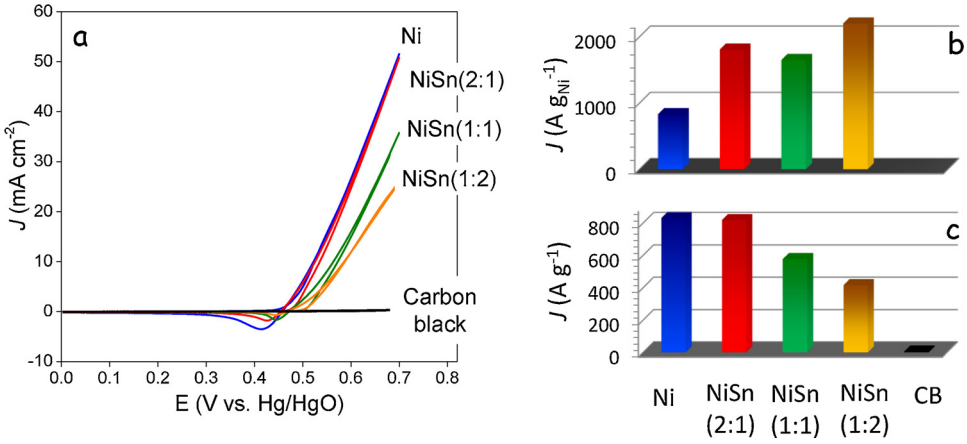

Fig. 8. (a) Cyclic voltammograms of CB, Ni, and NiSn-based electrodes in 0.50 M KOH with 0.50 M methanol at a sweep rate of 50 mV s^{-1}. (b) Mass current densities considering only the mass of Ni for Ni, and NiSn-based electrodes in 0.50 M KOH containing 0.50 M methanol at 0.70 V vs. Hg/HgO. (c) Mass current densities for CB, Ni, and NiSn-based electrodes in the same solution and at the same voltage.

NiSn NPs.

The electrocatalytic activity toward the MOR of NiSn NPs with different compositions was initially tested using cyclic voltammetry. Fig. 5 presents cyclic voltammograms of the five different electrocatalysts tested in 0.50 M KOH medium without (Fig. 5a) or with (Fig. 5b) 0.50 M methanol. The scan rate was set at 50 mV s^{-1} and the potential window measured extended from 0 V to 1.0 V vs Hg/HgO. Cyclic voltammograms in the absence of methanol were conducted to determine the potential range for Ni oxidation and oxygen evolution from water (OER).

The anodic oxidation of nickel in alkaline media has been extensively investigated. It is generally accepted that in alkaline medium, Ni undergoes oxidation to $Ni(OH)_2$ [11,30–32]. In the absence of methanol, for the Ni electrocatalyst, we measured the first anodic peak at ca. 0.50 V vs Hg/HgO and ascribed it to the oxidation of $Ni(OH)_2$ to NiOOH. Still during the forward scan, a second increase in the current density at 0.75 V vs Hg/HgO was attributed to OER. Subsequently, the formed NiOOH was reduced in the backward direction at a potential

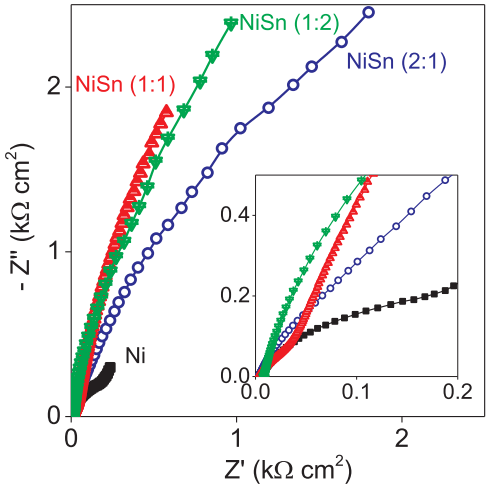

Fig. 9. Nyquist plot of the methanol oxidation on Ni- and NiSn-based electrodes in a 0.50 M KOH + 0.50 M methanol solution at 0.70 V vs Hg/HgO.

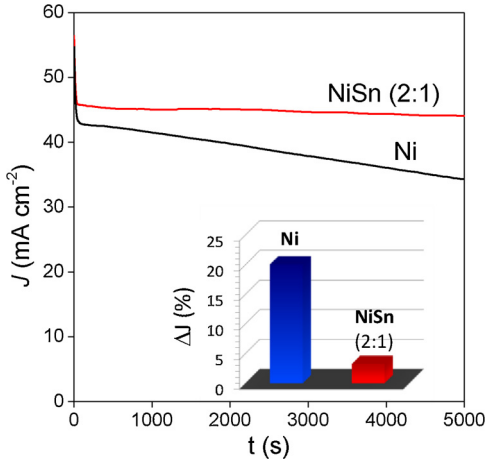

Fig. 10. Chronoamperometry of NiSn (2:1) and Ni electrodes at 0.70 V vs. Hg/HgO in 0.50 M KOH containing 0.50 M methanol.

value of ca. 0.50 V vs Hg/HgO.

Using NiSn bimetallic NPs, the current densities of the first anodic and cathodic peaks decreased as the Sn content increased (Fig. 5a). The current densities at the first oxidation peak were 10.5 mA cm^{-2} for Ni, 10.8 mA cm^{-2} for NiSn (2:1), 4.7 mA cm^{-2} for NiSn (1:1) and 1.7 mA cm^{-2} for NiSn (1:2) electrodes. In parallel, the corresponding oxidation and reduction onset potentials shifted with increasing Sn contents. The onset oxidation potential of Ni was 0.468 V vs Hg/HgO and that of NiSn was 0.482 V, 0.483 V and 0.516 V for (2:1), (1:1) and (1:2) compositions, respectively. Sn electrodes displayed no redox peaks in the measured potential window and showed an OER activity comparable to that of carbon black. Consistently, in spite of the non-homogeneous Ni and Sn distribution within each particle, only one oxidation and reduction peak was observed for each sample.

Fig. 5b shows cyclic voltammograms measured in the presence of methanol. The MOR onset was at ca. 0.43 V vs Hg/HgO, the same voltage at which $Ni(OH)_2$ undergoes oxidation to NiOOH. This is consistent with the proposed mechanisms of electrocatalytic MOR on Ni-based anodes, which involves the participation of the nickel oxyhydroxide in the methanol oxidation [9,18,33]:

$$Ni(OH)_2 + OH^- \leftrightarrow NiOOH + H_2O + e^-$$

$$NiOOH + CH_3OH \rightarrow Ni(OH)_2 + \text{products}$$

with carbonate, formaldehyde, formic acid, CO, and CO_2 as the possible products/intermediates of the MOR. Notice also in this direction, that the cathode peak, associated to the reduction of NiOOH to Ni $(OH)_2$ decreased or fully disappeared with the introduction of methanol, confirming the consumption of this compound during the MOR.

Fig. 5b shows how the activity toward the MOR of the NiSn electrodes decreased with the amount of Sn. The activity of the Sn electrode was very low, confirming that elemental Sn did not catalyze the OER and MOR reactions in the voltage range studied. Activity of NiSn electrocatalysts was generally lower than that of Ni, except for the NiSn with the higher Ni content (2:1), which provided higher current densities up to a certain voltage when the OER reaction kicked in. In this regard, note also that MOR and OER reactions occurred simultaneously at voltages above 0.75 V. Thus, to further test the activity toward MOR without influence of the OER, we limited the analyzed potential to the range from 0 to 0.70 V vs Hg/HgO.

Fig. 6 displays the cyclic voltammograms in the 0 V-0.70 V vs Hg/HgO range and at various scan rates of the Ni and NiSn electrodes within 0.50 KOH media and with no methanol. The anodic and cathodic peaks increased and shifted to higher and lower potentials respectively when increasing the scan rate. For all electrocatalysts, the ratio of the current densities at the anodic and cathodic peaks indicated the nickel redox reaction to be mostly reversible.

To quantify the redox $Ni(OH)_2 \leftrightarrow$ NiOOH reaction, the peak anodic (J_{pa}) and cathodic (J_{pc}) current densities, the half wave redox potential ($E_{1/2}$), the redox potential difference ($\triangle E_p$), the NiOOH surface coverage (Γ) and the proton diffusion coefficient (D), of the different electrocatalysts tested were determined (Table 2). Peak current densities were higher for NiSn (2:1) than for Ni-based electrodes, but decreased with the Sn content. Sharper oxidation and reduction peaks were obtained for all the NiSn-based electrodes compared with Ni, which could be related to the smaller size of the NiSn NPs. While $E_{1/2}$ increased with the Sn content, $\triangle E_p$ decreased with the incorporation of Sn, suggesting faster electron transfer kinetics. The surface coverage of $Ni(OH)_2$/NiOOH redox pairs participating in the reaction at each Ni-Sn electrode was calculated using the following equation [34,35]:

$$\Gamma = \frac{Q}{nFA}$$

where Q is the charge under the reduction/oxidation peak, which we averaged from forward and reverse scans, A is the geometrical electrode surface area, n is the number of transferred electron per reaction, i.e. 1, and F is the Faraday constant.

The calculated NiOOH surface coverages were independent of the scan rate in the low scan rate range ($\upsilon < 50$ mV s^{-1}). The coverage of electroactive species decreased as the amount of Sn in the NiSn NPs increased (Table 2). However, the coverage obtained from NiSn (2:1) electrocatalysts was very close to that of Ni. This experimental result was at first view surprising taking into account the lower overall amount of metal in NiSn catalysts due to the higher atomic mass of Sn, the lower content of Ni in the NiSn NPs compared with elemental Ni NPs and the Sn-rich surface of NiSn NPs. However, it could be in part explained by the smaller size of the NiSn NPs compared with the Ni NPs. Overall, the surface coverages obtained from the Ni and NiSn electrodes in the present work were almost an order of magnitude higher than values usually reported, which we associated to the large surface area of the NPs used here.

In the high scan rate range, a linear relationship could be fitted to the dependence of the peak current density with the square root of the voltage scan rate, pointing toward a diffusion-limited $Ni(OH)_2 \leftrightarrow$ NiOOH redox reaction [30,36]. In this regard, it is generally accepted that the proton diffusion is the rate limiting step in the oxidation of Ni $(OH)_2$ to NiOOH. Therefore, the proton diffusion coefficient (D) can be determined from equation [34]:

$$I_p = 2.69 \times 10^5 n^{3/2} A D^{1/2} C v^{1/2}$$

where I_p is the peak current and C is the initial concentration of redox

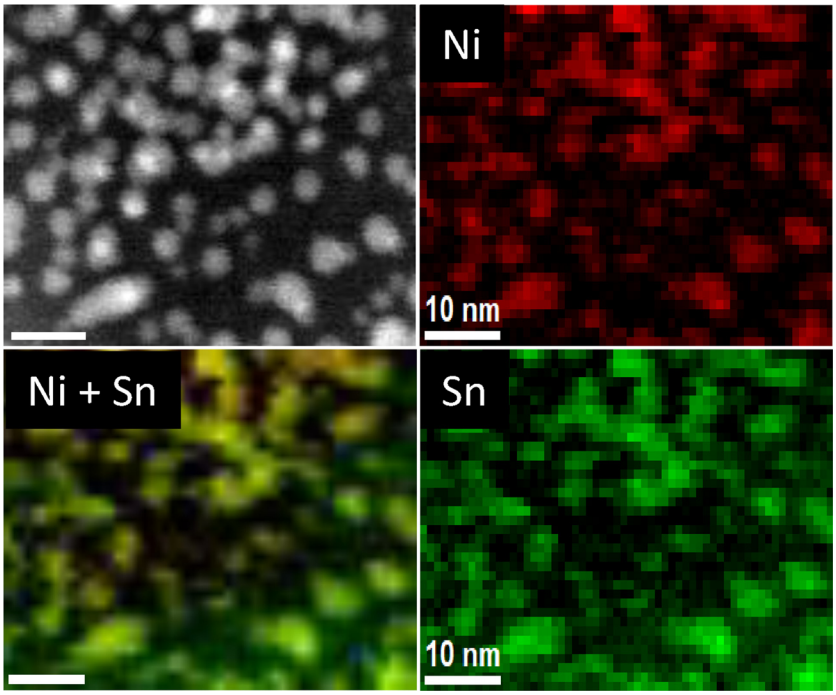

Fig. 11. EELS chemical composition maps of a NiSn (2:1) electrocatalyst after 10000s CA stability test: Individual Ni $L_{2,3}$-edges at 855 eV (red), Sn $M_{4,5}$-edges at 485 eV (green) and composite Ni-Sn map (For interpretation of the references to colour in this figure legend, the reader is referred to the web version of this article).

species that, taking into account a $Ni(OH)_2$ density of 3.97 g cm^{-3}, we estimated at 0.043 mol cm^{-3}.

The proton diffusion coefficient obtained from Ni nanoparticles was 1.2×10^{-11} $cm^2 s^{-1}$, consistent with previous works [36]. Remarkably, the diffusion coefficient for NiSn (2:1) was slightly higher, 1.9×10^{-11} $cm^2 s^{-1}$, but as Sn concentration increased, this apparent diffusion coefficient decreased (Table 2).

Fig. 7a–b displays cyclic voltammograms (50 mV s^{-1}) of the Ni and the NiSn (2:1) electrocatalyts in a media containing different methanol concentrations, from 0.05 M to 1.00 M. It can be observed that the Ni $(OH)_2$ oxidation peak gradually disappears within the large current density increase related to the MOR when the methanol concentration increases. Fig. 7c–d displays the dependence of the current density measured at 0.70 V vs Hg/HgO with the methanol concentration. The current density at 0.70 V vs Hg/HgO rapidly increased in the low methanol concentration range and stabilized at methanol concentrations around 0.30 M. A linear fit of the logarithmic plot of the current density of MOR versus the methanol concentration for the NiSn (2:1) electrode pointed toward an apparent methanol reaction order of around 0.4. A similar reaction order was obtained for all NiSn-based electrodes (Fig. S8). No clear linear relationship could be fitted to the Ni electrode (Fig. 7c).

While saturating at relatively low methanol concentrations, very high current densities and mass current densities were obtained for Ni and NiSn NP-based electrodes (Figs. 7, 8 and S9). Fig. 8a displays the cyclic voltammograms of the electrocatalysts based on Ni NPs, Sn NPs, CB, and Ni-Sn NPs in 0.50 M KOH with 0.50 M methanol. Mass current densities were calculated taking into account the mass of metal in each electrode (Fig. 8c). The calculated mass current density was 830 A g^{-1} for Ni and 820 A g^{-1} for NiSn (2:1)-based electrodes. When we increase the amount of Sn, the mass current densities decreased to 580 A g^{-1} and 420 A g^{-1} for NiSn (1:1) and NiSn (1:2), respectively. When only considering the mass of Ni as the active element to evaluate the mass current density (Fig. 8b), all NiSn NP-based electrodes showed similar performances, all much higher than that of elemental Ni NPs: 830 A g^{-1} for Ni, 1800 A g_{Ni}^{-1} for NiSn (2:1), 1650 A g_{Ni}^{-1} for NiSn (1:1) and 2250 A g_{Ni}^{-1}, for NiSn (1:2). A comparison of catalytic performance between our results and previously reported Ni-based catalysts towards MOR is listed in Table S1. From this comparison, we conclude that NiSn NPs are excellent candidates for the electro-oxidation of methanol in alkaline medium.

Fig. 9 displays the Nyquist plot of the impedance spectra of methanol oxidation on Ni, NiSn (2:1), NiSn (1:1) and NiSn (1:2) electrodes. The measurements were made in a 0.50 M KOH + 0.50 M methanol solution at 0.70 V vs Hg/HgO. We observed the impedance associated to the charge transfer for methanol electrochemical oxidation to increase with the amount of Sn.

Chronoamperometric measurements were used to determine the electrocatalysts stability. Fig. 10 shows the chronoamperograms of NiSn (2:1) and Ni electrodes in a 0.50 M KOH solution containing 0.50 M methanol at 0.70 V vs Hg/HgO. The current densities largely dropped in the first minutes and then relatively stabilized. Similarly fast initial drops were previously observed [14] and are generally attributed to the fact that initially active sites are free of adsorbed methanol molecules and no methanol depletion layer around the electrode exist, allowing a very fast initial reaction. In the first minutes, an equilibrium coverage of methanol at the catalyst surface and an equilibrium gradient of methanol around the electrode are stablished, dropping the current density to a lower value. The posterior progressive drop of current density is most likely related to the poisoning of the active sites at the electrode with reaction products. Fig. S10 displays the chronoamperograms obtained from the different electrodes in a magnetically stirred 0.50 M KOH solution containing 0.50 M methanol at 0.70 V vs Hg/HgO. In this case, no methanol depletion layer is formed and current densities do not suffer any initial drop. On the contrary, they increased in the first minutes to later decrease over the 10,000 s studied.

Fig. 11 shows a representative STEM micrograph of the NiSn (2:1) electrocatalyst after a 10,000 s stability test. A broader size distribution of the NCs was observed, which could be related to a partial aggregation during electrocatalyst formulation. In the same figure, the EELS chemical compositional maps of the NPs are displayed. While signal and resolution were not optimal due to the presence of the electrocatalyst additives, i.e. CB and Nafion, compositional maps showed the existence of Ni and Sn in all the nanoparticles and no clear phase

segregation could be identified.

Overall, NiSn-based electrodes clearly displayed improved stabilities over Ni-based electrocatalysts. This experimental fact could have two different explanations: (i) The presence of Sn can contribute to the oxidation of the MOR products that poisons the Ni surface sites. In this direction, lattice or adsorbed oxygen or OH^- groups on Sn metal, oxide or hydroxide could further oxidize MOR products that strongly adsorb onto the Ni sites poisoning its surface. (ii) Alternatively, the presence of Sn atoms within the Ni structure, forming a Ni_3Sn_2 phase, certainly modifies the electronic density of states of Ni, thus affecting its chemistry, which could prevent strong binding of particular poisoning species. Additional work would be required to exactly asses the mechanism of improvement of the electrode stability with the Sn incorporation.

4. Conclusion

In summary, a new synthetic route to produce NiSn intermetallic NPs with composition control was developed. Detailed electrochemical measurements showed that these NPs exhibited excellent performance for MOR in alkaline solution. Ni-rich NiSn-based electrocatalysts displayed slightly improved performances than Ni-based electrocatalysts. Most notorious was the significantly improved stability of NiSn catalysts compared with that of Ni. This work represents a significant advance in developing cost-effective electrocatalysts with high activity and stability for MOR in DMFCs.

Conflict of interest

The authors declare no competing financial interest.

Acknowledgments

J. Li and T. Zhang thank the China Scholarship Council for scholarship support. JA and TZ acknowledge funding from Generalitat de Catalunya 2014 SGR 1638 and the Spanish MINECO coordinated projects between IREC and ICN2 VALPEC and subprojects RESOL and ANAPHASE (ENE2017-85087-C3). ICN2 acknowledges support from the Severo Ochoa Programme (MINECO, Grant no. SEV-2013-0295) and is funded by the CERCA Programme / Generalitat de Catalunya. JL is a Serra Húnter Fellow and is grateful to ICREA Academia program and to MINECO/FEDER grant ENE2015-63969-R.

Appendix A. Supplementary data

Supplementary material related to this article can be found, in the online version, at doi:https://doi.org/10.1016/j.apcatb.2018.04.017.

References

[1] M. Sgroi, F. Zedde, O. Barbera, A. Stassi, D. Sebastián, F. Lufrano, V. Baglio, A. Aricò, J. Bonde, M. Schuster, Cost analysis of direct methanol fuel cell stacks for mass production, Energies 9 (2016) 1008.
[2] T. Schultz, S. Zhou, K. Sundmacher, Current status of and recent developments in the direct methanol fuel cell, Chem. Eng. Technol. 24 (2001) 1223–1233.
[3] S.S. Munjewar, S.B. Thombre, R.K. Mallick, A comprehensive review on recent material development of passive direct methanol fuel cell, Ionics (Kiel) 23 (2017) 1–18.
[4] P. Kumar, K. Dutta, S. Das, P.P. Kundu, An overview of unsolved deficiencies of direct methanol fuel cell technology: factors and parameters affecting its widespread use, Int. J. Energy Res. 38 (2014) 1367–1390.
[5] Z. Daşdelen, Y. Yıldız, S. Eriş, F. Şen, Enhanced electrocatalytic activity and durability of Pt nanoparticles decorated on GO-PVP hybride material for methanol oxidation reaction, Appl. Catal. B Environ. 219 (2017) 511–516.
[6] G. Long, X. Li, K. Wan, Z. Liang, J. Piao, P. Tsiakaras, Pt/CN-doped electrocatalysts: superior electrocatalytic activity for methanol oxidation reaction and mechanistic insight into interfacial enhancement, Appl. Catal. B Environ. 203 (2017) 541–548.
[7] M.A. Abdel Rahim, R.M. Abdel Hameed, M.W. Khalil, Nickel as a catalyst for the electro-oxidation of methanol in alkaline medium, J. Power Sources 134 (2004) 160–169.
[8] M. Zhou, P. Xiao, W. Guo, J. Deng, F. Liu, Y. Zhang, Electrochemical synthesis of monodisperse nickel with predominant orientation and High electro-oxidation activity for methanol, J. Electrochem. Soc. 161 (2014) H133–H137.
[9] R.M. Abdel Hameed, R.M. El-Sherif, Microwave irradiated nickel nanoparticles on Vulcan XC-72R carbon black for methanol oxidation reaction in KOH solution, Appl. Catal. B Environ. 162 (2015) 217–226.
[10] M.W. Khalil, M.A. Abdel Rahim, A. Zimmer, H.B. Hassan, R.M. Abdel Hameed, Nickel impregnated silicalite-1 as an electro-catalyst for methanol oxidation, J. Power Sources 144 (2005) 35–41.
[11] D. Wu, W. Zhang, D. Cheng, Facile synthesis of Cu/NiCu electrocatalysts integrating alloy, core–shell, and one-dimensional structures for efficient methanol oxidation reaction, ACS Appl. Mater. Interfaces 9 (2017) 19843–19851.
[12] I. Danaee, M. Jafarian, F. Forouzandeh, F. Gobal, M.G. Mahjani, Electrocatalytic oxidation of methanol on Ni and NiCu alloy modified glassy carbon electrode, Int. J. Hydrogen Energy 33 (2008) 4367–4376.
[13] R. Ding, J. Liu, J. Jiang, F. Wu, J. Zhu, X. Huang, Tailored Ni–Cu alloy hierarchical porous nanowire as a potential efficient catalyst for DMFCs, Catal. Sci. Technol. 1 (2011) 1406.
[14] X. Cui, P. Xiao, J. Wang, M. Zhou, W. Guo, Y. Yang, Y. He, Z. Wang, Y. Yang, Y. Zhang, Z. Lin, Highly branched metal alloy networks with superior activities for the methanol oxidation reaction, Angew. Chem. Int. Ed. 56 (2017) 4488–4493.
[15] S.L. Candelaria, N.M. Bedford, T.J. Woehl, N.S. Rentz, A.R. Showalter, S. Pylypenko, B.A. Bunker, S. Lee, B. Reinhart, Y. Ren, S.P. Ertem, E.B. Coughlin, N.A. Sather, J.L. Horan, A.M. Herring, L.F. Greenlee, Multi-component Fe–Ni hydroxide nanocatalyst for oxygen evolution and methanol oxidation reactions under alkaline conditions, ACS Catal. 7 (2017) 365–379.
[16] X. Cui, W. Guo, M. Zhou, Y. Yang, Y. Li, P. Xiao, Y. Zhang, X. Zhang, Promoting effect of Co in $Ni_m Co_n$ $(m + n = 4)$ bimetallic electrocatalysts for methanol oxidation reaction, ACS Appl. Mater. Interfaces 7 (2015) 493–503.
[17] I. Danaee, M. Jafarian, A. Mirzapoor, F. Gobal, M.G. Mahjani, Electrooxidation of methanol on NiMn alloy modified graphite electrode, Electrochim. Acta 55 (2010) 2093–2100.
[18] Q. Yi, W. Huang, J. Zhang, X. Liu, L. Li, Methanol oxidation on titanium-supported nano-scale Ni flakes, Catal. Commun. 9 (2008) 2053–2058.
[19] Y. Yu, Q. Yang, X. Li, M. Guo, J. Hu, A bimetallic Ni–Ti nanoparticle modified indium tin oxide electrode fabricated by the ion implantation method for studying the direct electrocatalytic oxidation of methanol, Green Chem. 18 (2016) 2827–2833.
[20] Y. Wang, X. Wang, Y. Wang, J. Li, Acid-treatment-assisted synthesis of Pt–Sn/graphene catalysts and their enhanced ethanol electro-catalytic activity, Int. J. Hydrogen Energy 40 (2015) 990–997.
[21] X. Wang, J. Lian, Y. Wang, The effect of Sn on platinum dispersion in Pt/graphene catalysts for the methanol oxidation reaction, Int. J. Hydrogen Energy 39 (2014) 14288–14295.
[22] D.-H. Lim, D.-H. Choi, W.-D. Lee, D.-R. Park, H.-I. Lee, The effect of Sn addition on a Pt/C electrocatalyst synthesized by borohydride reduction and hydrothermal treatment for a low-temperature fuel cell, Electrochem. Solid-State Lett. 10 (2007) B87.
[23] J. Liu, Y. Wen, P.A. van Aken, J. Maier, Y. Yu, Facile synthesis of highly porous Ni–Sn intermetallic microcages with excellent electrochemical performance for lithium and sodium storage, Nano Lett. 14 (2014) 6387–6392.
[24] Y. Liu, X. Liu, Q. Feng, D. He, L. Zhang, C. Lian, R. Shen, G. Zhao, Y. Ji, D. Wang, G. Zhou, Y. Li, Intermetallic $Ni_x M_y$ $(M =$ Ga and Sn) nanocrystals: a non-precious metal catalyst for semi-hydrogenation of alkynes, Adv. Mater. 28 (2016) 4747–4754.
[25] K. Kravchyk, L. Protesescu, M.I. Bodnarchuk, F. Krumeich, M. Yarema, M. Walter, C. Guntlin, M.V. Kovalenko, Monodisperse and inorganically capped Sn and Sn/SnO_2 nanocrystals for high-performance Li-ion battery anodes, J. Am. Chem. Soc. 135 (2013) 4199–4202.
[26] Y. Chen, X. Luo, H. She, G.-H. Yue, D.-L. Peng, Size- and structure-controlled synthesis and characterization of nickel nanoparticles, J. Nanosci. Nanotechnol. 9 (2009) 5157–5163.
[27] A. Yakymovych, H. Ipser, Synthesis and characterization of pure Ni and Ni-Sn intermetallic nanoparticles, Nanoscale Res. Lett. 12 (2017) 142.
[28] C. Schmetterer, H. Flandorfer, K.W. Richter, U. Saeed, M. Kauffman, P. Roussel, H. Ipser, A new investigation of the system Ni–Sn, Intermetallics 15 (2007) 869–884.
[29] C.D. Wager, W.M. Riggs, L.E. Davis, J.F. Moulder, G.E. Muilenderg, Handbook of X-ray Photoelectron Spectroscopy, Perkin-Elmer Corporation Physical Electronics Division, 1979.
[30] D.M. MacArthur, The hydrated nickel hydroxide electrode potential sweep experiments, J. Electrochem. Soc. 117 (1970) 422.
[31] P. Oliva, J. Leonardi, J.F. Laurent, C. Delmas, J.J. Braconnier, M. Figlarz, F. Fievet, Ad. Guibert, Review of the structure and the electrochemistry of nickel hydroxides and oxy-hydroxides, J. Power Sources 8 (1982) 229–255.
[32] Z. Jiang, Y. Xiang, J. Wang, Study of the oxidation layer on the nickel surface in 1 M NaOH solution using the in-situ photothermal spectroscopy method, J. Electroanal. Chem. Interfacial Electrochem. 316 (1991) 199–209.
[33] N.A.M. Barakat, M. Motlak, CoxNiy-decorated graphene as novel, stable and super effective non-precious electro-catalyst for methanol oxidation, Appl. Catal. B Environ. 154 (2014) 221–231.
[34] A.J. Bard, L.R. Faulkner, Electrochemical Methods Fundamentals and Applications, (2001).
[35] D. Chen, S.D. Minteer, Mechanistic study of nickel based catalysts for oxygen evolution and methanol oxidation in alkaline medium, J. Power Sources 284 (2015) 27–37.
[36] C. Zhang, S. Park, The anodic oxidation of nickel in alkaline media studied by spectroelectrochemical techniques, J. Electrochem. Soc. 134 (1987) 2966.

Journal of Materials Chemistry A

PAPER

View Article Online
View Journal | View Issue

Cite this: J. Mater. Chem. A, 2018, 6, 22915

Colloidal Ni–Co–Sn nanoparticles as efficient electrocatalysts for the methanol oxidation reaction†

Junshan Li,[ab] Zhishan Luo,*[a] Feng He,*[cd] Yong Zuo,[ab] Chaoqi Zhang,[ab] Junfeng Liu,[ab] Xiaoting Yu,[ab] Ruifeng Du,[ab] Ting Zhang,[e] Maria F. Infante-Carrió,[e] Pengyi Tang,[e] Jordi Arbiol,[ef] Jordi Llorca[g] and Andreu Cabot*[af]

The deployment of direct methanol fuel cells requires engineering cost-effective and durable electrocatalysts for the methanol oxidation reaction (MOR). As an alternative to noble metals, Ni-based alloys have shown excellent performance and good stability toward the MOR. Herein, we present a series of $Ni_{3-x}Co_xSn_2$ colloidal nanoparticles (NPs) with composition tuned over the entire Ni/Co range ($0 \leq x \leq 3$). We demonstrate electrodes based on these ternary NPs to provide improved catalytic performance toward the MOR in an alkaline medium when compared with binary Ni_3Sn_2 NPs. A preliminary composition optimization resulted in $Ni_{2.5}Co_{0.5}Sn_2$ NP-based electrodes exhibiting extraordinary mass current densities, up to 1050 mA mg^{-1}, at 0.6 V *vs.* Hg/HgO in 1.0 M KOH containing 1.0 M methanol. This current density was about two-fold higher than that of Ni_3Sn_2 electrodes (563 mA mg^{-1}). The excellent performance obtained with the substitution of small amounts of Ni by Co was concomitant with an increase of the surface coverage of active species and an enhancement of the diffusivity of the reaction limiting species. Additionally, saturation of the catalytic activity at higher methanol concentrations was measured for $Ni_{3-x}Co_xSn_2$ NP-based electrodes containing a small amount of Co when compared with binary Ni_3Sn_2 NPs. While the electrode stability was improved with respect to elemental Ni NP-based electrodes, the introduction of small amounts of Co slightly decreased the cycling performance. Additionally, Sn, a key element to improve stability with respect to elemental Ni NPs, was observed to slowly dissolve in the presence of KOH. Density functional theory calculations on metal alloy surfaces showed the incorporation of Co within the Ni_3Sn_2 structure to provide more effective sites for CO and CH_3OH adsorption. However, the relatively lower stability could not be related to CO or CH_3OH poisoning.

Received 24th August 2018
Accepted 25th October 2018

DOI: 10.1039/c8ta08242a

rsc.li/materials-a

Introduction

The development of renewable energy technologies able to reduce the use of fossil fuels is one of the biggest challenges we face this 21st century. To this end, direct alcohol fuel cells able to convert chemical energy stored in alcohols into electricity are regarded as a very promising energy conversion technology.[1–9] More particularly, direct methanol fuel cells (DMFCs) provide several advantages, including high energy density, high efficiency, low emissions, fast mechanical refueling and simple operation.[10–13] In addition, methanol not only provides a high energy density, but also easy storage and distribution, which makes it one of the most interesting fuels.[10,14] In this scenario, the development of electrocatalysts for the methanol oxidation reaction (MOR) has become a very dynamic research field.[12,15]

State-of-the-art electrocatalysts for the MOR are generally based on noble metals and their alloys, *e.g.* Pt,[16–21] PtNi,[22–28] PtCo,[29–32] PuCu,[33,34] PtPd,[35,36] and PtSn.[37–41] However, the low tolerance to CO and the high cost and scarcity of these materials have strongly limited the commercialization of DMFCs.[13,42–44] Therefore, over the past few years, researchers have devoted increasing attention to searching for alternative earth-abundant and cost-efficient MOR electrocatalysts.

[a]Catalonia Institute for Energy Research – IREC, Sant Adrià del Besòs, Barcelona, 08930, Spain. E-mail: luozs@mail.sustc.edu.cn; acabot@irec.cat
[b]Departament d'Electronica, Universitat de Barcelona, 08028 Barcelona, Spain
[c]Key Laboratory of Organic Solids, Institute of Chemistry, Chinese Academy of Sciences, Beijing 100190, P. R. China. E-mail: hefeng2018@iccas.ac.cn
[d]University of Chinese Academy of Sciences, Beijing 100049, P. R. China
[e]Catalan Institute of Nanoscience and Nanotechnology (ICN2), CSIC, BIST, Campus UAB, Bellaterra, 08193 Barcelona, Spain
[f]ICREA, Pg. Lluís Companys 23, 08010 Barcelona, Spain
[g]Institute of Energy Technologies, Department of Chemical Engineering, Barcelona Research Center in Multiscale Science and Engineering, Universitat Politècnica de Catalunya, EEBE, 08019 Barcelona, Spain

† Electronic supplementary information (ESI) available: Additional SEM-EDS, TEM, HRTEM, XPS, FT-IR, electrochemical characterization and DFT calculations. See DOI: 10.1039/c8ta08242a

While no single metal has provided electrocatalytic properties comparable to Pt and Pt-group metals, particular bimetallic compositions have demonstrated very promising performances and stabilities. Among the earth-abundant elements, the most promising MOR catalysts under alkaline conditions are bimetallic alloys based on Ni, *e.g.* Ni–Cu,[42,45–47] Ni–Mn,[48] Ni–Fe,[49,50] Ni–Co,[51–58] and Ni–Sn.[59] In a previous study, we demonstrated NiSn NPs to present outstanding performance for the electrocatalytic MOR in an alkaline medium, and particularly an enhanced stability compared with state-of-the-art elemental Ni NPs.[59] We hypothesized this improvement to be related to an influence of Sn on the electronic properties of Ni or the introduction of additional adsorption sites that promoted electrocatalysis of poisoning species.

A main advantage of bimetallic catalysts over elemental compositions is their additional degrees of freedom to control the surface electronic structure, to provide optimum active sites for one or various concatenated catalytic reactions, and to improve stability by combined catalytic reactions.[9,60–62] In the same direction, ternary compositions provide even larger opportunities to optimize electronic properties and provide suitable active sites for one or multiple reactions. However, few ternary alloy catalysts have been reported toward the MOR and other electrocatalytic reactions. This is in large part due to the difficulty of producing ternary alloys with controlled composition. For example, Hamza and co-workers demonstrated ternary oxide electrocatalysts $CuCoNiO_x$ supported on carbon nanotubes to have a notable activity toward the MOR.[63] Recently, Rostami *et al.* demonstrated that NiCuCo on graphite electrodes enhanced activity and stability towards the MOR.[54] However, in none of these previous studies the full potential of ternary compositions to optimize catalytic properties could be demonstrated because no composition adjustment was attempted.

In this work, we detail a procedure to produce ternary $Ni_{3-x}Co_xSn_2$ NPs with tuned composition in all the Ni/Co ratio range ($0 \leq x \leq 3$). Subsequently, these NPs are supported on carbon black and tested as electrocatalysts toward the MOR.

Experimental

Chemicals

Nickel(II) acetylacetonate ($Ni(acac)_2 \cdot xH_2O$ ($x \sim 2$), 95%, Sigma-Aldrich), cobalt(II) acetylacetonate ($Co(acac)_2$, 97%, Sigma-Aldrich), tin(II) acetate ($Sn(oac)_2$, 95%, Fluka), tri-*n*-octylphosphine (TOP, 97%, Strem), oleylamine (OAm, 80–90%, TCI), borane *tert*-butylamine complex (TBAB, 97%, Sigma-Aldrich), oleic acid (OAc, Sigma-Aldrich), hydrazine monohydrate (N_2H_4, 64–65%, reagent grade, 98%, Sigma-Aldrich), Nafion (10 wt%, perfluorinated ion-exchange resin, dispersion in water), methanol (anhydrous, 99.8%, Sigma-Aldrich), carbon black (CB, VULCAN XC72), potassium hydroxide (KOH, 85%, Sigma-Aldrich) and acetonitrile (CH_3CN, extra dry, Fisher) were used as received without any further treatment. Chloroform, hexane, acetone, and ethanol were of analytical grade and purchased from various sources. Milli-Q water was obtained from a PURELAB flex from ELGA. An argon-filled glove box was used for storing and handling sensitive chemicals.

Synthesis of colloidal $Ni_{3-x}Co_xSn_2$ NPs

All the syntheses were performed using standard airless techniques: a vacuum/dry argon gas Schlenk line was used for the synthesis. $Ni_{3-x}Co_xSn_2$ NPs were prepared following a similar protocol to the one we developed for the scale-up production of NiSn NPs.[59] In a typical synthesis of $Ni_{1.5}Co_{1.5}Sn_2$ NPs, 20 mL OAm, 0.3 mmol $Ni(acac)_2$, 0.3 mmol $Co(acac)_2$, 0.4 mmol $Sn(oac)_2$ and 1.0 mL OAc were loaded into a 50 mL three-necked flask and degassed under vacuum at 80 °C for 2 hours while being strongly stirred using a magnetic bar. Afterward, a gentle flow of argon was introduced, and then 5 mL of TOP was injected into the solution. Subsequently, the reaction flask was heated to 180 °C within 20 min, followed by quick injection of a solution containing 5 mmol TBAB in 5 mL degassed OAm. A visible color change, from deep pink to black was observed immediately. The reaction was maintained at this temperature for 1 hour before it was quenched using a water bath. The obtained NPs were collected by centrifuging and washing the solid product with acetone and chloroform three times. The as-prepared NPs were finally dispersed in chloroform and stored for further use. NPs were colloidally stable in chloroform for a couple of weeks. NPs with different nominal Ni/Co ratios, $Ni_{3-x}Co_xSn_2$ ($0 \leq x \leq 3$), were prepared following the same procedure (Scheme 1).

Ligand removal

The as-synthesized $Ni_{3-x}Co_xSn_2$ NPs dispersed in chloroform were precipitated through the addition of ethanol and centrifugation. Then, they were dispersed in a mixture containing 25 mL acetonitrile and 0.8 mL hydrazine hydrate and stirred for 4 hours. The NPs were then collected by centrifugation and washed with acetonitrile an additional three times. Finally, the NPs were dried under vacuum.

Characterization

The structural properties and chemical composition of the NPs were determined using a combination of characterization techniques. Powder X-ray diffraction (XRD) patterns were collected directly from the as-synthesized NPs on a Bruker AXS D8 Advance X-ray diffractometer with Ni-filtered (2 μm thickness) Cu K radiation ($\lambda = 1.5106$ Å) operating at 40 kV and 40 mA. 200 mesh carbon-coated transmission electron microscopy (TEM) grids from Ted-Pella were used as the substrate.

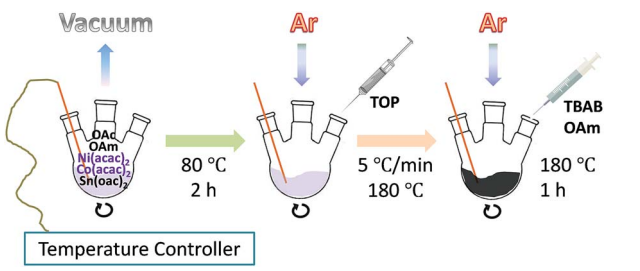

Scheme 1 Schematic drawing of the synthesis procedure to produce $Ni_{3-x}Co_xSn_2$ NPs.

A drop of as-synthesized NP dispersion was cast and dried on the grids before measurements. TEM analyses were carried out on a ZEISS LIBRA 120, operating at 120 kV. High-resolution TEM (HRTEM) and scanning TEM (STEM) studies were carried out using a FEI Tecnai F20 field emission gun microscope at 200 kV with a point-to-point resolution of 0.19 nm. High angle annular dark-field (HAADF) STEM was combined with electron energy loss spectroscopy (EELS) in a Tecnai microscope by using a GATAN QUANTUM filter. The Fourier transform infrared spectroscopy (FTIR) data of the as-synthesized NPs before and after ligand removal were recorded on an Alpha Bruker FTIR spectrometer with a platinum attenuated total reflectance (ATR) single reflection module. Scanning electron microscopy (SEM) analyses were performed on a ZEISS Auriga SEM with an energy dispersive X-ray spectroscopy (EDS) detector at 20 kV. X-ray photoelectron spectroscopy (XPS) was done on a SPECS system equipped with an Al anode XR50 source operating at 150 mW and a Phoibos 150 MCD-9 detector. The pressure in the analysis chamber was kept below 10^{-7} Pa. The area analyzed was about 2 mm × 2 mm. The pass energy of the hemispherical analyzer was set at 25 eV and the energy step was maintained at 0.1 eV. Data processing was performed with the Casa XPS program (Casa Software Ltd., UK). Binding energies were shifted according to the reference C 1 s peak that was located at 284.8 eV.

Preparation of catalyst inks

In a typical preparation of a catalyst ink, 5 mg of purified NPs together with 5 mg of CB were added to 2 mL Milli-Q water/ethanol solution (v/v = 1 : 1) containing 50 μL of a 10 wt% Nafion solution. Then the mixture was vigorously sonicated for 1 hour to obtain a homogeneous mixture. A glassy carbon (GC, 5 mm in diameter) electrode was polished using diamond paper and 0.05 μm alumina slurry, followed by water flush with Milli-Q water. Subsequently, the electrode was ultra-sonicated in ethanol and Milli-Q water separately for ~20 s before it was flushed with Milli-Q water again and dried under argon flow at room temperature. Finally, 5 μL of the prepared ink was evenly loaded onto the GC electrode and was allowed to dry naturally in air at room temperature.

Electrochemical characterization

An electrochemical workstation (AutoLab, Metrohm) was employed for the electrochemical measurements in open air at room temperature. The conventional three-electrode system consisted of a counter electrode (Pt mesh), a working electrode and a reference electrode (*vs.* Hg/HgO). The Hg/HgO was placed in a salt bridge of 1.0 M KOH. All the measurements were performed in a N_2-bubbled 1.0 M KOH solution with and without addition of variable concentrations of methanol with magnetic bar stirring. All potential values presented in this paper were referenced to the reference electrode, *vs.* Hg/HgO. Cyclic voltammetry (CV) and chronoamperometry (CA) measurements were performed to investigate the activity and stability for the MOR. The current densities were calculated taking into account the geometric surface area of the GC electrode (0.196 cm^{-2}) or the metal mass loading (~0.012 mg NPs). The CO poisoning experiments were conducted in 1.0 M KOH containing 1.0 M CH_3OH using CA at 0.6 V simply by introducing a gentle gas (10% CO + 90% He) flow into the solution.

DFT calculations

To figure out the change of activity of the Ni_3Sn_2 surface with the introduction of Co atoms, the adsorption of CH_3OH on the Ni_3Sn_2 and $Ni_{2.5}Co_{0.5}Sn_2$ surfaces was investigated using the Vienna ab-initio simulation package (VASP) based on the density functional theory (DFT).[64–67] An eight-layer slab was constructed in our models. During the structural optimization calculations, the atoms in the two bottom layers were fixed in their bulk positions, and those in the other six layers were allowed to relax. The (001) and (110) surfaces of both Ni_3Sn_2 and $Ni_{2.5}Co_{0.5}Sn_2$ were employed in our DFT calculations. The adsorption energies of CH_3OH on the surfaces, ΔE_{ads}, are defined as follows:

$$\Delta E_{ads} = E_{adsorbate/slab} - E_{slab} - E_{adsorbate}$$

where $E_{adsorbate/slab}$ is the total energy of CH_3OH on the surfaces, E_{slab} is the total energy of the isolated surfaces and $E_{adsorbate/slab}$ is the total energy of the isolated CH_3OH molecule. The first two terms were calculated with the same parameters. The third term was calculated by setting the isolated adsorbate in a box of 20 Å × 20 Å × 20 Å. Thus, negative ΔE_{ads} indicates exothermic chemisorption and positive values indicate an endothermic process.

Results and discussion

Synthesis of $Ni_{3-x}Co_xSn_2$ colloidal NPs

$Ni_{3-x}Co_xSn_2$ ($0 \leq x \leq 3$) colloidal NPs were produced from the reduction of appropriate amounts of the different metal salts in the presence of TOP, OAm and OAc (see the Experimental section and Scheme 1 for details). Fig. 1a and S1† display representative TEM micrographs of the quasi-spherical $Ni_{3-x}Co_xSn_2$ NPs produced. Table 1 displays the average diameter of NPs with different compositions. For the ternary compositions, a slight increase of size was obtained when increasing the amount of Co from 4.2 ± 0.7 to 5.4 ± 0.8 nm. The size of the binary Co_3Sn_2 NPs was slightly larger, 7.5 ± 1.0 nm (Table 1).

Ni_3Sn_2 and Co_3Sn_2 share the same orthorhombic crystal phase (*Pnam* space group) and have very similar lattice parameters, owing to their virtually equal ionic radius (0.135 nm).[68,69] Thus, very similar XRD patterns were obtained for all compositions, although the more noisy XRD patterns of the ternary structures pointed to slightly more defective crystals (Fig. 1c).

EDX analyses showed all compositions to be Sn-rich (Fig. S2† and Table 1), *i.e.* (Ni + Co)/Sn < 1.5. The Ni/Co ratio obtained by EDX analyses matched relatively well with the nominal composition. This match was not surprising taking into account the resemblance of the two elements, with similar standard reduction potentials, Ni^{2+} (−0.25 V) and Co^{2+} (−0.28 V).[69]

Fig. 2 shows a HAADF-STEM image, EELS composition mappings, a single NP line scan and a HRTEM micrograph from $Ni_{2.5}Co_{0.5}Sn_2$ NPs (see Fig. S3† for additional compositions). All

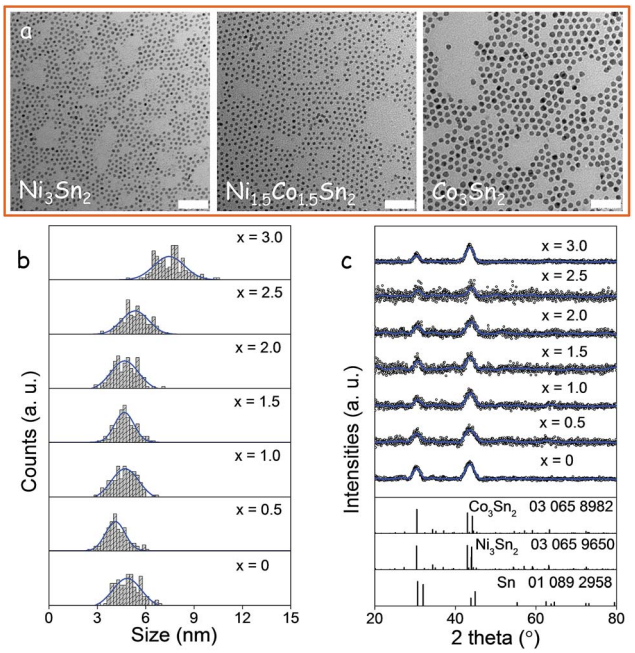

Fig. 1 (a) Representative TEM micrographs of $Ni_{3-x}Co_xSn_2$ NPs with different Co contents: $x = 0$, $x = 1.5$, and $x = 3.0$. Scale bars: 50 nm. (b) Size distribution histograms obtained from the TEM images of $Ni_{3-x}Co_xSn_2$ ($0 \leq x \leq 3$) NPs. (c) XRD patterns of $Ni_{3-x}Co_xSn_2$ ($0 \leq x \leq 3$) NPs.

Table 1 Average NP size (TEM) and Ni : Co : Sn composition of $Ni_{3-x}Co_xSn_2$ NPs

		EDX			
x $Ni_{3-x}Co_xSn_2$	Average size (nm)	Ni	Co	Sn[a]	(Ni + Co)/Sn
0.0	4.9 ± 0.8	2.5	0.0	2.0	1.25
0.5	4.2 ± 0.7	1.8	0.3	2.0	1.05
1.0	4.7 ± 0.7	1.4	0.7	2.0	1.05
1.5	4.7 ± 0.7	1.3	1.3	2.0	1.30
2.0	4.7 ± 0.7	0.8	1.4	2.0	1.10
2.5	5.4 ± 0.8	0.4	1.9	2.0	1.15
3.0	7.5 ± 1.0	0.0	2.1	2.0	1.05

[a] The amount of Sn was fixed to 2.0 to calculate the Ni and Co composition.

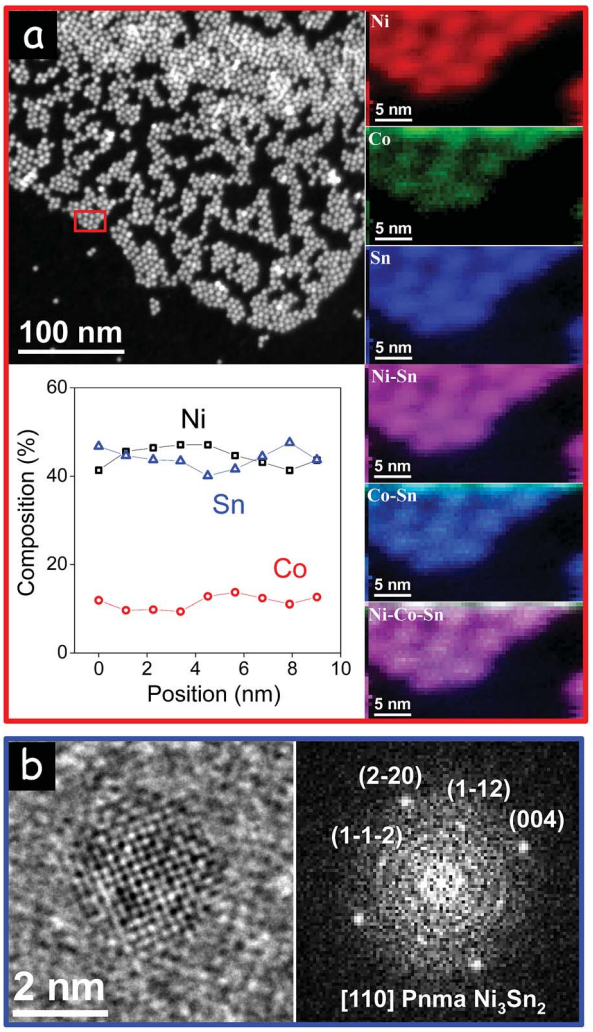

Fig. 2 (a) STEM micrograph, EELS chemical composition maps and a single NP line scan obtained from $Ni_{2.5}Co_{0.5}Sn_2$ NPs. Mappings correspond to the individual Ni $L_{2,3}$-edges at 855 eV (red), Co $L_{2,3}$-edges at 779 eV (green) and Sn M-edge at 485 eV (blue) as well as composites of Ni–Sn, Co–Sn and Ni–Co–Sn. (b) HRTEM micrograph of a single $Ni_{2.5}Co_{0.5}Sn_2$ NP and its corresponding power spectrum. Lattice fringe distances were measured to be 0.211 nm, 0.205 nm, 0.306 nm and 0.302 nm, at 89.14°, 44.38° and 50.22° which could be interpreted as the orthorhombic Ni_3Sn_2 phase visualized along its [110] zone axis.

NPs within each sample contained the three elements in similar ratios. Within each NP, the three elements were found to be homogeneously distributed as shown in the composition maps and the line scan of a single NP (Fig. 2a). HRTEM micrographs revealed NPs to have a crystal structure compatible with that of the Ni_3Sn_2 orthorhombic phase (space group = *Pnma*) with $a = 7.1100$ Å, $b = 5.2100$ Å and $c = 8.2300$ Å.

XPS analyses of the $Ni_{1.5}Co_{1.5}Sn_2$ sample showed all elements to be present in two oxidation states: a minoritarian metallic state and a majoritarian oxidized phase (Fig. S4†). This result pointed to partial surface oxidation of the NPs occurring due to their air exposure during purification, ligand removal and handling process.[59,70,71] Additionally, XPS analysis showed the surface of the $Ni_{1.5}Co_{1.5}Sn_2$ NPs to be slightly Sn rich compared with the global NP composition measured by EDX, with (Ni + Co)/Sn = 0.91. The Sn-rich surface could be created during the NP surface oxidation.

The presence of organic ligands at the surface of the NPs strongly limits their electronic interaction and their ability to interact with the media.[38] Therefore, the use of the NPs for applications where charge transfer or transport is involved requires the removal of the organic ligands used in the synthesis. Organic ligands were removed from the surface of $Ni_{3-x}Co_xSn_2$ NPs using a solution containing 1 M hydrazine hydrate in acetonitrile.[72,73] After successive cleaning with acetonitrile, the disappearance of peaks at 2890 and 2822 cm^{-1} in the FTIR spectra, corresponding to C–H stretching modes, proved the effectiveness of the ligand removal (Fig. S5†).

Electrochemical characterization

In our previous report, we showed electrodes based on Sn NPs to display no obvious oxidation and reduction peaks in the voltage range 0–0.6 V *vs.* Hg/HgO and to have a very limited performance toward the MOR and OER in an alkaline medium.[59] On the other hand, in an alkaline medium, Co is generally found in an oxidized form.[74–76] During the forward scan, at 0.15 V *vs.* Hg/HgO, cobalt is further oxidized probably to CoOOH and at *ca.* 0.55 V *vs.* Hg/HgO, CoOOH is further oxidized, possibly to CoO_2.[55,58,77,78] These phases are reduced during the reverse scan.

Fig. 3a displays a CV of Co_3Sn_2 NPs in 1 M KOH at a scan rate of 50 mV s^{-1}. Co_3Sn_2 NPs show a low activity toward the OER and small oxidation and reduction peaks during the positive and negative scans in the potential range 0–0.7 V *vs.* Hg/HgO, which correspond to the successive oxidation and reduction between cobalt oxide, hydroxide and/or oxyhydroxide phases.

In an alkaline medium, Ni is generally found in the form of $Ni(OH)_2$, which is oxidized to NiOOH at 0.45 V *vs.* Hg/HgO.[59,79–82] The formation of nickel oxyhydroxide is considered to be a key step in the electro-catalytic OER, which activates at $E \sim 0.65$ V *vs.* Hg/HgO.[42,57] Fig. 3b displays a CV of the electrode based on Ni_3Sn_2 NPs where an anodic peak corresponding to the oxidation of $Ni(OH)_2$ to NiOOH at 0.45 V *vs.* Hg/HgO is observed. In the reverse scan, a cathodic peak corresponding to the reduction of NiOOH to $Ni(OH)_2$ is clearly observed.

Fig. 4a shows representative CVs of the $Ni_{3-x}Co_xSn_2$ electrodes in 1 M KOH solution at 50 mV s^{-1}. Compared with Ni_3Sn_2, when increasing the content of Co ($0 < x < 1.5$) the anodic peak broadened and shifted to lower potentials, denoting a clear influence of Co on the Ni_3Sn_2 surface properties. At higher amounts of Co ($x \geq 1.5$), a double peak was clearly observed, pointing to the occurrence of two differentiated oxidation reactions. Similar trends were observed for the cathodic peak. Simultaneously, the peak current densities increased when adding small amounts of Co, but decreased at a higher Co loading (Table 2).

Fig. 4b and S6a–e† present the CVs of $Ni_{3-x}Co_xSn_2$ in 1.0 M KOH solution at different scan rates, between 10 and 100 mV s^{-1}. When increasing the scan rate, current densities increased, the position of the anodic peak shifted to higher potentials, and the position of the cathodic peak shifted to lower potentials. The peak shift was attributed to a limitation of the reaction kinetics, which we further analyzed.[83] In the samples containing larger amounts of Co and presenting two redox peaks, we assumed the peak at higher potential values related to a $Ni(OH)_2$ oxidation to NiOOH to be relevant for the MOR. Therefore, we just considered the peak at the highest potential values in the following calculations.

The peak current (I_P) was proportional to the sweep rate (v) in the range 10–50 mV s^{-1}. From the slope of I_P *vs.* v (Fig. 5c and S7†), the surface coverage of redox species (Γ^*) in the $Ni_{3-x}Co_xSn_2$ NPs was estimated:[59,84]

$$I_P = \left(\frac{n^2F^2}{4RT}\right)A\Gamma^* v$$

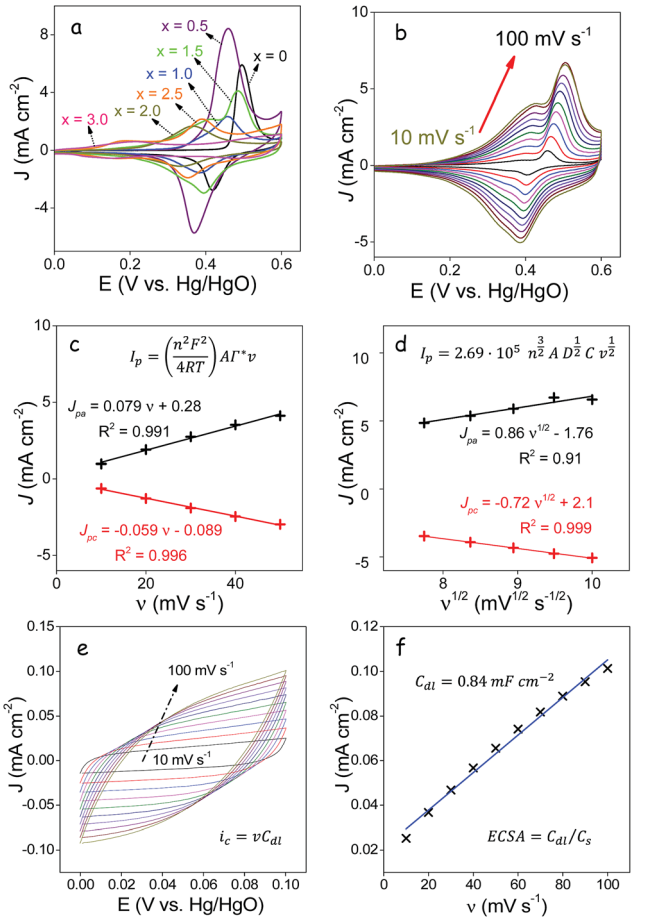

Fig. 4 (a) CVs of $Ni_{3-x}Co_xSn_2$ NP-based electrodes in 1.0 M KOH solution at a scan rate of 50 mV s^{-1}. (b) CVs of electrodes based on $Ni_{1.5}Co_{1.5}Sn_2$ ($x = 1.5$) NPs in 1.0 M KOH solution at increasingly higher potential sweep rates: 10, 20, 30, 40, 50, 60, 70, 80, 90, and 100 mV·s^{-1}. (c) Linear fitting of the anodic and cathodic peak current densities with the scan rate in the low scan rate range (10–50 mV s^{-1}) for the $Ni_{1.5}Co_{1.5}Sn_2$ NP-based electrode. (d) Linear fitting of the anodic and cathodic peak current densities with the square roots of the scan rate in the higher scan rate range (60–100 mV s^{-1}) for the $Ni_{1.5}Co_{1.5}Sn_2$ NP-based electrode. (e) CVs in the double layer region for the $Ni_{2.5}Co_{0.5}Sn_2$ electrode at scan rates of 10, 20, 30, 40, 50, 60, 70, 80, 90, and 100 mV s^{-1} in the non-faradaic range of 0–0.1 V *vs.* Hg/HgO. (f) Corresponding linear fit of the capacitive current density *vs.* scan rates to estimate C_{dl} and calculate the ECSA.

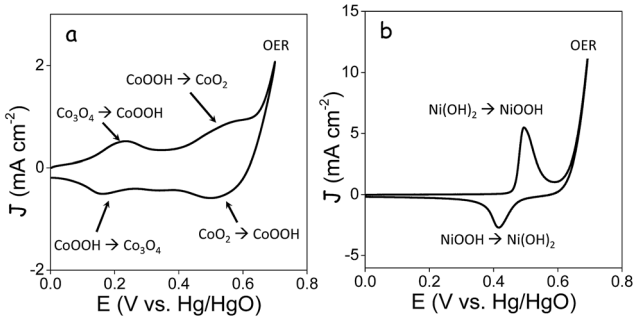

Fig. 3 (a) CV of Co_3Sn_2 electrodes in 1 M KOH solution at a scan rate of 50 mV s^{-1}. Tentative reduction and oxidation products are displayed. (b) CV of Ni_3Sn_2 electrodes in 1 M KOH solution at a scan rate of 50 mV s^{-1}.

Table 2 Summary of the electrocatalytic performance of $Ni_{3-x}Co_xSn_2$ NP-based electrodes[a]

x	E_{pa} V *vs.* Hg/HgO	J_{pa} mA cm^{-2}	E_{pc} V *vs.* Hg/HgO	J_{pa} mA cm^{-2}	ΔE V	Γ* mol cm^{-2} ($\times 10^{-8}$)	D cm^2 s^{-1} ($\times 10^{-9}$)	E_η V 10 mA cm^{-2}	J mA cm^{-2} @ 0.6 V	ΔJ @ 0.6 V
0	0.496	5.934	0.417	−2.765	0.079	8.6	8.4	0.525	34.4	−15.2%
0.5	0.461	8.436	0.369	−5.756	0.092	14.2	12.8	0.452	65.5	−23.5%
1.0	0.457	2.351	0.383	−1.564	0.074	4.1	2.9	0.479	51.8	−40.8%
1.5	0.486	3.921	0.393	−2.970	0.093	7.3	4.6	0.464	53.8	−31.7%
2.0	0.364	1.682	0.330	−1.125	0.034	3.1	2.2	0.483	39.4	−81.4%
2.5	0.391	2.187	0.356	−1.903	0.035	4.7	4.2	0.481	34.4	−64.2%
3.0	0.207	0.579	0.172	−0.541	0.035	—	—	—	—	—

[a] In samples showing two anodic/cathodic peaks, J_{pa}, E_{pa}, J_{pc}, E_{pc} and ΔE were measured from the highest voltage peak. CVs were recorded in 1.0 M KOH solution at a scan rate of 50 mV s^{-1}. E_η, J, and ΔJ were calculated from the CVs in 1.0 M KOH solution containing 2.0 M methanol at a scan rate of 50 mV s^{-1}.

where n, F, R, T and A are the number of transferred electrons (assumed to be 1), the Faraday constant (96 845 C mol^{-1}), the gas constant (8.314 J K^{-1} mol^{-1}), the temperature and the geometric surface area of the GC electrodes (0.196 cm^2), respectively.

On averaging the results obtained from the forward and reverse scans, the surface coverage of redox species of Ni_3Sn_2 NP-based electrodes was calculated to be 8.6×10^{-8} mol cm^{-2}. When introducing a small amount of Co, $Ni_{2.5}Co_{0.5}Sn_2$, the surface coverage increased to 1.4×10^{-7} mol cm^{-2}. Higher amounts of Co decreased this coverage to values below that of Ni_3Sn_2.

In the high scan rate range, 60–100 mV s^{-1}, the peak current increased linearly with the square root of the voltage scan rate, pointing to a diffusion-limited redox reaction[59,84]

$$I_p = 2.69 \times 10^5 n^{3/2} A D^{1/2} C v^{1/2}$$

where D is the diffusion coefficient of the reaction limiting species and C is the initial concentration of redox species. Qualitatively, we observed the slope of I_P *vs.* $v^{1/2}$ obtained from Ni_3Sn_2 NP-based electrodes to increase when adding small amounts of Co. This observation pointed to faster diffusion of the redox limiting species with the incorporation of Co. For Ni-based electrodes, the proton diffusion is generally accepted to be the rate limiting step that controls the oxidation reaction $Ni(OH)_2 \leftrightarrow NiOOH$.[59,85] Therefore, using the above equation and taking into account a proton density of 0.043 mol cm^{-3} for all the electrodes, the proton diffusion coefficient of the different materials was estimated.[59] The proton diffusion coefficient of Ni_3Sn_2 NP-based electrodes was 8.4×10^{-9} cm^2 s^{-1}. As qualitatively noted before, the diffusivity increased when introducing a small amount of Co within the structure: 1.3×10^{-8} cm^2 s^{-1} for $Ni_{2.5}Co_{0.5}Sn_2$, but decreased at higher Co concentrations: 2.9×10^{-9} cm^2 s^{-1} for Ni_2CoSn_2 and 4.6×10^{-9} cm^2 s^{-1} for $Ni_{1.5}Co_{1.5}Sn_2$.

The electrochemically active surface area (ECSA) was estimated by using the electrochemical double-layer capacitance (C_{dl}) on the basis of CVs recorded at different scan rates in the non-faradaic potential range (0–0.1 V *vs.* Hg/HgO).[86] Plotting i_c *vs.* yielded a straight line with a slope equal to C_{dl} (Fig. 4e) and then the ECSA was calculated by dividing C_{dl} by the specific capacitance:[87]

$$\mathrm{ECSA} = C_{dl}/C_s$$

where C_s is a general specific capacitance of 0.04 mF cm^{-2} based on a typical value reported for metal electrodes in aqueous NaOH solution.[88] For $Ni_{2.5}Co_{0.5}Sn_2$, the calculated value of C_{dl} was 0.84 mF cm^{-2}, and the ECSA was 21 cm^{-2}.

From the EDX analysis of the composition of the NPs during KOH cycling, we observed the amount of Sn to slowly decrease with the cycle number (Fig. S10†) pointing to the partial dissolution of Sn from the $Ni_{3-x}Co_xSn_2$ alloy nanoparticles.

Electrocatalytic activity toward the MOR

Fig. S6† compares the cyclic voltammograms in 1.0 M KOH solution of electrodes based on Co_3Sn_2 and Ni_3Sn_2 NPs in the absence and presence of a low concentration of methanol (0.5 M). Co_3Sn_2 showed much lower activities than the Ni_3Sn_2 catalyst toward both the OER and MOR. The OER onset was found at *ca.* 0.65 V *vs.* Hg/HgO for both samples. While no significant MOR activity was appreciated in the Co_3Sn_2 electrode, the MOR was activated at *ca* 0.45 V *vs.* Hg/HgO in Ni_3Sn_2-based electrodes. This voltage coincided with the formation of NiOOH. Indeed, it is generally accepted that in Ni-based catalysts, the MOR is activated by the formation of NiOOH, which is believed to directly participate in the reaction.[42,47,59]

$$Ni(OH)_2 + OH^- \rightarrow NiOOH + H_2O + e^-$$

$$NiOOH + CH_3OH \rightarrow Ni(OH)_2 + \text{products}$$

To avoid the OER in the test of the MOR over $Ni_{3-x}Co_xSn_2$ NP-based electrodes, the potential range scanned was limited to 0–0.6 V *vs.* Hg/HgO.

Fig. 5a shows representative CVs of a bare carbon black electrode and $Ni_{3-x}Co_xSn_2$ NP-based electrodes in 1.0 M KOH solution with 2 M methanol at a scan rate of 50 mV s^{-1}. Co_3Sn_2 presented very limited current densities toward the MOR, similar to the carbon black electrode. However, surprisingly, all $Ni_{3-x}Co_xSn_2$ NP-based electrodes showed higher activity than the Ni_3Sn_2 NP-based electrode, including a lower onset potential and higher mass current densities. The onset potential (@ 10 mA cm^{-2}) was reduced from 0.53 V for Ni_3Sn_2 to 0.45 V for

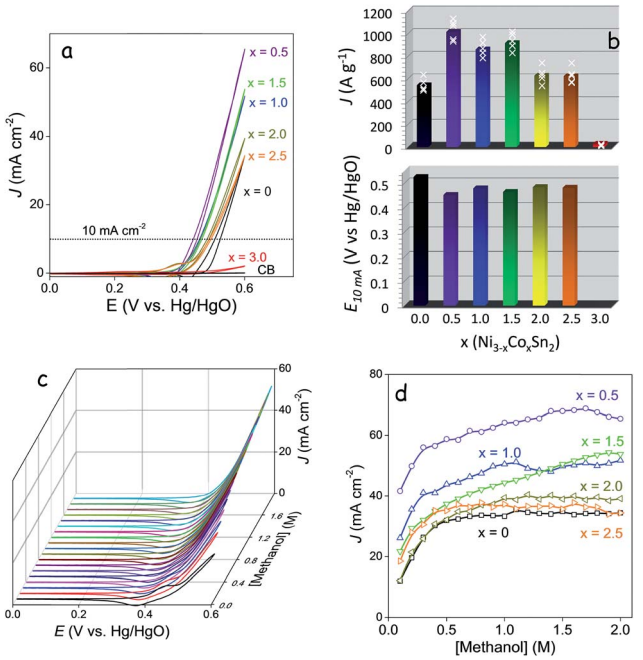

Fig. 5 (a) CVs of $Ni_{3-x}Co_xSn_2$ ($0 \leq x \leq 3$) and CB electrodes in 1.0 M KOH containing 2.0 M methanol at a scan rate of 50 mV s^{-1}. (b) Mass current density at 0.6 V and applied potential required to reach 10 mA cm^{-2} in $Ni_{3-x}Co_xSn_2$ ($0 \leq x \leq 3$) electrodes in 1.0 M KOH with 2.0 M methanol. Mass current densities measured from 5 electrodes with the same composition are presented. Bars reflect the average value of these 5 measurements. The standard deviations of the distributions were in the range from 7% to 10% for all the catalysts containing Ni and 20% for the Co_3Sn_2 catalyst that showed a much lower activity. (c) CVs of the $Ni_{1.5}Co_{1.5}Sn_2$ electrode in 1.0 M KOH solution with different methanol concentrations from 0.1 M to 2.0 M at a scan rate of 50 mV s^{-1}. (d) Comparison of the current density at 0.6 V of $Ni_{3-x}Co_xSn_2$ ($0 \leq x \leq 2.5$) electrodes as a function of methanol concentrations from 0.1 M to 2.0 M.

$Ni_{2.5}Co_{0.5}Sn_2$ and 0.46–0.48 V for the other Co-containing NP-based electrodes (Fig. 5). The mass current density, calculated from averaging the results obtained from 5 different electrodes with the same composition, was found to increase with the incorporation of Co into the Ni_3Sn_2 alloy, from 543 A g^{-1} for Ni_3Sn_2 to 1016 A g^{-1} for the $Ni_{2.5}Co_{0.5}Sn_2$ electrode (Fig. 5b). At higher Co/Ni ratios, the mass current density decreased with the Co content, but was kept above that of Ni_3Sn_2. In Table S1† a comparison of the performance toward the MOR of the $Ni_{3-x}Co_xSn_2$ NP-based electrodes with other Ni-based electrodes and a commercial Pt/C composite is presented. The comparison demonstrated that $Ni_{3-x}Co_xSn_2$ NP-based electrodes with a preliminary optimized composition, $Ni_{2.5}Co_{0.5}Sn_2$, outperformed most previously developed catalysts.

Fig. 5c, S8 and S9† show the CVs of $Ni_{3-x}Co_xSn_2$ NP-based electrodes in 1.0 M KOH solution with 0.1–2.0 M methanol at a scan rate of 50 mV s^{-1}. Fig. 5d and S7† present the current density at 0.6 V in 1.0 M KOH as a function of the methanol concentrations, from 0.1 to 2.0 M. For all electrodes, an initial rapid rise of the current density with the methanol concentration was observed. For Ni_3Sn_2, $Ni_{1.0}Co_{2.0}Sn_2$ and $Ni_{0.5}Co_{2.5}Sn_2$ electrodes, the current density stabilized at concentrations higher than 0.5 M methanol. However, the electrodes with a low Co loading still showed a slight increase of the current density above this concentration, which should be associated with lower poisoning of the active sites by methanol adsorption in $Ni_{3-x}Co_xSn_2$ ($x \leq 1.5$) NPs compared with Ni_3Sn_2 NPs (Fig. 5c, S8 and S9†). In particular, at 0.6 V *vs.* Hg/HgO, the $Ni_{2.5}Co_{0.5}Sn_2$ electrode displayed a current density of 41 mA cm^{-2} at 0.1 M, 59 mA cm^{-2} at 0.5 M and 65 mA cm^{-2} at 2.0 M. On the other hand, the Ni_3Sn_2 electrode was characterized by a current density of 12 mA cm^{-2} at 0.1 M, 32 mA cm^{-2} at 0.5 M and 34 mA cm^{-2} at 2.0 M at 0.6 V.

The long-term stability of $Ni_{3-x}Co_xSn_2$ NP-based electrodes was evaluated by CA measurements in 1.0 M KOH solution containing 2.0 M methanol at 0.6 V for 10 000 s (Fig. 6a). While an improved performance toward high methanol concentrations was obtained with the addition of small amounts of Co, the electrode stability decreased when adding increasingly higher amounts of Co, the Ni_3Sn_2 electrode being the most stable, followed by the $Ni_{2.5}Co_{0.5}Sn_2$. Compared with our previous work, the stability of the Ni_3Sn_2 and $Ni_{2.5}Co_{0.5}Sn_2$ electrodes was better than that of elemental Ni electrodes, which points to a beneficial role of Sn in this direction.[59] The improved stability with the presence of Sn could be related to a modification of the electronic structure or the promotion of the catalytic reaction of poisoning species, and could be limited by the partial dissolution of this element in the presence of KOH.

The stability of the $Ni_{2.5}Co_{0.5}Sn_2$ electrode was also evaluated at the same concentration of methanol with continuous CV scanning with 100 mV s^{-1}. As shown in Fig. 6b, the electrode lost 12.9% (500 circles), 21.5% (1000 circles) and 35.1% (1500 circles) of the current density of the 1st CV at 0.6 V. This performance decay could originate from (i) the progressive poisoning of the active sites by the reaction intermediates/products, (ii) a restructuration of the alloy NPs or a change of the NP electronic or chemical properties during the reaction,

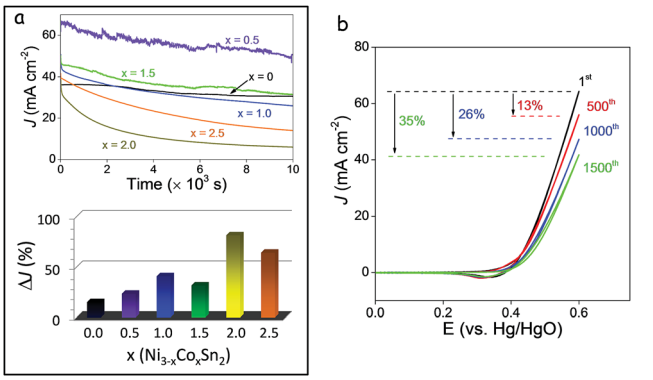

Fig. 6 (a) CA response of $Ni_{3-x}Co_xSn_2$ electrodes in 1.0 M KOH and 2.0 M methanol at 0.6 V for 10 000 s. Current density change, $\Delta J = (J_1 - J_2)/J_1$, during the 10 000 s tested, where J_1 and J_2 are the current densities measured at the 50th and 10 000th s, respectively. (b) CVs of the $Ni_{2.5}Co_{0.5}Sn_2$ electrode in 1.0 M KOH electrolyte with 2.0 M methanol at a scan rate of 100 mV s^{-1} at the 1st, 500th, 1000th and 1500th cycles.

potentially related to the presence of cobalt, and (iii) the gradual dissolution of Sn, whose presence was demonstrated to improve stability.

CO is generally considered as the most common intermediate/product degrading the catalyst performance over time through the blocking of its active sites.[35,41,43,56,58] Additional CA measurements were performed on the electrodes based on Ni_3Sn_2 NPs and $Ni_{2.5}Co_{0.5}Sn_2$ NPs in 1.0 M KOH and 1.0 M methanol at 0.6 V (Fig. 7). At a certain time ($t = 600$ s), a gentle flow of CO was bubbled into the solution to determine its effect on the current density. With the presence of additional CO, both electrodes suffered a similar loss in the current density: 14.9% for $Ni_{2.5}Co_{0.5}Sn_2$ and 15.6% for Ni_3Sn_2. The same experiment in the absence of CO resulted in a significantly larger decrease of current density for the $Ni_{2.5}Co_{0.5}Sn_2$ electrode: 7.7% for $Ni_{2.5}Co_{0.5}Sn_2$ and 6.0% for Ni_3Sn_2. This result demonstrates the Co-containing electrode not to be specially sensitive to CO poisoning when compared with the Ni_3Sn_2-based one.

DFT calculations

Complementary to the experimental work, to gain insight into the electronic effect that the Co incorporation had on the Ni_3Sn_2 alloy, DFT calculations of the surface of the metallic alloys were performed (see details in the Experimental section and Fig. S11–14†). DFT calculations showed that the adsorption energies of methanol (E_{ads}) on Ni sites at Ni_3Sn_2 (001) and (110) facets were −0.57 eV and −0.49 eV. These values slightly increased for Ni sites at $Ni_{2.5}Co_{0.5}Sn_2$ surfaces: −0.59 eV and −0.74 eV for $Ni_{2.5}Co_{0.5}Sn_2$ (001) and (110), respectively. The adsorption energies of methanol on Co sites at $Ni_{2.5}Co_{0.5}Sn_2$ (001) and (110) surfaces were −0.63 eV and −0.52 eV, respectively. The higher absolute values of E_{ads} on Ni than on Co at $Ni_{2.5}Co_{0.5}Sn_2$ surfaces pointed to the preferential adsorption of methanol molecules on the former. The higher E_{ads} obtained from the ternary alloy should imply higher methanol poisoning which is not observed in the measurements of the current density as a function of the methanol concentration. On the other hand, the adsorption energies of CO on Ni sites at $Ni_{2.5}Co_{0.5}Sn_{2.0}$ (001) and (110) surfaces, −2.46 eV and −2.16 eV, were also higher than those at Ni_3Sn_2 (001) and (110), −2.07 eV and −1.98 eV, which could result in higher CO poisoning that was not reflected in our experimental results. Further comprehensive DFT calculations including all the reaction steps and the appropriate alloy composition under reaction conditions would be required to evaluate the exact MOR mechanism.

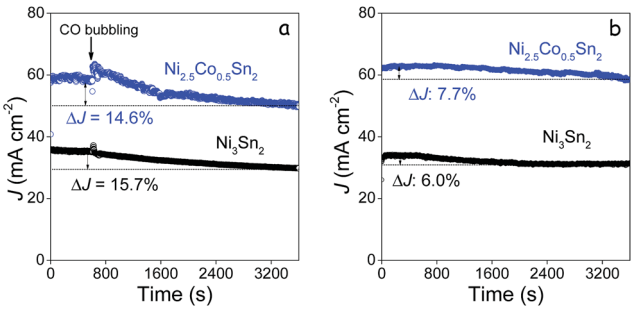

Fig. 7 CA of Ni_3Sn_2 NPs and $Ni_{2.5}Co_{0.5}Sn_2$ NPs in 1.0 M KOH and 1.0 M methanol at 0.6 V: (a) in the presence of a gentle CO flow (10% in He) added at $t = 600$ s. (b) Without additional CO incorporation into the solution. $\Delta J = (J_1 - J_2)/J_1$, where J_1 and J_2 are the current densities measured at the 600th and 3600th s, respectively.

Conclusions

In summary, a series of $Ni_{3-x}Co_xSn_2$ ($0 \leq x \leq 3$) quasi-spherical NPs with narrow size distribution were synthesized by a solution-based one-pot method. Detailed catalytic investigation of methanol oxidation showed that the introduction of small amounts of Co into the structure improved the electrocatalytic performance. A preliminary optimized catalyst composition, $Ni_{2.5}Co_{0.5}Sn_2$, showed a current density of 65.5 mA cm^{-2} and a mass current density of 1050 mA mg^{-1} at 0.6 V *vs.* Hg/HgO for the MOR in 1.0 M KOH containing 1.0 M methanol. While the introduction of Co slightly decreased the durability with respect to Ni_3Sn_2, $Ni_{2.5}Co_{0.5}Sn_2$ NP-based electrodes demonstrated significant stability during continuous cycling and increased activity at high methanol concentrations. In any case, the presence of Sn was found to be essential to improve stability with respect to elemental Ni, although Sn was observed to slowly dissolve in the presence of KOH. Overall, the excellent activity and stability towards the MOR of ternary $Ni_{3-x}Co_xSn_2$ NPs suggested them to be attractive anode materials for DMFCs.

Author contributions

The manuscript was prepared through the contribution of all the authors. A. Cabot and Z. Luo conceived and guided the project, and supervised the work. J. Li designed the experiments, produced the nanoparticles, conducted XRD, TEM, SEM-EDS and FT-IR characterization and electrochemical measurements, and wrote the first draft of the manuscript. F. He carried out the DFT calculations. Y. Zuo and C. Zhang performed experiments towards determining the ECSA. J. Liu, X. Yu and R. Du significantly contributed to the results and discussion. T. Zhang, M. F. Infante-Carrió, P. Tang and J. Arbiol performed structural and compositional characterization of NPs by means of HRTEM and EELS, and discussed the results. J. Llorca measured and discussed XPS data. The manuscript was corrected and improved by all the authors.

Conflicts of interest

There are no conflicts to declare.

Acknowledgements

This work was supported by the European Regional Development Funds and by the Spanish Ministerio de Economía y Competitividad through the project SEHTOP (ENE2016-77798-C4-3-R) and VALPEC (ENE2017-85087-C3). J. Li and T. Zhang thank the China Scholarship Council (CSC) for scholarship support. T. Zhang and J. Arbiol acknowledge funding from

Generalitat de Catalunya 2017 SGR 327. ICN2 acknowledges support from the Severo Ochoa Programme (MINECO, Grant no. SEV-2013-0295). IREC and ICN2 are funded by the CERCA Programme/Generalitat de Catalunya. Part of the present work has been performed in the framework of the Universitat Autònoma de Barcelona Materials Science PhD program. J. Llorca is a Serra Húnter Fellow and is grateful to the ICREA Academia program and to MINECO/FEDER grant ENE2015-63969-R and GC 2017 SGR 128.

Notes and references

1 X. Zhou, J. Qiao, L. Yang and J. Zhang, *Adv. Energy Mater.*, 2014, **4**, 1301523.
2 N. Demirdöven and J. Deutch, *Science*, 2004, **305**, 974–976.
3 X. Zhao, M. Yin, L. Ma, L. Liang, C. Liu, J. Liao, T. Lu and W. Xing, *Energy Environ. Sci.*, 2011, **4**, 2736.
4 T. Schultz, S. Zhou and K. Sundmacher, *Chem. Eng. Technol.*, 2001, **24**, 1223–1233.
5 Y. Feng, H. Liu and J. Yang, *Sci. Adv.*, 2017, **3**, e1700580.
6 J. N. Tiwari, R. N. Tiwari, G. Singh and K. S. Kim, *Nano Energy*, 2013, **2**, 553–578.
7 H. Huang and X. Wang, *J. Mater. Chem. A*, 2014, **2**, 6266–6291.
8 S. Wasmus and A. Küver, *J. Electroanal. Chem.*, 1999, **461**, 14–31.
9 G. A. Tritsaris and J. Rossmeisl, *J. Phys. Chem. C*, 2012, **116**, 11980–11986.
10 N. Kakati, J. Maiti, S. H. Lee, S. H. Jee, B. Viswanathan and Y. S. Yoon, *Chem. Rev.*, 2014, **114**, 12397–12429.
11 S. P. S. Badwal, S. Giddey, A. Kulkarni, J. Goel and S. Basu, *Appl. Energy*, 2015, **145**, 80–103.
12 S. S. Munjewar, S. B. Thombre and R. K. Mallick, *Ionics*, 2017, **23**, 1–18.
13 S. K. Kamarudin, F. Achmad and W. R. W. Daud, *Int. J. Hydrogen Energy*, 2009, **34**, 6902–6916.
14 S. S. Munjewar, S. B. Thombre and R. K. Mallick, *Renewable Sustainable Energy Rev.*, 2017, **67**, 1087–1104.
15 P. Kumar, K. Dutta, S. Das and P. P. Kundu, *Int. J. Energy Res.*, 2014, **38**, 1367–1390.
16 L. R. Merte, M. Ahmadi, F. Behafarid, L. K. Ono, E. Lira, J. Matos, L. Li, J. C. Yang and B. Roldan Cuenya, *ACS Catal.*, 2013, **3**, 1460–1468.
17 K. Sasaki, H. Naohara, Y. Choi, Y. Cai, W.-F. Chen, P. Liu and R. R. Adzic, *Nat. Commun.*, 2012, **3**, 1115.
18 Z. Daşdelen, Y. Yıldız, S. Eriş and F. Şen, *Appl. Catal., B*, 2017, **219**, 511–516.
19 C. Cui, L. Gan, M. Heggen, S. Rudi and P. Strasser, *Nat. Mater.*, 2013, **12**, 765–771.
20 S. Wu, J. Liu, D. Liang, H. Sun, Y. Ye, Z. Tian and C. Liang, *Nano Energy*, 2016, **26**, 699–707.
21 G. Long, X. Li, K. Wan, Z. Liang, J. Piao and P. Tsiakaras, *Appl. Catal., B*, 2017, **203**, 541–548.
22 J. Chen, Q. Niu, G. Chen, J. Nie and G. Ma, *J. Phys. Chem. C*, 2017, **121**, 1463–1471.
23 Q. Jiang, L. Jiang, H. Hou, J. Qi, S. Wang and G. Sun, *J. Phys. Chem. C*, 2010, **114**, 19714–19722.
24 K. W. Park, J. H. Choi, B. K. Kwon, S. A. Lee, Y. E. Sung, H. Y. Ha, S. A. Hong, H. Kim and A. Wieckowski, *J. Phys. Chem. B*, 2002, **106**, 1869–1877.
25 L. Li, Y. Wu, J. Lu, C. Nan and Y. Li, *Chem. Commun.*, 2013, **49**, 7486.
26 K.-W. Park, J.-H. Choi and Y.-E. Sung, *J. Phys. Chem. B*, 2003, **107**, 5851–5856.
27 S. Wang, G. Yang and S. Yang, *J. Phys. Chem. C*, 2015, **119**, 27938–27945.
28 L.-X. Ding, G.-R. Li, Z.-L. Wang, Z.-Q. Liu, H. Liu and Y.-X. Tong, *Chem.–Eur. J.*, 2012, **18**, 8386–8391.
29 S. Papadimitriou, S. Armyanov, E. Valova, A. Hubin, O. Steenhaut, E. Pavlidou, G. Kokkinidis and S. Sotiropoulos, *J. Phys. Chem. C*, 2010, **114**, 5217–5223.
30 K. W. Park, J. H. Choi, B. K. Kwon, S. A. Lee, Y. E. Sung, H. Y. Ha, S. A. Hong, H. Kim and A. Wieckowski, *J. Phys. Chem. B*, 2002, **106**, 1869–1877.
31 S. Chen, P. J. Ferreira, W. Sheng, N. Yabuuchi, L. F. Allard and Y. Shao-Horn, *J. Am. Chem. Soc.*, 2008, **130**, 13818–13819.
32 Y. Ma, L. Yin, T. Yang, Q. Huang, M. He, H. Zhao, D. Zhang, M. Wang and Z. Tong, *ACS Appl. Mater. Interfaces*, 2017, **9**, 36164–36172.
33 Y. Liao, G. Yu, Y. Zhang, T. Guo, F. Chang and C.-J. Zhong, *J. Phys. Chem. C*, 2016, **120**, 10476–10484.
34 H.-J. Qiu, X. Shen, J. Q. Wang, A. Hirata, T. Fujita, Y. Wang and M. W. Chen, *ACS Catal.*, 2015, **5**, 3779–3785.
35 G. You, J. Jiang, M. Li, L. Li, D. Tang, J. Zhang, X. C. Zeng and R. He, *ACS Catal.*, 2018, **8**, 132–143.
36 Y. Liu, M. Chi, V. Mazumder, K. L. More, S. Soled, J. D. Henao and S. Sun, *Chem. Mater.*, 2011, **23**, 4199–4203.
37 Y. Liu, D. Li, V. R. Stamenkovic, S. Soled, J. D. Henao and S. Sun, *ACS Catal.*, 2011, **1**, 1719–1723.
38 Z. Luo, J. Lu, C. Flox, R. Nafria, A. Genç, J. Arbiol, J. Llorca, M. Ibáñez, J. R. Morante and A. Cabot, *J. Mater. Chem. A*, 2016, **4**, 16706–16713.
39 F. Han, X. Wang, J. Lian and Y. Wang, *Carbon N. Y.*, 2012, **50**, 5498–5504.
40 X. Wang, J. Lian and Y. Wang, *Int. J. Hydrogen Energy*, 2014, **39**, 14288–14295.
41 D. Lim, D. Choi, W. Lee and H. Lee, *Appl. Catal.*, 2009, **89**, 484–493.
42 D. Wu, W. Zhang and D. Cheng, *ACS Appl. Mater. Interfaces*, 2017, **9**, 19843–19851.
43 W. Huang, H. Wang, J. Zhou, J. Wang, P. N. Duchesne, D. Muir, P. Zhang, N. Han, F. Zhao, M. Zeng, J. Zhong, C. Jin, Y. Li, S.-T. Lee and H. Dai, *Nat. Commun.*, 2015, **6**, 10035.
44 A. Serov and C. Kwak, *Appl. Catal., B*, 2009, **90**, 313–320.
45 I. Danaee, M. Jafarian, F. Forouzandeh, F. Gobal and M. G. Mahjani, *Int. J. Hydrogen Energy*, 2009, **34**, 859–869.
46 I. Danaee, M. Jafarian, F. Forouzandeh, F. Gobal and M. G. Mahjani, *Int. J. Hydrogen Energy*, 2008, **33**, 4367–4376.
47 X. Cui, P. Xiao, J. Wang, M. Zhou, W. Guo, Y. Yang, Y. He, Z. Wang, Y. Yang, Y. Zhang and Z. Lin, *Angew. Chem., Int. Ed.*, 2017, **56**, 4488–4493.
48 I. Danaee, M. Jafarian, A. Mirzapoor, F. Gobal and M. G. Mahjani, *Electrochim. Acta*, 2010, **55**, 2093–2100.

49 S. L. Candelaria, N. M. Bedford, T. J. Woehl, N. S. Rentz, A. R. Showalter, S. Pylypenko, B. A. Bunker, S. Lee, B. Reinhart, Y. Ren, S. P. Ertem, E. B. Coughlin, N. A. Sather, J. L. Horan, A. M. Herring and L. F. Greenlee, *ACS Catal.*, 2017, **7**, 365–379.
50 Y. Vlamidis, S. Fiorilli, M. Giorgetti, I. Gualandi, E. Scavetta and D. Tonelli, *RSC Adv.*, 2016, **6**, 110976–110985.
51 A. Roy, H. S. Jadhav, G. M. Thorat and J. G. Seo, *New J. Chem.*, 2017, **41**, 9546–9553.
52 S. Samanta, K. Bhunia, D. Pradhan, B. Satpati and R. Srivastava, *ACS Sustainable Chem. Eng.*, 2018, **6**, 2023–2036.
53 N. A. M. Barakat, M. Motlak, B.-S. Kim, A. G. El-Deen, S. S. Al-Deyab and A. M. Hamza, *J. Mol. Catal. A: Chem.*, 2014, **394**, 177–187.
54 T. Rostami, M. Jafarian, S. Miandari, M. G. Mahjani and F. Gobal, *Chin. J. Catal.*, 2015, **36**, 1867–1874.
55 P. Manivasakan, P. Ramasamy and J. Kim, *Nanoscale*, 2014, **6**, 9665–9672.
56 E. Umeshbabu and G. Ranga Rao, *Electrochim. Acta*, 2016, **213**, 717–729.
57 X. Cui, Y. Yang, Y. Li, F. Liu, H. Peng, Y. Zhang and P. Xiao, *J. Electrochem. Soc.*, 2015, **162**, F1415–F1424.
58 X. Cui, W. Guo, M. Zhou, Y. Yang, Y. Li, P. Xiao, Y. Zhang and X. Zhang, *ACS Appl. Mater. Interfaces*, 2015, **7**, 493–503.
59 J. Li, Z. Luo, Y. Zuo, J. Liu, T. Zhang, P. Tang, J. Arbiol, J. Llorca and A. Cabot, *Appl. Catal., B*, 2018, **234**, 10–18.
60 Y. Gu, J. Luo, Y. Liu, H. Yang, R. Ouyang and Y. Miao, *J. Nanosci. Nanotechnol.*, 2015, **15**, 3743–3749.
61 K. D. Gilroy, A. Ruditskiy, H.-C. Peng, D. Qin and Y. Xia, *Chem. Rev.*, 2016, **116**, 10414–10472.
62 P. Strasser, S. Koh, T. Anniyev, J. Greeley, K. More, C. Yu, Z. Liu, S. Kaya, D. Nordlund, H. Ogasawara, M. F. Toney and A. Nilsson, *Nat. Chem.*, 2010, **2**, 454–460.
63 A. Hamza, S. El-Refaei, A. Elzatahry and A. Abdullah, *Appl. Sci.*, 2017, **7**, 64.
64 G. Kresse and J. Furthmüller, *Phys. Rev. B: Condens. Matter Mater. Phys.*, 1996, **54**, 11169–11186.
65 G. Kresse and J. Hafner, *Phys. Rev. B: Condens. Matter Mater. Phys.*, 1994, **49**, 14251–14269.
66 G. Kresse and J. Hafner, *Phys. Rev. B: Condens. Matter Mater. Phys.*, 1993, **47**, 558–561.
67 G. Kresse and J. Furthmüller, *Comput. Mater. Sci.*, 1996, **6**, 15–50.
68 H. Fjellvåg, A. Kjekshus, R. Stomberg, R. Zingales, I. Vikholm, F. Urso, J. Weidlein and R. A. Zingaro, *Acta Chem. Scand.*, 1986, **40a**, 23–30.
69 R. Chang, *General Chemistry: The Essential Concepts*, American Chemical Society, 2006.
70 Y. Liu, X. Liu, Q. Feng, D. He, L. Zhang, C. Lian, R. Shen, G. Zhao, Y. Ji, D. Wang, G. Zhou and Y. Li, *Adv. Mater.*, 2016, **28**, 4747–4754.
71 M. He, L. Protesescu, R. Caputo, F. Krumeich and M. V. Kovalenko, *Chem. Mater.*, 2015, **27**, 635–647.
72 M. Walter, S. Doswald and M. V. Kovalenko, *J. Mater. Chem. A*, 2016, **4**, 7053–7059.
73 M. He, K. Kravchyk, M. Walter and M. V. Kovalenko, *Nano Lett.*, 2014, **14**, 1255–1262.
74 H. G. Meier, J. R. Vilche and A. J. Arvía, *J. Electroanal. Chem. Interfacial Electrochem.*, 1982, **138**, 367–379.
75 E. B. Castro, C. A. Gervasi and J. R. Vilche, *J. Appl. Electrochem.*, 1998, **28**, 835–841.
76 I. G. Casella and M. Gatta, *J. Electroanal. Chem.*, 2002, **534**, 31–38.
77 I. G. Casella and M. Gatta, *J. Electroanal. Chem.*, 2002, **534**, 31–38.
78 M. Walter, S. Doswald, F. Krumeich, M. He, R. Widmer, N. P. Stadie and M. V. Kovalenko, *Nanoscale*, 2018, **10**, 3777–3783.
79 M. W. Khalil, M. A. Abdel Rahim, A. Zimmer, H. B. Hassan and R. M. Abdel Hameed, *J. Power Sources*, 2005, **144**, 35–41.
80 L. Wang, G. Zhang, Y. Liu, W. Li, W. Lu and H. Huang, *Nanoscale*, 2016, **8**, 11256–11263.
81 J. Wang, D. Teschner, Y. Yao, X. Huang, M. Willinger, L. Shao and R. Schlögl, *J. Mater. Chem. A*, 2017, **5**, 9946–9951.
82 Y. Yu, Q. Yang, X. Li, M. Guo and J. Hu, *Green Chem.*, 2016, **18**, 2827–2833.
83 D. Chen and S. D. Minteer, *J. Power Sources*, 2015, **284**, 27–37.
84 A. J. Bard and L. R. Faulkner, 2001.
85 D. M. MacArthur, *J. Electrochem. Soc.*, 1970, **117**, 422.
86 J. D. Benck, Z. Chen, L. Y. Kuritzky, A. J. Forman and T. F. Jaramillo, *ACS Catal.*, 2012, **2**, 1916–1923.
87 C. C. L. McCrory, S. Jung, I. M. Ferrer, S. M. Chatman, J. C. Peters and T. F. Jaramillo, *J. Am. Chem. Soc.*, 2015, **137**, 4347–4357.
88 C. C. L. McCrory, S. Jung, J. C. Peters and T. F. Jaramillo, *J. Am. Chem. Soc.*, 2013, **135**, 16977–16987.

Electrochimica Acta 304 (2019) 246–254

Contents lists available at ScienceDirect

Electrochimica Acta

journal homepage: www.elsevier.com/locate/electacta

Compositionally tuned Ni_xSn alloys as anode materials for lithium-ion and sodium-ion batteries with a high pseudocapacitive contribution

Junshan Li [a, b, 1], Xijun Xu [c, d, 1], Zhishan Luo [a], Chaoqi Zhang [a], Xiaoting Yu [a], Yong Zuo [a], Ting Zhang [e], Pengyi Tang [e], Jordi Arbiol [e, f], Jordi Llorca [g], Jun Liu [c, d, **], Andreu Cabot [a, f, *]

[a] Catalonia Institute for Energy Research - IREC, Sant Adrià de Besòs, Barcelona, 08930, Spain
[b] Departament d'Electronica, Universitat de Barcelona, 08028, Barcelona, Spain
[c] Guangdong Provincial Key Laboratory of Advanced Energy Storage Materials, School of Materials Science and Engineering, South China University of Technology, Guangzhou, 510641, PR China
[d] SUNWODA-SCUT Joint Laboratory for Advanced Energy Storage Technology, South China University of Technology, Guangzhou, 510641, PR China
[e] Catalan Institute of Nanoscience and Nanotechnology (ICN2), CSIC and BIST, Campus UAB, Bellaterra, 08193, Barcelona, Spain
[f] ICREA, Pg. Lluís Companys 23, 08010, Barcelona, Spain
[g] Institute of Energy Technologies, Department of Chemical Engineering and Barcelona Research Center in Multiscale Science and Engineering, Universitat Politècnica de Catalunya, EEBE, 08019, Barcelona, Spain

ARTICLE INFO

Article history:
Received 27 November 2018
Received in revised form
28 January 2019
Accepted 25 February 2019
Available online 1 March 2019

Keywords:
Colloidal bimetallic nanoparticles
Nickel tin alloy
Anode materials
Lithium-ion batteries
Sodium-ion batteries

ABSTRACT

Nickel tin alloy nanoparticles (NPs) with tuned composition Ni_xSn ($0.6 \leq x \leq 1.9$) were synthesized by a solution-based procedure and used as anode materials for Li-ion batteries (LIBs) and Na-ion batteries (SIBs). Among the compositions tested, $Ni_{0.9}Sn$-based electrodes exhibited the best performance in both LIBs and SIBs. As LIB anodes, $Ni_{0.9}Sn$-based electrodes delivered charge-discharge capacities of 980 mAh g^{-1} after 340 cycles at 0.2 A g^{-1} rate, which surpassed their maximum theoretical capacity considering that only Sn is lithiated. A kinetic characterization of the charge-discharge process demonstrated the electrode performance to be aided by a significant pseudocapacitive contribution that compensated for the loss of energy storage capacity associated to the solid-electrolyte interphase formation. This significant pseudocapacitive contribution, which not only translated into higher capacities but also longer durability, was associated to the small size of the crystal domains and the proper electrode composition. The performance of Ni_xSn-based electrodes toward Na-ion storage was also characterized, reaching significant capacities above 200 mAh g^{-1} at 0.1 A g^{-1} but with a relatively fast fade over 120 continuous cycles. A relatively larger pseudocapacitive contribution was obtained in Ni_xSn-based electrodes for SIBs when compared with LIBs, consistently with the lower contribution of the Na ion diffusion associated to its larger size.

1. Introduction

Lithium ion batteries (LIBs) have become essential in portable electronic applications. However, while widely spread in the market, current LIBs are far from being optimized electrochemical energy storage devices [1–5]. LIBs still suffer from moderate durabilities and current densities, which are in large part associated to the limitations of actual electrode materials. Additionally, the availability of lithium poses middle-long term limitations to this technology [6,7]. Thus, the development of improved electrode materials for LIBs and alternative battery technologies based on more abundant ions, such as sodium, is a worthwhile endeavor.

Current commercial LIBs use graphite as anode material, what limits the theoretic maximum energy density to 375 mAh g^{-1} [8–11]. On the other hand, sodium ion batteries (SIBs) cannot make use of graphite due to the insignificant Na-insertion in this material [12–14]. As an alternative anode material for both LIBs and SIBs, Sn and Sn-based alloys have been extensively studied due to their abundance, low toxicity and high energy density, 992 mAh g^{-1} for LIBs and 847 mAh g^{-1} for SIBs, corresponding to the formation of

* Corresponding author. Catalonia Institute for Energy Research - IREC, Sant Adrià de Besòs, Barcelona, 08930, Spain.
** Corresponding author. Guangdong Provincial Key Laboratory of Advanced Energy Storage Materials, School of Materials Science and Engineering, South China University of Technology, Guangzhou, 510641, PR China.
E-mail addresses: msjliu@scut.edu.cn (J. Liu), acabot@irec.cat (A. Cabot).
[1] J. Li and X. Xu equally contributed to this work.

https://doi.org/10.1016/j.electacta.2019.02.098
0013-4686/

$Li_{22}Sn_5$ and $Na_{15}Sn_4$, respectively [15–18]. However, Sn undergoes huge volume changes during charge-discharge cycles that shorten its usage time [19–24]. This drawback can be partially overcome by reducing the size of the crystal domains in the electrode. The use of nanostructured electrodes provides additional advantages in terms of increasing rate capability, because of the shorter Li-ion diffusion paths, and increasing the pseudocapacitive contribution associated with the larger surface/volume ratios [25–30]. An additional strategy to improve stability is to alloy tin with non-active elements, reducing in this way the volume changes and potentially increasing the pseudocapacitive contribution. In this direction, bimetallic Sn-based allows such as Cu-Sn [31–33], FeSn [33–35], Co-Sn [34–53], and Ni-Sn [17,33,54–56] have been tested as base materials for LIB and/or SIB electrodes with excellent results.

Not considering pseudocapacitive effects, the main drawback of alloying Sn with non-active metals is the decrease of the maximum energy density potentially achieved with the amount on non-active metal introduced. Thus, the alloy composition needs to be finely and continuously tuned along the whole solid-solution range to find the optimal composition. However, most previous works have focused on studding the performance of intermetallic Sn-based alloys, with strongly constrained compositions. In the present work, we take advantage of the versatility of colloidal synthesis method to produce nanoparticles (NPs) of a range of Ni-Sn solid solutions with Ni:Sn ratios from 0.6 to 1.9. After removing surface ligands, we use these NPs to test the performance Ni-Sn solid solutions as anode materials for LIBs and SIBs.

2. Experimental

2.1. Chemicals

Nickel(II) acetylacetonate ($Ni(acac)_2 \cdot xH_2O$ (x~2), 95%, Sigma-Aldrich), tin(II) acetate ($Sn(oac)_2$, 95%, Fluka), oleic acid (OAc, Sigma-Aldrich), oleylamine (OAm, 80–90%, TCI), tri-*n*-octylphosphine (TOP, 97%, Strem), borane tert-butylamine complex (TBAB, 97%, Sigma-Aldrich), TIMCAL Graphite & Carbon Super P (Super P, KJ group), polyvinylidene fluoride (PVDF, KJ group), *N*-methy1-2-pyrrolidone (NMP, 99%, Aladdin), hydrazine monohydrate (N_2H_4 64–65%, reagent grade, 98%, Sigma-Aldrich) and acetonitrile (CH_3CN, extra dry, Fisher) were used as received without any further purification. Chloroform, acetone and ethanol were of analytical grade and purchased from various sources. An argon-filled glove-box was used for storing and dealing with sensitive chemicals.

2.2. Colloidal synthesis of NiSn NPs

All the syntheses were carried out using standard airless techniques using a vacuum/dry argon gas Schlenk line. Ni-Sn NPs were prepared following the scaled-up version of a protocol we previously detailed [57]. Briefly, 20 mL OAm, 1.0 mL OAc, 0.9 mmol $Ni(acac)_2 \cdot xH_2O$ and 0.6 mmol $Sn(oac)_2$ were loaded into a 50 mL three-neck flask containing a magnetic stirring bar. The reaction was strongly stirred and degassed under vacuum at 80 °C for 2 h to remove water, air, and low-boiling point impurities. Then, a gentle flow of argon was introduced, 5 mL of TOP were injected and the reaction flask was heated to 180 °C at 5 °C/min. Meanwhile, a reducing solution was prepared by dissolving 5 mmol TBAB in 5 mL OAm through sonication for 30 min, and subsequently degassed this mixture for 1 h at ambient temperature. This reducing solution was injected into the reaction flask containing the Ni and Sn precursor at 180 °C. Upon injection, a visible color change, from deep green to black, was immediately observed. The reaction was maintained at 180 °C for 1 h, followed by a rapid cool down to room temperature using a water bath. The content of the reaction mixture was transferred to two centrifuge tubes, followed by centrifuging at 9000 rpm for 3 min after introducing acetone as non-solvent. The precipitate was suspended in chloroform and centrifuged again after adding additional acetone. This process was repeated twice. Finally, the NPs were suspended in 10 mL chloroform.

2.3. Ligand removal

The native organic ligands were removed from the NP surface according to a previously published report [28,58]. Briefly, 25 mL acetonitrile and 0.8 mL hydrazine hydrate was introduced into a vial containing the precipitated NPs. The mixture was stirred for 4 h at room temperature and then collected by centrifuging at low speed. The product was further washed with acetonitrile and centrifuged at 2000 rpm for another 3 times. NPs were collected and stored in inert air atmosphere after drying under vacuum at room temperature.

2.4. Characterization

Powder x-ray diffraction (XRD) was measured on a Bruker AXS D8 Advance x-ray diffractometer with Cu K radiation ($\lambda = 1.5106$ Å) operating at 40 kV and 40 mA. Scanning electron microscopy (SEM) analyses were performed on a ZEISS Auriga SEM with an energy dispersive X-ray spectroscopy (EDS) detector at 20 kV. EDS analysis were performed after removing ligands from the NP surface. Transmission electron microscopy (TEM) analyses were carried out on a ZEISS LIBRA 120, operating at 120 kV, using a 200 mesh Carbon-coated grid from Ted-Pella as substrate. High-resolution TEM (HRTEM) and scanning TEM (STEM) studies were carried out using a field emission gun FEI Tecnai F20 microscope at 200 kV with a point-to-point resolution of 0.19 nm. High angle annular dark-field (HAADF) STEM was combined with electron energy loss spectroscopy (EELS) in the Tecnai microscope by using a GATAN QUANTUM filter. X-ray photoelectron spectroscopy (XPS) was done on a SPECS system equipped with an Al anode XR50 source operating at 150 mW and a Phoibos 150 MCD-9 detector. The pressure in the analysis chamber was kept below 10^{-7} Pa. The area analyzed was about 2 mm × 2 mm. The pass energy of the hemispherical analyzer was set at 25 eV and the energy step was maintained at 1.0 eV. Data processing was performed with the Casa XPS program (Casa Software Ltd., UK). Binding energies were shifted according to the reference C 1s peak that was located at 284.8 eV. The Fourier transform infrared spectrometer (FTIR) data were recorded on an Alpha Bruker spectrometer. Inductively coupled plasma optical emission spectrometry (ICP-OES) analyses were conducted on a Spectro Arcos FHS16 ICP-OES analyzer. Ni-Sn NPs (5 mg) were dissolved in 10 mL of aqua regia. Then, 0.5 mL of this dissolution was diluted in 24.5 mL of MilliQ water.

2.5. Electrochemical measurements

Ni-Sn NPs (80 wt%) were mixed with Super P (10 wt%), PVDF (10 wt%) and NMP. The obtained slurry was bladed onto a copper foil and dried at 80 °C for 24 h in a vacuum oven. Working electrodes were obtained by cutting the printed foil into circular disk with a diameter of 12.0 mm. The mass loading of active materials was estimated to be 0.7–1.2 mg cm^{-2}. To test the performance of electrodes based on Ni-Sn NPs, half cells were assembled in the glove box (H_2O and $O_2 < 0.1$ ppm) using Celgard 2400 as separator. As electrolyte for LIBs, a 1 M $LiPF_6$ solution in ethylene carbonate (EC)/diethyl carbonate (DEC) (1:1 in volume) with 5 vol% fluoroethylene carbonate (FEC) as additive was used. For SIBs, 1 M $NaClO_4$

in propylene carbonate (PC)/EC (1:1 in volume) with 5 vol% FEC was used as the electrolyte. Galvanostatic charge-discharge were measured by a battery test system (CT2001A, LAND) with cutoff potentials from 0.01 V to 3.0 V. Cyclic voltammograms (CV) were obtained using an electrochemical workstation (Gamry Interface 1000) in the voltage range of 0–3.0 V at scan rates from 0.1 mV s^{-1} to 1 mV s^{-1}. Electrochemical impedance spectroscopy (EIS) tests were performed using a sinusoidal voltage with amplitude of 10 mV and a scanning frequency from 100 kHz to 10 mHz.

3. Results and discussion

Ni_xSn NPs with tuned composition ($0.6 < x < 1.9$) were prepared by the co-reduction of proper amounts of nickel(II) acetylacetonate and tin(II) acetate at 180 °C by TBAB and in the presence of OAm and OAc (see experimental section for details). Following this procedure, quasi-spherical NPs with sizes in the range from 3.9 ± 0.7 nm to 4.6 ± 0.6 nm were produced (Fig. 1). ICP-OES and SEM-EDS analysis showed the Ni/Sn ratio of the Ni_xSn NPs to be 0.6, 0.9, 1.2 and 1.9 ± 0.1 for nominal Ni/Sn ratios of 0.75, 1.0, 1.5 and 2.0, respectively (Figure S1). XRD analysis displayed the crystallographic phase of all the alloys to resemble that of Sn or orthorhombic Ni_3Sn_2 (Fig. 1c). Main XRD peaks did not significantly shift with the introduction of different amounts of Ni. However, as the Ni amount increased, the material crystallinity decreased and additional peaks became visible, denoting the formation of a more complex crystal phase, which did not match well with any of the reported intermetallic Ni-Sn phases.

EELS chemical composition maps showed Ni and Sn to be present in all the NPs with similar ratio (Fig. 2 and S2). Additionally, uniform distributions of Ni and Sn within each NP were observed (Fig. 2a and S2). HRTEM analysis revealed the NPs to have a good crystallinity with a crystallographic phase in agreement with the Ni_3Sn_2 orthorhombic phase (space group = Pnma) with a = 7.1100 Å, b = 5.2100 Å and c = 8.2300 Å (Fig. 2b) [59].

As displayed in Fig. 3 and S4, XPS analysis of the Ni_xSn NPs showed Ni to be present in two different chemical states, which we associated with metallic Ni^0 (Ni $2p_{3/2}$ at 852.3 eV) and $Ni^{2+/3+}$ oxidation states (Ni $2p_{3/2}$ at 855.6 eV) [60]. The ratio of the two components was found to be $Ni^{2+/3+}/Ni^0 = 2.5$ for $Ni_{1.2}Sn$. Sn was also present in two chemical states, displaying a metallic (Sn $3d_{5/2}$ peak at 484.4 eV) and an oxidized component (Sn $3d_{5/2}$ peak at 486.2 eV) with a relative ratio $Sn^{2+/4+}/Sn^0 = 3.2$ for $Ni_{1.2}Sn$ [60]. The relative amount of the oxidized component depended on the previous history of the sample, particularly on the time it had been exposed to air before XPS analysis. We associated the oxidized states to the presence of an oxide layer at the Ni_xSn NPs surface, which had been grown during their manipulation and transportation in ambient conditions. The ratio of metals Ni/Sn obtained from XPS analysis was systematically lower than values obtained from bulk chemical analysis techniques, e.g. in $Ni_{1.2}Sn$ NPs, was Ni/Sn = 0.46, which pointed at a segregation of Sn to the NP surface, also consistent with the higher relative oxidized component in Sn than Ni. We hypothesize that this surface segregation could have taken place during oxidation [57,61,62].

Before testing the performance of Ni_xSn NPs as anode material in LIBs and SIBs, the organic ligands present at their surface were removed though a treatment with a mixture of hydrazine and acetonitrile. FTIR analysis confirmed the effectivity of this treatment through the disappearance of peaks at 2890 cm^{-1} and 2822 cm^{-1} that correspond to C-H stretching modes (Figure S5) [63].

To evaluate the performance of Ni_xSn NPs as anode material in LIBs and SIBs, coin-type half-cells with metallic Li or Na foil as

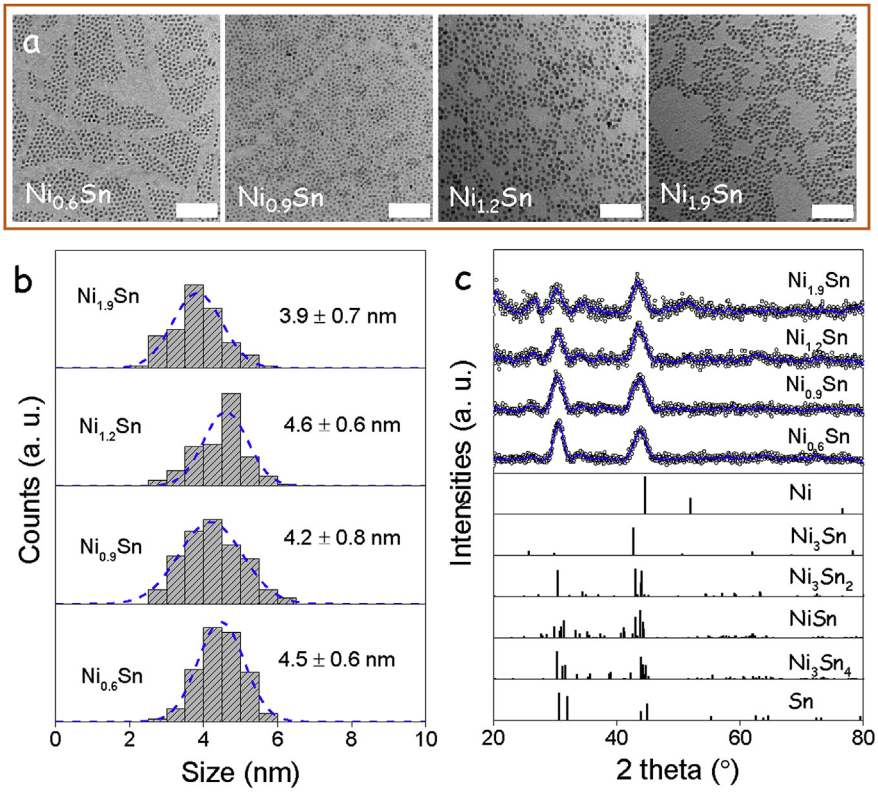

Fig. 1. a) TEM micrographs of Ni-Sn NPs with different compositions, as obtained from EDX and displayed in each image. Scale bar: 50 nm. b) Size distribution histograms of the Ni-Sn NPs; c) XRD patterns of the Ni-Sn NPs with different compositions. Sn, Ni and different Ni-Sn intermetallic XRD patterns are displayed as reference.

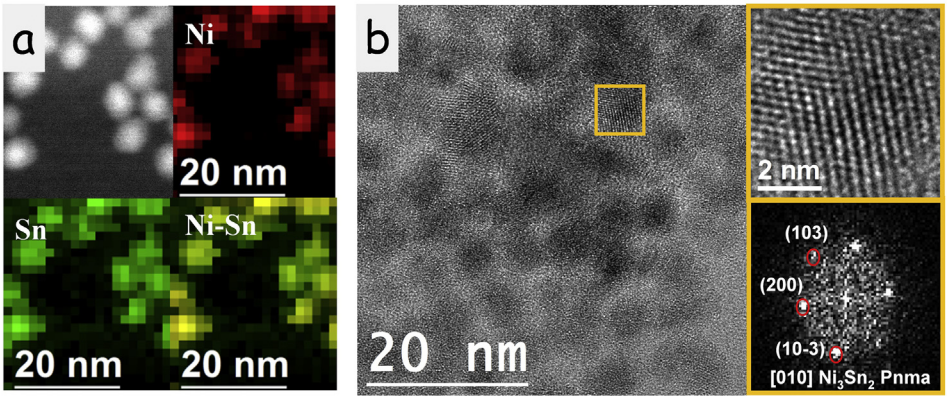

Fig. 2. a) STEM and EELS compositional maps of $Ni_{0.6}Sn$ NPs. b) HRTEM micrograph of $Ni_{0.6}Sn$ NPs exposed to atmosphere and displaying a core-shell type structure. The Ni_3Sn_2 lattice fringe distances were measured to be 0.260 nm, 0.337 nm and 0.269 nm, at 69.40 and 134.54° which could be interpreted as the orthorhombic Ni_3Sn_2 phase, visualized along its [010] zone axis.

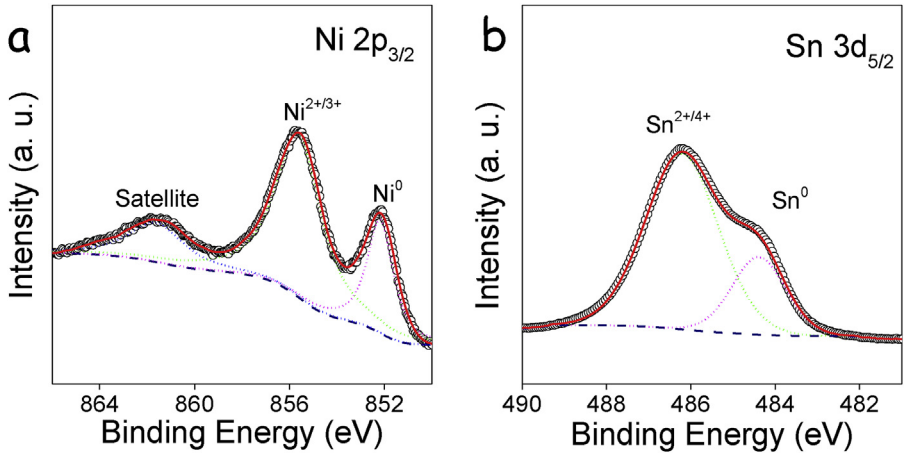

Fig. 3. XPS spectra of the Ni $2P_{3/2}$ region (a) and the Sn $3d_{5/2}$ region (b) of $Ni_{1,2}Sn$ NPs.

counter electrodes were assembled. Working electrodes were prepared by mixing Ni_xSn NPs with Super P, PVDF and NMP, and coating the resulting slurry onto Cu foil. Standard liquid electrolyte formulations were used: $LiPF_6$ in EC/DEC with FEC for LIBs and $NaClO_4$ in PC/EC with FEC for SIBs.

Fig. 4 shows representative initial CV profiles of the $Ni_{0.9}Sn$ NP-based electrode obtained at 0.1 mV s^{-1} in the applied potential region of 0–3.0 V vs. Li^+/Li and Na^+/Na, respectively. Significant differences were obtained between the 1st and following cycles, associated to the formation of the solid electrolyte interface (SEI) layer in both systems [17].

Lithium reversibly interacts with Sn with a theoretical capacity

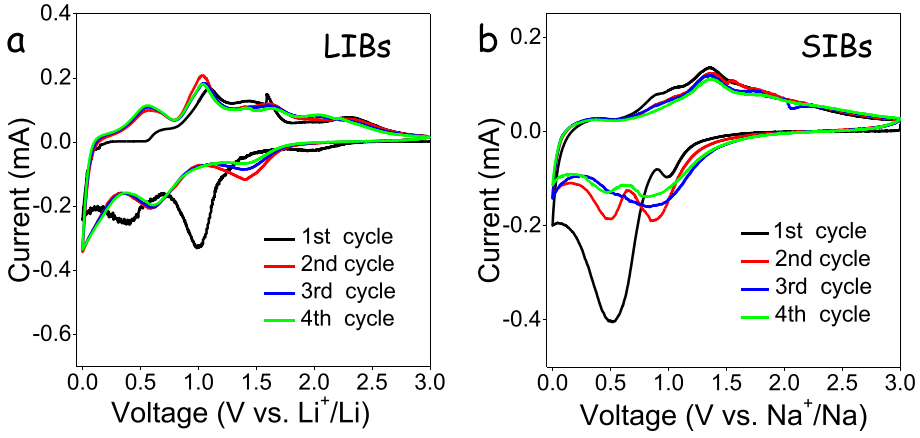

Fig. 4. Initial CV curves obtained from the $Ni_{0.9}Sn$ NP-based electrode at 0.1 mV s^{-1} in the voltage window 0–3.0 V *vs.* (a) Li^+/Li (b) Na^+/Na.

of 992 mAh g^{-1}, corresponding to the alloying reaction: Sn → $Li_{4.4}Sn$ [34]. Lithium does not react with Ni. Thus, assuming no capacity contribution from Ni, the theoretical specific capacity of $Ni_{0.6}Sn$, $Ni_{0.9}Sn$, $Ni_{1.2}Sn$ and $Ni_{1.9}Sn$ electrodes was 765 mAh g^{-1}, 687 mAh g^{-1}, 623 mAh g^{-1}, and 511 mAh g^{-1}, respectively.

The cycling performance of Ni_xSn NP-based electrodes was measured by galvanostatic charging-discharging at 0.2 A g^{-1}, as shown in Fig. 5 and S4. Ni_xSn NP-based electrodes delivered very large initial capacities, over 1200 mAh g^{-1}, well above their theoretical maximum. These large values were ascribed to the decomposition of the electrolyte to form the SEI layer. However, in the first few cycles, a strong capacity loss in the form of a decreased current density was observed due to the formed SEI layer. Upon continuous cycling, the charge-discharge capability decreased during dozens of cycles, but recovered after some additional cycles up to values well above their theoretical maximum capacity, e.g. 980 mAh g^{-1} after 340 cycles for the $Ni_{0.9}Sn$ electrode (Fig. 5b). On the other hand, the columbic efficiency was stabilized at ca. 99% after the first 10 cycles. Besides the SEI formation in the first few cycles, the phenomenon of a capacity decrease in the initial fifty cycles followed by an increase during subsequent cycling may be attributed to structural and compositional changes of the electrode material, resulting in a complex evolution of the electrical conductivity, the electrode porous volume and its surface area [64]. During cycling, a redistribution of Ni and Sn, and changes in the shape and size of the material domains take place, strongly influencing the electrical properties of the electrode, the amount of solid/electrolyte interphase accessible, the amount of material contributing to the storage capacity through ion diffusion and the amount of surface providing a pseudocapacitance contribution. Additionally, a capacity increase during repeated cycles is a common feature of Ni_xSn and other M_xSn (M = transition metal) alloys, which has been associated to the formation and dissolution of gel-like polymeric species in the SEI layer aided by the catalytic activity of the anode material [65–67]. Within this complex system, while the maximum theoretical capacity decreases with the amount of Ni introduced, $Ni_{0.9}Sn$ showed the highest capacity after several hundreds of cycles (Figure S6) among the different Ni_xSn compositions tested in the present work. The extra-capacity of Ni_xSn alloys, compared with their theoretical maximum, should be attributed to the ultra-small particle size and the related high surface area, which provided additional active sites for Li-ion storage that translated into an increased pseudocapacitive contribution. The relative stable cycling performance and high capacity retention could be also ascribed to the ultra-small particle size and the presence of Ni as a conductive buffer substrate, both parameters moderating the variation of stress during the alloying/dealloying process.

To further evaluate the rate capability of the $Ni_{0.9}Sn$ NP-based electrodes, galvanostatic measurements were carried out at different current densities, between 0.1 and 2.0 A g^{-1} (Fig. 6). $Ni_{0.9}Sn$ NP-based electrodes delivered average discharge capacities of 835, 702, 523, 378 and 261 mAh g^{-1} at 0.1, 0.2, 0.5, 1.0, 2.0 A g^{-1}, respectively. The notable rate capability of Ni_xSn-based electrodes was associated with their ultra-small particles size with high surface area shorting Li-ion diffusion paths and providing more channels for Li^+/electrons transporting. The inactive Ni as conductive part improved the electrical conductivity of the all Ni_xSn alloys also facilitating the diffusion of Li^+/electrons. A low charge transfer resistance of Ni_xSn-based electrodes was further confirmed by EIS measurements (Figure S12).

The kinetics of $Ni_{0.9}Sn$ NP-based electrodes in LIBs was investigated by collecting CV curves at different scan rates: 0.1, 0.2, 0.4, 0.7, 1.0 mV s^{-1} in the potential range of 0–3.0 V vs. Li^+/Li (Fig. 7a). The anodic peaks at 0.62 V and 1.04 V, and the cathodic peak at 0.54 V were observed to increase with scan rate. Generally, a potential relationship between the measured current (i) and the scan rate (v) can be considered [64–66].

$$i = av^b$$

According to previous reports, an ideal capacitive behavior is characterized by b = 1. On the other hand, when b is close to 0.5 the capacity is dominated by the diffusion process [65–67]. From our experimental results, the b values of the current peaks at 0.62, 0.54, 1.04 V were calculated to be 0.83, 0.66 and 0.63, respectively. All calculated b values above 0.5 indicated the $Ni_{0.9}Sn$ NP-based electrodes to be characterized by a significant pseudocapacitive contribution (Fig. 7b).

At a certain potential, the current density at each scan rate can be divided into two parts, a diffusion-controlled ($k_1v^{1/2}$) fraction associated to the Li^+ insertion and a capacitor-like fraction (k_2v) [65–67].

$$i(V) = k_1v^{1/2} + k_2v$$

Thus, k_1 and k_2 can be determined by plotting $i(V)/v^{1/2}$ vs. $v^{1/2}$, distinguishing in this way the two contributions. Fig. 7c shows a CV at 0.4 mV s^{-1} where the two components have been differentiated: the capacitive current as the blue shaded region and the diffusion component in red. Similarly, the two contributions are differentiated in the CVs at 0.1, 0.2, 0.7 and 1.0 mV s^{-1} in Figure S7. All these data are summarized in Fig. 7d. Overall, increasing capacitive contributions were obtained when increasing the scan rate, reaching a capacitive contribution up to 72% at 1.0 mV s^{-1}. This increased contribution with the scan rate is related to the slower

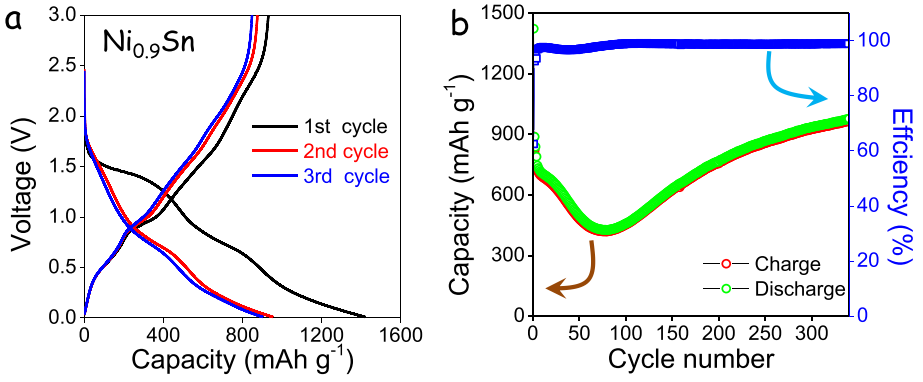

Fig. 5. a) First three charge-discharge curves at 0.2 A g^{-1} for the $Ni_{0.9}Sn$ electrode. b) Charge-discharge capacity and related columbic efficiency over 340 cycles at a current density of 0.2 A g^{-1}.

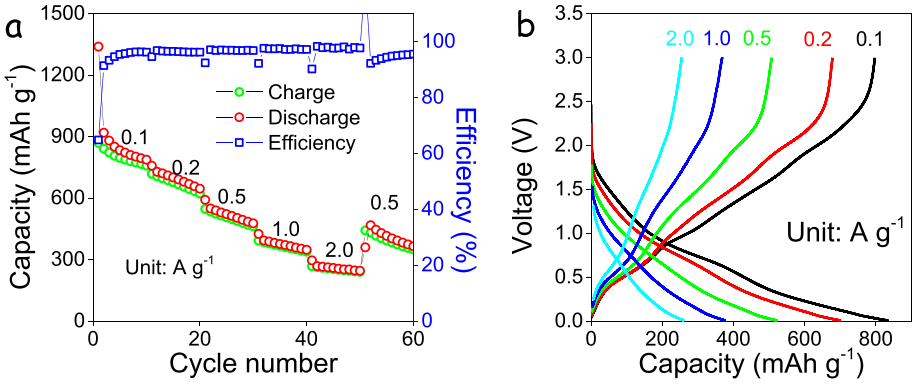

Fig. 6. Li-ion storage performance of the $Ni_{0.9}Sn$ electrode: a) Rate performance at 0.1, 0.2, 0.5, 1.0, 2.0 and 0.5 A g^{-1}. b) Charge-discharge curves at rates: 0.1, 0.2, 0.5, 1.0 and 2.0 A g^{-1}.

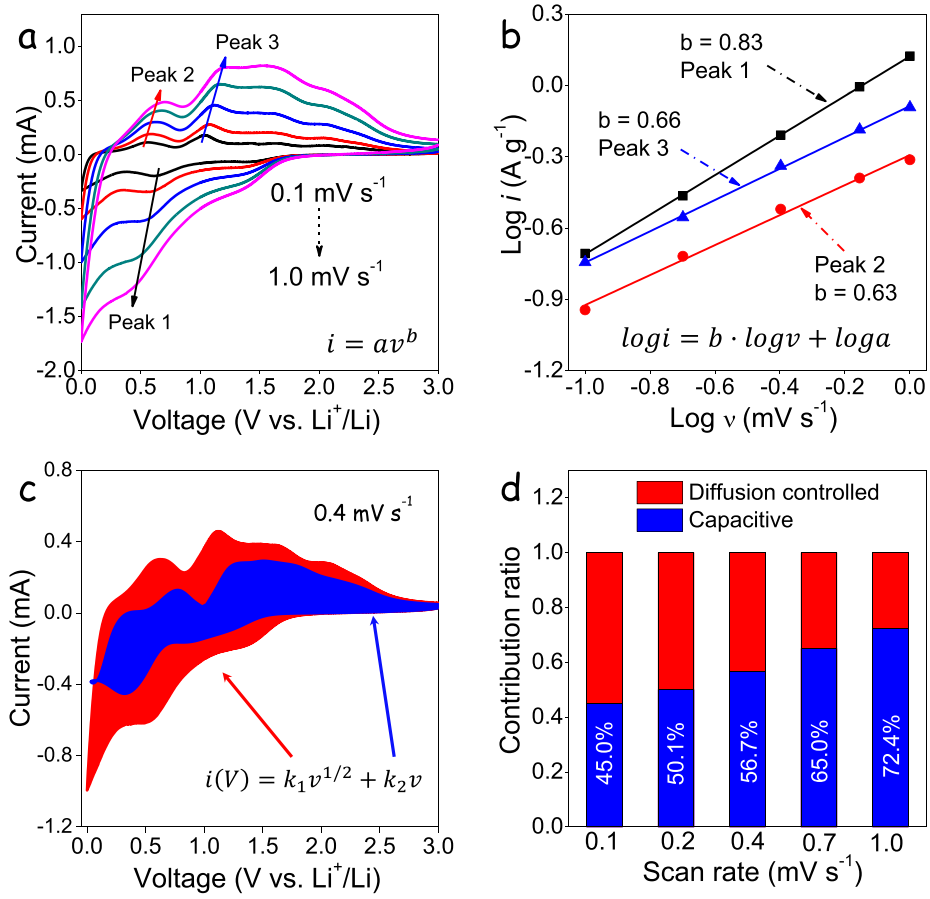

Fig. 7. Kinetic analysis of the Li-ion storage performance of the $Ni_{0.9}Sn$ electrode: a) CV curves at the scan rates of 0.1, 0.2, 0.4, 0.7, 1.0 mV s^{-1}. b) Logarithmic dependence between peak current density and scan rate at the peaks 0.62, 0.54 and 1.04 V. c) Capacitive contribution (blue region) to the total current contribution at 0.4 mV s^{-1}. d) Normalized contribution ratio of capacitive part and diffusion-controlled fraction at the scan rates of 0.1, 0.2, 0.4, 0.7, 1.0 mV s^{-1}. (For interpretation of the references to color in this figure legend, the reader is referred to the Web version of this article.)

Li^+ diffusion that translates into minor Li^+ in-depth alloying when compared with the faster and less rate-depended contribution of the surface reaction.

Similarly high capacitive contributions were obtained for all Ni_xSn NP-based electrodes except for $Ni_{0.6}Sn$, which showed a slightly lower, but still very significant contribution (Figure S8). We associated these large capacitive contributions to the small size of the Ni_xSn crystal domains. High capacitive contributions, such as the ones found for Ni_xSn alloys, are highly beneficial because surface processes are much faster and stable than diffusion-controlled alloying. The high capacitive contributions also illuminated the origin of the notable rate capability of Ni_xSn NP-based electrodes.

Sodium is also reversibly stored in Sn, with a maximum theoretical capacity of 847 mAh g^{-1} corresponding to the reaction: $Sn \rightarrow Na_{3.75}Sn$ [17]. Considering that Ni does not contribute to any Na-ion capacity, thus the theoretical capacity of $Ni_{0.6}Sn$, $Ni_{0.9}Sn$,

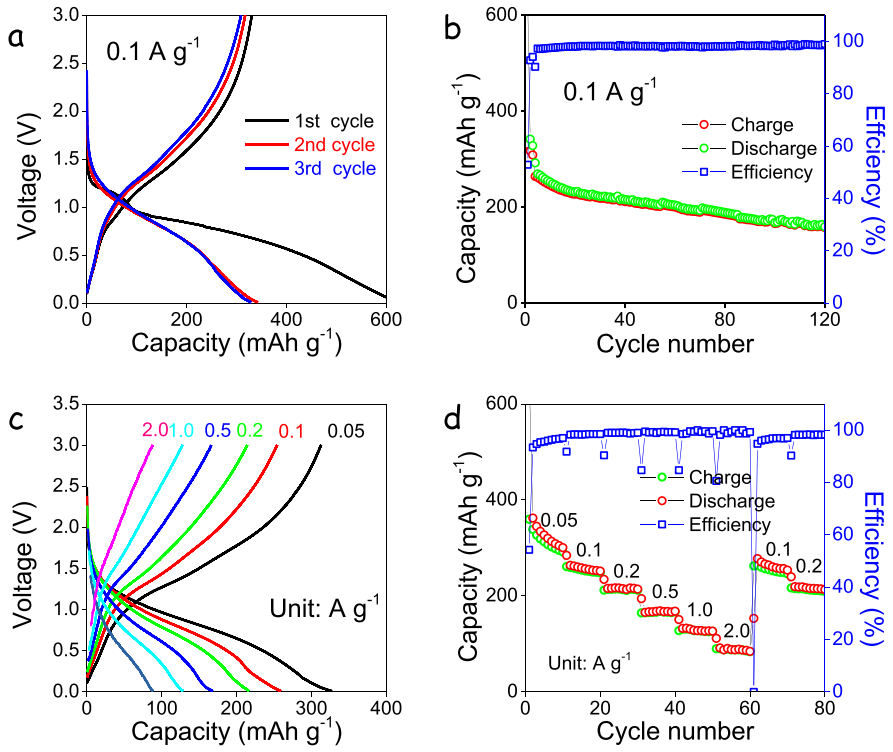

Fig. 8. Na-ion storage performance of the $Ni_{0.9}Sn$ electrode: a) Typical first three charging-discharging curves at 0.1 A g^{-1}. b) Charge-discharge capacity and related efficiency over 120 cycles at a current density of 0.1 A g^{-1}. c) Selected charging-discharging curves at 0.05, 0.1, 0.2, 0.5, 1.0 and 2.0 A g^{-1} rates. d) Rate capabilities of $Ni_{0.9}Sn$ at 0.05, 0.1, 0.2, 0.5, 1.0, 2.0, 0.1 and 0.2 A g^{-1}.

$Ni_{1.2}Sn$ and $Ni_{1.9}Sn$ electrodes is 653 mAh g^{-1}, 586 mAh g^{-1}, 532 mAh g^{-1}, and 437 mAh g^{-1}, respectively.

Fig. 8 and S9 present the Na-ion storage performance of Ni_xSn NP-based electrodes over 120 cycles at 0.1 A g^{-1}. Again, while capacity should decrease with the Ni content, $Ni_{0.9}Sn$ NPs exhibited the highest capacities among the different compositions tested. In the first cycles, Na-ion discharge-charge storage capacities above 300 mAh g^{-1} at 0.1 A g^{-1} were obtained for the $Ni_{0.9}Sn$ NP-based electrode. However, upon subsequent cycling, a monotonous capacity decrease was observed, decaying to 160 mAh g^{-1} at the 120th cycle. It is worth noting that the smaller Na-ion storage capacity, when compared with Li-ion, is ascribed to the larger radius of Na^+ than Li^+, causing less Na^+ in-depth alloying. EIS analysis further demonstrated a larger charge transfer resistance of Ni_xSn-based electrodes in SIBs than in LIBs (Figure S12). Rate-capability tests in the window 0.1–2.0 A g^{-1} showed the $Ni_{0.9}Sn$ NP-based electrode to deliver average discharge capacities of 327, 258, 217, 168, 128, and 88 mAh g^{-1} at 0.05, 0.1, 0.2, 0.5, 1.0, and 2.0 A g^{-1}, respectively. In addition, $Ni_{0.9}Sn$ NP-based electrodes showed similar capacities at 0.1 and 0.2 A g^{-1} after 30–40 more cycles at higher discharging-charging rate (Fig. 8d).

The kinetics of $Ni_{0.9}Sn$ NP-based electrodes in SIBs was investigated in a similar way as in LIBs, by collecting CV curves at different scan rates: 0.1, 0.2, 0.4, 0.7, 1.0 mV s^{-1}. $Ni_{0.9}Sn$ NP-based electrodes in SIBs were characterized with b values of 0.91 and 0.84 at 0.85 V and 1.36 V, respectively. Higher b values already pointed out at a relatively higher capacitance contribution in SIBs than LIBs. This phenomenon could be associated with the larger radius of Na^+, which increased the diffusion resistance into the interior of the materials and caused a larger fraction of Na^+ to exist on the surface, leading to higher capacitive contributions in SIBs than in LIBs. As shown in Figures S10 and 11, contributions up to 84% at 1.0 mV s^{-1} were measured from $Ni_{0.9}Sn$ NP-based electrodes in SIBs.

4. Conclusion

In summary, we reported the synthesis of Ni_xSn NPs with tuned composition ($0.6 \leq x \leq 1.9$) and their performance as anode material in LIBs and SIBs. Among the different compositions tested, best performances toward Li^+ ion and Na^+ ion insertion were obtained for $Ni_{0.9}Sn$ NP-based electrodes. This optimized cycling charge-discharge performance for LIBs provided 980 mAh g^{-1} at 0.2 A g^{-1} after 340 cycles. Additionally, $Ni_{0.9}Sn$ NP-based electrodes were tested in Na^+-ion half cells, exhibiting 160 mAh g^{-1} over 120 cycles at 0.1 A g^{-1}. From CV measurements at different current rates, it was found that the charging process was both capacitive and diffusion controlled, while the capacitive contribution was dominant in both LIBs and SIBs. The pseudocapacitive charge-storage accounted for a high portion of the whole energy storage capacity, which was associated to the small size and the composition of the Ni_xSn NPs used.

Author contributions

The manuscript was prepared through the contribution of all authors. A. Cabot and J. Liu conceived and guided the project, and supervised the work. J. Li designed the experiments, produced the NPs, conducted XRD, TEM, SEM-EDS and FT-IR characterization, and wrote the first draft of the manuscript. X. Xu performed the electrochemical measurements. Z. Luo, C. Zhang, X. Yu and Y. Zuo significantly contributed to the results discussion. T. Zhang, P. Tang, and J. Arbiol performed structural and compositional NCs characterization by means of HRTEM and EELS, and discussed the results.

J. Llorca measured and discussed XPS data. The manuscript was corrected and improved by all authors.

Conflicts of interest

The authors declare no competing financial interest.

Acknowledgments

This work was supported by the European Regional Development Funds and by the Spanish Ministerio de Economía y Competitividad through the project SEHTOP (ENE2016-77798-C4-3-R). J. Li thanks the China Scholarship Council for scholarship support. This project was supported by the National Natural Science Foundation of China (no. 51771076), the “1000 plan” from Chinese Government, and the Project of Public Interest Research and Capacity Building of Guangdong Province (no. 2017A010104004). T. Zhang, P. Tang and J. Arbiol acknowledge funding from Generalitat de Catalunya 2017 SGR 327 and the Spanish MINECO coordinated projects between IREC and ICN2 VALPEC and subprojects RESOL and ANAPHASE (ENE2017-85087-C3). ICN2 acknowledges support from the Severo Ochoa Programme (MINECO, Grant no. SEV-2013-0295) and is funded by the CERCA Programme / Generalitat de Catalunya. T. Zhang has received funding from the CSC-UAB PhD scholarship program. Part of the present work has been performed in the framework of Universitat Autònoma de Barcelona Materials Science PhD program. J. Llorca is a Serra Húnter Fellow and is grateful to ICREA Academia program and to MINECO/FEDER grant ENE2015-63969-R and GC 2017 SGR 128.

Appendix A. Supplementary data

Supplementary data to this article can be found online at https://doi.org/10.1016/j.electacta.2019.02.098.

References

[1] C.M. Park, J.H. Kim, H. Kim, H.J. Sohn, Li-alloy based anode materials for Li secondary batteries, Chem. Soc. Rev. 39 (2010) 3115–3141.
[2] D. Larcher, J.M. Tarascon, Towards greener and more sustainable batteries for electrical energy storage, Nat. Chem. 7 (2015) 19–29.
[3] J.B. Goodenough, K.S. Park, The Li-ion rechargeable battery: a perspective, J. Am. Chem. Soc. 135 (2013) 1167–1176.
[4] M.D. Slater, D. Kim, E. Lee, C.S. Johnson, Sodium-ion batteries, Adv. Funct. Mater. 23 (2013) 947–958.
[5] M.R. Palacín, Recent advances in rechargeable battery materials: a chemist's perspective, Chem. Soc. Rev. 38 (2009) 2565–2575.
[6] X. Liu, J. Zhang, W. Si, L. Xi, B. Eichler, C. Yan, O.G. Schmidt, Sandwich nano architecture of Si/reduced graphene oxide bilayer nanomembranes for Li-ion batteries with long cycle life, ACS Nano 9 (2015) 1198–1205.
[7] C. Yan, W. Xi, W. Si, J. Deng, O.G. Schmidt, Highly conductive and strain-released hybrid multilayer Ge/Ti nanomembranes with enhanced lithium-ion-storage capability, Adv. Mater. 25 (2013) 539–544.
[8] Y. Wen, K. He, Y. Zhu, F. Han, Y. Xu, I. Matsuda, Y. Ishii, J. Cumings, C. Wang, Expanded graphite as superior anode for sodium-ion batteries, Nat. Commun. 5 (2014) 4033.
[9] M.F. Oszajca, M.I. Bodnarchuk, M.V. Kovalenko, Precisely engineered colloidal nanoparticles and nanocrystals for Li-ion and Na-ion batteries: model systems or practical solutions? Chem. Mater. 26 (2014) 5422–5432.
[10] N. Liu, Z. Lu, J. Zhao, M.T. Mcdowell, H.W. Lee, W. Zhao, Y. Cui, A pomegranate-inspired nanoscale design for large-volume-change lithium battery anodes, Nat. Nanotechnol. 9 (2014) 187–192.
[11] J. Deng, H. Ji, C. Yan, J. Zhang, W. Si, S. Baunack, S. Oswald, Y. Mei, O.G. Schmidt, Naturally rolled-up C/Si/C trilayer nanomembranes as stable Anodes for lithium-ion batteries with remarkable cycling performance, Angew. Chem. Int. Ed. 52 (2013) 2326–2330.
[12] F. Nacimiento, P. Lavela, J.L. Tirado, J.M. Jiménez-Mateos, A facile carbothermal preparation of Sn-Co-C composite electrodes for Li-ion batteries using low-cost carbons, J. Solid State Electrochem. 16 (2012) 953–962.
[13] J.-Y. Hwang, S.-T. Myung, Y.-K. Sun, Sodium-ion batteries: present and future, Chem. Soc. Rev. 46 (2017) 3529–3614.
[14] M. Lao, Y. Zhang, W. Luo, Q. Yan, W. Sun, S.X. Dou, Alloy-based anode materials toward advanced sodium-ion batteries, Adv. Mater. 29 (2017).
[15] P.G. Bruce, B. Scrosati, J.M. Tarascon, Nanomaterials for rechargeable lithium batteries, Angew. Chem. Int. Ed. 47 (2008) 2930–2946.
[16] H. Tian, F. Xin, X. Wang, W. He, W. Han, High capacity group-IV elements (Si, Ge, Sn) based anodes for lithium-ion batteries, J. Mater. 1 (2015) 153–169.
[17] J. Liu, Y. Wen, P.A. Van Aken, J. Maier, Y. Yu, Facile synthesis of highly porous Ni-Sn intermetallic microcages with excellent electrochemical performance for lithium and sodium storage, Nano Lett. 14 (2014) 6387–6392.
[18] R. Marom, S.F. Amalraj, N. Leifer, D. Jacob, D. Aurbach, A review of advanced and practical lithium battery materials, J. Mater. Chem. 21 (2011) 9938–9954.
[19] J. Wen, Y. Yu, C. Chen, A review on lithium-ion batteries safety issues: existing problems and possible solutions, Mater. Express. 2 (2012) 197–212.
[20] B. Wang, B. Luo, X. Li, L. Zhi, The dimensionality of Sn anodes in Li-ion batteries, Mater. Today. 15 (2012) 544–552.
[21] C. Vaalma, D. Buchholz, M. Weil, S. Passerini, A cost and resource analysis of sodium-ion batteries, Nat. Rev. Mater. 3 (2018) 18013.
[22] M.N. Obrovac, V.L. Chevrier, Alloy negative electrodes for Li-ion batteries, Chem. Rev. 114 (2014) 11444–11502.
[23] N. Nitta, F. Wu, J.T. Lee, G. Yushin, Li-ion battery materials: present and future, Mater. Today. 18 (2015) 252–264.
[24] A.R. Kamali, D.J. Fray, Tin-based materials as advanced anode materials for lithium ion batteries: a review, Rev. Adv. Mater. Sci. 27 (2011) 14–24.
[25] M. Walter, S. Doswald, F. Krumeich, M. He, R. Widmer, N.P. Stadie, M.V. Kovalenko, Oxidized Co-Sn nanoparticles as long-lasting anode materials for lithium-ion batteries, Nanoscale 10 (2018) 3777–3783.
[26] M.F. Oszajca, M.I. Bodnarchuk, M.V. Kovalenko, Precisely engineered colloidal nanoparticles and nanocrystals for Li-ion and Na-ion batteries: model systems or practical solutions? Chem. Mater. 26 (2014) 5422–5432.
[27] K. Kravchyk, L. Protesescu, M.I. Bodnarchuk, F. Krumeich, M. Yarema, M. Walter, C. Guntlin, M.V. Kovalenko, Monodisperse and inorganically capped Sn and Sn/SnO2nanocrystals for high-performance Li-ion battery anodes, J. Am. Chem. Soc. 135 (2013) 4199–4202.
[28] M. He, M. Walter, K.V. Kravchyk, R. Erni, R. Widmer, M.V. Kovalenko, Monodisperse SnSb nanocrystals for Li-ion and Na-ion battery anodes: synergy and dissonance between Sn and Sb, Nanoscale 7 (2015) 455–459.
[29] C. Chen, Y. Wen, X. Hu, X. Ji, M. Yan, L. Mai, P. Hu, B. Shan, Y. Huang, Na^+ intercalation pseudocapacitance in graphene-coupled titanium oxide enabling ultra-fast sodium storage and long-term cycling, Nat. Commun. 6 (2015) 6929.
[30] T. Brezesinski, J. Wang, S.H. Tolbert, B. Dunn, Ordered mesoporous α-MoO3-with iso-oriented nanocrystalline walls for thin-film pseudocapacitors, Nat. Mater. 9 (2010) 146–151.
[31] W.X. Lei, Y. Pan, Y.C. Zhou, W. Zhou, M.L. Peng, Z.S. Ma, CNTs-Cu composite layer enhanced Sn-Cu alloy as high performance anode materials for lithium-ion batteries, RSC Adv. 4 (2014) 3233–3237.
[32] Y.M. Lin, P.R. Abel, A. Gupta, J.B. Goodenough, A. Heller, C.B. Mullins, Sn-Cu nanocomposite anodes for rechargeable sodium-ion batteries, ACS Appl. Mater. Interfaces. 5 (2013) 8273–8277.
[33] X.L. Wang, W.Q. Han, J. Chen, J. Graetz, Single-crystal intermetallic M-Sn (M = Fe, Cu, Co, Ni) nanospheres as negative electrodes for lithium-ion batteries, ACS Appl. Mater. Interfaces 2 (2010) 1548–1551.
[34] S. Wang, M. He, M. Walter, F. Krumeich, K.V. Kravchyk, M.V. Kovalenko, Monodisperse $CoSn_2$ and $FeSn_2$ nanocrystals as high-performance anode materials for lithium-ion batteries, Nanoscale 10 (2018) 6827–6831.
[35] L.O. Vogt, C. Villevieille, Elucidation of the reaction mechanisms of isostructural $FeSn_2$ and $CoSn_2$ negative electrodes for Na-ion batteries, J. Mater. Chem. A. 5 (2017) 3865–3874.
[36] N. Tamura, Y. Kato, A. Mikami, M. Kamino, S. Matsuta, S. Fujitani, Study on Sn–Co alloy anodes for lithium secondary batteries, J. Electrochem. Soc. 153 (2006) A1626.
[37] Z. Du, S. Zhang, Enhanced electrochemical performance of Sn-Co nano-architectured electrode for lithium ion batteries, J. Phys. Chem. C. 115 (2011) 23603–23609.
[38] C.M. Ionica-Bousquet, P.E. Lippens, L. Aldon, J. Olivier-Fourcade, J.C. Jumas, In situ 119 Sn mössbauer effect study of Li–CoSn 2 electrochemical system, Chem. Mater. 18 (2006) 6442–6447.
[39] J. Zhu, D. Wang, T. Liu, C. Guo, Preparation of Sn-Co-graphene composites with superior lithium storage capability, Electrochim. Acta. 125 (2014) 347–353.
[40] X. Shi, H. Song, A. Li, X. Chen, J. Zhou, Z. Ma, Sn-Co nanoalloys embedded in porous N-doped carbon microboxes as a stable anode material for lithium-ion batteries, J. Mater. Chem. A. 5 (2017) 5873–5879.
[41] G.O. Park, J. Yoon, J.K. Shon, Y.S. Choi, J.G. Won, S. Bin Park, K.H. Kim, H. Kim, W.S. Yoon, J.M. Kim, Discovering a dual-buffer effect for lithium storage: durable nanostructured ordered mesoporous Co-Sn intermetallic electrodes, Adv. Funct. Mater. 26 (2016) 2800–2808.
[42] B.O. Jang, S.H. Park, W.J. Lee, Electrospun Co-Sn alloy/carbon nanofibers composite anode for lithium A ion batteries, J. Alloy. Comp. 574 (2013) 325–330.
[43] X. Liu, J. Xie, H. Zhao, P. Lv, K. Wang, Z. Feng, K. Świerczek, Electrochemical properties of mechanochemically synthesized CoSn2-C nanocomposite-type anode material for Li-ion batteries, Solid State Ionics 269 (2015) 86–92.
[44] J.R. González, F. Nacimiento, R. Alcántara, G.F. Ortiz, J.L. Tirado, Electrodeposited CoSn2 on nickel open-cell foam: advancing towards high power lithium ion and sodium ion batteries, CrystEngComm 15 (2013) 9196–9202.
[45] R. Gnanamuthu, Y.N. Jo, C.W. Lee, Brush electroplated CoSn2alloy film for application in lithium-ion batteries, J. Alloy. Comp. 564 (2013) 95–99.

[46] G. Ferrara, C. Arbizzani, L. Damen, M. Guidotti, M. Lazzari, F.G. Vergottini, R. Inguanta, S. Piazza, C. Sunseri, M. Mastragostino, High-performing Sn-Co nanowire electrodes as anodes for lithium-ion batteries, J. Power Sources 211 (2012) 103–107.
[47] P.P. Ferguson, A.D.W. Todd, J.R. Dahn, Comparison of mechanically alloyed and sputtered tin-cobalt-carbon as an anode material for lithium-ion batteries, Electrochem. Commun. 10 (2008) 25–31.
[48] J. He, H. Zhao, J. Wang, J. Wang, J. Chen, Hydrothermal synthesis and electrochemical properties of nano-sized Co-Sn alloy anodes for lithium ion batteries, J. Alloy. Comp. 508 (2010) 629–635.
[49] S. Il Lee, S. Yoon, C.M. Park, J.M. Lee, H. Kim, D. Im, S.G. Doo, H.J. Sohn, Reaction mechanism and electrochemical characterization of a Sn-Co-C composite anode for Li-ion batteries, Electrochim. Acta. 54 (2008) 364–369.
[50] P. Chen, L. Guo, Y. Wang, Graphene wrapped SnCo nanoparticles for high-capacity lithium ion storage, J. Power Sources 222 (2013) 526–532.
[51] J. Shin, W.-H. Ryu, K.-S. Park, I.-D. Kim, Morphological evolution of carbon nanofibers encapsulating SnCo alloys and its effect on growth of the solid electrolyte interphase layer, ACS Nano 7 (2013) 7330–7341.
[52] J. Zhang, Y. Xia, Co-Sn alloys as negative electrode materials for rechargeable lithium batteries, J. Electrochem. Soc. 153 (2006) A1466.
[53] N. Mahmood, C. Zhang, F. Liu, J. Zhu, Y. Hou, Hybrid of Co3Sn2@Co nanoparticles and nitrogen-doped graphene as a lithium ion battery anode, ACS Nano 7 (2013) 10307–10318.
[54] D. wei ZHANG, C. ge YANG, J. DAI, J. wu WEN, L. WANG, C. hua CHEN, Fabrication of Sn-Ni alloy film anode for Li-ion batteries by electrochemical deposition, Trans. Nonferrous Met. Soc. China (English Ed.) 19 (2009) 1489–1493.
[55] M. Uysal, T. Cetinkaya, A. Alp, H. Akbulut, Active and inactive buffering effect on the electrochemical behavior of Sn-Ni/MWCNT composite anodes prepared by pulse electrodeposition for lithium-ion batteries, J. Alloy. Comp. 645 (2015) 235–242.
[56] X. Fan, P. Dou, A. Jiang, D. Ma, X. Xu, One-step electrochemical growth of a three-dimensional Sn-Ni@PEO nanotube array as a high performance lithium-ion battery anode, ACS Appl. Mater. Interfaces 6 (2014) 22282–22288.
[57] J. Li, Z. Luo, Y. Zuo, J. Liu, T. Zhang, P. Tang, J. Arbiol, J. Llorca, A. Cabot, NiSn bimetallic nanoparticles as stable electrocatalysts for methanol oxidation reaction, Appl. Catal. B Environ. 234 (2018) 10–18.
[58] M. Walter, S. Doswald, M.V. Kovalenko, Inexpensive colloidal SnSb nanoalloys as efficient anode materials for lithium- and sodium-ion batteries, J. Mater. Chem. A. 4 (2016) 7053–7059.
[59] H. Fjellvåg, A. Kjekshus, R. Stomberg, R. Zingales, I. Vikholm, F. Urso, J. Weidlein, R.A. Zingaro, Structural properties of Co3Sn2, Ni3Sn2 and some ternary derivatives, Acta Chem. Scand. 40a (1986) 23–30.
[60] C.D. Wager, W.M. Riggs, L.E. Davis, J.F. Moulder, G.E. Muilenderg, Handbook of X-Ray Photoelectron Spectroscopy, 1979.
[61] Y. Liu, X. Liu, Q. Feng, D. He, L. Zhang, C. Lian, R. Shen, G. Zhao, Y. Ji, D. Wang, G. Zhou, Y. Li, Intermetallic NixMy(M = Ga and Sn) nanocrystals: a non-precious metal catalyst for semi-hydrogenation of alkynes, Adv. Mater. 28 (2016) 4747–4754.
[62] M. He, L. Protesescu, R. Caputo, F. Krumeich, M.V. Kovalenko, A general synthesis strategy for monodisperse metallic and metalloid nanoparticles (In, Ga, Bi, Sb, Zn, Cu, Sn, and Their Alloys) via in situ formed metal long-chain amides, Chem. Mater. 27 (2015) 635–647.
[63] J. Li, Z. Luo, F. He, Y. Zuo, C. Zhang, J. Liu, X. Yu, R. Du, T. Zhang, M.F. Infante-Carrió, P. Tang, J. Arbiol, J. Llorca, A. Cabot, Colloidal Ni–Co–Sn nanoparticles as efficient electrocatalysts for the methanol oxidation reaction, J. Mater. Chem. A 6 (2018) 22915–22924.
[64] H.-S. Kim, J.B. Cook, S.H. Tolbert, B. Dunn, The development of pseudocapacitive properties in nanosized-MoO2, J. Electrochem. Soc. 162 (2015) A5083–A5090.
[65] V. Augustyn, P. Simon, B. Dunn, Pseudocapacitive oxide materials for high-rate electrochemical energy storage, Energy Environ. Sci. 7 (2014) 1597–1614.
[66] X. Xu, S. Ji, M. Gu, J. Liu, In situ synthesis of MnS hollow microspheres on reduced graphene oxide sheets as high-capacity and long-life anodes for Li- and Na-ion batteries, ACS Appl. Mater. Interfaces 7 (2015) 20957–20964.
[67] X. Xu, J. Liu, J. Liu, L. Ouyang, R. Hu, H. Wang, L. Yang, M. Zhu, A general metal-organic framework (MOF)-Derived selenidation strategy for in situ carbon-encapsulated metal selenides as high-rate anodes for Na-ion batteries, Adv. Funct. Mater. 28 (2018), 1707573.

ChemPubSoc Europe

DOI: 10.1002/cssc.201802662

CHEMSUSCHEM Full Papers

Co–Sn Nanocrystalline Solid Solutions as Anode Materials in Lithium-Ion Batteries with High Pseudocapacitive Contribution

Junshan Li[+],[a, b] Xijun Xu[+],[c, d] Zhishan Luo,[a] Chaoqi Zhang,[a] Yong Zuo,[a] Ting Zhang,[e] Pengyi Tang,[e] Maria F. Infante-Carrió,[e] Jordi Arbiol,[e, f] Jordi Llorca,[g] Jun Liu,*[c, d] and Andreu Cabot*[a, f]

Co–Sn solid-solution nanoparticles with Sn crystal structure and tuned metal ratios were synthesized by a facile one pot solution-based procedure involving the initial reduction of a Sn precursor followed by incorporation of Co within the Sn lattice. These nanoparticles were used as anode materials for Li-ion batteries. Among the different compositions tested, $Co_{0.7}Sn$ and $Co_{0.9}Sn$ electrodes provided the highest capacities with values above 1500 mAh g^{-1} at a current density of 0.2 A g^{-1} after 220 cycles, and up to 800 mAh g^{-1} at 1.0 A g^{-1} after 400 cycles. Up to 81% pseudocapacitance contribution was measured for these electrodes at a sweep rate of 1.0 mV s^{-1}, thereby indicating fast kinetics and long durability. The excellent performance of Co–Sn nanoparticle alloy-based electrodes was attributed to both the small size of the crystal domains and their suitable composition, which buffered volume changes of Sn and contributed to a suitable electrode restructuration.

Introduction

Lithium-ion batteries (LIBs) have become the dominant energy storage technology in portable applications. However, their energy density, charging rate, and stability are critical performance parameters which still have plenty of room for improvement by optimizing both anode and cathode materials.[1–4] At the anode, current commercial LIBs use graphite which has a relatively low maximum theoretical capacity (372 mAh g^{-1} to form LiC_6).[5] Alternatively, anode materials such as Sn, Ge, and Si provide platforms with potentially higher Li storage capacities: $Li_{22}Sn_5$ (994 mAh g^{-1}), $Li_{22}Ge_5$ (1600 mAh g^{-1}), and $Li_{22}Si_5$ (3000 mAh g^{-1}), respectively.[6–8] Even though Si is the most abundant element and has the highest potential storage capacity, Sn and Sn-based compounds are particularly appealing owing to their relatively high abundance, low cost and high electrical conductivity.[7,9]

In terms of stability, the huge lattice expansion and contraction of the anode material during cycling strongly reduces the battery performance owing to a loss of electrical connection by electrode pulverization. In case of Sn, the Sn/$Li_{22}Sn_5$ reaction has an associated 300% volume change, which inevitably leads to major structural rearrangements generally resulting in a loss of capacity.[10,11] Different strategies have been proposed to tackle this major issue. One main approach is to alloy the active phase, Sn, with a second element that can buffer the volume changes.[12,13] In this direction, Sn-based alloys with Ni,[14–17] Co,[18–30] Fe,[31,32] Cu,[33,34] and Sb[35–37] have demonstrat-

[a] J. Li,[+] Z. Luo, C. Zhang, Y. Zuo, Prof. A. Cabot
Catalonia Institute for Energy Research—IREC
Sant Adrià de Besòs, Barcelona, 08930 (Spain)
E-mail: acabot@irec.cat

[b] J. Li,[+]
Departament d'Electronica
Universitat de Barcelona
08028 Barcelona (Spain)

[c] X. Xu[+] Prof. J. Liu
Guangdong Provincial Key Laboratory of Advanced Energy Storage Materials
School of Materials Science and Engineering
South China University of Technology
Guangzhou 510641 (P. R. China)
E-mail: msjliu@scut.edu.cn

[d] X. Xu,[+] Prof. J. Liu
SUNWODA-SCUT Joint Laboratory for Advanced Energy Storage Technology
South China University of Technology
Guangzhou 510641 (P. R. China)

[e] T. Zhang, P. Tang, M. F. Infante-Carrió, J. Arbiol
Catalan Institute of Nanoscience and Nanotechnology (ICN2)
CSIC and BIST
Campus UAB, Bellaterra, 08193 Barcelona (Spain)

[f] J. Arbiol, Prof. A. Cabot
ICREA
Pg. Lluís Companys 23, 08010 Barcelona (Spain)

[g] J. Llorca
Institute of Energy Technologies
Department of Chemical Engineering and Barcelona Research Center in Multiscale Science and Engineering
Universitat Politècnica de Catalunya
EEBE, 08019 Barcelona (Spain)

[+] These authors contributed equally to this work.

Supporting Information and the ORCID identification number(s) for the author(s) of this article can be found under: https://doi.org/10.1002/cssc.201802662.

ed superior cycling performance than bare Sn anodes. Among the different Sn-based alloys tested, Co–Sn electrodes have shown particularly promising performances as anode materials for LIBs.[31] Co–Sn–C composites have even been used in commercial batteries, which has motivated a notable interest in this system.[38–42] Previous works have mostly focused on the intermetallic Co–Sn alloys: Co_3Sn_2, CoSn, and $CoSn_2$. Among intermetallics, $CoSn_2$ has provided the highest capacities owing to its highest Sn content, but Co_3Sn_2 has shown the best cycling performance.[28] However, beyond intermetallic phases, a range of Co–Sn solid solutions exist that are yet to be explored.

Apart from alloying the active material to improve cycling performance, the use of nanostructured electrodes can also reduce the overall stress generated on the material domains during lithiation, thus diminishing mechanical disintegration and improving stability. Furthermore, nanosized materials present additional advantages such as faster rate capabilities because of the shorter Li-ion diffusion paths and a potentially large pseudocapacitive contribution associated with their very high surface/volume ratio.[43–46] This pseudocapacitive contribution is particularly appealing because it can significantly improve both the rate performance and stability of LIBs.

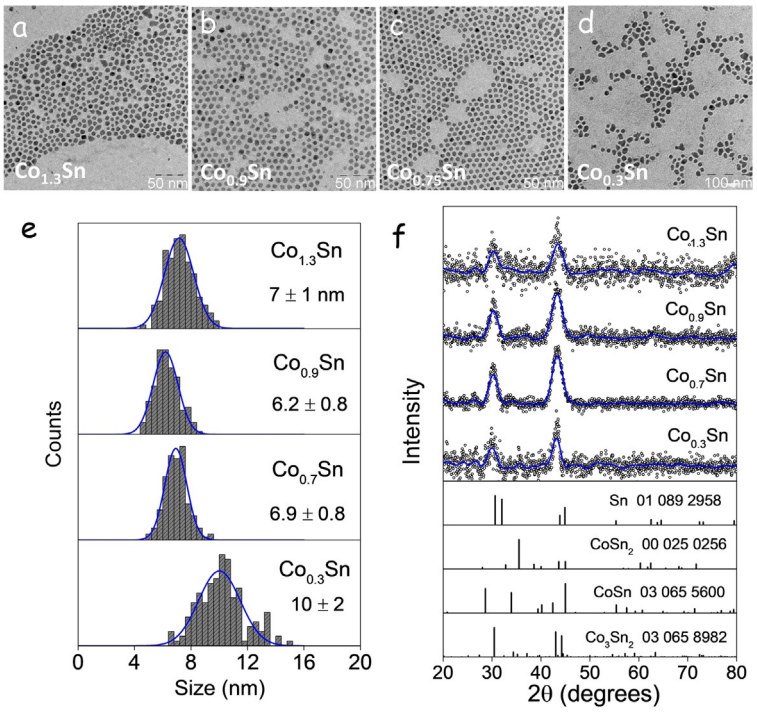

Figure 1. a–d) TEM images of different Co–Sn NPs with the obtained EDX compositions displayed in each image. e) Size distribution histograms of the Co–Sn NPs. f) XRD patterns of the different NPs. XRD patterns of pure Sn and different Co–Sn intermetallics are shown as reference.

In the present work, we take advantage of the versatility of colloidal synthesis methods to produce Co–Sn solid solution nanoparticles (NPs) with tuned Co/Sn atomic ratios ranging from 0.3 to 1.3. After removing the surface ligands, we used these NPs to test the performance of Co–Sn solid solutions as anode materials for LIBs, defined an optimal composition, and demonstrated the high energy-storage capacity, a high pseudocapacitive contribution, and notable stability of this system.

Results and Discussion

Colloidal Co–Sn NPs were produced by the reduction of tin(II) acetate and cobalt(II) acetylacetonate with borane tert-butylamine (TBAB) at 180 °C, in a solution containing oleylamine (OAm), oleic acid (OAc), and tri-n-octylphosphine (TOP, for details see the Experimental Section). Figure 1 a–d shows the representative TEM images and size distribution histograms of the produced quasi-spherical NPs. The average NP size was estimated to be 6–7 nm for all compositions except for the most Sn-rich NPs, which had an average size of 10 nm. XRD analysis showed that the NPs exhibited the Sn crystal structure independent of the Co/Sn ratio. However, the XRD peaks appeared shifted to lower angles, corresponding to the introduction of a slightly larger atom, Co, within the Sn lattice. The formation of Co–Sn solid solutions was somehow surprising considering that previous works reported the formation of intermetallics, that is, $CoSn_2$, CoSn, and Co_3Sn_2 upon co-reducing proper amounts of the two elements. We associate the differences in the products obtained between our synthesis protocol and previous works to the relatively low synthesis temperatures used, which prevented the crystallization of independent Co NPs and Co–Sn intermetallic phases.

Energy dispersive X-ray (EDX) analysis showed the Co/Sn ratio in the Co–Sn solid-solution NPs to be: 1.3, 0.9, 0.7, and 0.3, resulting from the nominal Co/Sn precursor ratios of 2.0, 1.5, 1.0, and 0.5, respectively. The final Co-poor NP stoichiometry (with respect to the nominal) and the pink color of the supernatant obtained after NP precipitation revealed that some of the cobalt precursor remained unreacted after 1 h at 180 °C. We also observed that the same reaction conditions did not result in the formation of Co NPs in the absence of Sn precursor. On the contrary, the same reaction in the absence of Co resulted in the formation of Sn NPs. We believe that in the reaction conditions used, the Sn precursor was first reduced to nucleate Sn NPs. Taking advantage of the lower energy for heterogeneous growth over homogeneous nucleation, during the 1 h period at 180 °C, Co ions within the solution were incorporated into the initial Sn nuclei upon reduction with TBAB. The Sn crystal structure was conserved through this synthesis mechanism, which is in contrast with the results obtained in previous works that make use of higher reaction, alloying, or annealing temperatures to produce Co–Sn intermetallic alloys.

X-ray photoelectron spectroscopy (XPS) analysis (Figure S2, see the Supporting Information) revealed the Co/Sn ratio of the $Co_{0.9}Sn$ NPs to be 0.7, which indicated a slightly Sn-rich surface. We hypothesized that this Sn-rich surface was related to a slight oxidation of the NPs exposed to ambient conditions. We believe that air exposure resulted in a slight restructuration

of the alloy owing to the higher affinity of Sn for oxygen, which drives the diffusion of Sn to the surface.[47]

Figure 2a shows the scanning transmission electron microscopy (STEM) images and electron energy loss spectroscopy (EELS) chemical composition maps of the $Co_{0.9}Sn$ NPs. All $Co_{0.9}Sn$ NPs were observed to contain the two elements in a similar ratio. Co and Sn distributions were observed to be mostly homogeneous within each NP. However, most NPs presented a Sn-rich shell which is consistent with XPS analysis. High resolution TEM (HRTEM) micrographs (Figure 2b) clearly displayed a core–shell structure of the NPs. From the HRTEM analysis, the core crystal structure could be assigned to the $Co_{2.9}Sn_2$ orthorhombic phase (space group = *Pnma*) with a = 7.1450 Å, b = 5.2500 Å, and c = 8.1730 Å, or to the Co_3Sn_2 hexagonal phase (space group = P63/mmc) with a = b = 4.1130 Å and c = 5.1850 Å (SI).[48] This result is in contradiction with XRD, EDX, and XPS analysis. We hypothesize that the solid-solution NPs having $Co_{0.9}Sn$ composition and Sn structure were formed initially. Upon exposure to air, these NPs developed a Sn-rich surface associated with a differential reactivity of the two elements with oxygen.[49–51] During the HRTEM analysis, within the electron beam, the core having a higher Co content owing to the diffusion of Sn to the surface, crystallized into an intermetallic Co_3Sn_2 phase with potentially additional Sn segregation on the surface.

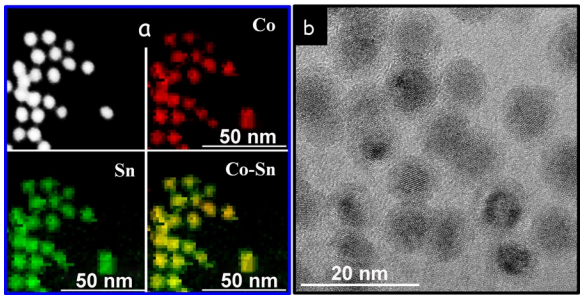

Figure 2. a) STEM and EELS compositional maps of the $Co_{0.9}Sn$ NPs. b) HRTEM micrograph of the $Co_{0.9}Sn$ NPs exposed to atmosphere displaying a core–shell structure.

These Co–Sn solid solution NPs were then explored as anode material in LIBs. Before testing their performance, the organic ligands used to control the growth of the NPs in solution were removed by treating with a mixture of hydrazine and acetonitrile.[36,37] Fourier transform infrared spectroscopy (FTIR) analysis confirmed the effectiveness of the ligand removal step (Figure S4). The LIB anodes were prepared by casting a non-aqueous slurry containing 80 wt% of active material, polyvinylidene (PVDF, 10 wt%) as a polymer binder, and Super P as a conductive additive (10 wt%). After vacuum drying, all anodes had similar mass loading of the active material (ca. 0.79–1.36 mg). All electrodes were tested under the same conditions using coin-type half cells with metallic Li as counter electrodes (see the Experimental Section).

The electrochemical performance of Co–Sn NP-based electrodes was initially assessed through cyclic voltammetry (CV) with a scan rate of 0.1 mV s^{-1} in the potential window of 0–3.0 V (versus Li^+/Li). As shown in Figure 3, all CV cycles showed a similar trend. However, the initial two cycles displayed more pronounced peaks than the following ones at 1.31 and 2.05 V in the forward scan and 0.65 and 1.45 V in the reverse scan.

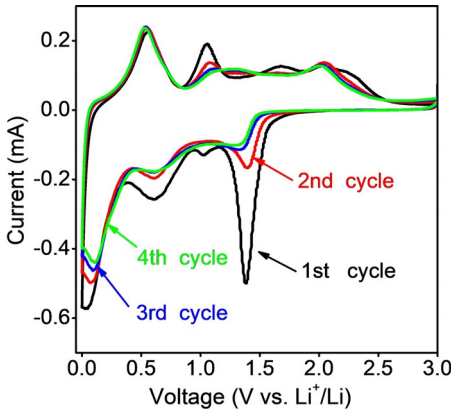

Figure 3. Initial cyclic voltammograms obtained from the $Co_{0.9}Sn$ electrode in the voltage window 0–3.0 V versus Li^+/Li at 0.1 mV s^{-1}.

The differences were ascribed to the formation of a solid electrolyte interphase (SEI) layer during the initial cycles and the reduction of the surface SnO_x layer formed during NP manipulation and electrode preparation, which is in agreement with previous reports.[52,53] The overlap of the third and subsequent cycles indicates a reasonable stability of the electrode. The two obvious peaks around 0.65 and 0.05 V in the reverse scan were assigned to the reversible lithium insertion in the Co–Sn alloy to form $Li_{4.4}Sn$.[54] During the anodic sweep, peaks at 0.52 V were related to the extraction of Li ions from the electrode. Qualitatively similar voltammograms were obtained for all four compositions tested.

Figure 4a–d displays the first three charge–discharge cycles at a current density of 0.2 $A g^{-1}$ for electrodes containing the different Co–Sn NPs. For all the tested compositions, small charging and discharging plateaus were observed at around 0.4 V and 1.6 V, respectively. The charge voltage at around 0.4 V was in good agreement with previous results.[29,55] Figure 4e–f shows the charge–discharge capacity and the related efficiency over 400 cycles at a current density of 1.0 A g^{-1} (activated at 0.2 and 0.5 A g^{-1} for 10 cycles, respectively). The low initial coulombic efficiency measured for all the electrodes, roughly 50%, was associated with the SEI formation. During the first few cycles, the coulombic efficiency increased to approximately 98% and remained stable at this value for several hundreds of cycles. All compositions showed the following similar trend: 1) an initial very fast decrease of the capacity which was attributed to the SEI formation, followed by 2) a slower loss of capacity associated with a partial disintegration of the anode material, 3) a capacity recovery after a certain number of cycles, and 4) a moderate but sustained decrease of capacity at much larger cycle numbers. We hypothesize the reactivation to be partly associated with a rearrangement of the active material domains within the anode, thereby making a larger amount of electroactive material accessible to Li ions. Al-

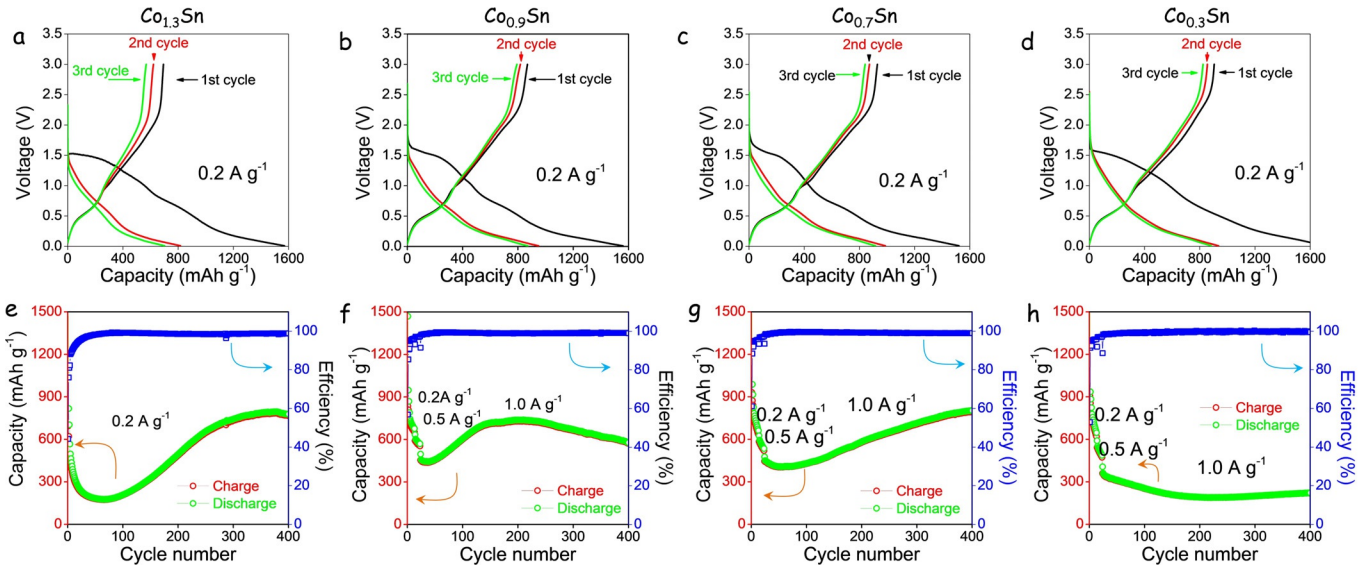

Figure 4. a–d) Initial charge–discharge curves at 0.2 A g^{-1} for the different electrodes with compositions displayed on the top of each graph. e–h) Charge–discharge capacity and related efficiency of the electrodes over 400 cycles at a current density of 1.0 A g^{-1}: activated at 0.2 and 0.5 A g^{-1} for 10 cycles each. For the $Co_{1.3}Sn$ electrode only data at 0.2 A g^{-1} is shown.

though, at the same time electrical conductivity is reduced as observed from the electrochemical impedance spectroscopy (EIS) analysis provided below. This rearrangement of the active material could also provide larger surface areas and increase the pseudocapacitive contribution to the total energy storage capacity.[56] On the other hand, a restructuration of the active material at the atomic scale, and particularly its amorphization, could facilitate lithium insertion.

$Co_{0.9}Sn$ and $Co_{0.7}Sn$ electrodes showed the highest Li-storage capacities among the tested compositions. As shown in Figure S5, the coulombic efficiency for the $Co_{0.9}Sn$ electrode was just 55.7% at 0.2 A g^{-1} during the first cycle, with a high discharge (869 mAh g^{-1}) and charge capacity (1560 mAh g^{-1}). A strong capacity loss was observed during the initial cycles; the charge and discharge capacities were reduced to 629 mAh g^{-1} and 647 mAh g^{-1} with 97.2% coulombic efficiency at the 24th cycle. With continuous cycling, the coulombic efficiency remained stable and the charge and discharge capacities gradually increased up to 1534 mAh g^{-1} and 1555 mAh g^{-1} at the 220th cycle. The extraordinarily high capacities obtained, which is above the theoretical maximum for not only Co–Sn alloys but also for pure Sn, may be attributed to the ultra-small particle size of the active anode material, which provides additional active sites for Li-ion storage and a larger density of diffusion channels for Li ions to access all the active material.[56–60]

To evaluate the rate capability of the Co–Sn electrodes, galvanostatic cycling was performed at current rates between 0.05 to 4 A g^{-1} (Figure 5a). Figure 5b presents the corresponding charge–discharge profiles from 0.05 to 4.0 A g^{-1}. For $Co_{0.9}Sn$, the electrode delivered a discharge capacity of 804, 702, 598, 532, 448, 365, and 267 mAh g^{-1} at 0.05, 0.1, 0.2, 0.5, 1.0, 2.0, and 4.0 A g^{-1}, respectively.

Figure S6 compares the EIS data obtained from electrodes with different Co–Sn compositions, and from the $Co_{0.9}Sn$ electrode in the first and the 400th cycle, all acquired at 1 A g^{-1}. A straightforward dependence of the anode–electrolyte charge transfer resistance on the Co–Sn alloy composition could not be observed from the Nyquist plots. However, the lowest resistances were obtained for the optimum compositions $Co_{0.7}Sn$ and $Co_{0.9}Sn$. The electrode resistance increased with cycling and two semicircles evolved, one corresponding to the SEI layer impedance and the other to the charge-transfer impedance on the electrode–electrolyte interphase. In the low frequency region, slopes well above 1 for all compositions and both fresh and cycled samples indicated a significant capacitive behavior.

The kinetics of the Co–Sn electrodes was further investigated using CV at different scan rates ranging from 0.1 to 1 mV s^{-1}. Figure 5c presents the CV curves obtained from the $Co_{0.9}Sn$ electrode at the scan rates of 0.1, 0.2, 0.4, 0.7, and 1.0 mV s^{-1} in the potential range 0–3.0 V versus Li^+/Li. Three anodic peaks were observed at 0.52, 1.31, and 2.05 V with all of them increasing with the scan rate.

Two main charge-storage mechanisms determine the electrode storage capacity: 1) a diffusion-controlled contribution associated with the $Li_{22}Sn_5$ alloy formation, and 2) a surface-related capacitive contribution known as the pseudocapacitive contribution.[61] The pseudocapacitive contribution is particularly attractive because it is a much faster and stable process, whereas the diffusion-controlled alloying is slower and generally provides relatively poor cycle life.

Generally, the relationship between the measured current (i) and the scan rate (v) can be expressed according to Equation (1):

$$i = av^b \quad (1)$$

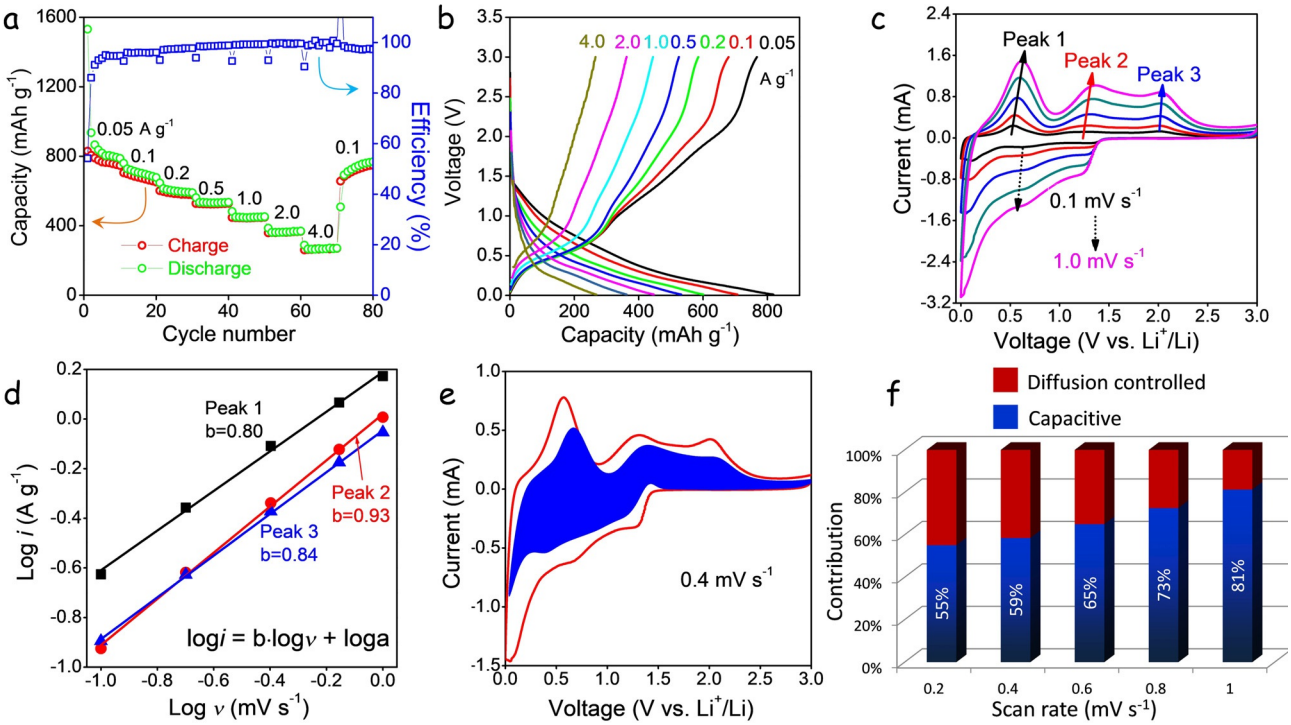

Figure 5. Li-ion storage performance of the $Co_{0.9}Sn$ electrode: a) Charge–discharge curves and b) rate performance at 0.05, 0.1, 0.2, 0.5, 1.0, 2.0, and 4.0 A g^{-1}. c) CV curves at the scan rates of 0.1, 0.2, 0.4, 0.7, and 1.0 mV s^{-1}. d) Logarithmic dependence between peak current density and scan rate at the anodic peaks of 0.52, 1.31, and 2.05 V. e) Capacitive contribution to the total current contribution at 0.4 mV s^{-1}. f) Normalized capacitive and diffusion-controlled contribution at the scan rates of 0.1, 0.2, 0.4, 0.7, and 1.0 mV s^{-1}.

in which *a* and *b* are adjustable constant parameters. According to previous reports, a diffusion-controlled process is characterized by a scan rate dependence with $b = 0.5$, whereas an ideal capacitive behavior translates into $b = 1$.[62–64] From the linear fit of the logarithmic plot of the current versus scan rate (Figure 5d), *b* values of 0.80, 0.93, and 0.84 were calculated at 0.52, 1.31, and 2.05 V, respectively. These values indicate fast kinetics resulting from a pseudocapacitive effect.

At each potential, the current density contribution at a given scan rate could be divided into two parts, a diffusion-controlled ($k_1\nu^{1/2}$) and a capacitor-like ($k_2\nu$) fraction [Eq. (2)]:

$$i(V) = k_1\nu^{1/2} + k_2\nu \quad (2)$$

To distinguish the fraction of the current arising from Li^+ insertion and that from a capacitive process at each specific potential, k_1 and k_2 were determined by plotting $i(V)/\nu^{1/2}$ versus $\nu^{1/2}$.[44,62] Figure 5e shows the CV profiles at 0.4 mV s^{-1} and compares the capacitive current (blue shaded region) with that of the total measured current (red curve) for the $Co_{0.9}Sn$ electrode. The relative pseudocapacitive contributions at sweep rates of 0.1, 0.2, 0.4, 0.7, and 1.0 mV s^{-1} were observed to be 55%, 59%, 65%, 73%, and 81%, respectively (Figures 4f and S7). For comparison, the pseudocapacitive study of the $Co_{0.3}Sn$ electrode is presented in Figure S8. The calculated contributions at sweep rates of 0.1–1.0 mV s^{-1} were lower than that of $Co_{0.9}Sn$. These results clearly suggest that the pseudocapacitive charge-storage amount does occupy a high portion of the whole energy storage capacity, which is associated with the small size of the Co–Sn NPs used and their Sn-rich and oxidized surface.

To estimate the practical application of Co–Sn NP-based anodes, they were tested in the range of 0.01–1.5 V versus Li/Li^+. As shown in Figures 6a–b and S9, over continuous charge–discharge cycles the $Co_{0.7}Sn$ and $Co_{0.9}Sn$ electrodes show the highest capacity and stability, stabilizing at 360 mAh g^{-1} at 0.5 A g^{-1}. This value is comparable to the theoretical capacity of graphite-based electrodes. The rate capability of the $Co_{0.9}Sn$ electrode is also shown in Figure 6c–d. Specifically, the electrode could deliver discharge capacities of 520, 453, 421, 388, 336, and 253 mAh g^{-1} at 0.1, 0.2, 0.5, 1.0, 2.0, and 4.0 A g^{-1}, respectively. Additionally, this electrode delivered a stable charge–discharge capacity at 0.1 A g^{-1} after continuous 60 cycles at variable charging rate.

Conclusions

Co–Sn solid-solution NPs with an average size in the range of 6–10 nm were synthesized using a simple one-pot colloidal-based approach. The Co_xSn NP composition, $1.3 \leq x \leq 0.3$, was adjusted by tuning the ratio of the initial precursors. The low synthesis temperature favored the nucleation of Sn NPs and the subsequent inclusion of Co to the Sn lattice, thereby forming a solid solution with the Sn crystal phase instead of an intermetallic compound. The same strategy could be used to produce a much more extended range of Co–Sn compositions.

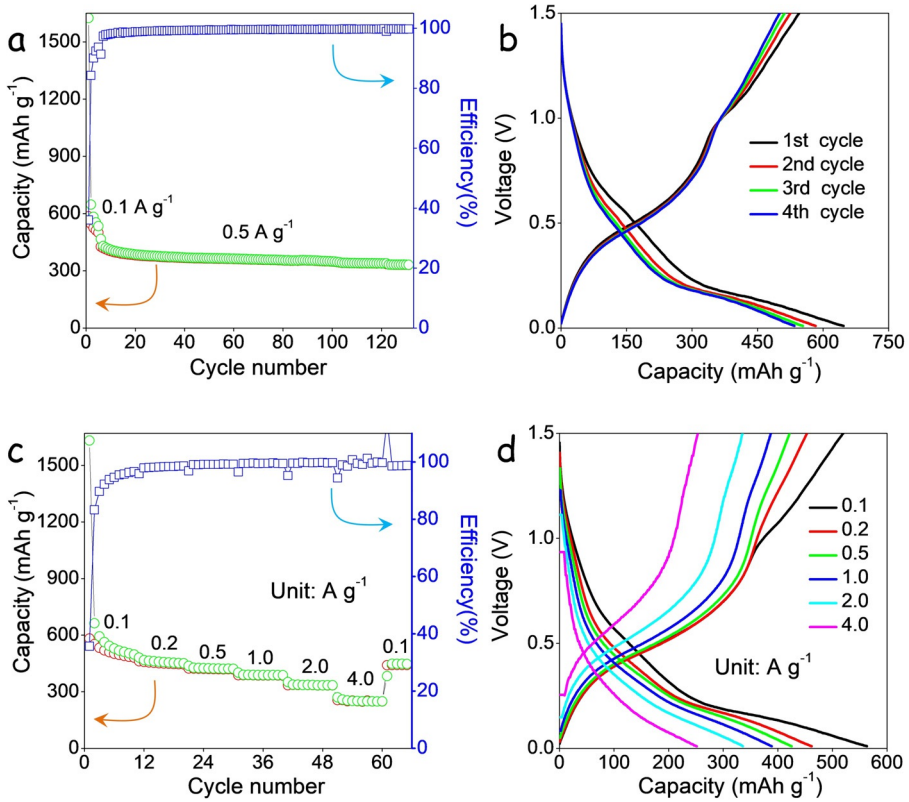

Figure 6. Li-ion storage performance of the $Co_{0.9}Sn$ electrode in the range 0–1.5 V versus Li/Li^+: a) Charge–discharge curves at rates: 0.1, 0.2, 0.5, 1.0, 2.0, 4.0, and 0.1 A g^{-1}. b) Rate performance at 0.1, 0.2, 0.5, 1.0, 2.0, and 4.0 A g^{-1}. c) Charge–discharge capacity and related efficiency over 130 cycles at a current density of 0.5 A g^{-1}: activated at 0.1 A g^{-1} for 10 cycles. d) Initial charge–discharge curves at 0.1 A g^{-1}.

Co–Sn NPs presented a Sn-rich surface after exposure to air. These Co–Sn solid solutions were tested as anode materials for LIBs in a half-cell battery system. Among the different compositions tested, $Co_{0.9}Sn$ and $Co_{0.7}Sn$ NPs provided the best performance with a charge–discharge capacity of above 1500 mAh g^{-1} at a current density of 0.2 A g^{-1} after 220 cycles and up to 800 mAh g^{-1} at 1.0 A g^{-1} after 400 cycles in the range 0–3.0 V. The two electrodes delivered an average of 360 mAh g^{-1} at 0.5 A g^{-1} in the range 0–1.5 V. These values are larger than that of graphite currently used in commercial devices and also larger than the theoretical maximum for Co–Sn alloys and pure Sn. The kinetic analysis of $Co_{0.9}Sn$ NPs by CV revealed these charge–discharge capacities to include a very large pseudocapacitive contribution, up to 81% at a sweep rate of 1 mV s^{-1}, which was attributed to the small size of the particles.

Experimental Section

Colloidal synthesis of Sn and Co–Sn NPs: Syntheses were performed using standard air-free techniques. All the reagents and solvent were of analytical grade and used without further purification. In a typical synthesis, for Co–Sn NPs with nominal composition Co/Sn = 3:2, cobalt(II) acetylacetonate (0.6 mmol; $Co(acac)_2$, 99%, Sigma–Aldrich) and tin(II) acetate (0.4 mmol; $Sn(OAc)_2$, 95%, Fluka) were added into a 50 mL three-neck round-bottomed flask. Subsequently, oleylamine (20 mL; OAm, 80–90%, TCI) and oleic acid (1.0 mL; OAc, Sigma–Aldrich) were loaded along with a magnetic bar in a three-neck flask connected with a thermometer, condenser, and septum. The flask was heated to 80 °C and degassed under vacuum for 2 h and then filled with Ar. Thereafter, tri-n-octylphosphine (5 mL; TOP, 97%, Strem) was injected, and the solution was heated up to 180 °C at 5 °C min^{-1}. Right after reaching 180 °C, 5 mL of a degassed OAm solution containing borane tert-butylamine (5 mmol; TBAB, 97%, Sigma–Aldrich) was injected. Upon injecting this reducing complex, the solution became black. The reaction mixture was maintained at 180 °C for an additional hour to allow the NPs to grow. After 1 h of reaction, the heating mantle was removed, and the solution was cooled down to room temperature in approximately 3 min using a water bath. NPs were collected by centrifugation after adding an excess of acetone. The precipitate was dispersed in chloroform and centrifuged a second time with an excess of acetone. This washing process was repeated thrice. Finally, NPs were stored in chloroform.

Ligand removal: 25 mL of acetonitrile containing 0.8 mL hydrazine hydrated were added into a vial containing about 100 mg of precipitated NPs. The solution was vigorously stirred for 4 h and centrifuged. The NPs were further washed with acetonitrile three more times, followed by vacuum-drying at room temperature. The product was kept in an Ar-filled glove box.

Characterization: XRD patterns were recorded at room temperature on a Bruker AXS D8 Advance X-ray diffractometer with CuK_α radiation ($\lambda = 1.5106$ Å) operating at 40 kV and 40 mA. TEM analyses were performed on a ZEISS LIBRA 120 instrument operating at 120 kV. HRTEM and STEM studies were performed using a field

emission gun FEI Tecnai F20 microscope at 200 kV with a point-to-point resolution of 0.19 nm. HAADF-STEM was combined with EELS in the Tecnai microscope by using a GATAN QUANTUM filter. Composition analyses were performed using a ZEISS Auriga SEM equipped with an EDS detector operated at 20 kV. XPS measurements were performed in normal emission mode using an Al anode XR50 source operating at 150 mW and a Phoibos 150 MCD-9 detector. FTIR data was recorded on an Alpha Bruker spectrometer.

Electrochemical measurements: To evaluate the intrinsic electrochemical performance of Co–Sn NPs, the working electrode was prepared by mixing dried NPs, Super P and polyvinylidene fluoride (PVDF) with a weight ratio of 80:10:10 in an appropriate amount of *n*-methy1-2-pyrrolidone (NMP) to obtain a slurry. This mixture was coated onto a Cu foil and dried in a vacuum oven at 80 °C for 24 h. Subsequently, the foil was cut into disks with a diameter of 12 mm. The typical mass loading of active materials was estimated to be 0.7–1.2 mg cm^{-2}. To test the performance of electrodes based on Co–Sn NPs, half cells were assembled in the glove box (H_2O and $O_2 < 0.1$ ppm) using Celgard2400 as separator. A $LiPF_6$ solution (1 M) in ethylene carbonate (EC)/diethyl carbonate (DEC) (1:1 volume) with 5 wt% fluoroethylene carbonate (FEC) as additive was used as the electrolyte. Galvanostatic charge–discharge curves were measured by a battery test system (CT2001A, LAND) with cutoff potentials from 0.01 V to 1.5 and 3.0 V. Cyclic voltammetry (CV) curves were acquired using an electrochemical workstation (Gamry Interface 1000) in the voltage range from 0–3.0 V and the scan rate from 0.1 to 1 mV s^{-1}.

Author contributions

The manuscript was prepared through the contribution of all authors. A. Cabot and J. Liu conceived and guided the project and supervised the work. J. Li designed the experiments, produced the nanoparticles, conducted the XRD, TEM, SEM-EDS, and FTIR characterizations, and wrote the first draft of the manuscript. Z. Luo, C. Zhang, and Y. Zuo significantly contributed to the results discussion. X. Xu performed the electrochemical measurements. T. Zhang, P. Tang, M. F. Infante-Carrió, and J. Arbiol performed structural and compositional NCs characterization by means of HRTEM and EELS and discussed the results. J. Llorca measured and discussed the XPS data. The manuscript was corrected and improved by all authors.

Acknowledgements

This work was supported by the European Regional Development Funds and by the Spanish Ministerio de Economía y Competitividad through the project SEHTOP (ENE2016-77798-C4-3-R). J. Li thanks the China Scholarship Council for scholarship support. This project was supported by the National Natural Science Foundation of China (no. 51771076), the "1000 plan" from Chinese Government, and the Project of Public Interest Research and Capacity Building of Guangdong Province (no. 2017A010104004). TZ, PYT, MFIC and JA acknowledge funding from Generalitat de Catalunya 2017 SGR 327 and the Spanish MINECO coordinated projects between IREC and ICN2 VALPEC and subprojects RESOL and ANAPHASE (ENE2017-85087-C3). ICN2 acknowledges support from the Severo Ochoa Programme (MINECO, Grant no. SEV-2013-0295) and is funded by the CERCA Programme/ Generalitat de Catalunya. JL is a Serra Húnter Fellow and is grateful to ICREA Academia program and to MINECO/FEDER grant ENE2015-63969-R. TZ has received funding from the CSC-UAB PhD scholarship program. Part of the present work has been performed in the framework of Universitat Autònoma de Barcelona Materials Science PhD program.

Conflict of interest

The authors declare no conflict of interest.

Keywords: anode · bimetallic nanoparticles · colloidal · lithium-ion batteries · solid solutions

[1] C. M. Park, J. H. Kim, H. Kim, H. J. Sohn, *Chem. Soc. Rev.* **2010**, *39*, 3115–3141.
[2] M. N. Obrovac, V. L. Chevrier, *Chem. Rev.* **2014**, *114*, 11444–11502.
[3] R. Marom, S. F. Amalraj, N. Leifer, D. Jacob, D. Aurbach, *J. Mater. Chem.* **2011**, *21*, 9938–9954.
[4] P. G. Bruce, B. Scrosati, J. M. Tarascon, *Angew. Chem. Int. Ed.* **2008**, *47*, 2930–2946; *Angew. Chem.* **2008**, *120*, 2972–2989.
[5] L. X. Ding, G. R. Li, Z. L. Wang, Z. Q. Liu, H. Liu, Y. X. Tong, *Chem. Eur. J.* **2012**, *18*, 8386–8391.
[6] H. Tian, F. Xin, X. Wang, W. He, W. Han, *J. Materiomics* **2015**, *1*, 153–169.
[7] B. Wang, B. Luo, X. Li, L. Zhi, *Mater. Today* **2012**, *15*, 544–552.
[8] C. K. Chan, R. N. Patel, M. J. O'Connell, B. A. Korgel, Y. Cui, *ACS Nano* **2010**, *4*, 1443–1450.
[9] H. Ying, W. Q. Han, *Adv. Sci.* **2017**, *4*, 1700298.
[10] N. Nitta, F. Wu, J. T. Lee, G. Yushin, *Mater. Today* **2015**, *18*, 252–264.
[11] J. B. Goodenough, K. S. Park, *J. Am. Chem. Soc.* **2013**, *135*, 1167–1176.
[12] M. R. Palacín, *Chem. Soc. Rev.* **2009**, *38*, 2565–2575.
[13] M. F. Oszajca, M. I. Bodnarchuk, M. V. Kovalenko, *Chem. Mater.* **2014**, *26*, 5422–5432.
[14] D.-W. Zhang, C. G. Yang, J. Dai, J.-W. Wen, L. Wang, C.-H. Chen, *Trans. Nonferrous Met. Soc. China* **2009**, *19*, 1489–1493.
[15] J. Liu, Y. Wen, P. A. Van Aken, J. Maier, Y. Yu, *Nano Lett.* **2014**, *14*, 6387–6392.
[16] X. Fan, P. Dou, A. Jiang, D. Ma, X. Xu, *ACS Appl. Mater. Interfaces* **2014**, *6*, 22282–22288.
[17] M. Uysal, T. Cetinkaya, A. Alp, H. Akbulut, *J. Alloys Compd.* **2015**, *645*, 235–242.
[18] N. Tamura, Y. Kato, A. Mikami, M. Kamino, S. Matsuta, S. Fujitani, *J. Electrochem. Soc.* **2006**, *153*, A1626.
[19] Z. Du, S. Zhang, *J. Phys. Chem. C* **2011**, *115*, 23603–23609.
[20] C. M. Ionica-Bousquet, P. E. Lippens, L. Aldon, J. Olivier-Fourcade, J. C. Jumas, *Chem. Mater.* **2006**, *18*, 6442–6447.
[21] G. O. Park, J. Yoon, J. K. Shon, Y. S. Choi, J. G. Won, S. Bin Park, K. H. Kim, H. Kim, W. S. Yoon, J. M. Kim, *Adv. Funct. Mater.* **2016**, *26*, 2800–2808.
[22] B. O. Jang, S. H. Park, W. J. Lee, *J. Alloys Compd.* **2013**, *574*, 325–330.
[23] J. R. González, F. Nacimiento, R. Alcántara, G. F. Ortiz, J. L. Tirado, *CrystEngComm* **2013**, *15*, 9196–9202.
[24] R. Gnanamuthu, Y. N. Jo, C. W. Lee, *J. Alloys Compd.* **2013**, *564*, 95–99.
[25] G. Ferrara, C. Arbizzani, L. Damen, M. Guidotti, M. Lazzari, F. G. Vergottini, R. Inguanta, S. Piazza, C. Sunseri, M. Mastragostino, *J. Power Sources* **2012**, *211*, 103–107.
[26] J. He, H. Zhao, J. Wang, J. Wang, J. Chen, *J. Alloys Compd.* **2010**, *508*, 629–635.
[27] J. Shin, W.-H. Ryu, K.-S. Park, I.-D. Kim, *ACS Nano* **2013**, *7*, 7330–7341.
[28] J. Zhang, Y. Xia, *J. Electrochem. Soc.* **2006**, *153*, A1466.
[29] S. Wang, M. He, M. Walter, F. Krumeich, K. V. Kravchyk, M. V. Kovalenko, *Nanoscale* **2018**, *10*, 6827–6831.
[30] M. Walter, S. Doswald, F. Krumeich, M. He, R. Widmer, N. P. Stadie, M. V. Kovalenko, *Nanoscale* **2018**, *10*, 3777–3783.
[31] X. L. Wang, W. Q. Han, J. Chen, J. Graetz, *ACS Appl. Mater. Interfaces* **2010**, *2*, 1548–1551.
[32] L. O. Vogt, C. Villevieille, *J. Mater. Chem. A* **2017**, *5*, 3865–3874.

[33] W. X. Lei, Y. Pan, Y. C. Zhou, W. Zhou, M. L. Peng, Z. S. Ma, *RSC Adv.* **2014**, *4*, 3233 – 3237.
[34] Y. M. Lin, P. R. Abel, A. Gupta, J. B. Goodenough, A. Heller, C. B. Mullins, *ACS Appl. Mater. Interfaces* **2013**, *5*, 8273 – 8277.
[35] Z. Liu, T. Song, U. Paik, *J. Mater. Chem. A* **2018**, *6*, 8159 – 8193.
[36] M. Walter, S. Doswald, M. V. Kovalenko, *J. Mater. Chem. A* **2016**, *4*, 7053 – 7059.
[37] M. He, M. Walter, K. V. Kravchyk, R. Erni, R. Widmer, M. V. Kovalenko, *Nanoscale* **2015**, *7*, 455 – 459.
[38] J. Zhu, D. Wang, T. Liu, C. Guo, *Electrochim. Acta* **2014**, *125*, 347 – 353.
[39] X. Liu, J. Xie, H. Zhao, P. Lv, K. Wang, Z. Feng, K. Świerczek, *Solid State Ionics* **2015**, *269*, 86 – 92.
[40] F. Nacimiento, P. Lavela, J. L. Tirado, J. M. Jiménez-Mateos, *J. Solid State Electrochem.* **2012**, *16*, 953 – 962.
[41] S. Il Lee, S. Yoon, C. M. Park, J. M. Lee, H. Kim, D. Im, S. G. Doo, H. J. Sohn, *Electrochim. Acta* **2008**, *54*, 364 – 369.
[42] P. Chen, L. Guo, Y. Wang, *J. Power Sources* **2013**, *222*, 526 – 532.
[43] H.-S. Kim, J. B. Cook, S. H. Tolbert, B. Dunn, *J. Electrochem. Soc.* **2015**, *162*, A5083 – A5090.
[44] V. Augustyn, P. Simon, B. Dunn, *Energy Environ. Sci.* **2014**, *7*, 1597 – 1614.
[45] T. Brezesinski, J. Wang, S. H. Tolbert, B. Dunn, *Nat. Mater.* **2010**, *9*, 146 – 151.
[46] L. Yang, X. Li, S. He, G. Du, X. Yu, J. Liu, Q. Gao, R. Hu, M. Zhu, *J. Mater. Chem. A* **2016**, *4*, 10842 – 10849.
[47] J. Li, Z. Luo, F. He, Y. Zuo, C. Zhang, J. Liu, X. Yu, R. Du, T. Zhang, M. F. Infante-Carrió, P. Tang, J Arbiol, A Cabot, *J. Mater. Chem. A* **2018**, *6*, 22915 – 22924.
[48] H. Fjellvåg, A. Kjekshus, R. Stomberg, R. Zingales, I. Vikholm, F. Urso, J. Weidlein, R. A. Zingaro, *Acta Chem. Scand.* **1986**, *40a*, 23 – 30.
[49] M. He, L. Protesescu, R. Caputo, F. Krumeich, M. V. Kovalenko, *Chem. Mater.* **2015**, *27*, 635 – 647.
[50] J. Li, Z. Luo, Y. Zuo, J. Liu, T. Zhang, P. Tang, J. Arbiol, J. Llorca, A. Cabot, *Appl. Catal. B* **2018**, *234*, 10 – 18.
[51] Y. Liu, X. Liu, Q. Feng, D. He, L. Zhang, C. Lian, R. Shen, G. Zhao, Y. Ji, D. Wang, G. Zhou, Y. Li, *Adv. Mater.* **2016**, *28*, 4747 – 4754.
[52] C. H. Cui, X. J. Liu, H. H. Li, M. R. Gao, H. W. Liang, H. Bin Yao, S. H. Yu, *ChemCatChem* **2012**, *4*, 1560 – 1563.
[53] N. Mahmood, C. Zhang, F. Liu, J. Zhu, Y. Hou, *ACS Nano* **2013**, *7*, 10307 – 10318.
[54] C. Lupu, J. G. Mao, J. W. Rabalais, A. M. Guloy, J. W. Richardson, *Inorg. Chem.* **2003**, *42*, 3765 – 3771.
[55] K. Kravchyk, L. Protesescu, M. I. Bodnarchuk, F. Krumeich, M. Yarema, M. Walter, C. Guntlin, M. V. Kovalenko, *J. Am. Chem. Soc.* **2013**, *135*, 4199 – 4202.
[56] R. Hu, Y. Ouyang, T. Liang, H. Wang, J. Liu, J. Chen, C. Yang, L. Yang, M. Zhu, *Adv. Mater.* **2017**, *29*, 1605006.
[57] Y. He, A. Li, C. Dong, C. Li, L. Xu, *Chem. Eur. J.* **2017**, *23*, 13724 – 13733.
[58] J. Qin, X. Zhang, N. Zhao, C. Shi, E. Liu, J. Li, C. He, *RSC Adv.* **2014**, *4*, 49247 – 49256.
[59] J. Qin, D. Liu, X. Zhang, N. Zhao, C. Shi, E. Z. Liu, F. He, L. Ma, Q. Li, J. Li, C. He, *Nanoscale* **2017**, *9*, 15856 – 15864.
[60] Z. Wang, D. Wang, S. Luo, S. Bao, Y. Liu, X. Qi, C. He, C. Shi, N. Zhao, *New J. Chem.* **2017**, *41*, 393 – 402.
[61] C. Chen, Y. Wen, X. Hu, X. Ji, M. Yan, L. Mai, P. Hu, B. Shan, Y. Huang, *Nat. Commun.* **2015**, *6*, 6929.
[62] T.-C. Liu, *J. Electrochem. Soc.* **1998**, *145*, 1882.
[63] X. Xu, S. Ji, M. Gu, J. Liu, *ACS Appl. Mater. Interfaces* **2015**, *7*, 20957 – 20964.
[64] X. Xu, J. Liu, J. Liu, L. Ouyang, R. Hu, H. Wang, L. Yang, M. Zhu, *Adv. Funct. Mater.* **2018**, *28*, 1707573.

Manuscript received: November 19, 2018
Revised manuscript received: January 23, 2019
Accepted manuscript online: January 24, 2019
Version of record online: February 27, 2019